Université de Nice Sophia-Antipolis
École Doctorale Sciences Fondamentales et Appliquées

THÈSE de DOCTORAT

présentée par

Iva KAROVICOVA

MULTIEPOCH INFRARED INTERFEROMETRIC OBSERVATIONS OF EVOLVED STARS AT THE VLTI

soutenue à l'Observatoire de la Côte d'Azur
le 29 Juin 2011
devant le jury composé de :

Quirrenbach Andreas	Université de Heidelberg, Allemagne	Président
Fossat Eric	Observatoire de la Côte d'Azur, France	Directeur de thèse
Wittkowski Markus	European Southern Observatory, Allemagne	Co-Directeur de thèse
Hron Josef	Université de Vienne, Autriche	Rapporteur
van Belle Gerard	European Southern Observatory, Allemagne	Rapporteur
Lopez Bruno	Observatoire de la Côte d'Azur, France	Examinateur
Chesneau Olivier	Observatoire de la Côte d'Azur, France	Invité

to my parents

Contents

Abstract

This thesis presents multi-epoch interferometric observations of evolved stars on the Asymptotic Giant Branch (AGB). The Asymptotic Giant Branch is populated by low to intermediate mass stars (0.8-9 $M_{\odot}$) in the final stage of their stellar evolution. Pulsating AGB stars suffer from strong mass loss via a dense and dusty outflow from an extended stellar atmosphere returning gas and dust to the interstellar medium. The processes leading to the violent mass loss are not well understood and are therefore under intense investigation.

Due to the AGB stars' large diameters and high luminosities, evolved stars are ideal targets for high angular resolution observations. The AGB stars presented in this thesis were observed over several pulsation cycles using the near-infrared AMBER and mid-infrared MIDI instruments at the Very Large Telescope Interferometer (VLTI). The goal of this study is to investigate the connection between the pulsation mechanism, the dust chemistry of AGB stars, and the condensation sequence in order to better understand the mass loss process.

The thesis studies a sample of four evolved stars, the oxygen-rich Mira variables RR Aql, S Ori, GX Mon, and R Cnc. We obtained multi-epoch MIDI observations and individual AMBER observations. The presented data are modeled using basic models of uniform disks and Gaussian profiles. The AMBER data, along with the basic models, are modeled using dust-free self-excited dynamic model atmospheres (P and M series). These models represent the stellar atmosphere including the continuum forming atmosphere and overlying molecular layers (Ireland et al., 2004a,b). In addition to the basic models, the MIDI data are fitted by a radiative transfer model of the circumstellar dust shell where the central stellar intensity profile is described by the previously mentioned series of dust-free dynamic model atmospheres, which are based on self-excited pulsation model. The radiative transfer model is computed using the radiative transfer code *mcsim_mpi* (Ohnaka et al., 2006). The modeling approach follows the work presented by Wittkowski et al. (2007). For all stars, two dust species of silicate and Al_2O_3 grains were examined. In order to investigate the expected variability of our mid-infrared photometric and interferometric data, model simulations using variations of model phase and dust shell parameters were performed.

The observed visibility spectra for all studied stars do not show indications of variations as a function of pulsation phase and cycle within our investigated phases and uncertainties (5%–20%). The observed photometry spectra may indicate intra-cycle and cycle-to-cycle variations

with a significance of 1–5 σ. However, the photometry variations cannot be confirmed within our uncertainties. Our study shows that the photometric and visibility spectra for all stars can be well described by the radiative transfer model of the dust shell that uses a dynamic model atmosphere describing the central source.

For all epochs, we found the best fitting models consisting of a dynamic model atmosphere, and dust shells parameters including the optical depth of the dust shell, the inner radii, the power-law index of the density distribution, and the photospheric angular diameter. The optically thin dust shell of RR Aql can be well modeled using silicate grains alone. The addition of an Al_2O_3 dust shell did not improve the model fit. However, the model simulations indicate that the presence of an inner Al_2O_3 dust shell with low optical depth compared to the silicate dust shell can not be excluded. GX Mon can be modeled with a combination of Al_2O_3 and silicate grains. The dust shell of S Ori and R Cnc can be well modeled using only Al_2O_3 dust grains without a contribution of silicates. The inner boundary radii of Al_2O_3 appears around 2-2.5 photospheric radii and the inner boundary radii of silicate appears around 4-5 photospheric radii.

The modeling simulations performed in this thesis confirmed that significant intra-cycle and cycle-to-cycle visibility variations are not expected at mid-infrared wavelengths within our uncertainties. The effects of the pulsation on the mid-infrared flux and visibility values are expected to be less than 25% and 20%, respectively, and are too low to be detected within the measurement uncertainties.

This study represents the first comparison between interferometric observations and a combination of a radiative transfer modeling with dynamic atmosphere models over an extended range of pulsation phases covering several cycles.

Résumé

Cette thèse exploite des mesures interférométriques multi-époques d'étoiles évoluées de la branche asymptotique des géantes (AGB) du diagramme HR. Il s'agit d'étoiles de masses petites à intermédiaires (0.8–9 $M_\odot$) en phase finale de leur évolution. Ces étoiles pulsantes subissent une perte de masse très importante via un vent stellaire dense et poussiéreux qui enrichit l'environnement stellaire en gaz et en poussières. Ces processus de perte de masse sont encore mal compris et font l'objet de beaucoup d'investigations. Grâce à leur luminosité et diamètre très importants, ces étoiles sont des cibles privilégiées d'observations à Haute Résolution Angulaire. Les étoiles AGB étudiées ici ont été mesurées pendant plusieurs cycles d'oscillation au moyen des deux interféromètres AMBER et MIDI du VLTI, donc en proche et moyen infra-rouge. Le but de cette investigation est la connexion entre le mécanisme de pulsation, la condensation et la chimie des poussières dans le but de mieux comprendre leur perte de masse . J'ai étudié un échantillon de 4 étoiles évoluées, les variables de type Mira riches en oxygène RR Aql, S Ori, GX Mon et R Cnc, au moyen de données MIDI multi-époques et de données AMBER individuelles. Ces données sont modélisées par des modèles standard de disques uniformes ou gaussiens. Les données AMBER sont modélisées par une atmosphère auto-excitée sans poussière incluant les couches moléculaires juste supérieures responsables du continuum spectral (modèles des séries P et M, (Ireland et al., 2004a,b). Les données MIDI permettent de rajouter à ce modèle l'enveloppe gazeuse radiative. Le transfert radiatif de l'enveloppe utilise le code *mcsim_mpi* (Ohnaka et al., 2006) et prolonge le travail de Wittkowski et al. (2007). Deux types de poussière sont envisagés, silicates et Al_2O_3. Les modèles ont été simulés à différentes phases et avec différents paramètres de l'enveloppe de poussière pour étudier la variabilité de la photométrie et de la dimension interférométrique en infra-rouge moyen. Les visibilités spectrales n'ont pas permis, pour aucune de nos étoiles, de mettre en évidence de variation significative intra-cycle ou d'un cycle à l'autre, dans nos barres d'erreur de 5 à 20%. Notre étude montre que les spectres de visibilité et de photométrie des 4 étoiles sont bien décrits pas le modèle d'enveloppe radiative au dessus d'une source centrale décrite par un modèle d'atmosphère dynamique. L'enveloppe de poussière optiquement mince de RR Aql est bien modélisée par des grains de silicates. L'addition de grains de Al_2O_3 n'améliore pas l'ajustement du modèle, mais n'exclut pas la présence d'une enveloppe interne optiquement plus mince que celle de silicates. GX Mon est bien modélisé par une combinaison de Al_2O_3 et de silicates, alors que les enveloppes de S Ori et R Cnc sont modélisables par des grains de Al_2O_3

seul sans contribution de silicates. Les rayons intérieurs des enveloppes sont de l'ordre de 2 à 2.5 rayons photosphériques pour Al_2O_3 et de 4 à 5 pour le silicate. Les modélisations effectuées dans ce travail de thèse confirment que les variations inter et intra-cycle attendues ne sont pas détectables dans la précision de nos mesures. Cette étude est la première comparaison entre des mesures interférométriques couvrant plusieurs cycles d'oscillation et des modèles couvrant une large gamme de phases des oscillations.

Motivation

The general motivation of this project is to help understand a number of long-standing key questions regarding the last evolutionary stage of low to intermediate mass stars on the Asymptotic Giant Branch (AGB). The intense mass loss observed during the AGB phase leads to the expulsion of gas and dust to the surrounding interstellar medium (ISM), enriching it by the products of the nucleosynthesis processes that took place in the core of these stars. Approximately 80% of all stars evolve through the AGB phase. AGB stars are therefore the main source of dust in our Galaxy ($>$ 50 %), returning a significant fraction of matter to the ISM and providing material for star and planet formation.

AGB stars are characterized by a significant mass loss that leads to the formation of a circumstellar envelope surrounding the star's core. The mechanisms responsible for this strong mass loss are still not fully understood, and are under intense investigation. Due to the complex interplay between pulsation, shock wave propagation, dust formation and radiation pressure, there are currently no models for oxygen-rich AGB stars able to reproduce the phenomena from first principles. Therefore, it is important to study all the processes leading to the mass loss and obtain observational constraints on the mass loss. The interior structure of AGB stars is characterized by a central and inert carbon-oxygen (C/O) core surrounded by two separate nuclear burning layers. The photospheric abundance of C/O determines the molecular composition in the atmosphere of the star (Höfner, 2009). The stars are specified by either C-rich (C$>$O) or O-rich (C$<$O) chemistry. As a consequence of the third dredge-up (which brings the chemical elements towards the stellar surface) the C/O ratio is expected to increase during the stellar evolution. Due to large amplitude, pulsations and dynamic effects such as shock fronts, the outer part of the extended stellar atmosphere becomes very cool and dense, and provides suitable condition for the formation of molecules and dust grains by condensation from the gas phase. As a consequence of the large opacity, dust created in the outer part of the atmosphere absorbs radiation from the star, and the wind is believed to be driven by radiation pressure on the dust particles which drags gas along through collisions. The mass is expelled via a dense and dusty outflow from an extended stellar atmosphere with rates of up to 10^{-4}M$_{\odot}$/year (Matsuura et al., 2009), and expansion velocities of 5-30 km/s (Höfner, 2005). However, it still remains unclear whether dust is sufficiently opaque to drive massive winds from oxygen-rich envelopes (Woitke, 2006; Höfner & Andersen, 2007). Even-

tually about 70% of the matter disperses into space in a so called 'super-wind' phase (during $\sim$ tens of thousand years), and the AGB stars evolve toward the planetary nebulae phase (Sedlmayr, 1994). The aim of the work presented here is to analyze circumstellar envelopes around AGB stars in order to better constrain the mass loss phenomenon.

AGB stars emit a large part of their flux at infrared (IR) wavelengths. Ground based observations are limited to distinct bands in the near-IR (J, H, K) and mid-IR (L, M, N and Q) due to atmosphere molecular absorption bands and a thermal background radiation, which adds to the radiation of the star and its circumstellar environment. However, in comparison with space based observations, ground based telescopes allow observations of strongly variable AGB stars at many different epochs over their pulsation cycle. The resolution of any telescope is limited by atmospheric fluctuations and by the size of its aperture (diameter of the telescope D). The angular resolution, Θ, is given by $\sin\Theta = 1.22\lambda/D$ where λ is the observed wavelength. For observations of highly complex sources such as AGB stars, high angular resolution is essential (typical photospheric angular diameter up to $\sim$10 mas). To resolve complex and very distant objects sufficiently, one would need to build a telescope with a very large aperture. Interferometry is a unique technique that offers a cost-effective alternative by combining light beams from two or more comparatively small telescopes, emulating a virtual telescope up to hundreds of meters across (distances between the telescopes are referred to as baselines). By increasing these baselines, the system is capable of very high resolutions, offering the resolving power of a virtual telescope of diameter D represented by the baseline. High angular resolution of a few milliarcseconds allows precise measurements of stellar diameters, as well as intensity profiles across stellar disks of nearby stars. Systems with three or more telescopes additionally allow the measurement of the so called closure phase which provides information about the geometry of the observed object (symmetry/asymmetry). High luminosities and very extended atmospheres are characteristics that highlight AGB stars as ideal targets for high angular resolution observations.

The AMBER (near-infrared) and MIDI (mid-infrared) instruments at the Very Large Telescope Interferometer (VLTI) of the European Southern Observatory located on Cerro Paranal in Chile allow us to investigate the location and features of molecular and dust layers of the stars over their pulsation cycles. Near-infrared interferometric observations can help us to estimate the stellar photospheric diameter, the effective temperature, the center-to-limb intensity variations, while mid-infrared interferometric observations provide information regarding the molecular shells and the dust formation zone. In particular, the goal of this project is to study the connection between the pulsation mechanism and the dust condensation sequence and in turn, better understand the mass loss process.

Despite remarkable progress in theoretical and observational studies, many physical aspects of AGB stars remain poorly understood. The presented project is focused on answering the following

questions: (i) What is the role of stellar pulsation and its connection to dust formation, and mass loss? (ii) What is the detailed atmospheric stratification and chemical composition of evolved stars? (iii) What dust species are relevant to a given AGB phase? (iv) Do the dust species change as a result of the pulsational cycle? (v) How does the amount of dust generated vary from cycle to cycle, and (vi) what is the shaping mechanism during the evolution from AGB to planetary nebulae (PNe) phase?

To answer these questions we have investigated multi-epoch interferometric observations of four oxygen-rich Mira variables RR Aql, S Ori, GX Mon, and R Cnc. The observations were conducted at various projected baselines lengths and position angles using the Very Large Telescope Interferometer (VLTI). This allows us to compare interferometric data obtained at different pulsation phases and cycles observed at very similar points in the *uv* plane. Since the visibility directly depends on the projected baseline lengths and position angles, the observations are probing layers in the same, or very closely located, depth of the atmosphere. This unique and rich sample of interferometric data allow the monitoring of the photometry and visibility spectra over their pulsation cycle(s). The data are compared to dust-free dynamic model atmosphere series representing the central source, and radiative transfer model describing the dust shell. Dynamic stellar model atmospheres with consistently included dust formation are, in particular for oxygen-rich stars, still very rare. Hence, the data are compared to the best modeling approach currently available. The investigation will provide the following:

- accurate study of the photometry and visibility spectra and their features in the mid-infrared region of the electromagnetic spectrum for four AGB stars RR Aql (13 epochs), S Ori (14), GX Mon (12), and R Cnc (2) over several pulsation cycles.
- monitoring of variability as a function of phase and cycle
- analysis of near-infrared observations for RR Aql
- determination of corresponding UD and Gaussian FWHM diameter for each data set and spectral channel
- determination of photospheric angular diameters derived by fitting the data to self-excited dust free dynamic models atmospheres (near-infrared)
- determination of photospheric angular diameters derived by fitting the data to an ad hoc radiative transfer model of the dust shell where the central stellar source is described by dust-free dynamic model atmosphere (mid-infrared) series
- investigation of dust chemistry for each star

- monitoring of variations of optical depth for the studied dust species, inner boundary radii of the dust shells, and density distribution.
- investigation of deviations from circular symmetry
- modeling simulations of intra-cycle and cycle-to-cycle photometry and visibility variations theoretically expected at mid-infrared wavelength.

The results from the project will allow refinements and enhancements of state-of-the-art dynamic model atmospheres and radiative transfer modeling codes, which will help us to understand the physical processed involved.

In this thesis the first two Chapters are devoted to the general introduction. First, the introduction gives the basic theory of AGB stars (Chapter 1.1) including evolutionary states (Sec. 1.1.1 and Sec. 1.1.2), variability (Sec. 1.1.4), molecule and dust formation (Sec. 1.1.5), and mass loss of AGB stars (Sec. 1.1.7). Chapter 2 focuses on infrared interferometry. After a short section on the theoretical background of optical interferometry (Sec. 2.1) the Chapter is devoted to the AMBER and MIDI instruments at the VLTI. Along with a description of the instruments (Sec. 2.2.4 and Sec. 2.2.5), the Chapter consists of sections regarding the preparation of interferometric observations (Sec. 2.3), near- and mid- infrared observables at the VLTI (Sec. 2.3.2 and Sec. 2.3.2), as well as data reduction procedures dedicated to the AMBER and MIDI data (Sec. 2.5 and Sec. 2.4).

The practical part of the thesis and the description of investigated data collected during observational runs at the VLTI starts in Chapter 3. All the following Chapters consists entirely of work I conducted myself during my PhD. I was responsible for the data reduction, processing of all observational data, application of the modeling approach, determination of all presented stellar parameters, and conducting test simulations in order to interpret the performed results. The only exception is the development of the highly complex dust-free dynamic atmosphere models (Sec. 4.1 and of the radiative transfer code (Sec. 4.2), which was done by Ireland et al. (2004a), Ireland et al. (2004b) and Ohnaka et al. (2006).

Chapter 3 briefly summarizes the theory of the data calibration, and describes in detail the calibration procedure of the large sample of data reduced within this project. This includes monitoring and comparison of ambient conditions (Sec. 3.2) during the observations of RR Aql (April 2004 – July 2007), S Ori (February 2006 – March 2009), GX Mon (February 2006 – April 2008), and R Cnc (December 2008 – march 2009), as well as different data reduction and calibration approaches and their impact on the results (Sec. 3.4 and Sec. 3.5).

Chapter 4 explains the modeling analysis applied in this thesis. Section 4.1 introduces the complete self-excited dynamic model atmospheres of Mira stars Hofmann et al. (1998), Bessell

et al. (1996), Ireland et al. (2004a), Ireland et al. (2004b). Section 4.2 prefaces ad hoc radiative transfer models using the radiative transfer code **mpi_mcsim** (Ohnaka et al., 2006), and Section 4.3 contains the final modeling approach of an ad hoc radiative transfer modeling of the dust shell where the central stellar source is described by readily available and established dust-free dynamic model atmosphere series (Wittkowski et al., 2007). Section 4.4 outlines the steps involved in the processing of the simulations, and shows the model simulations performed in order to investigate the theoretical intra-cycle and cycle-to-cycle photometry and visibility variations for the presented stars.

Chapters 5– 9 describe interferometric observations of Mira variables RR Aql, S Ori, GX Mon, and R Cnc. Chapter 5 consists of the investigations of 13 epochs of interferometric observations of RR Aql with the MIDI instrument at the VLTI. Section 5.3.1 and Section 5.3.2 contain the analysis and monitoring of photometry and visibility spectra, and Section 5.3.5 describes the performed analysis and derived stellar parameters. Chapter 6 summarizes AMBER observations of RR Aql. Chapter 7, 8, and 9 investigate MIDI observations of S Ori, GX Mon and R Cnc at 14, 12 and 2 epochs. The brief section 9.5 of Chapter 9 contains preliminary results of R Cnc observations with various instruments obtained by our collaborators.

Chapter 10 outlines the future steps and observational possibilities offered by new or planned instruments.

Chapter 11 summarizes all performed work and derived results.

The appendix includes Sections devoted to the selection of a 'star of the month' for the AMBER instrument operations team (Appendix A), tables of calibrators used during the MIDI observations (Appendix B), and all observed epochs with the MIDI instrument (RR Aql–Appendix C, S Ori–Appendix D, GX Mon–Appendix E, and R Cnc–Appendix F).

Chapter 1

Introduction

This section is meant to be a brief introduction to the theory of stars on the Asymptotic Giant Branch. As such, only basic information is provided and details have been excluded. For further information the reader is referred to comprehensive reviews on the AGB stars, in particular Habing & Olofsson (2003), Lattanzio (2003), Herwig (2005), from where most of the following content was adopted.

1.1 AGB stars

AGB stars are one of the major sources of the chemical enrichment of galaxies, and their nucleosynthesis, taking place in the core of the star, plays an important role in our understanding of the origin of the elements. The name "Asymptotic Giant Branch" is reflecting a morphology of the evolutionary track as some of the AGB stars are asymptotically approaching the giant branch. The stars' evolution is determined by the mass at which the first nuclear reactions are initiated. The stars are divided into three classes (Iben & Renzini, 1983): Low mass stars with masses of 0.8 - 1.0 $<$ M $<$ 2 - 2.3 $M_{\odot}$, Intermediate mass stars with masses of 2 - 2.3 $<$ M $<$ 4 - 5 $M_{\odot}$ and massive stars with masses of 4 - 5 $<$ M $<$ 8 - 9 $M_{\odot}$. The limits between the different classes are not know precisely and also depend on the initial chemical composition. In this thesis, we only focus on low- and intermediate-mass stars. The following Sections 1.1.1 and 1.1.2 will describe the evolutionary stage prior to the AGB.

1.1.1 Pre-AGB low mass stars (1 $M_{\odot}$)

In the stage prior to the AGB, low mass stars radiatively burn H in their core in proton-proton chain reactions. The fusion of H continues until H is exhausted, at which point the core is composed of He (He-4) and a degenerated electron gas surrounded by an H burning layer. Since the fusion temperature of He is higher than for H, the star's core is not hot enough to initiate the He fusion. As there is no more fusion in the core, and thus no more radiation pressure to counterweight gravity, the core of the star collapses. As a result, the temperature in the core and peripheral layers raises, initiating the fusion of the H in the layer surrounding the core. At this stage the star is quickly leaving the main sequence. As the star ascends the giant branch, its radius

expands, and its luminosity increases while the temperature decreases. The material is less tightly gravitationally bound to the star, and the mass-loss rate increases while the outer envelope cools down. At these lower temperatures the opacity increases, and convection becomes the dominant energy transport mechanism. The convection reaches deeper regions where He is converted from burning H, and "dredges-up" some products to the surface in the so called 'First Dredge-Up'. He and products of the CN cycles such as ^{14}N and ^{13}C are mixed and carried upwards. The heavy He core contracts, accompanied by an increase of temperature and density.

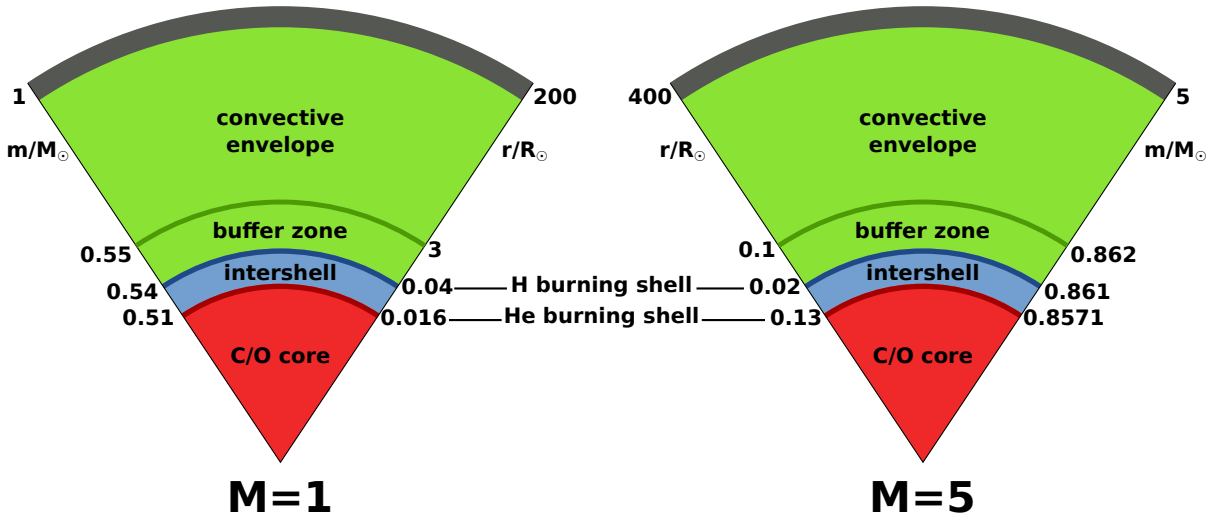

Figure 1.1: Structure of an AGB stars showing the mass and radius scaling for the layers within an AGB star of 1 $M_\odot$ (left) and 5 $M_\odot$ (right). (Based on Habing & Olofsson (2003))

When the temperature is high enough (about 100 million degrees), an intense ignition of the He burning occurs via triple-alpha reactions. The extra released energy increases the local temperature, and due to the degeneracy, the burning rate further increases. This is called the core helium flash. However, it takes more than one of these flashes to remove the degeneracy on the core. Each subsequent flash is much weaker and occurs closer to the center than the one before it. Eventually, the He core burns steadily and the core expands dramatically as a result of the energy input from the burning He. The expansion causes the H shell to be pushed outward and to cool down. This temporarily stops the H burning until the core contracts again. The star now has two energy sources: an He-burning core and an H burning shell. As He-4 burns, it initially produces ^{12}C. However, once a substantial amount of ^{12}C is present, ^{16}O is produced from ^{12}C(α,γ)^{16}O. After exhaustion of He in the core, the star ascends the giant branch for the second time. This is the beginning of the Asymptotic Giant Branch. Figure 1.1 shows the schematic structure of the star. Above the electron degenerative C/O core in the center lies the He burning shell and H burning shell providing the energy output of the star. These nuclear burning layers are surrounded by a deep convective envelope.

1.1.2 Pre-AGB intermediate mass stars (5 $M_\odot$)

For intermediate mass stars, the H is converted into He through the CNO cycles. The CNO reaction is the dominant source of energy in stars more massive than about 1.3 times the mass of the Sun. In such stars, the core is convective with an homogeneous, mixed composition. When

all the H is exhausted and converted into He-4, the star moves out of the main sequence. An H-burning shell is formed on the edge of the H-exhausted core. The star then moves toward the giant branch. Due to the convective core in earlier stages of the evolution of AGB star, the core is larger in comparison to low mass stars. The star expands in radius and the temperature of the outer envelope decrease. At these lower temperatures the opacity increases, and the energy transport mechanism is dominated by the convection. Due to the convection in the regions where the CNO cycling takes place, products such as ^{14}N from ^{12}C and ^{16}O are carried to the surface in a process known as the First Dredge-Up. Compared to the less massive stars, He is burned gently without the flash in the hot core, which in this case is less dense, avoiding degenerate ignition. The convection reaches as well regions of CNO cycling. The energy of the star is produced by two energy sources: an He-burning core and an H-burning shell. As He-4 burns it initially creates ^{12}C, and subsequently ^{16}O from ^{12}C(α,γ)^{16}O. After conversion of all of the He, the star ascents the (asymptotic) giant branch for the second time. Large amount of energy produced by the initial burning of the He shell pushes out the H-shell to regions with lower temperatures. This cooling down halts the H-burning in the shell, and later increases the opacity. The convection penetrates very deep inwards into regions where the products of H-burning are dredged up during the so called 'Second Dredge-Up'. The products of H-burning, primarily He as well as ^{14}N from CNO cycling, are mixed to the surface. The Second Dredge-up therefore increases the amount of ^{14}N and decrease the ^{12}C and ^{16}O. The following contraction of the envelope reactivates the H-burning shell. The energy is initially provided by the He shell. At the end of the second dredge-up when the H shell is reactivated, and the He shell is set to its new position, it is the H burning shell which provides most of the stellar luminosity. The Second Dredge-Up, which occurs only for stars more massive than 4 $M_\odot$, is actually already part of the next evolutionary state: the early stage of AGB evolution (E-AGB). Later on, when thermal pulses occur, the star is referred to as the thermally pulsing AGB (TP-AGB).

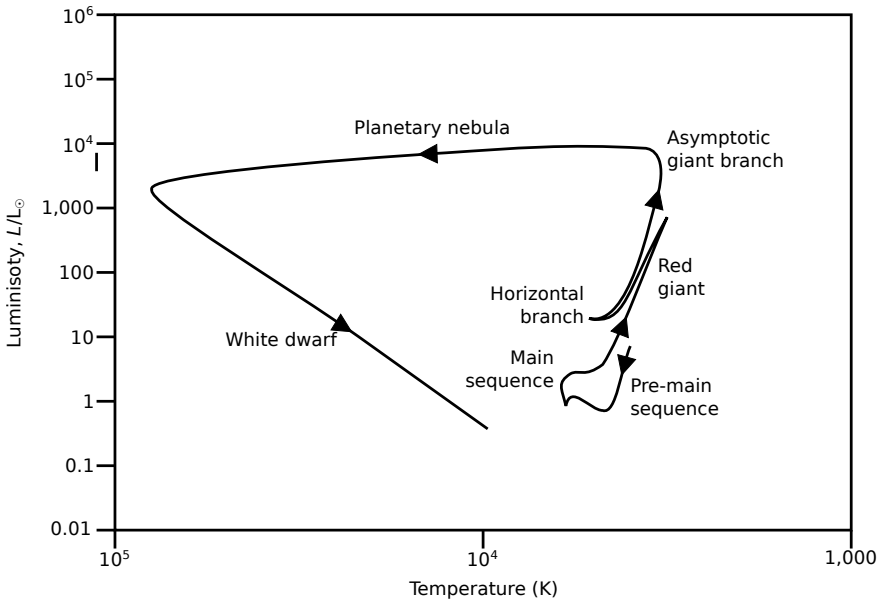

Figure 1.2: Schematic evolutionary track of a low- to intermediate mass AGB star (based on Lattanzio & Boothroyd 1997)

1.1.3 Early AGB and Thermally pulsing AGB

The AGB phase can be separated in two distinct periods: the early AGB (E-AGB) and thermally pulsing AGB (TP-AGB). The E-AGB is similar for both type of stars regardless of their initial stellar masses. The energy is provided by H-burning and He-burning shell surrounding the very compact, convective, electron degenerated, C/O core, with a radius about of 1% of $R_\odot$. The convective envelope has a chemical composition similar to the one of the interstellar medium in which the star was created. Even though the region containing the core of the star and the H and He layers accounts for half of its mass, its size is very small ($R\sim0.035R_\odot$ for stars of 1 $M_\odot$), and is similar to the size of a white dwarf. At this stage, the volume of the convective envelope accounts for most of the star's volume ($R\sim225R_\odot$ for stars of 1 $M_\odot$). The shells have almost the same mass, and they are very close to each other, because the He shell is driven outward due to the burning, and the H shell is moving the opposite direction pushed inward by the convective envelope i.e. the dredge-up. For the intermediate mass stars, this has the consequence of stopping the fusion reaction of H. The convective envelope then penetrate the H layer and the products of H burning (He and ^{14}N from the CNO cycle) are dredged up to the surface: it is the second dredge-up. Low mass stars do not have the second dredge-up but only the first and third dredge up.

The H fusion increases the mass of the degenerated C/O core, and the luminosity of the AGB stars, which is directly linked to their core mass, will increase. The thickness of the burning He layer decreases, and the layer moves away from the center of the star. As a consequence, the temperature of H layer increases, and the fusion processes can be again restarted. The star in this stage enters the thermally pulsing AGB (TP-AGB). The thin He layer around the C/O core is thermally unstable and burns episodically during flashes in so called thermal pulsations. The process of a thermal pulsation can be briefly described as follow: when H burns, it forms He, which contributes to the increase of the mass of the inner layer and compresses the burning He which is in a degenerated state. The fusion of He then follows a process similar to the He flash. The pressure then pushes away the burning H layer, which in turn cools down, and thus stops the fusion reaction of H. The H layer will be later reheated as previously, and the fusion reaction of H will start again, generating the new thermal pulse. These pulses then appear periodically. During the thermal pulse, the He layer has for a very short period a luminosity of $\sim10^7$ $L_\odot$. A convective zone then reaches the He burning layer mixing the products in this region. This zone is composed approximately of 25% C and 75% He. Shortly after the thermal pulse, the luminosity decreases while the size of the star increases. This cooling therefore leads to the interruption of the fusion in the H layer. The convection penetrates deeper within the star, and these thermal pulsation are then repeated periodically. After a few pulses, the convection penetrates the zone with material created during the flashes, dredging recently created C atoms to the surface. This is the third dredge up which is of the utmost importance for the chemistry of the circumstellar envelopes. This third dredge up differs from the previous ones due to the fact that it happens periodically after the thermal pulses. Figure 1.2 shows the evolutionary track of the star on the AGB.

1.1.4 Variability and Pulsation

AGB stars can be identified as Long-Period Variables (LPVs), pulsating in brightness, with a typical period between 40 days to 2 or 3 years. The period of the pulsation is a function of

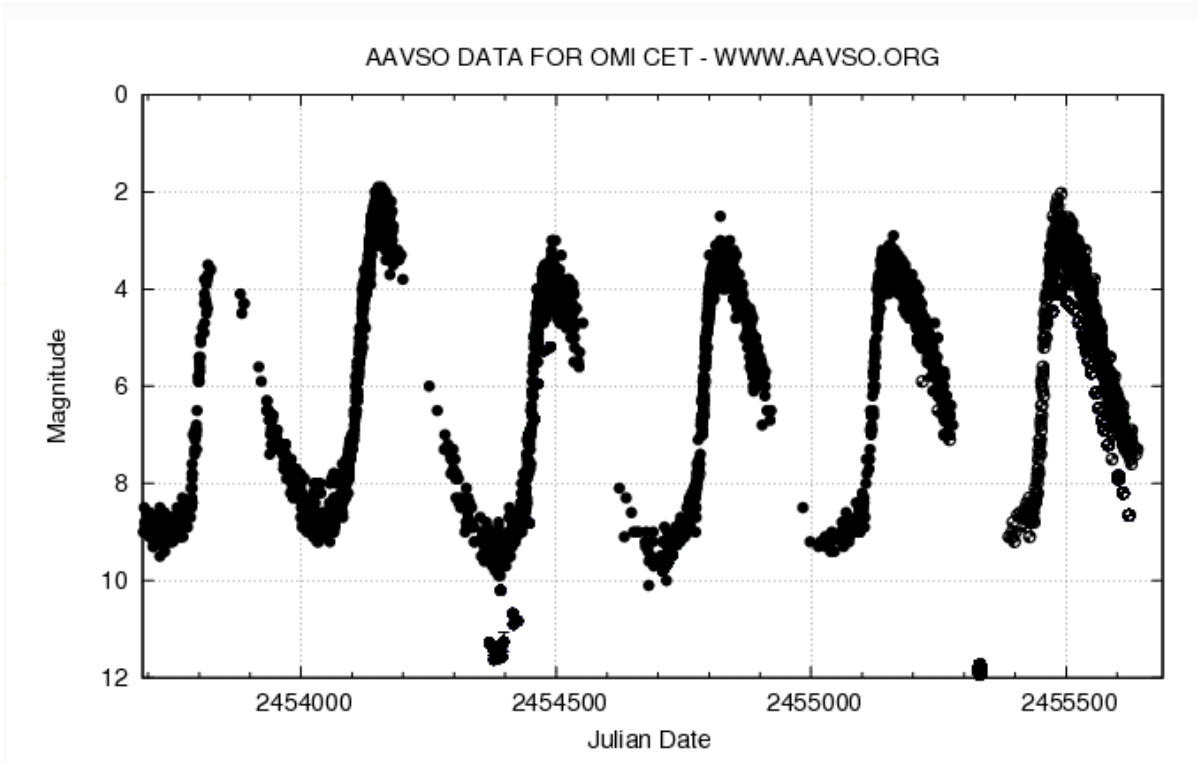

Figure 1.3: Visual light-curve of *o* Cet based on data from the AAVSO database as a function of Julian Date.

the mass and radius of the star. These pulsations produce a change in temperature along with radius, which cause a large variation in luminosity. Amplitudes range from barely detectable to factors of 200 or more ($>$ 5 magnitudes) of visual brightness. AGB stars can be 10^4–10^5 times more luminous than the Sun. The stars are classified in three groups (Kopolov et al.1998): Mira variables, semi-regular variables, or irregular variables. The classification is determined by the variability of the pulsation cycle in the V-band. Mira variables show large amplitudes ($>$ 2.5 magnitudes) and long regular periods which range between 80-1000 days. The other classes of AGB stars are called non Miras. The semi-regular variable of type *a* are called SRa and show fairly regular intensity variations, but with lower amplitude then the Miras (less then 2.5 mag in the visible), and periods between 35-1200 days. Semi-regular variables of type *b* called SRb show difficulties to determine periodicity (average cycle is between 20-2300 days), or alternative variations and irregular changes. Finally, irregular variable Lb show very weak or no periodicity.

In this thesis we focus on Mira variable stars only. Mira variables with symmetric light curves generally show broad alumina emission, while those with more asymmetric light curves show classic silicate emission (Sloan & Price, 1998). The authors suggested that these differences may arise from differences in the photospheric C/O ratio. It is known that the variability of Mira stars can be explained by radial pulsation in the fundamental mode (Wood et al., 1999). Figure 1.3 shows the light curve of the Mira star *o* Cet.

1.1.5 Molecule and dust formation

The chemical composition of dust grains and molecules formed in the circumstellar envelope reflects the chemical composition of the stellar atmosphere (Höfner, 2009), in particular the relative abundance of carbon and oxygen (C/O). The C and O combine to form a very stable CO molecule, and therefore only the atoms of the most abundant element will take part in the nucleation process and grain accretion. The stars are specified by either C-rich (C > O) or O-rich (C < O) chemistry. As a consequence of the third dredge-up, which brings the chemical elements towards the stellar surface, the C/O ratio increase during the stellar evolution. The chemistry of C-rich stars envelopes is very different than for O-rich stars. The dust from C-rich stars is mainly composed of amorphous carbon, graphite and SiC while the dust from O-rich stars is mainly composed of alumina, amorphous silicates or crystalline silicates. The other characteristics of the circumstellar envelopes such as opacity, geometry, kinematic etc, can vary considerably.

We define three types of stars based on their C/O ratio.

M type stars with C/O < 1. Their low resolution optical spectra is dominated by molecular band of TiO.

C type stars with C/O > 1 and a spectrum dominated by molecular bands of C_2 and CN.

S type stars with C/O ≈ 1 are placed in a transitory evolution state between M and C type stars. It is generally believed that the stars are following an M-S-C sequence.

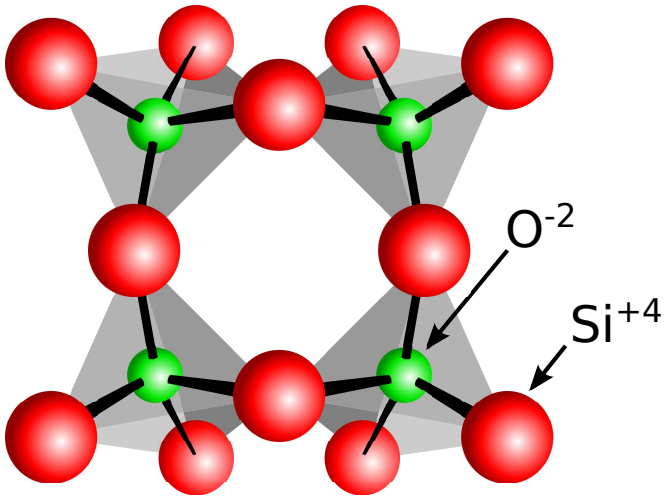

Figure 1.4: The lattice structure of silicate. The positions of Si and oxygen are indicated. Figure based on Askeland (1994)

1.1.6 Dust condensation sequence

The formation and growth of dust grains is still a widely unsolved problem. Many condensation calculations have been performed in order to explain the observed dust components and to predict the presence of not yet identified dust species. Gail & Sedlmayr (1999) have derived the condensation sequence for a gas with a composition representing the outflow of AGB stars. The calculation shows that for oxygen-rich stars the dust in the circumstellar shell is a multi-component mixture. Here, we mention only two dust components related to the investigations performed in this thesis: Al_2O_3 and silicate condensates.

Two broad emission features at roughly 9.7 μm and 18 μm are observed in a number of objects in the infrared spectral region. These are generally believed to be associated with silicate condensates. A broad emission feature around 13 μm is usually ascribed to corundum dust grains (Vardya et al., 1986), (Onaka et al., 1989), (Little-Marenin & Little, 1990), (Stencel et al., 1990), (Begemann et al., 1997), (Sloan & Price, 1998). Some other features observed between 10 μm and 19 μm are associated with metal oxides and/or crystalline silicates (Goebel et al., 1994).

Silicate Condensates

Infrared emission feature at 9.7 μm and 18 μm are characteristic for amorphous silicates. These emission features are generally believed to be associated with vibrational modes of the fundamental SiO_4 tetrahedron in silicate condensates of a largely disordered lattice structure (Fig. 1.4). Non-stoichiometric varieties, with random ratios between the Fe/Mg, Si, together with oxygen, form the main dust components responsible for most of the dust opacity and the emission of infrared radiation. Amorphous silicates are also know as glasses. The condensation of amorphous silicates proceeds at temperatures below the glass temperature. An amorphous structure is formed by molecules that stick to the surface of the grain, and immediately freeze out without having sufficient energy to find energetically favorable lattice positions. The spectrometers on board of ISO showed that in addition to amorphous silicates the crystalline silicates were found in the circumstellar environment of evolved star (Waters et al., 1996). It is under debate how both crystalline and amorphous silicates can be formed in the outflow of evolved stars. It is believed that crystalline silicates are not present in the dust shells around low mass rate AGB stars with optically thin dust shell. However, Kemper et al. (2001) showed that due to a temperature difference between amorphous and crystalline silicates it is possible to include up to 40% of crystalline silicate material in the circumstellar dust shell, without the spectra showing the characteristic spectral features.

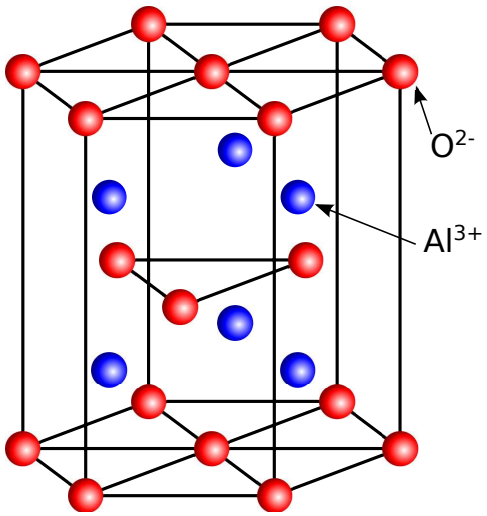

Figure 1.5: The lattice structure of corundum. The positions of aluminium and oxygen are indicated. Figure based on Askeland (1994)

Al_2O_3 – Corundum

Corundum is the crystalline form of aluminium oxide Al_2O_3. However, for historical reasons, many authors also refer to the amorphous form of Al_2O_3, which is seen in stellar environments, as corundum. It is associated with a broad Al-O vibrational band which is reported to peak around 11.5 to 11.8 μm (Begemann et al., 1997) or 13 μm (Koike et al., 1995). Corundum condensates at 1758 K and is considered to be the first solid that condensates in the outflow of oxygen-rich stars (Gail & Sedlmayr, 1999). It has been suggested that corundum serves as a seed nuclei for the subsequent silicate formation (e.g.: Deguchi, 1980; Vardya et al., 1986; Kozasa & Sogawa, 1997a,b). Due to the higher condensation temperature, these refractory grains can exist relatively close to the star. Further out, where the temperature allows formation of lower temperature condensates, Al_2O_3 become coated with silicates. Al_2O_3 grains condensate before silicate grains, not only because of the higher condensation temperature, but also due to the greater affinity of oxygen for aluminium compared to silicon (Stencel et al., 1990) (Fig. 1.5).

Little-Marenin & Little (1990) argued that there is an evolutionary sequence in the spectral features. This sequence starts with a featureless continuum, then develops toward strong silicate features. This is in accordance with a theoretical dust condensation sequence by Tielens (1990) that predicts primary condensation of refractory oxides. If in the cooler regions, further out in the circumstellar shell, the densities are high enough, the formation of silicate dust can occur. In cases where the densities are not high enough for the formation of the silicate dust, the dust condensation sequence can "freeze-out". This would imply that stars with low mass-loss rates will predominantly exhibit an oxide mineralogy while stars with high mass-loss rates will form substantial amount of silicate dust. This scenario was confirmed by Blommaert et al. (2006) showing that for low mass-loss rate stars the dust content is dominated by Al_2O_3 grains.

An alternative scenario was suggested by Sloan & Price (1998). According to the authors, the chemistry of the dust (i.e. the condensation sequence) is driven by the C/O abundance of the outflowing gas. In this scenario, less evolved star - stars with low C/O ratio - produce larger amounts of silicate grains compared to alumina grains due to the abundance of oxygen atoms, and therefore we should see strong silicate features. For more evolved stars - stars with C/O ratio close to the unity -, most of the oxygen will be bound up in CO molecules and oxygen will remain for grain condensation in order to form silicate grains. Al_2O_3 grains will therefore dominate in the dust shell. The second scenario suggests an increasing oxide dust content with an increasing mass-loss rate during the evolution of the star along the AGB.

Studying the dust present in the circumstellar envelopes in detail can help us understand the dust condensation sequence and its connection to the observed spectral features which could be eventually directly related to the evolutionary state of the star evolving on the AGB.

1.1.7 Mass-loss and Stellar wind

AGB stars exhibit strong mass loss due to the stellar wind. The loss of the mass is a major physical phenomenon during the AGB phase. The mechanisms explaining this strong mass loss during the AGB phase are still not well understood. It is believed that this mass loss is due to the combination of the stellar pulsation and the radiation pressure on the dust particles. The periodical motion induced by the internal pulsation of the star generates sound waves which propagate through the environment. The amplification of the sound waves results in the creation

of shock waves. These shock waves are able to move mass upwards and expel the molecules to great distances from the central star where dust grains can be formed. The radiation pressure on these dust grains pushes them away and drags gas by frictions. The particles escaping from the gravitational attraction of the star will then form a circumstellar envelope surrounding the star. The circumstellar dust consists of $\sim 1\%$ or less of the total mass of the object rest being gas.

The mass-loss rate that characterizes AGB stars can be as strong as 10^{-4} $M_{\odot}$/year). This means that the stars can loose 1 $M_{\odot}$ in a period as short as 10^4 years. The ejection of matter can reach a very high rate but slow speed (the wind speed in most AGB stars is within 3 - 30 km/s). The significant mass loss (10^{-4} $M_{\odot}$/year) is able to completely obscure the central star (OH/IR stars). In general, the mass-loss rate of AGB stars is lower (10^{-7} – 10^{-6}/year). The medium is thus more transparent (the dust shell is optically thin), and will let more light escape from the central source (Miras). This allows investigation of the characteristics of the star and its circumstellar environment. It is generally believed that the mass-loss rate increases during the AGB phase, and that Miras eventually evolve into OH/IR stars (van der Veen et al., 1998).

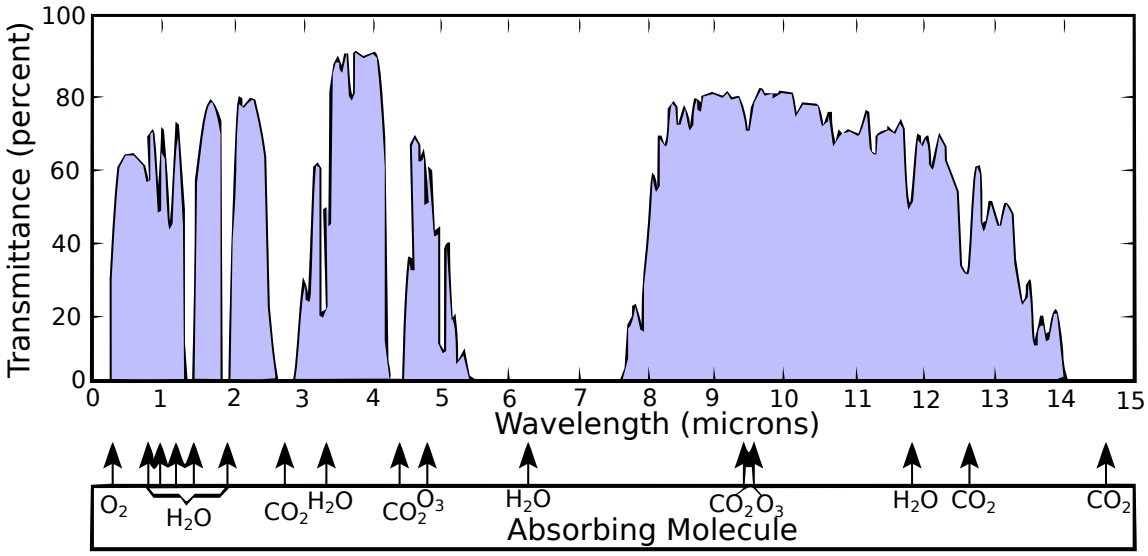

Figure 1.6: Schematic atmospheric transmissivity at infrared wavelengths. The absorbing molecules are indicated (Image courtesy of U.S. Navy).

1.2 Infrared atmosphere

The characteristic temperatures of the stellar photospheres of AGB stars have typical values T $>$ 2000 K, and stellar light is therefore mainly emitted in the visual and near-infrared. The dust absorbs the radiation and re-emits it in the mid-infrared wavelengths. Ground based infrared observations are unfortunately strongly affected by the turbulence and transmissivity of the terrestrial atmosphere. Infrared detectors can therefore only detect radiations which are not absorbed by the Earth atmosphere.

The main infrared absorption source in the atmosphere is water vapor (but also molecules of CO_2, O_3, CO, CH_4, N_2O), which blocks large parts of the infrared spectrum. Observations can

be successfully carried out on tops of mountains with an extremely dry atmosphere, pointing the telescope at a small zenith angle. The observations can proceed in so called observing "windows" centered at 1.1 – 1.4 (J-band), 1.5 – 1.8 (H), 2.0 – 2.4 (K), 3.0 – 4.0 (L), 4.6 – 5.0 (M), 7.5 – 14.5 (N), 17 – 25 (Q), and 28 – 40 (Z) μm. Figure 1.6 shows a sketch of the atmospheric absorption bands. In this thesis, we are mainly interested in J, H, K (near-infrared), and N (mid-infrared) bands. It should be noted, that another problem with infrared observations comes from the fact that our atmosphere, as well as the telescopes and instruments, emits radiation at these wavelengths.

1.3 Infrared Interferometric observations of AGB stars

In the following Section we briefly outline infrared interferometric studies of evolved stars.

Interferometric observations at near-infrared wavelengths (NIR) are well-suited to study the regions close to the central star. The investigation of these regions can provide detailed information regarding the conditions near the continuum-forming photosphere such as effective temperature, center-to-limb intensity variations, the stellar photospheric diameter, and its dependence on wavelength and pulsation phase (e.g. Haniff et al., 1995; Perrin et al., 1999; van Belle et al., 1996; Young et al., 2000a; Thompson et al., 2002a,b; Quirrenbach et al., 1992; Fedele et al., 2005; Ohnaka, 2004; Millan-Gabet et al., 2005; Woodruff et al., 2008). The variation of angular diameter as a function of wavelength and time has been researched and quantified (Woodruff et al., 2008). Multi-wavelength, multi-epoch interferometric angular diameter study on six oxygen-rich Mira stars at 3.08 μm detected cyclic diameter variations (Thompson et al., 2002a). These variations are believed to stem from time-dependent changes of density and temperature (hence varying molecular opacities) in different layers of these stars. The NIR diameters predicted by uniform disk models appear to be too small and the authors suggest incorporating additional and/or enhanced opacity mechanisms. New theoretical, self-excited, dynamic model atmospheres of oxygen rich stars have been created and successfully applied (Tej et al., 2003; Hofmann et al., 1998; Ireland et al., 2004b,a, 2008; Wittkowski et al., 2008). The self-excited dynamic model atmospheres, including molecular layers (particularly water vapor and CO), were fitted to J,H, and K spectro-interferometry observation of S Ori (Wittkowski et al., 2008). The models explain reasonably well, clear variations in the apparent angular size with wavelength. Studying the brightness distribution of AGB stars is one of the main channels to understand the origins of asymmetries seen in the subsequent evolutionary stage of strongly asymmetric planetary nebulae. Many observations of late type stars show clear evidence of departure from circular symmetry well before the planetary nebulae (PNe) phase (Ragland et al., 2006, 2008; Karovska et al., 1991, 1997; Tuthill et al., 2000; Thompson et al., 2002a). Recent observations using AMBER provide unique opportunities of direct measurements of the stellar intensity distribution (imaging), one of the most challenging programs of optical interferometry (Ragland et al., 2008; Le Bouquin et al., 2009).

Mid-infrared (MIR) interferometric observations can ideally resolve and investigate molecular shells and the dust formation zone of evolved stars. Interferometry in the mid-infrared domain is sensitive to the chemical composition and geometry of dust shells, their temperature, inner radii, radial distribution, and the mass-loss rate (e.g. Danchi et al., 1994; Monnier et al., 1997, 2000;

Weiner et al., 2006). Recently, long-term observations of the O-rich AGB star W Hya with the Infrared Spatial Interferometer (ISI) have been reported by Wishnow et al. (2010). The data has been fitted with curves which are the sum of two uniform disk (UD) functions: one for the star and another for the dust shell. The data showed temporal variations in the visibility which arise from the outward expansion of the dust shell. The reported increase in the radius of this shell, from 47 to 67 mas over the course of a year, indicates a velocity of 9 km/s, given a distance to the star of 104 pc. Lopez et al. (1997) presented long-term observations at 11 μm of o Ceti obtained with ISI. The observed visibilities change from one epoch to another and are not consistent with simple heating or cooling of the dust with change in luminosity as a function of stellar phase, but rather with large temporal variations in the density of the dust shell. The data were compared to axially symmetric radiative transfer models and suggest inhomogeneities or clumps. Tevousjan et al. (2004) studied the spatial distribution of dust around four late-type stars with ISI at 11.15 μm. It was found that the visibility curves change with the pulsation phase of the star. The dust grains were modeled as a mixture of silicate and graphite. The results suggest that the dust shells appear to be closer to the star at minimum pulsation phase, and farther away at maximum phase, also demonstrated by Wittkowski et al. (2007). Ohnaka et al. (2007) reported on temporal visibility variations of the carbon-rich Mira variable V Oph with the instruments VINCI and MIDI at the VLTI. This temporal variation of the N-band angular sizes is largely governed by the variations of the opacity and the geometrical extension of the molecular layers (C_2H_2 and HCN) and the dust shell (amC + SiC).

Figure 1.7 shows the sketch of an AGB star with regions resolved by interferometric instruments.

1.3.1 Envelope geometry

It has been shown that many AGB stars already show asymmetric brightness distribution across their stellar disk and circumstellar envelope (Ragland et al., 2006). The observations of envelopes of AGB stars studied with high angular resolutions (few milliarcsec) using optical interferometry could help us understand the origin of the breaking point toward the strongly asymmetric PN. These asymmetries can appear due to the non-isotropic characteristics of the expulsion of the star matter (Weigelt et al. 2002), (Monnier et al., 2004). Other data reveal bipolar jets which could be related to the presence of a companion which would be able to distort the circumstellar envelope of these stars (Huggins, 2007). The other processes leading to the asymmetric brightness distribution may include the emergence of magnetic fields or large-scale photospheric convection (Schwarzschild, 1975; Freytag & Höfner, 2008; Balick & Frank, 2002; Kwok, 2008)

We briefly note, that the extended CSE display one or more of the three most common maser molecules: SiO, H_2O, and OH based on the abundances of the particular maser species. The radial maser distribution in the CSE can be investigated by radio interferometry. SiO masers appear closer to the star in the stellar atmosphere, while the masing molecules H_2O and OH lie further out at larger distances of the stellar wind region. An atlas of AGB stars envelopes, compiled from radio interferometry observations at resolution of a few arcsec, shows that 30% of the AGB stars display envelope geometries strongly departing from spherical geometry (Neri et al., 1998).

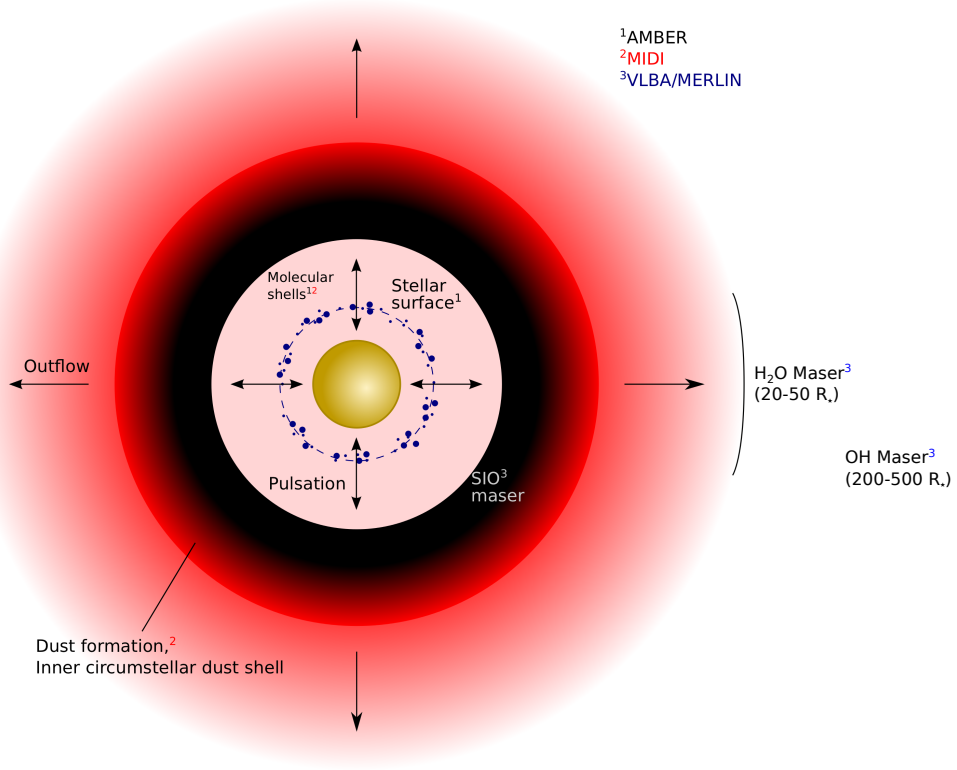

Figure 1.7: A sketch of the atmosphere and circumstellar environment of AGB star which illustrates the different regions that can be resolved and investigated using AMBER, MIDI at the VLTI and VLBI. (Image courtesy of ESO)

Chapter 2

Optical Interferometric Observations at the VLTI

The following chapter summarizes the basic principles of interferometry. For a complete introduction to optical interferometry the reader is referred to comprehensive reviews by Lawson (2000), Monnier (2003) and Quirrenbach (2001). Most of the following content is adapted from these publications and from the VLTI Summer School in 2006 and the proceedings of the Michelson Summer Workshop in 1992, and the theses of Tristram (2007) and Ratzka (2005).

2.1 Basics of Optical Interferometry

2.1.1 Monochromatic point source

Figure 2.1 represents a model of two-aperture interferometer with two identical apertures A_1 and A_2. The apertures are located at three-dimensional positions $\mathbf{x}_1$ and $\mathbf{x}_2$, separated by a displacement $\mathbf{B} = \mathbf{x}_1 - \mathbf{x}_2$, known as the *baseline*. A single celestial point source is located at relative position $\mathbf{S}$ from the interferometer. Each aperture is pointing in the direction that is given by the unit vector $\hat{\mathbf{s}} = \mathbf{S}/|\mathbf{S}|$. After approximation, the source is considered as monochromatic with wavelength λ, and with a sufficient distance from the interferometer that the phase-front of the incident optical radiation field is planar. The angular frequency of the plane wave is $\omega = 2\pi\nu$. The field at positions $\vec{x}_A$ and $\vec{x}_B$ is given by

$$\vec{E}_A = \vec{E}_{A,0}\, e^{i\vec{k}\vec{x}_A - i\omega t} \tag{2.1}$$

$$\vec{E}_B = \vec{E}_{B,0}\, e^{i\vec{k}\vec{x}_B - i\omega t} \tag{2.2}$$

$$= \vec{E}_{B,0}\, e^{i\vec{k}\vec{x}_A + i\vec{k}\vec{B} - i\omega t} \tag{2.3}$$

where $\vec{k} = \text{-}k\vec{s} = 2\pi/\lambda \cdot \vec{s} = \omega/\mathrm{c} \cdot \vec{s}$ is the wave vector and λ is the wavelength. Without loss of generality, the common phase can be omitted, hence

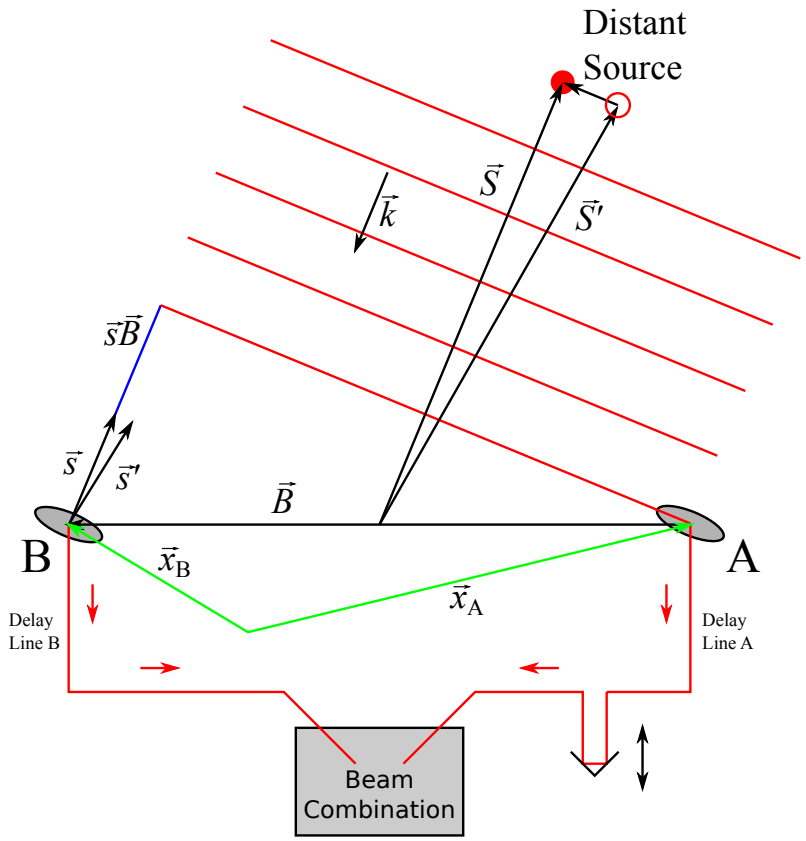

Figure 2.1: Schematic sketch of an astronomical interferometer. Light from the target is intercepted by the two telescopes, is relayed to the delay lines, and mixed in the beam combiner see Figure 2.2) (adapted from Haniff, 2007)

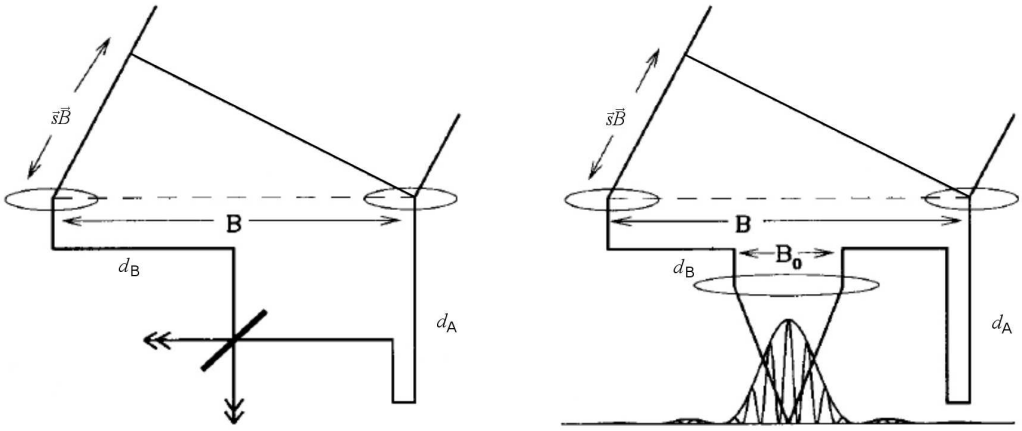

Figure 2.2: A schematic sketch of two possible ways to interfere the light. Michelson recombiner - the beam is combined in the pupil plane (left), Fizeau recombiner - the beam is combined in the image plane (right). See text for details.

$$\vec{E}_A = \vec{E}_{A,0}\, e^{-i\omega t} \tag{2.4}$$
$$\vec{E}_B = \vec{E}_{B,0}\, e^{ik\vec{s}\vec{B}}\, e^{-i\omega t} \tag{2.5}$$
$$\tag{2.6}$$

This means that the phase shift between the signal and the two apertures is determined by the difference in optical path, $\vec{s} \cdot \vec{B}$. The light is then propagated along the path via mirrors and delay lines, with total lengths d_A and d_B towards the detector. This introduces an additional relative phase and the electromagnetic fields become:

$$\vec{E}_A = \vec{E}_{A,0}\, e^{ikd_A}\, e^{-i\omega t} \tag{2.7}$$
$$\vec{E}_B = \vec{E}_{B,0}\, e^{ikd_B}\, e^{-ik\vec{s}\vec{B}}\, e^{-i\omega t} \tag{2.8}$$

In contrast to radio interferometers, optical or infrared detectors measure only a time-averaged intensity $I_{det} = \left|\vec{E}\right|^2 = \vec{E} \cdot \vec{E}^\star$ of the total electrical field $\vec{E} = \vec{E}_A + \vec{E}_B$

$$I_{det} = (\vec{E}_A + \vec{E}_B) \cdot (\vec{E}_A^\star + \vec{E}_B^\star) \tag{2.9}$$
$$= \vec{E}_{A,0}^2 + \vec{E}_{A,0}\vec{E}_{B,0}\, e^{ik(d_A - d_B + \vec{s}\vec{B})}\, \vec{E}_{A,0}\vec{E}_{B,0}\, e^{-ik(d_A - d_B + \vec{s}\vec{B})} + \vec{E}_{B,0}^2 \tag{2.10}$$
$$= I_a + I_B + \sqrt{I_A I_B} \cdot 2\cos\left[k\,(d_A - d_B + \vec{s}\vec{B})\right] \tag{2.11}$$
$$= I_{src}(\eta_A + \eta_B + 2\sqrt{\eta_A \eta_B} \cdot \cos k\delta) \tag{2.12}$$

where the identity $2\cos\alpha = \mathrm{e}^{i\alpha} + \mathrm{e}^{-i\alpha}$ was used. In order to take into account the different intensities $I_A = \eta_A I_{src} = \left|\vec{E}_A\right|^2$ and $I_B = \eta_B I_{src} = \left|\vec{E}_B\right|^2$ of the beams from the two telescopes, *e.g.* due to a different size of the telescopes or the different transmission characteristics of the optical elements, the factors η_A and η_B were introduced. The *optical path difference* (OPD) is given by $\delta = d_A - d_B + \vec{s}\vec{B}$.

Both, changing the external optical delay, $\vec{s} \cdot \vec{B}$ (OPD_{extern}), *e.g.* by changing the pointing of the telescope or the position of the source, and the internal optical delay $d = d_A - d_B$ (OPD_{intern}), *e.g.* by shifting the so-called optical delay lines leads to an oscillation of the intensity I_{det}. The oscillations are known as interferometric *fringes*.

Resolution of an Interferometer

The angular resolution of an interferometer can be estimated by applying the Rayleigh criterion. A second source at $\vec{S}'$ is resolved, when the peak of the fringe pattern for the first source falls into at least the first minimum on the fringe pattern of the second source. This means that the two fringe patterns are shifted by half a wavelength with respect to each other.

$$k\,(d + \vec{s}\vec{B}) = k\,(d + \vec{s}'\vec{B}) + \pi \tag{2.13}$$

This can be simplified to

$$(\vec{s} - \vec{s}')\,\vec{B} = \frac{\lambda}{2} \tag{2.14}$$

where $k = 2\pi/\lambda$ was used. The left side of the equation can be rewritten with the baseline projecting on the separation vector $\vec{\zeta} = \vec{s} - \vec{s}'$, that is $(\vec{s} - \vec{s}')\,\vec{B} = \zeta B_{proj}$, where B_{proj} is a *projected baseline*. For the resolution of the interferometer we obtain

$$\zeta_{Rayleigh} = \frac{\lambda}{2B_{proj}} \tag{2.15}$$

Alternatively, the resolution can be defined as the inverse of the spatial frequency of the fringe pattern, that is,

$$\zeta_{fringe} = \frac{\lambda}{B_{proj}} \tag{2.16}$$

Beam Combination

Interferometric combination of incoming beams can be divided into two classes according to the method of the beam combination. *Fizeau Interferometers (Image-Plane)* combine the beams in the image plane (Fig. 2.2). The fringes are produced by directly focussing the beams onto the detector. This is very similar to Young's experiment. *Michelson Interferometers (Pupil-Plane)* superimpose the coplanar incoming beams by using a beam combiner (half-coated mirror).

After passing the beam combiner, the two electrical fields are given by

$$\vec{E}_1 = \sqrt{t}\vec{E}_A + \sqrt{r}\vec{E}_B\, e^{i\frac{\pi}{2}}\vec{E}_2 = \sqrt{r}\vec{E}_A\, e^{i\frac{\pi}{2}} + \sqrt{t}\vec{E}_B \tag{2.17}$$

The phase shift $e^{i\frac{\pi}{2}}$ is introduced by the reflection on the half-silvered mirror. The factors r and t are the coefficients for reflection and for transmission of the intensities I_A and I_B respectively. The intensities measured by the detectors are given by:

$$I_1 = tI_A + rI_B + 2\sqrt{tI_A rI_B}\cdot \sin k\delta I_2 = rI_A + tI_B + 2\sqrt{rI_A tI_B}\cdot \sin k\delta \tag{2.18}$$

Because the two output beams have the opposite phase, they can be subtracted from one another:

$$\begin{aligned} I &= I_1 - I_2 = (r - t)\,(I_A - I_B) + 4\sqrt{rtI_A I_B}\cdot \sin k\delta && (2.19)\\ &= I_{src}\,[(r - t)\,(\eta_A - \eta_B) + 4\sqrt{rt\eta_A\eta_B}\cdot \sin k\delta] && (2.20)\\ & && (2.21) \end{aligned}$$

For an ideal interferometer, $\eta_A = \eta_B = 1$ and for a perfect beam splitter, $r = t = 0.5$, so that the background $I_{back} = I_{src}\,(r-t)\,(\eta_A - \eta_B)$ vanishes and only the interferometric component remains:

$$\begin{aligned} &= 4\,Isrc\sqrt{rt\eta_A\eta_B}\cdot \sin k\delta] && (2.22)\\ &= 2I_{src}\sin k\delta && (2.23) \end{aligned}$$

In the following, only this interferometric contribution to the total intensity I will be considered.

2.1.2 Polychromatic sources

So far it was assumed that the light emitted from an astronomical source is monochromatic. However, in reality astronomical sources emit light in a large wavelength range with a spectral intensity $I_{src}(k)$ (the optical set-up has moreover finite passbands $\eta_A(k)$ and $\eta_B(k)$). The electromagnetic waves at different wavelengths are mutually uncorrelated. The interferometric component of the intensity is then the integral over all wave numbers.

$$I_{int} = \int 4\, I_{src}(k) \sqrt{r(k)t(k)\eta_A(k)\eta_B(k)} \cdot \sin k\delta \, \mathrm{d}k \tag{2.24}$$

Assuming a wavelength-independent intensity, a perfect beam splitter, and an ideal interferometer with a bandpass in the form of a top hat function centered at k_0 and with a width Δk, the factors $\eta_A(k)$ and $\eta_A(k)$ are then given as

$$\eta_A(k) = \eta_B(k) = \eta(k) = \begin{cases} \eta_0 & \text{for } k_0 - \Delta k/2 < k < k_0 + \Delta k/2 \\ 0 & \text{else.} \end{cases} \tag{2.25}$$

I_{int} then takes form

$$I_{int} = 2 I_0 \eta_0 \int_{k_0-\Delta k/2}^{k_0+\Delta k/2} \sin k\delta \mathrm{d}k \tag{2.26}$$

The integration gives

$$I_{int} = 2 I_0 \eta_0 \Delta k \, \sin k_0\delta \, \frac{\sin(\Delta k/2 \cdot \delta)}{\Delta k/2 \cdot \delta} \tag{2.27}$$

$$= 2 I_{bp} \, \sin k_0\delta \, \sin c\,(\Delta k/2 \cdot \delta) \tag{2.28}$$

where $I_{bp} = I_0\eta_0\Delta k$ is the total collected power in the bandpasses.

Fringes are observed only if the optical delay δ is smaller then the coherence length Λ_{coh}

$$\Lambda_{coh} = \frac{\lambda_0^2 - \Delta\lambda^2/4}{\Delta\lambda} \approx \frac{\lambda_0^2}{\Delta\lambda}, \tag{2.29}$$

where the approximation is valid for $\Delta\lambda \ll \lambda$.

If the interferometric signal is dispersed with a spectral resolution of $\mathrm{R} = \lambda_0/\Delta\lambda$, then $\Lambda_{coh} = R\lambda_0 - \lambda_0/4R$.

The sinc function is the Fourier transform $\mathcal{F}[\eta(k)]$ of the spectral filter function $\eta(k)$. This is true for all shapes of bandpasses and source intensities, *i.e.*

$$I_{int} = 2 I_{bp} \, \sin \, k_0\delta \, \mathcal{F}[\eta(k)](\Lambda_{coh}, \delta) \tag{2.30}$$

2.1.3 Extended sources

Most of the astronomical sources emit light at different wavelengths, but additionally they are not pure point sources as well. An extended source can be then described as a superposition of point sources which are mutually incoherent:

$$I_{int} = \int 4I(\vec{s})\sqrt{rt\eta_A\eta_B}\,\sin\left(k(d - \vec{s}\vec{B})\right)\,\mathrm{d}\vec{s} \tag{2.31}$$

$$= \frac{2\sqrt{rt\eta_A\eta_B}}{i}\,[e^{ikd}\int I(\vec{s})\,e^{-ik\vec{s}\vec{B}}\,\mathrm{d}\vec{s} - e^{-kd}\int I(\vec{s})\,e^{ik\vec{s}\vec{B}}\,\mathrm{d}\vec{s}] \tag{2.32}$$

The two integrals can be interpreted as two-dimensional Fourier transforms of the intensity distribution $I_{\vec{s}}$:

$$\mathcal{I}(\vec{B}_{proj}/\lambda) = \int I(\vec{s})\,e^{ik\vec{s}\vec{B}}\,\mathrm{d}\vec{s} = \int I(\vec{s})e^{2\pi i\frac{\vec{s}\vec{B}}{\lambda}}\,\mathrm{d}\vec{s} = \mathcal{F}[I(\vec{s})](\vec{B}_{proj}/\lambda) \tag{2.33}$$

$$= \tilde{I}(\vec{B}_{proj}/\lambda)\,e^{i\phi(\vec{B}_{proj}/\lambda)} \tag{2.34}$$

The complex number of the Fourier transform is expressed as the absolute value $\tilde{I}$ and the phase ϕ, both function of *spatial frequency* $\vec{u} = \vec{B}_{proj}/\lambda$. The Fourier transform of a real function, like the intensity distribution $I_{\vec{s}}$ is Hermitian:

$$\mathcal{I}(-\vec{u}) = \tilde{I}(-\vec{u})\,e^{i\phi(-\vec{u})} = \tilde{I}(\vec{u})\,e^{-i\phi(\vec{u})} = \mathcal{I}^{\star}(\vec{u}) \tag{2.35}$$

This essentially means that, if two telescopes are exchanged, only the phase changes its sign. $\mathcal{V}(\vec{u}) = \mathcal{I}(\vec{u})$ is called the *complex visibility*. The *normalized visibility* is a real number:

$$V(\vec{u}) = \frac{|\mathcal{V}(\vec{u})|}{|\mathcal{V}(\vec{0})|} = \frac{\tilde{I}(\vec{u})}{\tilde{I}(\vec{0})} \tag{2.36}$$

where $\tilde{I}(\vec{0}) = \int(\vec{s})e^{2\pi i\vec{s}\vec{0}}\,d\vec{s} = I_{src}$ is the total flux of the source. $\mathrm{V}(\vec{0}) = 0$ is by definition 0, and I_{int} can be then written as

$$I_{int} = 2\sqrt{rt\eta_A\eta_B}\cdot[\frac{e^{ikd}}{i}\cdot\tilde{I}(\vec{u})\cdot e^{-i\phi(\vec{u})} - \frac{e^{-ikd}}{i}\cdot\tilde{I}(\vec{u})\cdot e^{i\phi(\vec{u})}] \tag{2.37}$$

$$= 4\sqrt{rt\eta_A\eta_B}\cdot\tilde{I}(\vec{u})\cdot\sin\left(kd - \phi(\vec{u})\right) \tag{2.38}$$

$$= 4\sqrt{rt\eta_A\eta_B}\cdot I_{src}\cdot V(\vec{B}_{proj}/\lambda)\cdot\sin\left(kd - \phi(\vec{B}_{proj}/\lambda)\right) \tag{2.39}$$

and it can be determined for unknown delay d and phase from the interferometric flux I_{int} via

$$V(\vec{B}_{proj}/\lambda) = \frac{|I_{int}|}{4\sqrt{rt\eta_A\eta_B}\cdot I_{src}} \tag{2.40}$$

2.1.4 Source morphologies

The normalized visibility $V(B_\lambda)$ defined in the previous section is the normalized Fourier transform of the brightness distribution of the source $I(\vec{s})$. This relation is called the *van Cittert-Zernike theorem*. We can now calculate the expected visibility for an arbitrary baseline and an arbitrary morphology of the source. If (r, q) are orthogonal angular coordinates on the sky with r measured

parallel to the projected baseline $\vec{B_{proj}}$ and q normal to it, then

$$I_{proj}(r) \;=\; \int I(r,q)\mathrm{d}q \tag{2.41}$$

and (u, v) are the coordinates describing the spatial frequencies u and v of the brightness distributions. We can relate the u an v to the baseline vector $\vec{B} : u = B_u/\lambda$, $v = B_v/\lambda$ where B_u and B_v are the projection on the baseline vector on the two axes. We define $r = sqrtu^2 + v^2$. In the following the basic examples of brightness distribution will be discussed.

Point source

The intensity I_0 of the point source, located at a position x_0, can be mathematically described by a Dirac δ-function:

$$I(x) = I_0\delta(x - x_0) \tag{2.42}$$

The Fourier transform of the δ function is a constant. The normalized visibility is given by

$$V(B_\lambda) = 1 \tag{2.43}$$

the source remains unity independent on the length of the baseline, that means, independent of the spatial frequency.

Uniform disk

One of the important basic morphology is a uniform circular disk of angular diameter θ. A uniform disk is often used as a first approximation to model the visibility function of resolved stars. The integrated intensity distribution I(x) is a semi-ellipse, and it is mathematically described by:

$$I(x) = \begin{cases} I_0\sqrt{1 - \left(\frac{2x}{\theta}\right)} & \text{for } -\frac{\theta}{2} < x < \frac{\theta}{2} \\ 0 & \text{else.} \end{cases} \tag{2.44}$$

The Fourier transform gives the corresponding visibility

$$V(B_\lambda) = \left|\frac{2J_1(\pi\theta B_\lambda)}{\pi\theta B_\lambda}\right|, \tag{2.45}$$

where $J_1(x) = (2\pi)^{-1}\int_0^{2\pi} cos(\tau - xsin\tau)d\tau$ is the Bessel function of the first kind of the order 1. The function has several roots, where the phase jumps by 2π.

Gaussian distributions

$$I(x) = I_0\, exp\left(-\frac{4\ln 2}{\sigma^2}x^2\right) \tag{2.46}$$

The Fourier transform of a Gaussian distribution is again a Gaussian distribution, and it is given by

$$V(B_\lambda) = exp\left(- \frac{(\pi\theta B_\lambda)^2}{4\ln 2} \right) \tag{2.47}$$

The function of the uniform disk will be used in following Section 3.3 for determination of the diameter of the calibration star. In the Chapters 5– 9 a uniform disk and a Gaussian distribution will be used for the first estimation of the diameter of science objects.

2.2 ESO Infrared Interferometers

In the following sections, infrared interferometers at Paranal Observatory will be described in more detail. Most of the following content is adapted from the VLT White Book (ESO, 1998). A broader overview of VLTI instruments and subsystems can also be found in Wittkowski et al. (2005) and Wittkowski et al. (2007). The following is meant to be a brief summary of basic information and procedures involved in interferometric observations with the VLTI instruments MIDI and AMBER, which were used for acquiring data presented in this thesis.

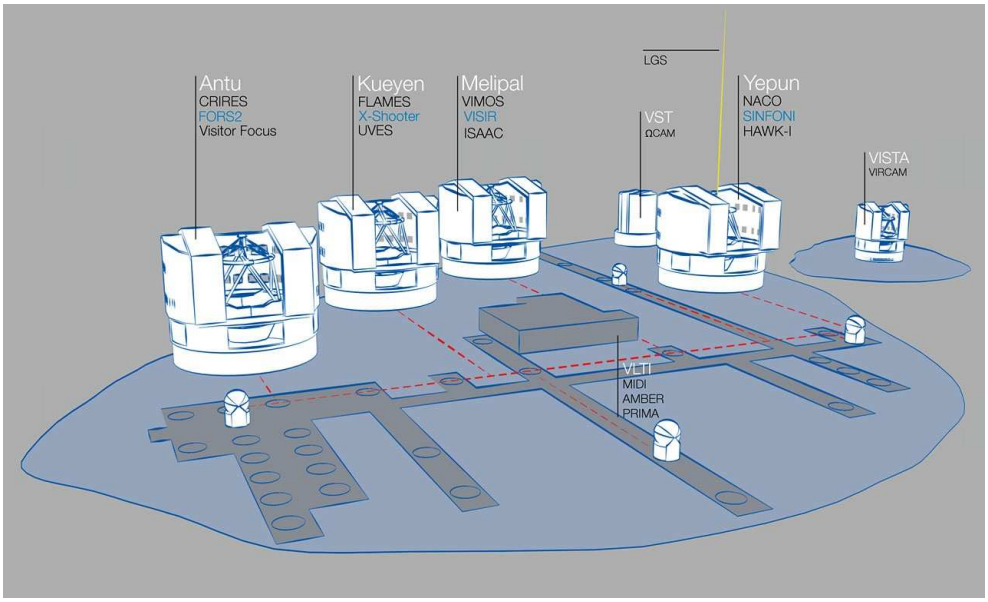

Figure 2.3: A sketch of the VLTI platform. The sketch show four *unit telescopes*, from the left to right UT1 (Antu), UT2 (Kueyen), UT3 (Melipal), and UT4 (Yepun) and the four *auxiliary telescopes*. Operating instruments are listed above each unit telescope. The VLT *survey telescope* (VST) is located between UT3 and UT4. The interferometric laboratory is located in the middle of the platform. The rails in the foreground used to move the auxiliary telescopes are indicated in dark gray (Image courtesy of ESO).

2.2.1 Paranal Observatory

The *European Southern Observatory* (*European Organization for Astronomical Research in the Southern Hemisphere, ESO*) is an intergovernmental organization for astronomical research in-

volving 16 countries that built and operate the La Silla Paranal observatory. The Paranal Observatory consists of four *Very Large Telescopes* (VLT), the *Antu* telescope, the *Kueyen* telescope, the *Melipal* telescope, and the *Yepun* telescope organized in an array formation. Each of the Unit Telescopes (UTs) has a primary mirror of 8.2 m in aperture controlled by active optics (Noethe et al. 2002). Additionally, the four UTs are accompanied by four smaller movable Auxiliary Telescopes (ATs) with primary mirrors of 1.8 m aperture. All telescopes are located on the *Cerro Paranal* mountain at 2,635 m altitude mountain in the Atacama Desert in the Republic of Chile. Paranal Observatory lies at 24° 40′ S, 70° 25′ W in northern Chile, one of the driest places on Earth. The Observatory is situated 12 km from the sea, with the closest city of Antofagasta 130 km away. The exceptional climatic conditions without light pollution or dust from industry makes this place ideal for astronomical observations.

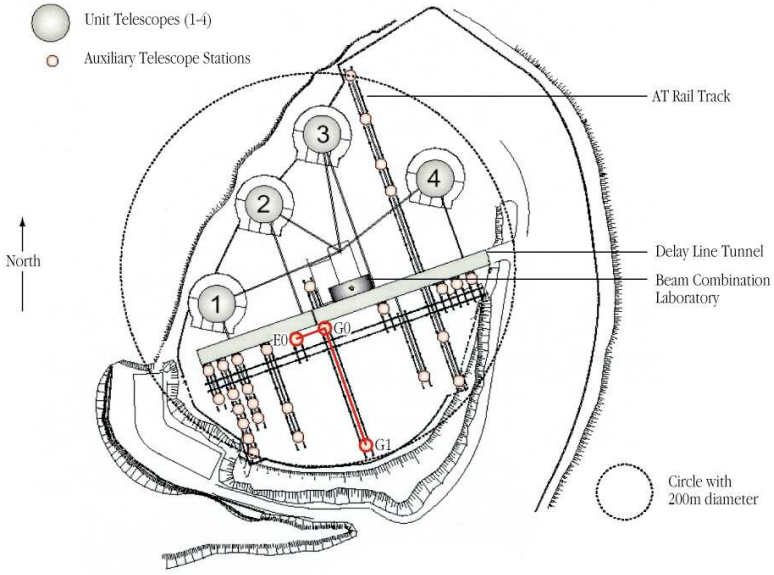

Figure 2.4: A sketch of the location of the individual telescopes stations. The labels $1-4$ indicate the locations of the four 8 m unit telescopes (UTs). The auxiliary telescopes (ATs) can be located on any of the VLTI stations represented by the small circles. Stations E0, G0, and G1 are indicated in the image. (Image adapted from Glindemann et al., 2000).

2.2.2 The VLTI

The principal role of the VLT (UTs) is to operate the telescopes independently. However, the UTs or ATs can work together in an interferometric mode as a single, large, coherent interferometric instrument. The VLT Interferometer (or VLTI) combines light from multiple telescopes, and is capable of reaching very high angular resolutions by simulating a virtual telescope with a large aperture. The angular resolution is set by the baseline configuration. The interferometric mode using UTs is about 10% percent of the observational time. Interferometry with the UTs is conducted mostly during bright time (close to the Full Moon). AT telescopes are dedicated to full-time interferometric measurements. A large number of stations for the ATs are available in a non-redundant way providing a large number of baseline configurations. The longest distance between two ATs is $\sim$ 200 meters and $\sim$ 130 meters for the UTs. The position of the telescope

stations is shown in Figure 2.4 The VLTI instruments and their operation are fully integrated, hiding the complexity of the interferometry to the regular users. This makes the interferometric observations simpler to prepare and execute. Nevertheless, the user has to be aware of the complexity of the process during the analysis and interpretation of the data.

2.2.3 Instruments at the VLTI

The optical/infrared interferometric facilities offered by the VLTI have made it worldwide the first general user interferometer for the astronomical community. The VLTI consists of two main instruments, AMBER and MIDI, performing observations at near- and mid-infrared wavelengths. The VLTI also includes the VINCI instrument, the *VLT Interferometer Commissioning Instrument* operating in the K-band - decommissioned (Kervella et al., 2003), the PRIMA facility, the *Instrument for Phase-Referenced Imaging and Microarcsecond Astrometry* covering J, H, K and N-band (van Belle et al., 2008), and the FINITO *Fringe-tracking Instrument of NIce and TOrino* operating in the H-band. The VLTI is equipped with a set of additional subsystems including a tip/tilt system, the System for Tip-tilt Removal with Avalanche Photodiodes STRAP (Bonaccini et al., 2000), and with the Adaptive Optics system MACAO on the UT, the *Multi Application Curvature Adaptive Optics* (Arsenault et al., 2003). IRIS stands for *InfraRed Image Sensor* and measures the tilt of up to 4 beams following fast guiding. All these subsystems permit to improve the sensitivity of the observations. The VLTI includes the *delay lines* in the *delay line tunnel*, and the *interferometric laboratory* where all the interferometric instruments are located.

Figure 2.5: MIDI in the interferometric laboratory (Image courtesy of ESO).

First fringes with VINCI were observed in March 2001. Regular MIDI/UT observations started at period P73 (Apr 2004 - Sep 2004), and at P76 (Oct 2005 - Mar 2006) the first observations with MIDI/ATs and AMBER/UTs were made. They were complemented by FINITO with AMBER for ATs at P80 (Oct 2007 - Mar 2008), and UTs at P82 (Oct 2008 - Mar 2009). In the same period the first fringes with the PRIMA instrument were obtained. Regular observations with

PRIMA are planned for 2012. The main instruments are described in more detail in the following sections. The instrument descriptions, the user documentations, the template manuals, links to data reduction software and cookbook for all VLTI instruments can be found on the ESO web-site[1].

2.2.4 The MIDI Instrument at the VLTI

The MID-infrared Interferometric instrument (MIDI) at the VLTI combines two beams in the pupil plane (Michelson recombiner). The light is collected either from two VLT Unit-Telescopes (UTs), or two VLT Auxiliary-Telescopes (ATs). The spectroscopic optics provide raw visibilities at different wavelengths within the N-band covering wavelengths of 7–13 μm. The instrument provides spectral resolutions of R=30 or R=230. MIDI (Fig. 2.5) benefits from the whole VLTI infrastructure including delay-lines, beam-compressors, etc. The UTs are equipped with MACAO adaptive optics that guarantees close to diffraction-limited image quality for targets brighter than V=17. The ATs with STRAP tip-tilt correctors permit a limiting magnitude for guiding of V=13.5. The MIDI instrument was built through a collaboration of several European institutes. The MIDI consortium consists of 12 institutes mostly from the Netherlands, Germany, and France. The principal investigator of the instrument is Christoph Leinert (Leinert et al., 2003). The "first fringes" were obtained in December 2002.

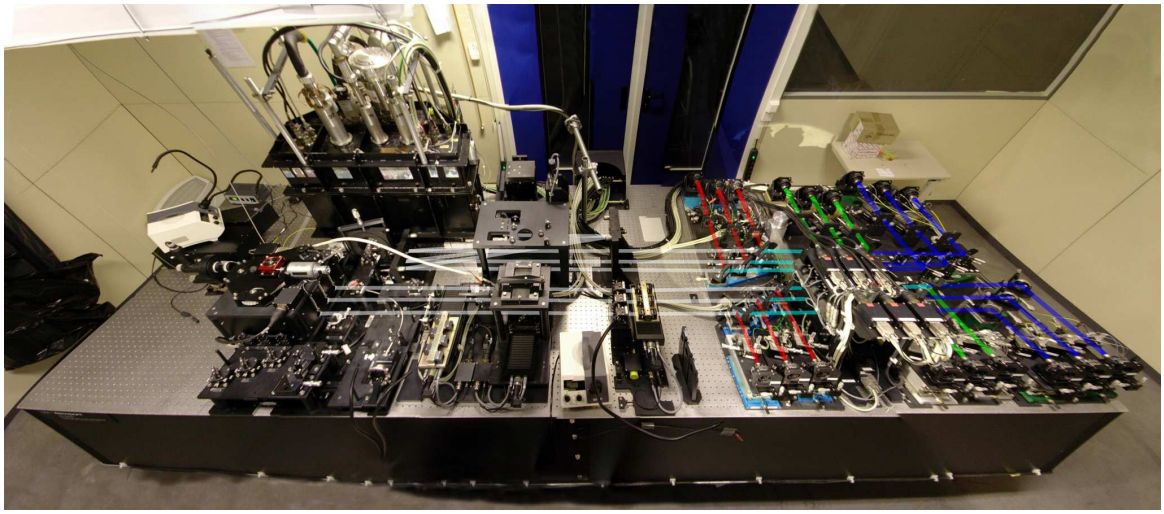

Figure 2.6: AMBER in the interferometric laboratory (Image courtesy of ESO).

2.2.5 The AMBER Instrument at the VLTI

The AMBER instrument (Fig. 2.6) - the Astronomical Multi-BEam combineR (Petrov 2007) - at the VLTI is an interferometric beam combiner that combines beams from three telescopes in the image plane (Fizeau recombiner). It operates at near-infrared wavelengths covering the J, H, and K bands (1-2.5 μmm). The AMBER project is a collaboration between five institutes: Departement Fresnel de l'Observatoire de la Côte d'Azur (Nice, OCA, France), Departement

[1] http://www.eso.org/sci/software/pipelines/

d'Astrophysique de l'Universitaire de Nice - Sophia Antipolis (Nice, UNSA, France), Laboratoire d'Astrophysique de l'Observatoire de Grenoble (Grenoble, LAOG, France), Max-Planck Institut fur Radioastronomie (Bonn, MPIfR, Germany), Osservatorio Astrofisico di Arcetri (Firenze, OAA, Italy) with contributions from other institutes.

AMBER offers spectrally dispersed visibilities for three different spatial frequencies (3 baselines) and one closure phase. The instrument currently offers High Resolution mode HR (R$\sim$12000) in the K-band (HR-K), Medium Resolution MR (R$\sim$1500) in the K- and H-band (MR-K, MR-H) and Low Resolution LR (R$\sim$30) in the K-, H-, and J- band (LR-K and LR-HK). The field of view of AMBER is limited to the Airy disk of each individual aperture, i.e. 250 mas for the ATs and 60 mas for the UTs in the K band. The highest angular resolution for the longest baseline (200 m) using ATs is reaching 2 mas in the K-band, and using UTs the limiting angular resolution is 3 mas. In the J-band the limiting values are approximately halved. Since P80 (Oct 2007 - Mar 2008) VLTI is offering for ATs AMBER together with FINITO that extended the limiting magnitude K_{mag}=5. At P82 (Oct 2008 - Mar 2009) this combination was also offered for UTS, and the current limiting magnitude in the K-band is K_{mag}=7.5.

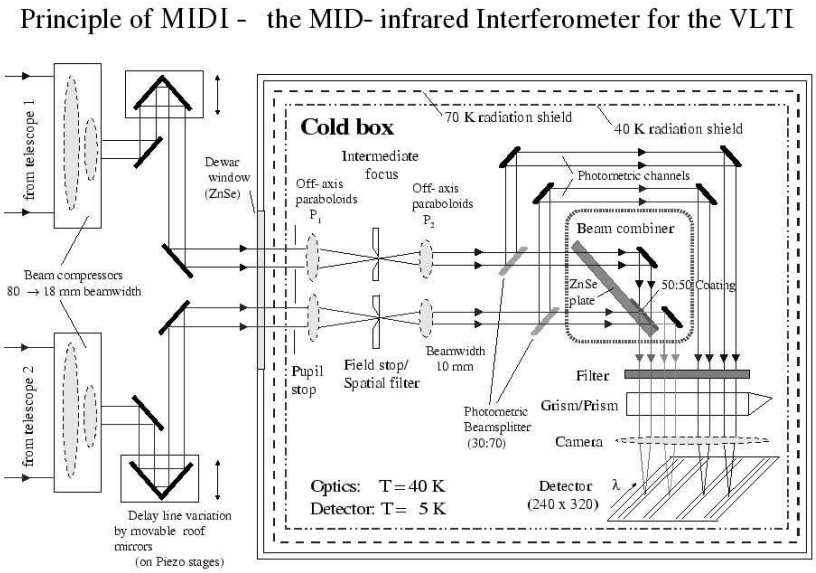

Figure 2.7: Sketch of the optical layout of MIDI. The light coming from the VLTI delay lines enters from the left. It passes the MIDI internal delay lines and it enters the cold box. After reimaging, the light is combined in the beam combiner and then passes through a filter or a dispersive element in order to reach the detector. (Image courtesy of ESO).

Elements of the MIDI interferometric instrument

The elements of the MIDI instrument are illustrated Figure 2.7. The instrument is composed of two main parts, the warm optical bench and the cold optical bench. The light path within MIDI can be summarized as follows:
The collimated beams from the telescopes are in the warm optical bench compressed by the VLTI Beam-Compressors. The optical path difference between the beams is introduced by piezo-driven roof mirrors. Each pass generates one interferogram - a "scan". The beams then enters the

cryostat (cold optical bench) where most of the optics is cooled down to several tenths of K to insulate from the environmental thermal radiation. After passing through the pupil-stops, where thermal radiation from the background and stray-light are reduced, the beams are focused on to the field-stops. The beam-combination is done close to the pupil plane. The beams can be combined either in the HIGH SENS mode or in the SCI PHOT mode. In the HIGH SENS mode, with no simultaneous photometric measurement of beams before the combination, the beam splitters are not inserted into the light path and the photometry is observed after the interferometric signal. Separated photometric measurements of both beams are recorded by blocking, first the light from one (beam A), then from the other telescope (beam B), and recording a few thousand object frames with an exposure time of a few ms. In higher precision the SCI PHOT mode allows a simultaneous measurements of the photometric and interferometric channels. The beam combiner extracts the photometry channels from the two beams (30% extraction), and the remainder is interfered to produce two channels with the interferometric signal. The beams are spectrally filtered, dispersed by the GRISM or PRISM dispersive element inserted in the light path. The detector is characterized by a fast frame readout, in order to deal with the atmospheric coherence time, and also to minimize the instrument/sky background.

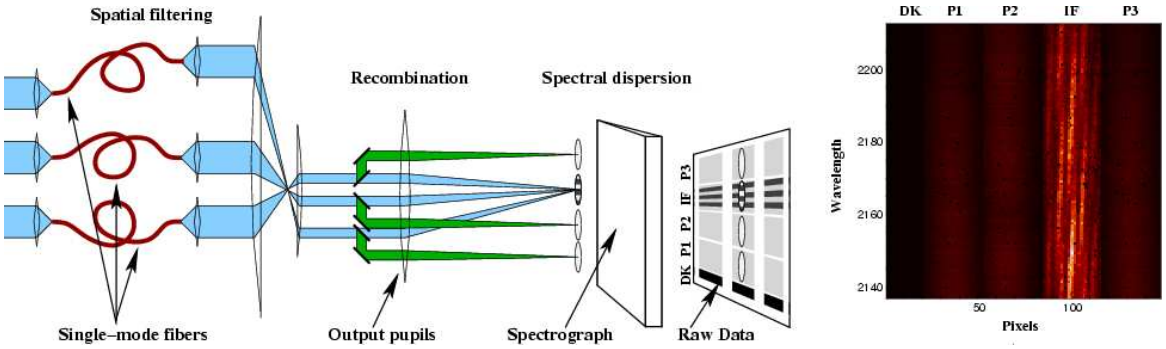

Figure 2.8: Sketch of the AMBER instrument. The light enters the instrument from the left and is propagating from left to right until the raw data are recorded on the detector (left). AMBER reconstituted image from the raw data recorded during the 3-telescope observation. DK corresponds to a dark region, Pk are the vertically dispersed spectra obtained from each telescope, and IF is the spectrally dispersed interferogram (right). Image courtesy of Tatulli et al. (2007).

Elements of the AMBER interferometric instrument

The elements of the AMBER instrument are described in the following section (Fig. 2.8).

In order to produce high accuracy measurements it is necessary to spatially filter the incoming beams. Each of them is forced to contain only a single coherent mode separated for J, H, K. Spatial filtering changes the phase fluctuations of the atmospheric turbulent wavefront into intensity fluctuations. To achieve such a high filtering quality, single mode optical fibers are used. At the output of the fibers, a set of three collimated and parallel beams form a non-redundant set up. The beams are focused by a common optical element in an Airy pattern containing fringes (beam combination in the image plane). The Airy pattern contains Young fringes with spacing specific to each baseline. This allows the separation of the interferograms in Fourier space. In order to minimize detector noise each spectral channel is concentrated in a single column of pixels by cylindrical optics. After being anamorphosed by the cylindrical optics, the Airy disk goes

through the spectrograph slit. This standard long-slit spectrograph has three different spectral resolutions of: Prism, LR mode, 30; MR grism, MR mode, 1500; HR grism, HR mode, 12000. It must be cooled down to $\sim$ –60°C, including an image plane cold stop and a cold pupil mask. The fringes are dispersed by the spectrograph on a two dimensional Rockwell/HAWAI I detector with 1024 x 1024 pixels, where only one 512 x 512 pixel quadrant is used. The detector is cooled by liquid nitrogen to 78 K. The spectral width of the detector is 0.8 μm - 2.5 μm. The photometric signals corresponding to the three incoming beams and the interferometric signal are always taken simultaneously. These signals are taken for each elementary frame and in each AMBER spectral channel, i.e. in each column of the detector. A fraction of each beam is collected before the beam combination and sent through the dispersive element to the detector to monitor the photometry variations.

2.3 Observation

2.3.1 Preparing observations

After defining the scientific goal, it is necessary to choose the best target candidates for the observations. To prepare interferometric observations, the following steps are required. Most of the following content is based on Morel (IOT overview), Malbet (2002), Percheron (2008).
First, it is necessary to clarify which region of the object and which characteristics need to be to investigated. If baselines are imposed by ESO for a certain period, the angular size of the target is the next important determining factor, and it has to be suitable for the chosen instrument & baseline. After choosing the most appropriate VLTI instrument, AMBER or MIDI, the target must satisfy parameters directly related to the instrument. It is necessary to verify the feasibility of the observations including: brightness at K band, brightness at H- band (in case of using FINITO), brightness in V for the off-axis guide star (AMBER), and brightness at N band (MIDI). This involve recommended correlated magnitudes. On account of requested spectral resolution, it can be chosen the observational mode. For an absolute visibility calibration *cal-sci-cal* sequence is recommended, for relative visibility *cal/sci* pairs are sufficient. All fundamental information for the preparation of VLTI observations are listed on the ESO web-pages including dedicated tools VisCalc and CalVin.

The *uv* coverage and VisCalc

The *uv* plane represents the projection of the distance and configuration of the telescopes - baselines in the Fourier plane. The coordinates of this plane u and v are given by the spatial frequencies $B_\lambda = B_{proj}/\lambda$, and their axes are oriented in the same direction as *right ascension* R.A.=α and *declination* Dec.=δ. The inverse Fourier transform of the visibility and phase measurements at the *uv* points give an intensity brightness distribution of the object at these positions. The goal is to measure visibility and phase at as many different positions as possible (Fig. 2.9). This is achieved by adding more points to the *uv* plane. Increasing the *uv* coverage, so called aperture synthesis, helps to reconstruct an image of the object that would be observed with the hypothetical telescope with a large aperture. Aperture synthesis can be accomplished either by adding measurements at different baseline configurations, or by taking advantage of the rotation of the Earth that would relocate the projected baseline with respect to the object. However, since the telescope time is limited, and the number of simultaneously operating telescopes is restricted to 2 for MIDI and

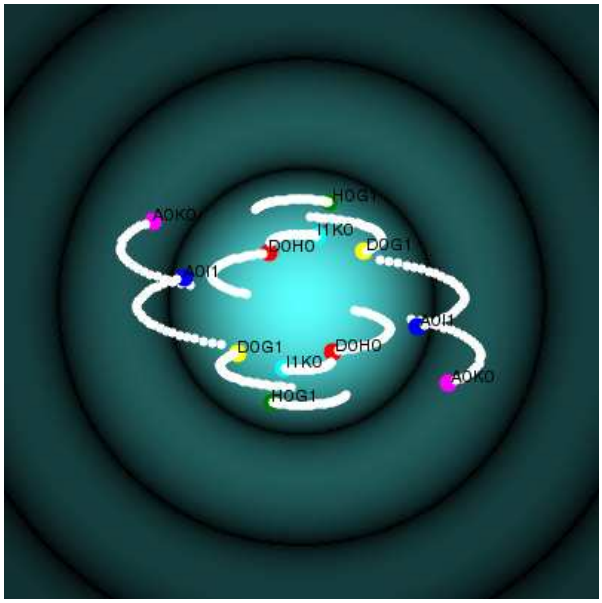

Figure 2.9: Coverage of the *uv* plane for the VLTI observations using the VisCalc.

3 for the AMBER instrument, the *uv* tracks for the science case have to be carefully selected. The VisCalc tool is specially dedicated to the determination of Visibility amplitude Calculation and the observability of the target. The basic input of VisCalc consists of the size, geometry and declination of the target and selection of the instrument, observational filter, and VLTI configuration. The baseline configuration(s), and number of required visibility points are determined by the science case. The choice of telescope configuration is influenced by the expected complexity of the object. To determine the diameter of a simple spherically symmetric object, a single triangle configuration (3 telescopes) is sufficient. For an asymmetric object it is necessary to chose ideally two perpendicular baseline configurations. With increasing complexity of the object, various baseline in sizes and orientations are required to reconstruct an image. Along with estimations of visibility amplitude over the night, the output of VisCalc, includes pointing restrictions occurring due to the altitude limit (30 deg.), the limited delay line ranges, and for some of the AT stations shadowing effects due to the UTs etc.

Choosing calibrators: CalVin

The visibility function on the known astronomical calibrator star is measured in order to estimate the effects introduced by the atmospheric turbulence and the distortion due to the instrument specification. The procedure of restoring the true visibility measurements of the science object is described in detail in Section 3.3. The calibrator star used to calibrate the science observation is selected by the Principal Investigator (PI). Suitable calibrator stars can be selected using the Calibrator Selector CalVin, a tool designated for the selection of calibrators from an underlying fixed list of calibrators. These calibrators are specially selected for the VLTI instruments (up to P86 - April 2011). The calibrators for the MIDI instrument have been chosen by the MIDI consortium and ESO. This selection is based on Cohen stars (Cohen et al., 1999). The AMBER calibrators are selected from the Mérand-BordéÌĄCatalog described in Bordé et al. (2002) and

Mérand et al. (2005). The calibrator is chosen based on different users criteria predefined in the CalVin template. The search for the best calibrator is usually constricted by the two main criteria: a distance between the science object and the calibrator, and an estimated angular diameter of the calibrator. The diameter of the calibrator should be much smaller than the diameter of the science object (see Ses. 3.3). The calibrator-science or calibrator-science-calibrator pair have to follow some observational constraints. Along with the observing conditions such as sky transparency, seeing or moon conditions, the LST range (equivalent RA) of the calibrator has to be within half an hour of the LST of the science object.

2.3.2 Different quantities observable with the VLTI instruments MIDI and AMBER

Different quantities observable with MIDI:

The measured interferometric visibility $V_{lm}(\lambda)$ is used to derive the following different quantities measured by MIDI for each baseline l-m in each spectral channel.

- Correlated flux.
- Absolute visibility $V_{lm}(\lambda)$ in each spectral channel (5-10% accuracy).
- Differential phase $\Delta\Phi_{lm}(\lambda)$
  $\Phi_{lm}(\lambda)$ and $\overline{\Phi_{lm}}$ are the phase in each spectral channel and the mean phase determined in the full N-band region, respectively. The measured phase difference $\Delta\Phi_{lm}(\lambda)$ is:

  $\Delta\Phi_{lm}(\lambda)=\Phi_{lm}(\lambda)-\overline{\Phi_{lm}}$
- Spectra in the N band with two spectral resolution 30 (PRISM) and 230 (GRISM).

Different quantities observable with AMBER:

The measured visibility $V_{lm}(\lambda)$ and the phase $\Phi_{lm}(\lambda)$ is used to derive the following different quantities measured by AMBER for each baseline l-m in each spectral channel.

- Absolute visibility $V_{lm}(\lambda)$ in each spectral channel (3% accuracy).
- Differential visibility $V_{lm}(\lambda)/\ V_{lm}(\lambda_0)$ is the ratio of the visibility in each spectral channel to the visibility in a reference spectral channel. It can be calibrated more precisely than the absolute visibility to remove channel-dependent effects. (1% accuracy).

- Differential phase $\Delta\Phi_{lm}(\lambda)$
  $\Phi_{lm}(\lambda)$-$\Phi_{lm}(\lambda_0)$ is the phase in each spectral channel minus the phase in a reference spectral channel. The measured phase difference $\Delta\Phi_{lm}(\lambda)$ is the sum of:

  $\Delta\Phi_{lm}(\lambda)$=$\Delta\Phi_{lm*}(\lambda)$+$\Delta\Phi_{lma}(\lambda)$+$\Delta\Phi_{lmI}(\lambda)$

  where $\Delta\Phi_{lm*}(\lambda)$ is introduced by the source, $\Delta\Phi_{lma}(\lambda)$ is the contribution of the differential atmospheric refraction, and $\Delta\Phi_{lmI}(\lambda)$ is the instrumental chromatic phase difference between the beams l and m. With a new phase difference $\Delta\Phi_{lm}(\lambda)$:

  $\Delta\Phi_{lm}(\lambda)$=$\Delta\Phi_{lm*}(\lambda)$-$\Delta\Phi_{lma}(\lambda)$+$\Delta\Phi_{lmI}(\lambda)$

  The difference eliminates the instrumental term $\Delta\Phi_{lmI}(\lambda)$, the atmospheric term $\Delta\Phi_{lma}(\lambda)$ can be measured on a reference star, and $\Delta\Phi_{lm*}(\lambda)$ can be neglected. The absolute phase $\Phi(\lambda)$ has no meaning till the phase referencing equipment is available.

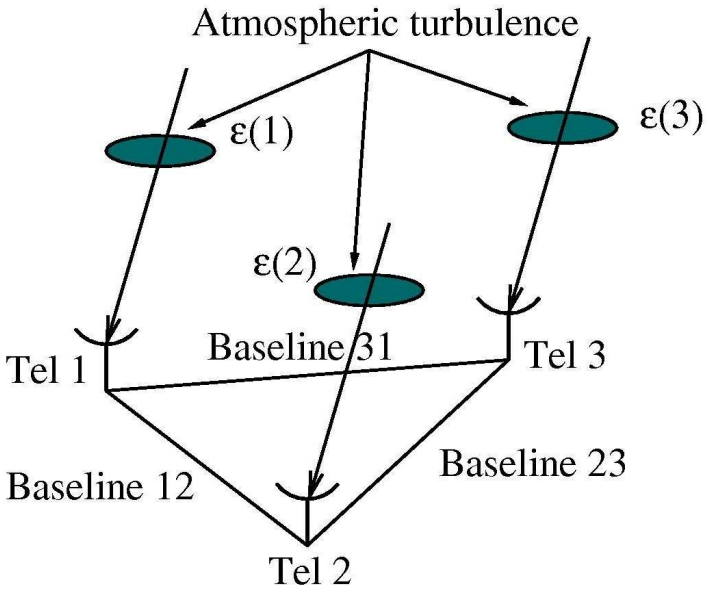

Figure 2.10: The basic principle of closure phase measurement as applied to a simple 3-element interferometer. See text for details (adapted from Haniff, 2007).

- Closure phase $\Phi_{123}(\lambda)$
  is a measured quantity for which a minimum of three telescopes are required. It is used to eliminate the effects of astronomical seeing in optical and infrared observations using astronomical interferometers, and it mainly measures the phase of the object. Phase errors introduced at any telescopes in an array causes equal but opposite phase shifts. These shifts are cancelled out in the closure phase (Fig. 2.10). Each measured visibility phase, $\Phi_0(i\text{-}j)$, is equal to the unperturbed visibility phase, $\Phi(i\text{-}j)$, accompanied by phase errors,$\phi(i)$ and $\phi(j)$. These errors are associated with the unknown optical disruption above each telescope i and j.

The closure phase is a sum of:

$\Phi(1\text{-}2) = \Phi_0(1\text{-}2) + [\phi(2) - \phi(1)]$
$\Phi(2\text{-}3) = \Phi_0(2\text{-}3) + [\phi(3) - \phi(2)]$
$\Phi(3\text{-}1) = \Phi_0(3\text{-}1) + [\phi(1) - \phi(3)]$

When all the measured visibility phases are summed, all the errors introduced by unknown optical paths are canceled out.

$\Phi(1\text{-}2) + \Phi(2\text{-}3) + \Phi(3\text{-}1) = \Phi_0(1\text{-}2) + \Phi_0(2\text{-}3) + \Phi_0(3\text{-}1)$

- Spectra in the J, H, and K band with three spectral resolutions 30 (LR), 1500 (MR), 12000 (HR).

2.3.3 Observation sequence for the VLTI instruments MIDI and AMBER

In the following Section the observational sequence for the VLTI instruments AMBER and MIDI is described (based on the MIDI User Manual, (Morel et al., 2008)). All observations with the VLTI instruments are undertaken in so-called Observational Blocks (OBs). The OBs consist of all necessary information such as: the coordinates of the science target, instrumental setup including baseline configuration, the instrumental mode, Detector Integration Time (DIT), filter, etc. The observation sequence is executed using the OBs provided by the observer. In order to obtain absolute calibrated values and to account for instrumental losses, the same observational settings are applied to both the science target and the calibrator star.

In the following the observational sequence is briefly described:

1. Pointing:

   telescope pointing toward the science target using a near by *guide star*, and delay line pointing to the expected position of 0 OPD (Optical Path Differences). Coudé guiding diverts the light to the *Adaptive Optics* (AO) system MACAO (UT) or STRAP (AT). The AO system uses a *Coudé guide star* for wavefront sensing. The desired spectral resolution is chosen, as well as the wavelength range, and DIT. Internal instrument calibration of the chosen instrument configuration is conducted (P2VM for the AMBER instrument)

2. Image optimization:

   For the interference of the beams the images from the telescopes are aligned to overlap. The background images are obtained by the standard chopping technique (MIDI). During chopping, alternating images of the target and sky are observed. This is done by tilting the secondary mirror. After subtracting the frames, ideally, only the flux from the target remains. Since 2006 image optimization uses IRIS in the interferometric laboratory to stabilize the beam position.

3. Fringe search:

   Once the beams are overlapping, the light is combined in the beam combiner, and spectrally dispersed by the PRISM or GRISM (MIDI). Two interferograms of opposite phase are recorded by the detector. Chopping is not needed for the interferometric measurements as

the background is uncorrelated and cancels out during the data reduction. The fringe signal is searched by scanning the OPD over a few mms by moving the tracking delay lines. The expected position of the 0 OPD is determined by using a model. If FINITO (external fringe tracking) is used, the fringe tracking is done by FINITO.

4. Recording data:

   When the path difference is stabilized, close to the 0 OPD, where a strong signal appears, detector frames are recorded. For a better signal, the measurements close to the 0 OPD are repeated many times. Dark exposures, fringe exposures, and sky exposures are also recorded (for AMBER).

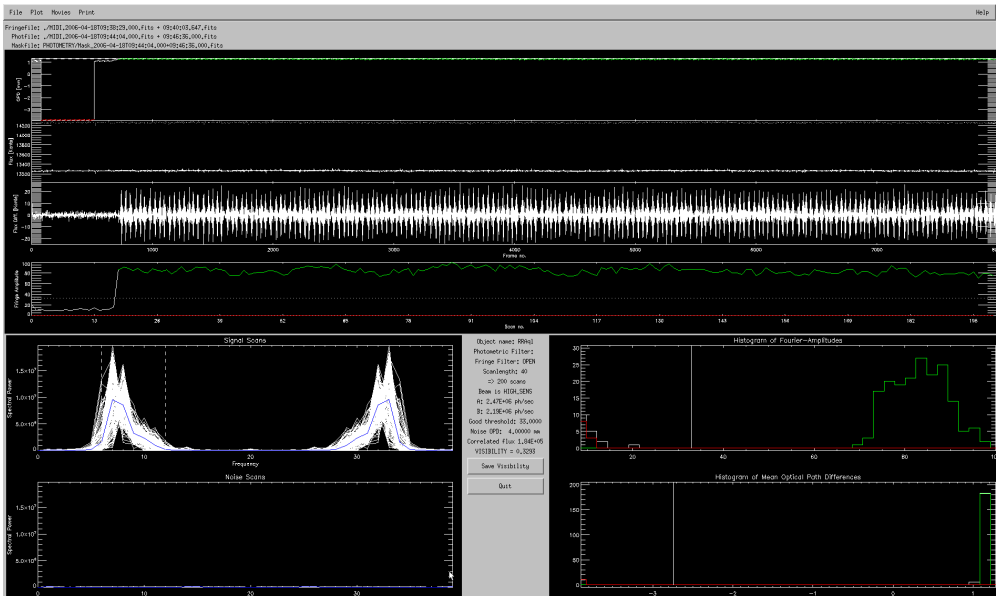

Figure 2.11: Graphical User Interface (GUI) of MIA including: histogram of mean optical path differences, mean optical path difference in the OPD panel, signal and noise scans (spectral power vs. spatial frequency), histogram of fourier amplitudes, fringe amplitudes vs. scan number in the fourier fringe amplitude.

2.4 MIDI data reduction MIA+EWS

Data reduction of the VLTI/MIDI data is provided by two main data reduction packages: the *Expert Work Station (EWS)* and the *MIDI Interactive Analysis (MIA)*. Both packages are publicly available[2] and are distributed as a single program package "*MIA+EWS*". The package consists of C-routines that carry out most of the computation, and IDL front-ends. The IDL routines check the input (select the data), and then call shell scripts that call a whole set of C-routines. Finally, the IDL routines visualize the data. The *MIA* power spectrum analysis is an incoherent method to determine the fringe amplitude. *MIA* is developed by Rainer Köhler. *EWS* uses a coherent method, and was written by Walter Jaffe.

[2]http://www.strw.leidenuniv.nl/ nevec/MIDI/ (Köhler, 2005)

The following outline the steps of data reduction proces (based on Ratzka (2005); Tristram (2007):

- Compression

  A mask is applied to each frame. The masks are specified for data taken in the HIGH_SENS mode and PRISM or in the SCI_PHOT mode and GRISM. The program adds up the pixels in the y-direction (spatial). This converts each two-dimensional frame into a one-dimensional spectrum.

- Formation of fringes and high-pass filter

  The interferometric channels are initially out of phase compared to each other. The compressed data file of the two interferometric channels are subtracted from each other, in order to get the fringe signal. This removes the background by almost 90%. Then the high-pass filter is applied, reducing the sky and instrumental backgrounds.

- Fourier transform (F.T.) to compute complex visibilities

  The known instrumental OPD is removed, and F.T. applied. The data then becomes complex

- Coherent reduction (*EWS*)

  Group delay analysis

  The FFT of the output from the previous step searches for the group delay. Several frames are averaged together in order to suppress the image peak and increase the S/N.

- Form aligned frames

  The Group Delay and the instrumental delay are removed simultaneously from the original frame.

- Editing

  In this step, unreliable frames are dropped out. Two criteria should be accomplished. There is a maximum allowable distance between tracking OPD and the Group delay OPD depending on the used spectral resolution. A large OPD jump in the estimate of the Group Delay signifies substantial OPD variation during that integration.

- Coherent average

  To estimate the complex dispersed visibility, all reliable frames are averaged together.

- Incoherent reduction (*MIA*)

  The total power method

  Each fringe scan is transformed from delay space to frequency space by Fourier transform. The power spectrum has two peaks. Their position and form is defined by the wavelength present in the band and the rate of the OPD changes. The raw correlated flux corresponds to the integrated power inside the correct frequency interval. However, the fluctuations (sky, amplifier gain, photon noise etc.) still need to be corrected. To estimate these fluctuations, at the start of the observations a few frames are taken off-fringe.

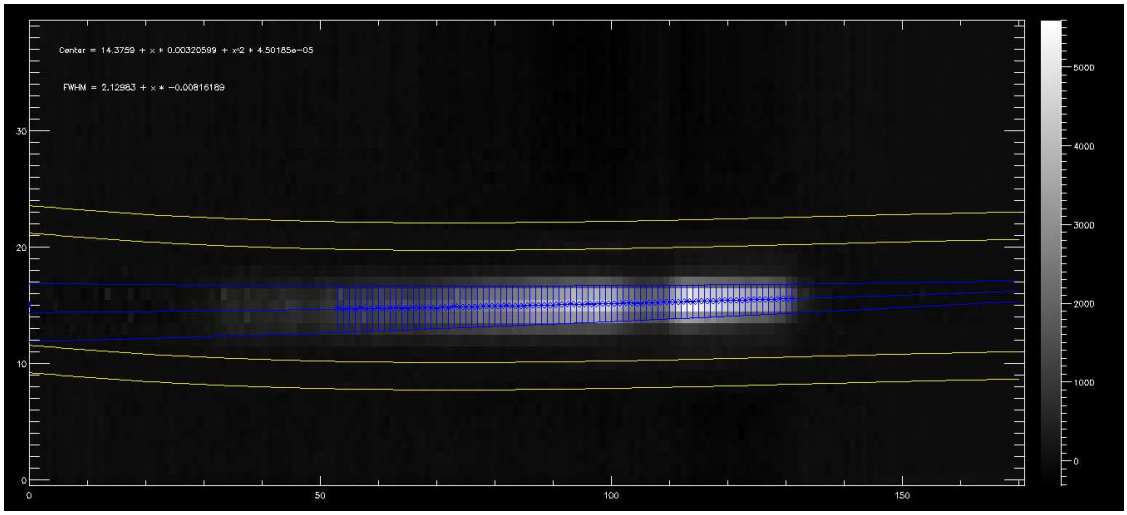

Figure 2.12: Masked photometry signal.

- Photometry (*EWS+MIA*)

  The photometry is done in the same manner for *MIA* and *EWS* analysis. Off- and on- source frames measured by standard chopping are averaged separately. The target frames and the sky frames are afterwards subtracted from each other. This leads to four spectra $I_{A,1}$, $I_{B,1}$, $I_{A,2}$, $I_{B,2}$, - where sub-script A and B represent each telescope and 1 and 2 represents each side of the beam splitter. The created mask is identical to that used for computing the visibilities.

- Normalization

  The averaged visibility is at this point divided by the masked geometric mean photometry. This is called the raw visibility. This result is still uncalibrated for the instrumental/atmospheric effects. The instrumental effects are zeroed by calibrating the science visibilities with the calibrator visibilities.

- Calibration

  The whole calibration process is done in the same way for the science target and for the calibrator. The EWS analysis offers internal calibration. The output gives: calibrated visibility and phase, and calibrated photometry with and without mask (in Jy). The program also produces postscripts files with plots of those parameters.

2.5 AMBER data reduction yoric

The latest version of the amdlib package (version 2.0 beta 2b) and the yorick interface provided by the AMBER consortium and the Jean-Marie Mariotti Center[3] is available for data reduction of the AMBER data. The amdlib package consists of *C* routines (basic routines used for all AMBER data reduction packages including the ESO AMBER pipeline). A yorick package calls

[3]http://www.mariotti.fr/data_processing_amber.html

the routines to visualize the data and the results.

Raw visibility and closure phase values can be computed using the following data reduction procedures (based on Tatulli et al. (2007)):

1. Cosmetic corrections in the raw data
    - Loading of the Bad Pixel Map (BPM)
    - Loading of the Flat Field Map (FFM)
    - Spatial distortions, Wavelength calibration
    - Computation of the Pixel-to-Visibility Matrix (P2VM)
    - Calibration of the 'carrying waves'
2. Computing visibility values
    - Detecting fringes
    - Fitting of amplitude and phase of the complex coherent fluxes
    - Correction for biases
    - Calculation of piston values using cross spectra
    - Computation of unbiased V2 values
    - Computation of phase closures
3. Frame selection
    - Definition of criteria to select the 'best' frames (piston, fringe S/N, flux ratio)
    - Visibility calibration

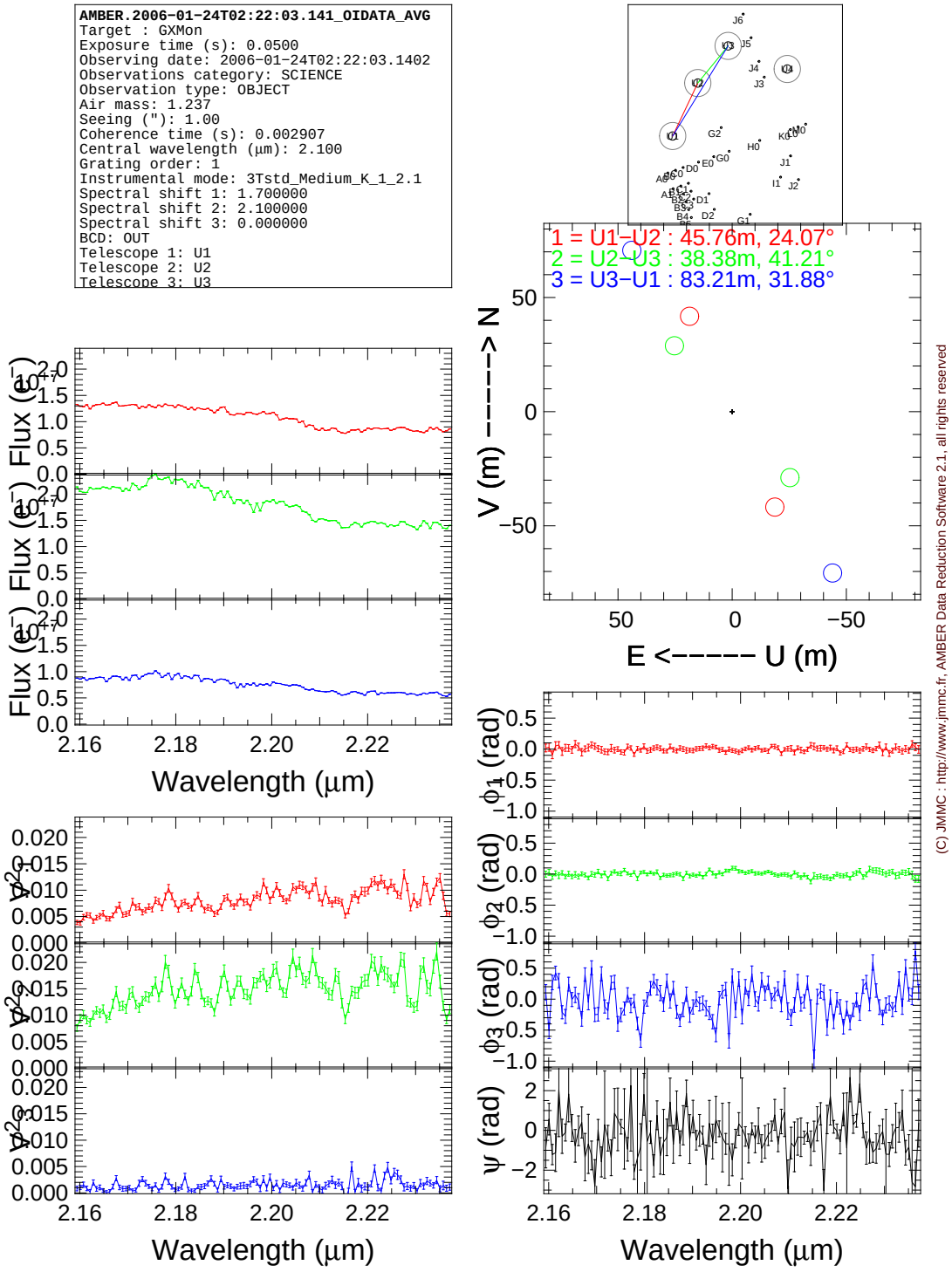

Figure 2.13: Output from the yoric interface.

Chapter 3

Data Calibration

The following Chapter outlines the practical processing of the acquired data. The data consist of multi epoch interferometric observations of four oxygen-rich Mira variables RR Aql (April 2004 – July 2007), S Ori (February 2006 – March 2009), GX Mon (February 2006 – April 2008), and R Cnc (December 2008 – March 2009). Section 3.3 briefly summarizes the data calibration theory, and Sections 3.4 and 3.5 describe in detail the data calibration procedures applied to the large sample of data reduced within this thesis. This includes the monitoring of ambient conditions during the observations and the selection of suitable calibrators. The sections also contain a comparison of different data reduction methods as well as a comparison of different calibration approaches and their impact to the quality of the acquired data. The presented procedures were used for all observing runs used in this thesis.

3.1 Introduction

Long Baseline Interferometry is a powerful method allowing an exceptionally high angular resolution from the ground. However, as all optical techniques based on ground based telescopes, infrared interferometry is also strongly affected by atmospheric turbulence. The sites for building the interferometers are carefully selected to minimize possible limitations caused by the atmospheric effects. Along with choosing a site with excellent quality for interferometric observations, the accuracy of the measurements can be improved by using various techniques such as adaptive optics (AO), fringe tracking, and data calibration.

Adaptive optics (AO) is a technology that reduces the effect of wavefront distortions by improving the performance of optical systems. The distortion of the flat wavefront of the light coming from the object is compensated after measurement from several wavefront sensors. Because science targets are often too faint, a nearby brighter guide star (or as an alternative a laser beam) can be used instead. The wavefront perturbation in each pixel is calculated on a timescale of a few milliseconds. To correct the wavefront errors introduced by the atmosphere, the pixelated map of the wavefronts is fed into the deformable mirror, and the shape of the surface of the mirror is reshaped accordingly to correct the distortions. The system keeps the image of the

guide star or any other object always at the maximum image sharpness achievable by the mirror. The VLT Interferometer (VLTI) uses a 60 elements curvature adaptive optics system MACAO, (Multi-Application Curvature Adaptive Optics). MACAO is operating at the Coudé focus of each 8.2 m VLT Unit Telescope. This system corrects the distortions of the light beams before they are directed towards the common focus at the VLTI, and thus increase enormously the sensitivity resulting in the higher efficiency of the VLTI.

The FINITO (Fringe-tracking Instrument of NIce and TOrino) is significantly improving the limiting magnitude of the VLTI instruments. FINITO measures the optical path difference (OPD) variation between the light beams. An error signal of the piston disturbances introduced by atmospheric turbulence is sent over short periods of time to the OPD Controller which in return sends a correction signal to the delay lines. The output beams have nearly ideal flat wavefronts. Residual errors from AO are translated into beam intensity fluctuations by the spatial filtering process. FINITO operates in the H-band (λ = 1.65 μm, $\Delta\lambda$ = 300 nm) as a three beam fringe tracker. FINITO supports the closure phase measurement capability. It significantly improves sensitivity and accuracy of each VLTI instrument (AMBER, MIDI) by increasing their coherent exposure time from few milliseconds to several minutes. The system compensates for the transversal and longitudinal atmospheric dispersion by combining the collimated beams from two or three telescopes at a time. The full potential of FINITO is achieved when observing at the highest spectral resolution. The current limiting magnitude for the faintest object observed using the large telescopes (UTs) at the VLTI is 7.5 in the near infrared (K_{corr} = K_{mag} - 2.5$\log_{10}$(V), where V is the Visibility of the object). At mid-infrared wavelengths, the limiting magnitude of the VLTI is 4 (1 Jy at 12 μm), significantly fainter than at the near-infrared.

One of the most crucial steps in the data processing is the data calibration. Good data calibration is important and can significantly improve the quality and accuracy of scientific results. The calibration partly reduces the influence of atmospheric turbulence as well as effects caused by the technical specifications of the instrument. These source of perturbations include: wavefront errors introduced by each of the apertures, the fluctuations of OPD between two apertures, mechanical vibration, and the polarization effects in the instrument. These perturbations cause fringe variations and smears the fringes. This leads to underestimated measured visibility. In order to account for visibility losses and to determine the absolute flux values for each science target, astronomical calibrator stars with known flux and diameter values are observed. A more detailed description of the data calibration is described in Section 3.4.

3.2 Monitoring of Ambient Conditions

For the data calibration, all calibrator data sets observed with the same instrumental setup as our science target were reduced in this work. The data were collected during the same night using the same stations. The calibrator data sets include publicly available data taken by other programs observed over the night. The number of available calibrator stars per night depends on the number of calibrator stars observed with the same instrumental setup as our science target.

During each night the ambient conditions for all the observations were carefully monitored. Figure 3.1 shows examples of the ambient conditions for two nights of our observations of the Mira variable RR Aql (Section 5). The observations were conducted on 10/04/2004 and 01/04/2008. The Figures show the DIMM (Differential Image Motion Monitor) seeing (") (top left), airmass (bottom left), relative humidity (%) (top right), and coherence time (bottom right) as a function

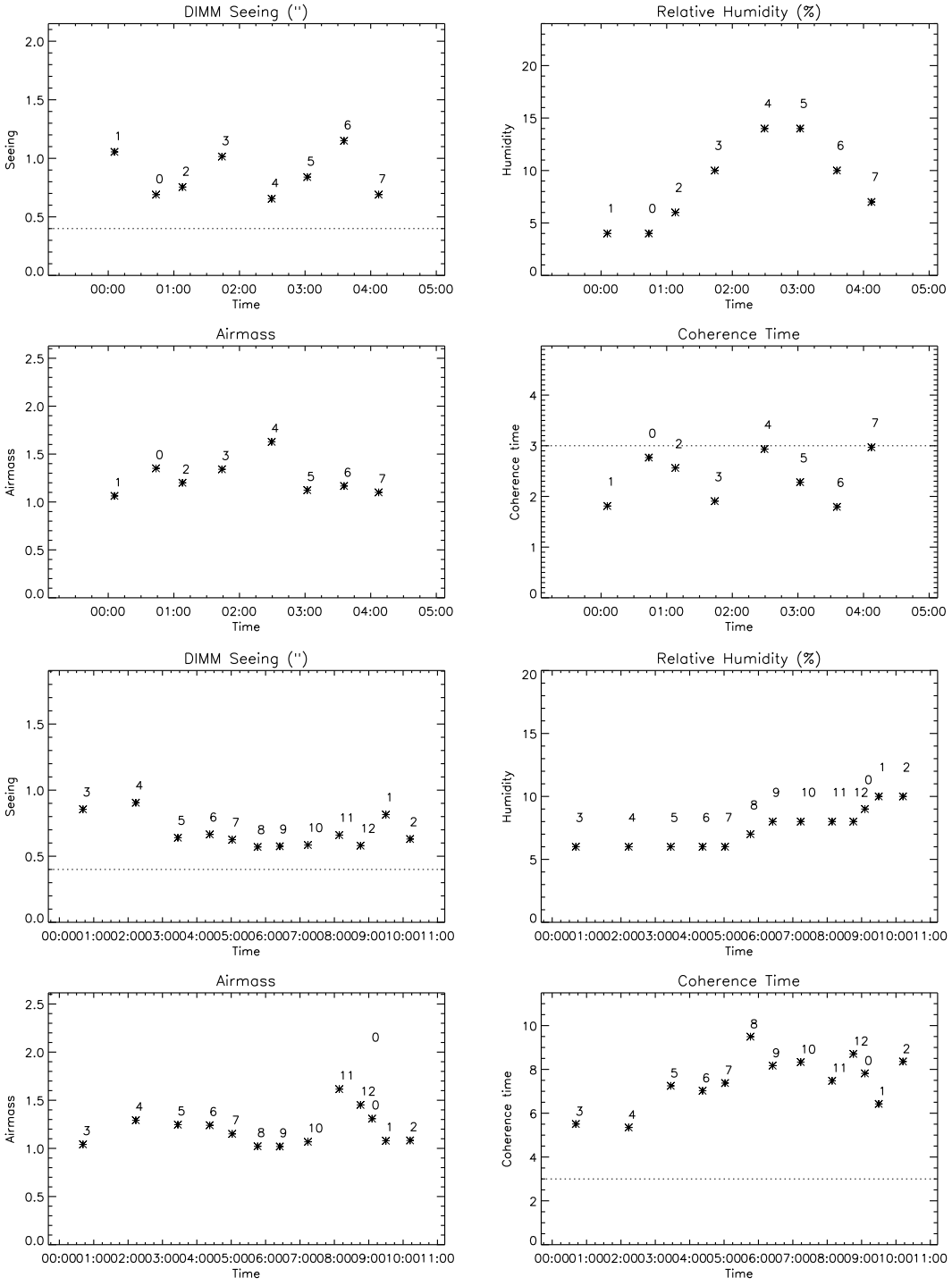

Figure 3.1: Ambient conditions for two nights with different number of available calibrators observed in the same mode as our science target RR Aql. The panels include the DIMM (Differential Image Motion Monitor) seeing (") (top left), airmass (bottom left), relative humidity (%) (top right), and coherence time (bottom right) as a function of the time of observation. The calibrator stars are indicated by numbers from 1 to the number of calibrators observed during the specific night. The science target is indicated by 0.

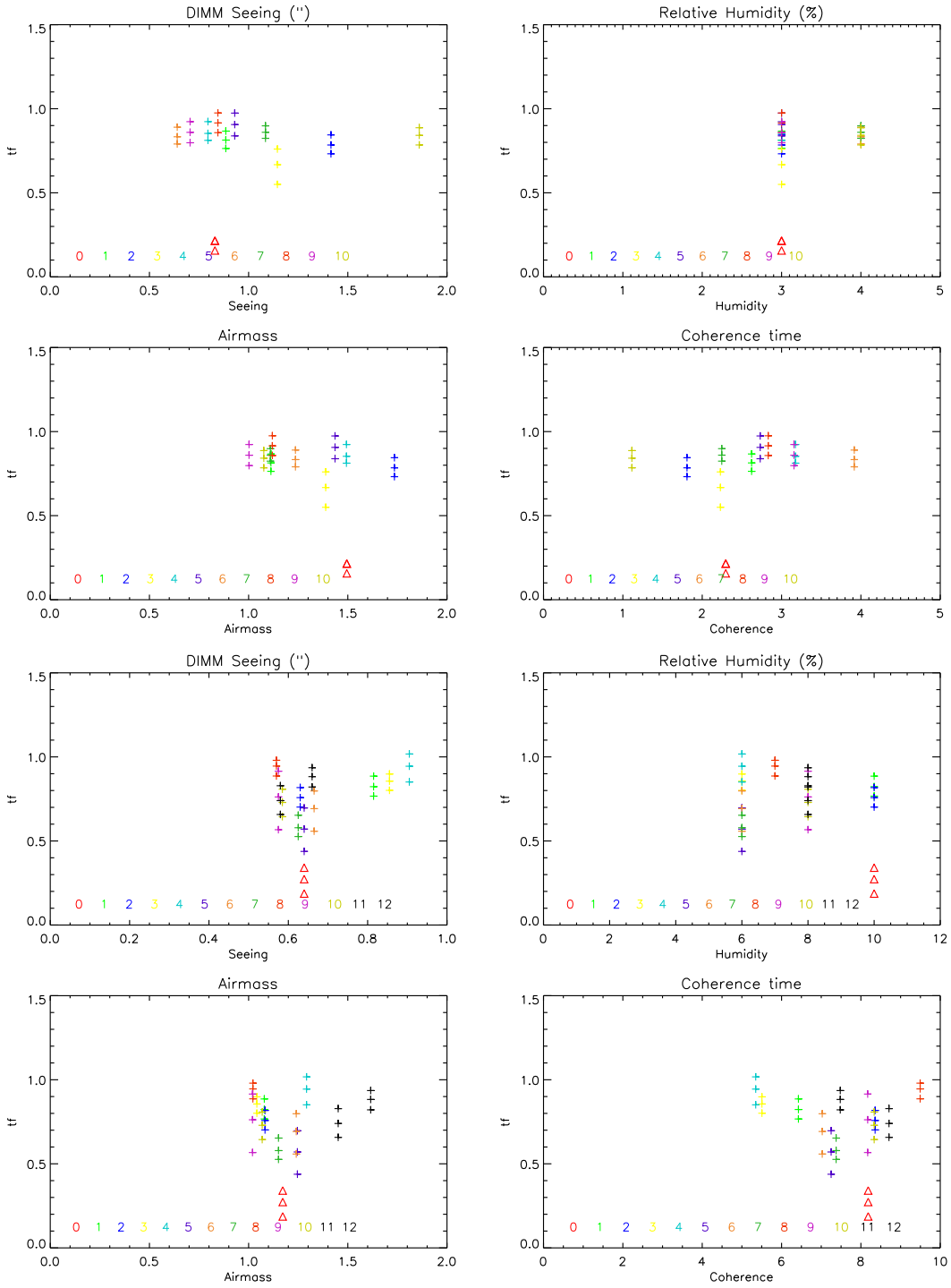

Figure 3.2: Transfer function (TF) as a function of ambient conditions for two nights with different number of available calibrators observed in the same mode as our science target RR Aql. The panels include the TF as a function of DIMM (Differential Image Motion Monitor) seeing (") (top left), airmass (bottom left), relative humidity (%) (top right), and coherence time (bottom right). The calibrator stars are as well as in the previous panels indicated by numbers from 1 to the number of calibrators observed during the specific night. The science target is indicated by 0.

of the time of observation. The calibrator stars are indicated by numbers from 1 to the number of calibrators observed during the specific night. The science target is indicated by 0. The numbers assigned to the calibrator stars are not organized in any special order. However, the first two numbers are reserved for the main calibrators (defined by the Principal Investigator (PI)). These calibrators are close on sky and observed immediately before or after our science target. The numbers are assigned to remaining calibrator stars as they were observed during the night. The values of the ambient conditions are mostly used to indicate the quality of the atmosphere during the observations. If the measured seeing, humidity, airmass, and coherence time were significantly different for a calibrator star compared to our science target, or/and constraints due to the wind or clouds occur, the calibrator star was either omitted from further analysis or the calibrated visibility values and photometries were processed with more attention. Vice versa, for dates with unexpected (lower/higher) visibility or photometry values, the ambient conditions were checked in more detail. The observations presented here were conducted in Service Mode (SM) or Visitor Mode (VM).

3.3 Visibility and Photometry Calibration - theory

In the following Section we will focus in more detail on the theoretical process of the data calibration. The observed visibility and flux differ from the real values due to perturbations introduced either by the atmospheric conditions or by the instrument itself. In order to reconstruct the true values we calibrate the data by using astronomical calibrators. The calibrator stars are ideally bright objects in the used wavelengths without showing any peculiar spectral features, with a diameter giving an instrumental response like a point source. This is a theoretical idealization. For real observations we have to make some compromises, and to relax some of the constrains.

Calibrated science target visibility were calculated using the instrumental transfer function (TF). The theoretical calibrator is a point source. The instrumental response to this calibrator star in terms of visibility should be unity. The theoretical Transfer Function of the instrument is:

$$\mathrm{TF}^2 = \frac{V^2_{\mathrm{meas}}}{1} \tag{3.1}$$

where V^2_{meas} is the squared visibility observed on the calibrator star and 1 is unity, the theoretical visibility of a point source.

The visibility function of the point source is not changing in any observed wavelength. To fulfill the condition to find a bright point source brings us to one of the compromises. The point-like sources are far from the observer, and on the other side available bright stars do not behave as point sources. One has to chose a calibrator star, which is at least brighter than the science target, and/or to choose a calibrator star which is rather bright, but slightly larger than a point like source. This object is assumed to be unresolved by the interferometer. The typical size of the calibrator is less than a few milli-arcsecond. The Transfer Function in that case is:

$$\mathrm{TF}^2 = \frac{V^2_{\mathrm{meas}}}{V^2_{\mathrm{theor}}} \tag{3.2}$$

where $V^2_{\rm meas}$ is the squared visibility observed on the calibrator star and $V^2_{\rm theor}$ is the theoretical visibility expected for the observation of the calibrator star in the absence of turbulence and instrumental effects. It is defined as a Uniform Disk with a known diameter:

$$V^2_{\rm theor} = 2{\rm J}_1 \frac{\pi\Theta B_\lambda}{\pi\Theta B_\lambda} \tag{3.3}$$

where $\rm J_1$ is 1^{st} order Bessel function, B_λ is a radial spatial frequency (Section 2.1.4), and Θ is the known diameter.

In order to receive the same response from the detector and optics of the instrument, a main calibrator is selected from calibrator stars with a spectral type similar to the science target. However, the requirement for a similar spectral type as the scientific target will not allow us to choose a calibrator brighter than the object. Also the requirement of the same spectral type can introduce some unwanted spectral features. To avoid a variation of the system, including both the atmospheric turbulence and variation introduced by the instrument, the calibrator star is observed either immediately before and/or after the science target. The calibrators chosen for individual science targets are observed not only close in time, but also close on sky to receive the wavefront from both objects passing through the same atmosphere. This constraint cannot as well be always fulfilled as the sky coverage of such bright, non-multiple, non-variable objects with a known diameter is rather limited. The instrumental settings (projected baseline, position angle) are as well the same for both objects.

For the determination of the calibrated science target visibility spectra, two intensities are used $I_{\rm geo}$ (after applying the same mask for both science and calibrator data), and $I_{\rm arit}$. $I_{\rm geo}$ is the total flux computed as a geometric mean of the intensities, in order to account for a possible inequality of the two beams from the two telescopes (see Sect. 2.1.1).

$$\begin{aligned} {\rm I_{geo}} &= \sqrt{\rm I_{A1}I_{B1}}\sqrt{\rm I_{A2}I_{B2}} && (3.4)\\ &= 2\sqrt{\rm rt\eta_A\eta_B}I_{\rm src} && (3.5)\\ &= f{\rm I_{src}} && (3.6) \end{aligned}$$

where for each telescope A and B, and for each side of the beam spliter 1 and 2 is:

$$\begin{aligned} {\rm I_{A1}} &= t\eta_A I_{\rm src} && (3.7)\\ {\rm I_{A2}} &= r\eta_A I_{\rm src} && (3.8)\\ {\rm I_{B1}} &= r\eta_B I_{\rm src} && (3.9)\\ {\rm I_{B2}} &= t\eta_B I_{\rm src} && (3.10) \end{aligned}$$

where r and t are the coefficients for reflection and for transmition of the intensities I_A and I_B. The factors η_A and η_B are taking into account the different intensities of the beams from the two telescopes. Isrc is the intensity of the source.

The raw correlated flux is determine according to:

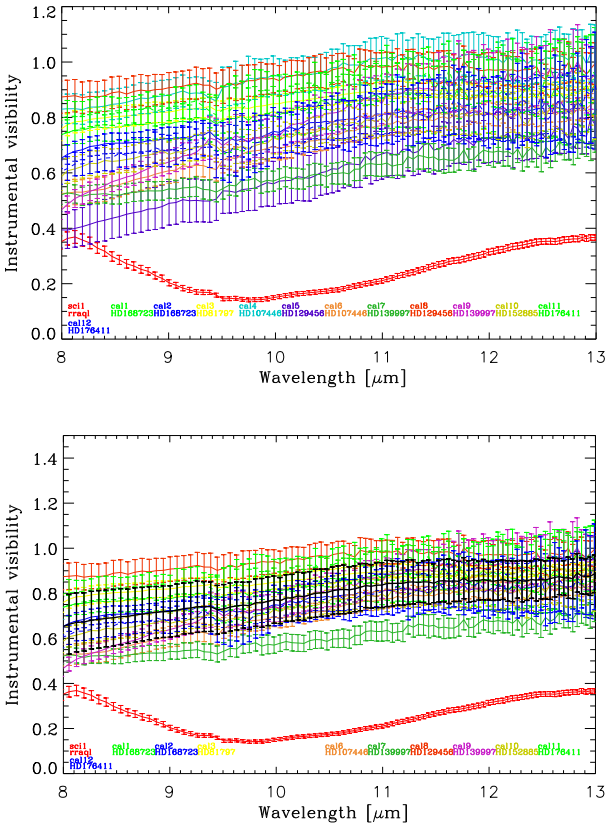

Figure 3.3: Instrumental visibility as a function of the wavelength 8–13 μm. The panels show transfer functions for different calibrators and the uncalibrated visibility of the science target. The observed calibrators are listed in the bottom of the panels with corresponding colors. The science target is indicated in red. The top panel shows all available calibrators per specific night. The bottom panel shows calibrators without the omitted ones overplotted by the average of transfer functions of all selected calibrators with the error bars computed as the standard deviation of the selected transfer functions.

$$\mathrm{I_{cor}} = f I_{\mathrm{src}} \mathrm{V} \tag{3.11}$$

where $f = 2\sqrt{rt\eta_A\eta_B}$ is a factor correcting for the inequalities of the beams.

The total flux $\mathrm{I_{arit}}$ is determined (without applying the mask) as arithmetic mean of the fluxes from each of the beams from the two telescopes

$$\begin{aligned} \mathrm{I_{arit}} &= \frac{1}{2}(\mathrm{I_{A1}} + \mathrm{I_{A2}} + \mathrm{I_{B1}} + \mathrm{I_{B2}}) && (3.12)\\ &= \frac{1}{2}(\mathrm{r} + \mathrm{t})(\eta_{\mathrm{A}} + \eta_{\mathrm{B}})\mathrm{I_{src}} && (3.13)\\ &\approx \mathrm{I_{src}} && (3.14) \end{aligned}$$

The raw visibility as a function of wavelength is determined according to:

$$\mathrm{V_{raw}}(\lambda) = \frac{\mathrm{I_{cor}}}{\mathrm{I_{geo}}} \tag{3.15}$$

Calibrated science target visibility spectra were calculated:

$$\mathrm{V_{calibr}}(\lambda) = \frac{V_{\mathrm{raw,sci}}(\lambda)}{V_{\mathrm{TF}}(\lambda)} \tag{3.16}$$

$$= \frac{V_{\mathrm{raw,sci}}(\lambda)}{V_{\mathrm{raw,cal}}(\lambda)} V_{\mathrm{theor,cal}}(\lambda) \tag{3.17}$$

where $V_{\mathrm{TF}}(\lambda)$ is the transfer function (eq: 3.2).

3.4 Visibility Calibration

In this thesis, all the interferometric data was processed as described in the following section. The measured instrumental transfer functions are trended using ambient condition data. Figure 3.2 shows examples of the transfer function as a function of ambient conditions for two nights of our observations of the Mira variable RR Aql (Section 5). The observations were conducted on 19/04/2005 and 10/04/2004. The Figures show the Transfer Function (TF) as a function of DIMM Seeing (") (top left), Airmass (bottom left), Relative Humidity (%) (top right), and Coherence Time (bottom right). The calibrator stars are again indicated by numbers from 1 to number of calibrators, and the science target is indicated by 0 as previously for the plots of the ambient conditions versus time of observations.

The Transfer Function for each calibrator star was computed according to Equation 3.2. The TFs were plotted versus the visibility amplitude of the science target. The top panel of Figure 3.3 shows an example of the instrumental visibility amplitude as a function of wavelength (10/04/2004). Each calibrator is indicated by a certain color corresponding to the color and acronym of the calibrator as well as the number of the calibrator written on the bottom of each plot. The numbers are again corresponding to the numbers introduced in the plots of the ambient conditions. The error bars are given by the measured uncertainties. Calibrators with values of instrumental visibility larger than unity, calibrators with very noisy values and large error bars, or on the other hand calibrators with very low unexpected values compare to the other calibrators are rejected from our further analysis. The bottom panel of Figure 3.3 shows the same plot without the omitted calibrators.

In this thesis, visibility spectra were calculated by using two approaches. In the first case the instrumental transfer function was derived as an average of transfer functions from all available calibrators (after elimination of out of range instrumental functions). This means that all calibrators were observed during the same night with the same telescope configuration and instrumental mode as our science target. The errors of these transfer functions are given by the standard deviation of all transfer function measurements per night.

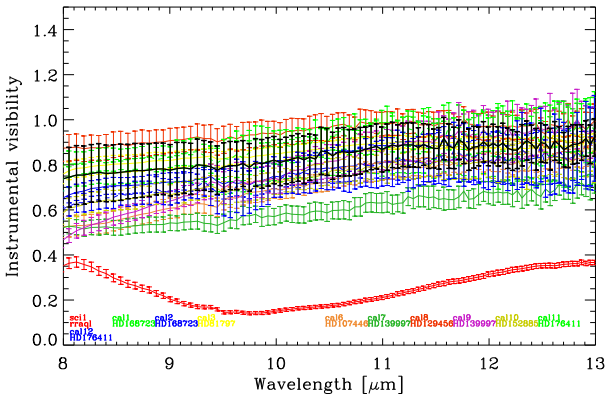

Figure 3.4: Instrumental visibility as a function of the wavelength 8–13 μm. The panel shows transfer functions for different calibrators and the uncalibrated visibility of the science target. The observed calibrators are listed in the bottom of the panels with corresponding colors. The science target is indicated in red. The panel shows calibrators without the omitted ones overplotted by the transfer function of main calibrator(s)(while Figure 3.3 shows the average of transfer functions of all selected calibrators), with the error bars computed as the standard deviation of all selected transfer functions.

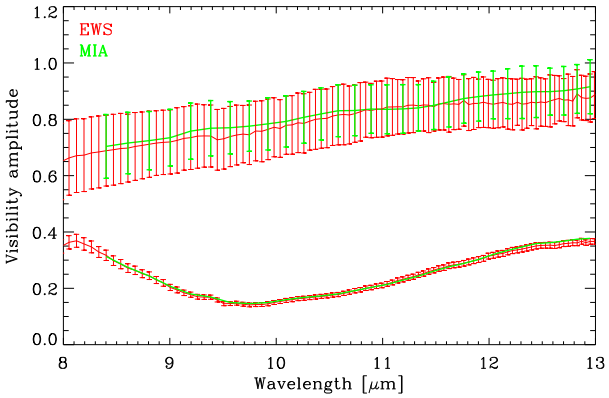

Figure 3.5: Instrumental visibility as a function of the wavelength 8–13 μm. The panel shows the comparison of transfer functions and uncalibrated visibilities of the science target derived by the MIA (green) and EWS (red) data reduction procedures. The error bars are available only for the EWS analysis.

Figure 3.3 shows the average transfer function (indicated by the thick black line) and the corresponding error bars. To estimate the uncertainty of the transfer functions for nights when only one calibrator was available, we used typical values based on nights when many calibrator stars were observed.

In the second case the instrumental transfer function is given by the main calibrator determined by the PI. In the case where two calibrators were observed immediately before and after the science target, the instrumental transfer function is given by the average of these two main calibrators. In both cases the errors of such transfer function are given by the standard deviation

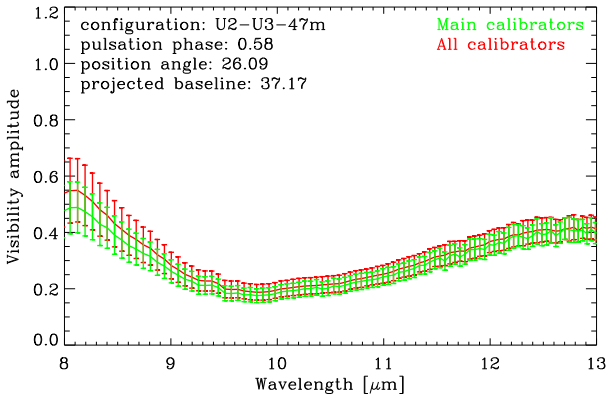

Figure 3.6: Visibility amplitude as a function of the wavelength 8–13 μm. The panel shows the comparison of calibrated visibilities derived by calibrating the data using all calibrators or only the main calibrator(s). The basic observational setup is also listed in the panel.

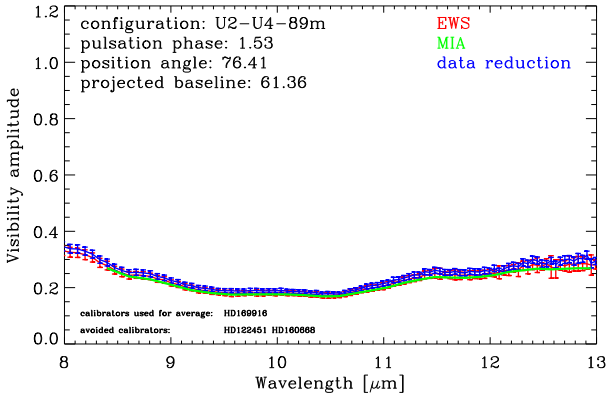

Figure 3.7: Visibility amplitude as a function of the wavelength 8–13 μm. The panel shows the comparison of calibrated visibilities derived by MIA (green), EWS (red), and our data reduction (blue) procedures with the corresponding error bars. The basic observational setup as well as main and omitted calibrators are also listed in the panel.

of all transfer function measurements per night. This transfer function is again indicated by the thick black line plotted over the transfer functions (Fig. 3.3).

Both methods, MIA and EWS, for the data reduction were applied to independently verify the data reduction results. Figure 3.5 shows an example of the instrumental visibility for the science target and an average transfer function of the calibrator derived from both data reduction methods (10/04/2004). The green line without indication of error bars correspond to the MIA analysis. The red line indicates the EWS analysis with corresponding error estimates.

Figure 3.6 shows an example of the resulting visibility amplitudes as a function of wavelength derived from the two approaches described above. The red line represents the calibrated science

target visibility spectra computed with a transfer function obtained as an average from all transfer functions, and the green line represents the calibrated spectra computed using the main calibrator (or using an average from two main calibrators). In the plot, the telescope configuration, the ground distance between the telescopes, the visual pulsation phase of observations, the position angle, and the projected baseline length are specified. Results from all observations were carefully checked and analyzed. Apart from a few exceptions the obtained calibrated visibilities correspond to each other, and in the following we chose to use the results from all transfer functions. Such exceptions include days when the main calibrator and the science target was observed in clearly different ambient conditions.

The visibility spectra were also compared in terms of the influence of the two different data reduction approaches. Figure 3.7 shows an example of the resulting visibility amplitude as a function of wavelength derived from MIA (green line), EWS (red), and the results produced by integrated EWS calibration procedure (blue). Details of the observations, including the acronym of the main calibrator and omitted calibrators from the average of all the transfer functions, are again specified in the plot. The obtained data reduction values correspond to each other for all the observations. We chose to use in the following the results derived from the EWS analysis, which offer error estimations.

The final errors on the observed visibilities are mostly systematic, and include the error of the coherence factor of the science target and the calibrators, the adopted diameter errors, and the standard deviation of the transfer function over the night. The error estimate is computed as:

$$ews_{\mathrm{vis\,err}} = \sqrt{(\frac{f_{\mathrm{cal}}}{cts_{\mathrm{cal}}} cts_{\mathrm{sci\,err}})^2 + (\frac{cts_{\mathrm{sci}} f_{\mathrm{cal}}}{cts_{\mathrm{cal}}^2} cts_{\mathrm{cal\,err}})^2 + (\frac{cts_{\mathrm{sci}}}{cts_{\mathrm{cal}}} f_{\mathrm{cal\,err}})^2} \tag{3.18}$$

3.5 Flux Calibration

The calibrated correlated flux is computed as:

$$\mathrm{F}_{cor}(\lambda) = \frac{\mathrm{I}_{\mathrm{cor,sci}}}{\mathrm{I}_{\mathrm{cor,cal}}} \mathrm{F}_{\mathrm{cal}} \tag{3.19}$$

where $\mathrm{F}_{\mathrm{tot}}$ is the correlated flux in Jansky, $\mathrm{I}_{\mathrm{cor,sci}}$ is defined according to Equation 3.11. $\mathrm{F}_{\mathrm{cal}}$ is the spectrum of the calibrator in Jy.

The calibrated total flux is computed as:

$$\mathrm{F}_{\mathrm{tot}}(\lambda) = \frac{\mathrm{I}_{\mathrm{arit,sci}}}{\mathrm{I}_{\mathrm{arit,cal}}} \mathrm{F}_{\mathrm{cal}} \tag{3.20}$$

where F_{tot} is the total flux in Jy, $\mathrm{I}_{arit,sci}$ is previously (eq: 3.14) defined as an arithmetic mean of a one-dimensional photometry, one for each telescope A, B and side of a beam spliter 1 and 2. $\mathrm{I}_{cal,arit}$ is the same for calibrator. F_{cal} is the spectrum. The $\mathrm{I}_{arit,sci}$, $\mathrm{I}_{arit,cal}$ are counted in ADU

(Analog-to-Digital converter Unit), and F_{cal} in Jy.

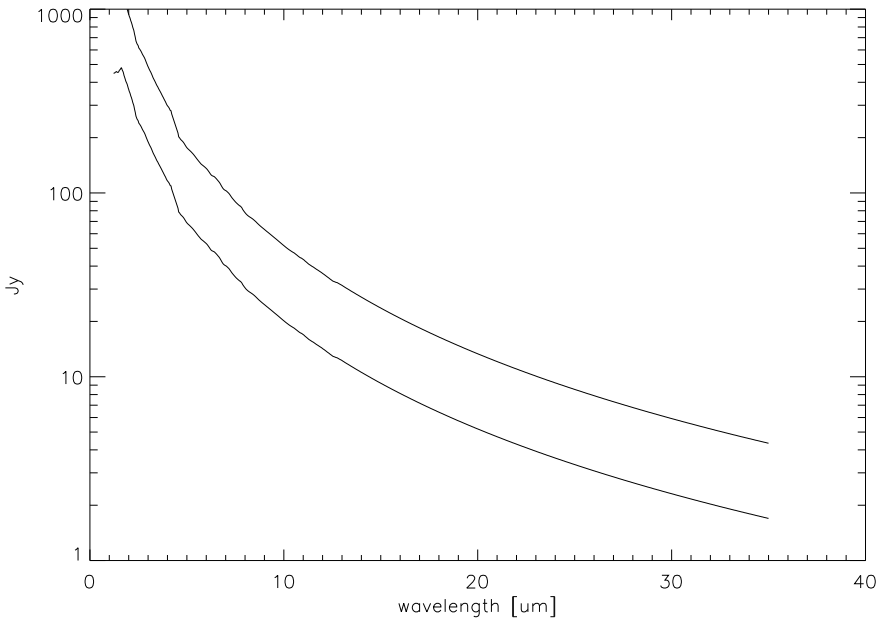

Figure 3.8: The flux in Jy as a function of wavelength. This shows an example of the absolutely calibrated spectrum for calibrator HD 165135, and the new scaled spectrum for calibrator HD 4128 where the absolutely calibrated spectrum was not directly available.

Absolutely calibrated spectra are available in Cohen et al. (1999) for most calibrator stars. If the absolutely calibrated spectrum was not directly available in Cohen, IRAS, or other source, we used instead a spectrum of a calibrator with similar spectral type and similar effective temperature (see the instrument consortium's catalog[1]). The spectra of such calibrators were scaled with the IRAS flux at 12 μm to the level of our calibrator.

$$\mathrm{F_{new}} = \frac{\mathrm{F_{Cohen}}}{\mathrm{F_{Cohen}}(12\mu m)}\mathrm{F_{new}}(12\mu m) \tag{3.21}$$

where $\mathrm{F_{new}}$ is the scaled spectrum of our calibrator, $\mathrm{F_{Cohen}}$ is the Cohen spectrum, $\mathrm{F_{Cohen}}$(12 μm) is the IRAS flux of the Cohen's calibrator with known spectrum, and $\mathrm{F_{new}}$(12 μm) is the IRAS flux of our calibrator. Figure 3.8 shows the flux in Jy as a function of wavelength. It shows an example of the absolutely calibrated spectrum for calibrator HD 165135, and the new scaled spectrum for calibrator HD 4128 where the absolutely calibrated spectrum was not directly available. In addition, we verified that our synthetic spectra obtained by this procedure are valid by scaling known spectra of two Cohen calibrators.

Figure 3.9 shows the Photometry in ADU/s as a function of wavelength. It shows an example of observations (23/06/2006) where two science targets were observed during the same night (the

[1] http://www.ster.kuleuven.ac.be/∼tijl/MIDI_calibration/mcc.txt

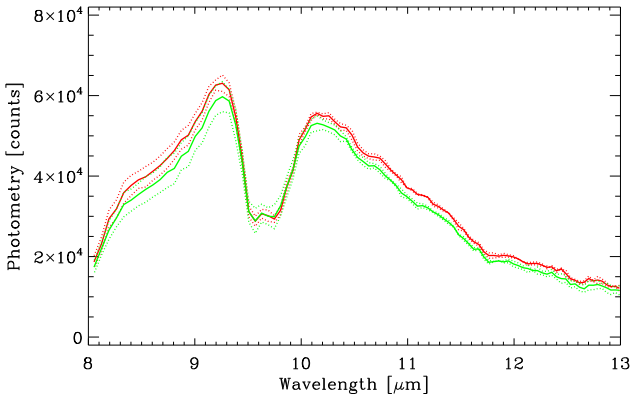

Figure 3.9: Photometry in ADU/s as a function of wavelength 8–13 μm for two observations of the same science target observed during the same night (thick lines). The received flux is similar for both telescopes A and B (thin dotted lines, the colors corresponds to the individual science targets).

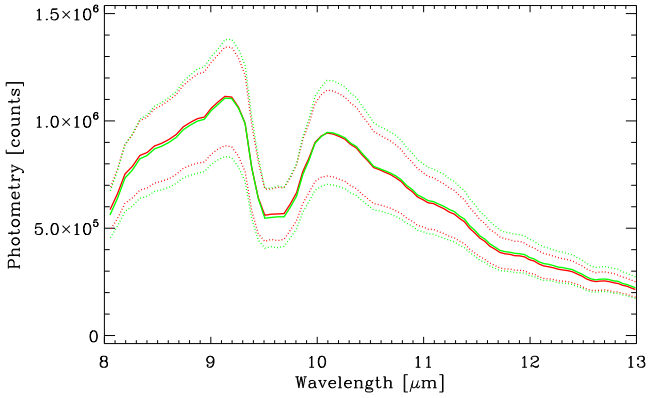

Figure 3.10: Photometry in ADU/s as a function of wavelength 8–13 μm for two observations of the same science target observed during the same night (thick lines). The received flux is different for both telescopes A and B (thin dotted lines, the colors corresponds to the individual science targets).

green and red line for each science target). The beams from telescope A and B are indicated by dotted lines with corresponding colors. The thick line represents the average of observations from each telescope. Figure 3.10 shows an example of observations (20/07/2005) where as well two science targets were observed. During this night, the flux in counts received by each telescope differs by up to 42%. However, the final averaged values correspond to each other for both science targets. Figure 3.11 shows an example of observations (29/07/2004) where the ambient conditions were very unstable. There have been also restrictions due to the exceeding limits for the speed of the wind. Five science targets were observed during the same night. Each of the science targets is indicated by a different color. The observations show very inconsistent values. Results based on such nights had to be carefully processed.

Generally, the flux of the observed photometric standard stars ranges from a few Jansky to more than 100 Jy (see Fig. 3.12). The Figure shows total photometry in Jy as a function of

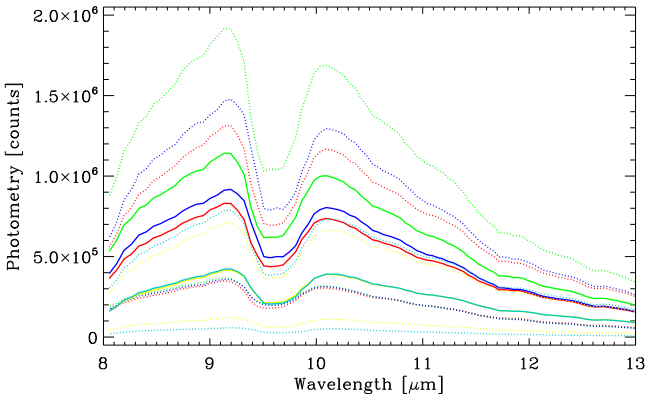

Figure 3.11: Photometry in ADU/s as a function of wavelength 8–13 μm for five observations of the same science target observed during the same night (thick lines). The received flux is different for all observations and also for both telescopes A and B (thin dotted lines, the colors corresponds to the individual science targets).

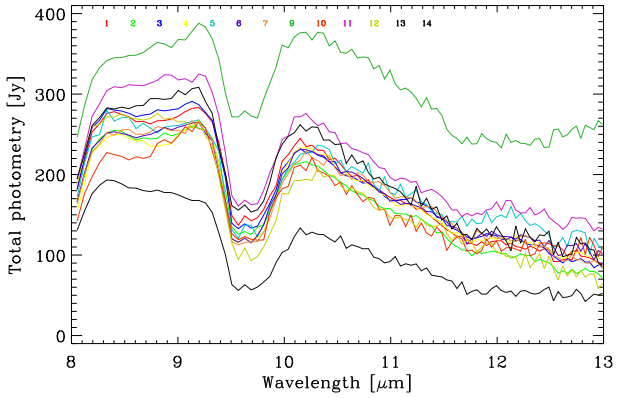

Figure 3.12: Total photometry in Jy as a function of wavelength 8–13 μm for 14 calibrator stars.

wavelength. It shows an example of observations (23/06/2006) where 14 calibrator stars were observed. As well as for the science target received counts for each calibrator can be as well influenced by the ambient condition or other instrumental variation.

Analogous to visibilities, photometric data were compared using two different approaches for the computation of the total photometry: an average counts from all calibrators versus results using the main calibrator. Figure 3.13 shows an example of the total photometry in Jy as a function of wavelength (20/07/2005). The red line represents results derived using all available calibrators observed during the same night. The green line represents the total photometry derived using the main calibrator, and the blue line shows in comparison the result from EWS integrated calibration. The errors are computed as:

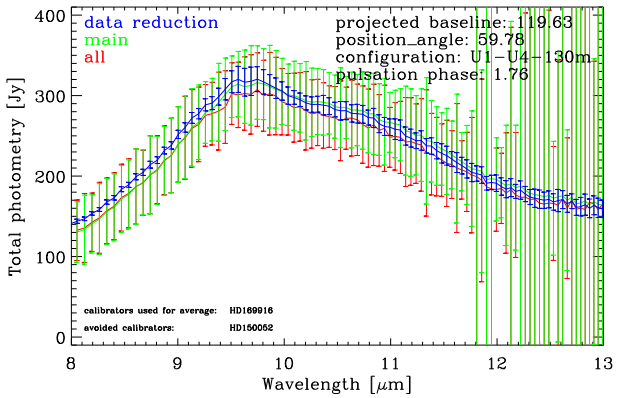

Figure 3.13: Total photometry in Jy as a function of wavelength 8–13 μm for the science target. The panel shows the comparison of total photometry derived by the MIA (green) and EWS (red) data reduction (blue) procedures with the corresponding error bars. The basic observational setup as well as the main and omitted calibrators are also listed in the panel.

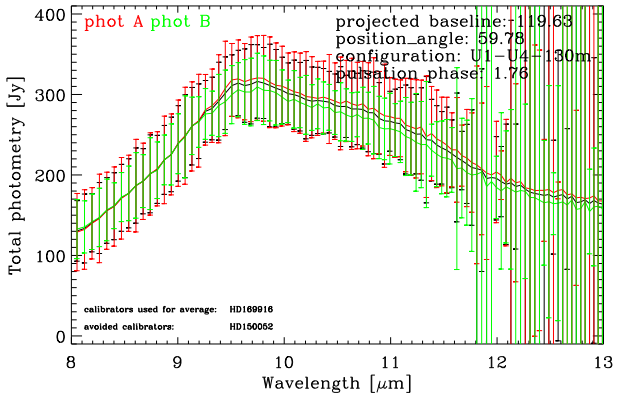

Figure 3.14: Total photometry in Jy as a function of wavelength 8–13 μm for the science target. The panel shows the comparison of total photometry received from telescope A and B with the corresponding error bars. The basic observational setup as well as the main and omitted calibrators are also listed in the panel.

$$F_{err} = \sqrt{(\frac{f_{\rm cal}}{cts_{\rm cal}} cts_{\rm sci\,err})^2 + (\frac{cts_{\rm sci} f_{\rm cal}}{cts^2_{\rm cal}} cts_{\rm cal\,err})^2 + (\frac{cts_{sci}}{cts_{cal}} f_{cal\,err})^2} \tag{3.22}$$

The projected baseline length, the position angle, the visual pulsation phase of observations, the telescope configuration, and the ground distance between the telescopes are again specified in the plot. In the following, the photometry results are derived using one or two main calibrators observed close on sky and in time compared to the science target. In a few cases, when the atmospheric absorption was strongly affecting the spectra around 9.5μm, we used another similar calibrator instead of the main calibrator observed in the same night with the same flux level.

The previous figures show the total photometry derived as a calibrated arithmetic mean from two telescopes A and B each of them split by the beam spliter to the beam 1 and 2. Figure 3.14 shows an example of the total photometry in Jy as a function of wavelength where the red line in the plot represents the calibrated arithmetic mean from the beam spliter of telescope A and the green line represents the calibrated arithmetic mean from the beam spliter of telescope B (20/07/2005). The black line indicate the average of these two results after the calibration. Both approaches lead to the same results.

All different approaches were done for all individual observations.

The visibility and photometry beyond 12 μm of the calibrators often exhibit a random behavior due to the low signal to noise ratio in this range. Some of the values are out of realistic range. The resulting calibrated visibility and photometry show therefore in several cases affected values in the wavelength range between 12 to 13 μm. This effect should be taken into account.

Chapter 4

Modeling

This chapter describes in detail the modeling approach applied to the data within this thesis. Sections 4.1–4.2 are theoretical introductions, and Section 4.4 is a practical application introducing the modeling of our data. We modeled the stellar atmosphere and circumstellar envelope using basic models of a Uniform Disk (UD) and a Gaussian profile, as introduced in Section 2.1.4. These models were applied to both AMBER and MIDI observations. Section 4.1 introduces the dynamic model atmospheres developed by Hofmann et al. (1998); Bessell et al. (1996); Ireland et al. (2004a,b), and the content of the Section is based on these references. We used these models for modeling the AMBER data (Sec. 6.3). Section 4.2 outlines the radiative transfer modeling of the circumstellar dust shell. Dynamic model atmospheres representing the central source *and* the dust shell in a self-consistent way are still very rare. This is particularly true for oxygen-rich stars. Nevertheless, some advances in this domain have already been successfully achieved (Ireland & Scholz, 2006; Höfner & Andersen, 2007; Ireland et al., 2008; Höfner, 2008). In this work we used for the MIDI data (chapters 5–9) the best possible modeling approach of a combination of an ad-hoc radiative transfer model describing the dust shell where the central source is represented by available and established dust-free dynamic model atmosphere series, as introduced by (Wittkowski et al., 2007) (Sec. 4.3). In Section 4.4 we perform simulations using this modeling approach in order to investigate the theoretical photometry and visibility variations. These tests are divided into three sections. In the first section the atmosphere of the star is modeled with the silicate being the main component of the dust shell. In the second section the atmosphere with Al_2O_3 as the main component is modeled, while the last section is devoted to the atmosphere of the star with a combination of these two dust species. The simulations investigate various dust shell parameters including the optical depth of the investigated dust species, inner boundary radii of the dust shell, density distribution and projected baselines length as well as theoretical intra-cycle and cycle-to-cycle photometry and visibility variations. These tests are directly related to the following chapters (Section 5 - 9) that are investigating the oxygen-rich Mira variables RR Aql (with silicate as a major component of the dust shell), S Ori (Al_2O_3), GX Mon (Al_2O_3 + silicate), and R Cnc (Al_2O_3).

Table 4.1: Mira model series - Hofmann

Series	Mode	P(days)	$M/M_\odot$	$L/L_\odot$	$R_p/R_\odot$	l/H_p	T_{eff}	ΔM_{bol}	Δv
Z	f	334	1.0	6310	236	2.82	3370	1.0	36
D	f	330	1.0	3470	236	1.76	2900	1.0	31
E	o	328	1.0	6310	366	1.26	2700	0.7	15
P	f	332	1.0	3470	241	2.06	2860	1.3	40
M	f	332	1.2	3470	260	1.73	2750	1.2	42
O	o	320	2.0	5830	503	0.93	2250	0.5	22

4.1 Dust free dynamic model atmospheres

For the interpretation of interferometric and spectroscopic observations of Mira variables, it is crucial to compare the observed data with atmosphere models based on pulsation models. We modeled the dust-free stellar atmosphere, including the continuum-forming photosphere and overlying molecular layers, using the complete, self-excited dynamic model atmospheres of Mira stars. The models have been developed Hofmann et al. (1998); Bessell et al. (1996); Ireland et al. (2004a,b). The following section is based on these references. These models have already successfully explained observations (e.g. Hofmann et al., 2000, 2001), (Hofmann et al. 2002), (Woodruff et al., 2004), (Fedele et al., 2005). We have used the P and M series by Ireland et al. (2004a,b) and references therein. The P and M series are based on nonlinear pulsation models designed to represent the prototypical Mira variable *o* Ceti presented by Bessell et al. (1996). Bessell et al. (1996) introduced three series *Z*, *D*, and *E*. The detailed pulsating envelope structures were obtained by a three-stage process including: 1-A time sequence of self-excited pulsation models of the whole envelope (down to T 10^7 K). However, with a relatively coarse zoning of the outer layers. 2- From the self-excited models series the time dependence of radius R and luminosity L for a mass zone with T 4000-5000K was obtained. Afterward, these values were used as the inner boundary conditions for the second series of pulsation model calculations with fine mass zoning of the outer layers. 3- Selected models were taken from these pulsation series and their density structure was used as input to a model atmosphere calculation. From these calculations Mira spectra were computed.

The models represent the prototype Mira variable *o* Ceti, and therefore have pulsation periods very close to the 332 day period of this star. For all models, a mass of 1 $M_\odot$ and solar abundances were assumed. Two values of stellar luminosity were used. The first one ($L = 6310 L/L_\odot$) based on the (M_{bol}, log P) relation for long period variables (LPVs) in the LMC (Feast et al., 1989; Hughes & Wood, 1990). The second was chosen in order to give $T_{\rm eff}$ = 2900 K, which earlier calculation (Bessell et al., 1989; Bessell & Scholz, 1989; Wood, 1990) indicate as a good approximation to the mean $T_{\rm eff}$ of *o* Ceti. The linear pulsation code of Fox & Wood (1982) was applied to compute the required pulsation period of 332 days based on a range of adopted $T_{\rm eff}$ values. The $T_{\rm eff}$ values were obtained by varying the ratio l/H_p of mixing length to pressure scale height. The parameters of the first three 'parent' models are summarized in Table 4.1 In the study, both fundamental mode and first-overtone models were examined. However, only the fundamental models were able to produce the observed light and velocity amplitudes, suggesting that Mira variables are fundamental mode pulsators (Bessell et al., 1996).

The first model series *Z*, *D*, and *E* were extended by Hofmann et al. (1998) by three more model series *P*, *M* and *O*, which were again created by series of nonlinear pulsation models. The

individual model density structures were then used as an input to a model atmosphere code with which non-grey temperature structures and CLV curves were constructed. The pulsation of the atmospheric outer layers of the models used by Bessel was produced by applying a piston to the sub-atmospheric layers. The time variation of radius and luminosity at the piston was obtained from sequences of complete self-excited pulsation models that included all mass from the core (r $\sim$ 0.3 R) to the upper photosphere ($\tau_{\rm Ross} \sim 0.001$). The Rosseland radius ,$R_{\rm Ross}$, is given by the distance from the star's center to the layer at which the Rosseland optical depth equals unity. The piston concept of the Hofmann models that only considers the behavior of the outer layers, was abandoned in the new models and the atmospheric structures were taken directly from complete self-excited pulsation models. The pulsation code was updated to include the opacities produced by the OPAL group (Iglesias & Rogers, 1993).

Table 4.2: Mira model series - Ireland - P series

Model	$P + \Theta_{\rm vis}$	L ($L_\odot$)	R (R_p)	$R_{1.04}$ (R_p)	$T_{\rm eff}$ (K)	$T_{1.04}$ (K)
P05	0+0.50	1650	1.20	0.90	2160	250
P08	0+0.80	4260	0.74	.74	3500	3500
P10	1+0.00	5300	1.03	1.04	3130	3120
P11n	1+0.10	5650	1.17	1.19	2990	2970
P12	1+0.23	4540	1.38	1.30	2610	2680
P13n	1+0.30	3450	1.53	1.26	2310	2530
P14n	1+0.40	2920	1.73	1.19	2080	2510
P15n	1+0.50	1910	1.88	0.84	1800	2690
P15	1+0.60	1600	1.49	0.85	1930	2560
P17n	1+0.71	2100	0.76	0.75	2900	2910
P18	1+0.87	4770	0.77	0.77	3520	3520
P19n	1+0.90	5260	0.86	0.86	3410	3410
P20	1+0.99	4960	1.04	1.04	3060	3060
P21n	2+0.11	4750	1.23	1.21	2790	2810
P22	2+0.18	4400	1.32	1.26	2640	2700
P23n	2+0.30	3570	1.36	1.24	2470	2590
P24n	2+0.40	2380	1.38	1.16	2210	2420
P25	2+0.53	1680	1.17	0.91	2200	2500
P27n	2+0.70	2190	0.71	0.72	3020	3010
P28	2+0.83	5200	0.79	0.79	3550	3500
P29n	2+0.89	4990	0.97	0.97	3180	3170
P30	2+0.98	5840	1.13	1.14	3060	3050
P35	3+0.50	1760	1.13	0.81	2270	2680
P38	3+0.80	5110	0.78	0.78	3570	3570
P40	4+0.00	4820	1.17	1.16	2870	2880

The series were constructed to reproduce the M-type Mira prototypes *o* Cet and R Leo. The hypothetical non-pulsating "parent" stars have masses $M/{\rm M}_\odot$ = 1.0 (P series), 1.2 (M series), and 2.0 (O series) (The 20% increase in mass does imply an increase of $\sim$ 1.5 in envelope mass). Furthermore, the models have Rosseland radius $R_p/{\rm R}_\odot$ = 241 (P), 260 (M), 503 (O) and effective temperatures $T_{\rm eff}$ = 2860 K (P), 2750 K (M), and 2250 K (O). The models have again solar

Table 4.3: Mira model series - Ireland - M series

Model	Θ_{vis}	L ($L_\odot$)	R (R_p)	$R_{1.04}$ (R_p)	T_{eff} (K)	$T_{1.04}$ (K)
M05	0+0.49	1470	0.93	0.84	2310	2420
M06n	0+0.60	2430	0.78	0.78	2860	2860
M08	0+0.77	4780	0.81	0.81	3320	3320
M09n	0+0.89	5060	1.30	1.03	2970	2970
M10	1+0.02	4910	1.19	1.18	2750	2760
M11n	1+0.11	4360	1.26	1.21	2590	2640
M12n	1+0.21	3470	1.30	1.18	2410	2540
M12	1+0.27	2990	1.33	1.12	2300	2500
M14n	1+0.40	1670	1.17	0.91	2110	2400
M15	1+0.48	1720	0.88	0.83	2460	2530
M16n	1+0.60	2460	0.77	0.77	2860	2860
M18	1+0.75	4840	0.81	0.81	3310	3310
M18n	1+0.84	4980	0.99	1.00	3020	3010
M19n	1+0.90	5070	1.08	1.09	2900	2900
M20	2+0.05	4550	1.23	1.20	2650	2680
M21n	2+0.10	4120	1.26	1.21	2550	2610
M22	2+0.25	2850	1.27	1.40	2330	2490
M23n	2+0.30	2350	1.25	1.03	2230	2460
M24n	2+0.40	1540	1.09	0.87	2160	2410
M25n	2+0.50	2250	0.80	0.79	2770	2780

abundances, luminosity $L/\mathrm{L}_\odot = 3470$, and a pulsation period of 332 days, close to the periods of o Cet (332 days) and R Leo (310 days). As in the Bessell study, two luminosities were considered: a value of $\mathrm{L} \sim 6000 L/\mathrm{L}_\odot$ based on the ($\mathrm{M_{bol}}$, log P) period-luminosity-relation for the LMC and a second: $\mathrm{L} \sim 3500 L/\mathrm{L}_\odot$ corrected to solar metallicity. The luminosity and mass were adopted and the mixing length was adjusted the give the correct period in the non-adiabatic pulsation code. Non-grey temperatures were computed in the approximations of local thermodynamic and radiative equilibrium, i.e. instantaneous relaxation of shock-heated material behind the shock front was assumed. The density stratifications were determined from shock driven outflows and subsequent infall of matter (Tej et al., 2003). The non-linear pulsation models of Mira variables generally produce much larger amplitudes than observed. In order to stabilize the limiting amplitude, Bessel had to introduce a non-physical damping via the α parameter. Hofmann overcomes this problem by allowing the models to relax over a large number of cycles (Wood, 1995; Yaari & Tuchman, 1995). Hofmann models, in comparison to the Bessel models, show substantially more extended atmospheres and display stronger cycle-to-cycle variations.

In addition to the models presented by Bessel (Z, D, and E), Hofmann (P, M and O), and Tej (who extended the phase coverage of the models), Ireland et al. (2004b,a) introduced new phases of the P and M model series. The models were constructed in the same way as in the previous studies. The P model series of Hofmann covers four successive pulsation cycles. Ireland et al. (2004a,b) selected two cycles that show a very low and a very high contamination of near-continuum bandpasses according to Jacob & Scholz (2002). These models are available for 20 phases in 3 cycles for the M series, and 25 phases in 4 cycles for the P series. Tables 4.2 and 4.3

also list $R_{1.04}$ and $T_{1.04}$ ($T_{1.04} \sim (L/R^2_{1.04})^1/4$). Since the 1.04 μm bandpass shows very little contamination, $R_{1.04}$ is the monochromatic $\tau_{1.04} = 1$ optical-depth radius (Scholz & Takeda, 1987; Jacob & Scholz, 2002). This quantity is non-observable, but it tends to be close to an observable interferometric fit radius. The absolute zero-point of any phase assignment is uncertain by at least 0.1. Ireland et al. (2004b,a) reassigned more accurate phases to the full set of Hofmann/Tej models and a new set of supplementary models. This was done in order to study detailed phase effects. In the M series, the cycle-to-cycle variations are much less pronounced compared to the P series. After reducing mass, red giant pulsation models show increases in the irregularity of the pulsation. The model series do not include dust formation. The transition region between the dust-free stellar atmosphere and the dust-driven stellar wind region is a significant cause of modeling uncertainty. There is a radius cutoff of 5 R_p and a minimum temperature of 740 K. The temperature of about 1200 K where silicate grains may formed, in the case of dust-free M models, reached at around 2 continuum radii. This is true for most phases. At pre-maximum phases of the second cycle it is about 3 continuum radii. For the P series, the region reaching 1200 K is more phase and cycle-dependent and ranges from around 2 to more than 4 continuum radii. Corundum condensation occurs in comparison to silicate at about 1400 K. However, dust temperatures in a dusty atmosphere tend to be higher at a given distance from the star center than gas temperatures in a dust-free atmosphere.

4.2 Radiative transfer model

Dust shells around AGB stars have often been modeled using ad-hoc radiative transfer calculation (see Danchi et al. (1994); Lorenz-Martins & Pompeia (2000); Ohnaka et al. (2005, 2006)). For our MIDI data the dust shell surrounding the central star was modeled using the Monte Carlo radiative transfer code **mcsim_mpi** (Ohnaka et al. (2006)). This section briefly describes the modeling of the dust shell based on Ohnaka et al. (2006). The **mcsim_mpi** code can deal with different density distributions such as spherically symmetric, axisymmetric, and general three-dimensional cases. The **mcsim_mpi** code can also model multiple grain species which may have different density distributions. Dust with multiple grain sizes is treated as different grain species. The code also includes calculation of polarization. The basics of the Monte Carlo technique is explained in Wolf et al. (e.g. 1999); Niccolini et al. (e.g. 2003); Wolf (e.g. 2003). In simulation, a number of photon packets are emitted from the surface of the central radiation source and travel through the circumstellar dust envelope while interacting with dust grains.

The model space is divided into many cells and the density and the temperature is assumed to be constant in each cell. The initial position of a photon packet on the stellar surface, its direction, and the frequency of each initial photon packets are randomly determined. The spectral shape of the emitted photon packets should follow blackbody radiation of the given effective temperature $T_{\rm eff}$. The energy of each photon packet is given by $L_\star \Delta t/N$, where $L_\star$ is the stellar luminosity, Δt is the time interval of the simulation, and N is the total number of photon packets. The photon packet moves along its path, until the accumulated optical depth reaches τ_ν, the value chosen at the beginning. Every photon packet can proceed τ_ν before the next interaction with dust grains (absorption or scattering). τ_ν is chosen as $\tau_\nu = -\ln(1 - p)$, where p is a random number uniformly distributed between 0 and 1. The integration of τ_ν is performed along the path of the photon

packet.

$$\int \sum_{i=1}^{N_{sp}} \rho_i(\mathbf{r})(\kappa_{v,i} + \sigma_{v,i})dl, \tag{4.1}$$

where $\rho_i(\mathbf{r})$ is the number density of the i-th grain species at the position $\mathbf{r}$, $\kappa_{\nu,i}$ and $\rho_{,i}$ are the absorption and scattering cross sections of the i-th grain species, respectively, and N_{sp} is the number of different grain species. If multiple grain species exist, the probability for absorption (P_{abs}) or scattering (P_{sca}) with the i-th grain species is given by

$$P_{abs} = \frac{\rho_i(\mathbf{r})(\kappa_{v,i})}{\sum_{i=1}^{N_{sp}} \rho_i(\mathbf{r})(\kappa_{v,i} + \sigma_{v,i})}, P_{sca} = \frac{\rho_i(\mathbf{r})(\sigma_{v,i})}{\sum_{i=1}^{N_{sp}} \rho_i(\mathbf{r})(\kappa_{v,i} + \sigma_{v,i})}, \tag{4.2}$$

respectively. After scattering, the new direction of the photon packet is determined by a random number. For simplicity isotropic scattering is assumed. After absorption, the new direction is isotropically chosen, and the new frequency is chosen based on the temperature. The final frequency of the photon packet escaping the circumstellar envelope toward a given viewing angle, is registered within N_ν frequency bins which are distributed equidistantly in the logarithmic scale between ν_{min} (set to 256.3 x 10^{11} Hz (1000 μm)) and ν_{max} (3 x 10^{15} Hz (0.1 μm)). When all photons escape from the envelope, images at a given wavelength viewed from an arbitrary angle can be created by ray tracing. The monochromatic mean intensity (J_ν) and the temperature in a particular cell is available. J_ν is given by (Lucy 1999)

$$J_v dv = \frac{1}{4\pi}\frac{1}{V}\frac{L_\star}{N}\sum_{dv} l \tag{4.3}$$

where V is the volume of the cell, for all photon packets with frequencies in (ν, ν + dν). The calculation of the intensity expected for any line of sight by ray tracing is expressed as

$$I_v = I_v^\star + \int S_v e^{-\tau_v} d\tau_v,\ I_v^\star = B_v(T_{eff})e^{-\tau_v^\star}, \tag{4.4}$$

where $\tau_\nu^\star$ is the optical depth from the observer to the stellar surface along the line of sight defined by the viewing angle of the observer. The integration is performed along the line of sight. The $I_\nu^\star$ represents the intensity coming from the central star. If the line of sight does not intersect with the central star, it is set to zero. $S_\nu^\star$ is the source function. Isotropic scattering is given by

$$S_v = \frac{\sum_{i=1}^{N_{sp}} \rho_i(\mathbf{r})(\kappa_{v,i}B_v(T_i(\mathbf{r})) + \sigma_{v,i}J_v(\mathbf{r}\ ))}{\sum_{i=1}^{N_{sp}} \rho_i(\mathbf{r})(\kappa_{v,i} + \sigma_{v,i})} \tag{4.5}$$

where T_i ($\mathbf{r}$) is the temperature of the i-th grain species at the position $\mathbf{r}$, and B_ν (T_i ($\mathbf{r}$)) is the Planck function of that temperature.

The reliability of the **mcsim_mpi** code was tested for spherically symmetric cases by comparison of the results with those obtained with the DUSTY code. The DUSTY code is a publicly available radiative transfer code (Ivezic & Elitzur, 1997). The spectrum of the central star is represented by blackbody radiation with an effective temperature of 3000 K. For axisymmetric cases the **mcsim_mpi** code was compared to calculations using five different multi-dimensional

radiative transfer codes for a flattened, torus-like density distribution (Pascucci et al. 2004). All the results for both spherically symmetric and axisymmetric cases show very good agreement.

4.3 Modeling of the mid-infrared interferometric data

This section outlines a combination of an ad-hoc radiative transfer modeling of the dust shell with a self excited dust-free dynamic model atmospheres (referred to as a "global" model) that was used for the modeling of the mid-infrared MIDI data. From the comparison of the observations with the models, fundamental stellar parameters can be derived. The comparison of measured visibility and photometry spectra with theoretical predictions also indicates whether any of the models is a fair representation of observed oxygen-rich Mira variable stars. In the following the theoretical approach is described, based on Wittkowski et al. (2007).

The total flux and visibility values of the "global" model are computed as a simple addition of the center-to-limb intensity variations (CLVs) of the dust-free model atmosphere of the M series and of the pure dust-shell. The pure dust-shell is obtained by subtracting the contribution of the attenuated input radiation. The model covers the wavelength range 0.32 - 23 μm, and for wavelengths beyond 23 μm the source is extended by a blackbody approximation. The total flux values of the combined atmosphere and dust shell model ("global") were computed for each spectral channel as:

$$f_{\rm total} = f_{\rm star}^{\rm att} + f_{\rm dust} \tag{4.6}$$

and the total visibility as:

$$V_{\rm total} = \frac{f_{\rm star}^{\rm att}}{f_{\rm total}} V_{\rm star} + \frac{f_{\rm dust}}{f_{\rm total}} V_{\rm dust} \tag{4.7}$$

where $f_{\rm star}^{\rm att}$ represents the attenuated flux from the dust-free model atmosphere, $f_{\rm dust}$ represents the flux from the dust shell alone, and $f_{\rm total}$ is the addition of these two terms. $V_{\rm star}$ and $V_{\rm dust}$ are the synthetic visibilities computed for the dust-free model atmosphere and for the dust shell, respectively (see below).

This simple addition is possible, since it was confirmed that the inner boundary radius of the dust shell is clearly larger than that of the layer at which the atmosphere becomes optically thick at mid-infrared wavelengths Wittkowski et al. (2007). The extended low-intensity atmospheric molecular layers of the dust-free atmosphere model and the dust shell in the 'global' models could in some cases be overlapping. However, in this case the stellar atmosphere and dust shell are spatially separated.

4.3.1 Defining synthetic values from the stellar contribution

The central star is in our case substituted by the spectral energy distribution (SED) of the respective model atmosphere. For comparison with observations, we have chosen the M models series. Monochromatic CLVs were calculated at 3000 equally-spaced frequencies. The wavelength range covers $8\mu{\rm m} \leq \lambda \leq 13\mu{\rm m}$ with radii r between $R_{\rm out}^{\rm star} = 5$ x R_p (Ohnaka et al., 2006). The CLVs were calculated including H_2O and SiO lines. The line opacities were computed assuming local thermodynamic equilibrium (LTE).

The visibility values based on the stellar contribution are calculated for each spectral channel c of MIDI as (Wittkowski et al. 2007, David et all. 2000)

$$\mathrm{V}_c^{\mathrm{total}} = \frac{\int_{v_{min}(c)}^{v_{max}(c)} \int_0^{R_{\mathrm{out}}^{\mathrm{star}}} I_v^{\mathrm{star}}(r)\ e^{-\tau(v)}\ J_0\ (\pi\ \Theta_{\mathrm{out}}^{\mathrm{star}}\ (B/\lambda))\ r\ \mathrm{d}r\ \mathrm{d}v}{\int_{v_{min}(c)}^{v_{max}(c)} \int_0^{R_{\mathrm{out}}^{\mathrm{star}}} I_v^{\mathrm{star}}(r)\ \mathrm{e}^{-\tau(v)}\ r\ \mathrm{d}r\ \mathrm{d}v} \tag{4.8}$$

where B is the projected baseline length, and the $e^{-\tau(v)}$ describes the extinction by the dust shell. It should be mentioned, that this computation is valid for EWS analysis as it directly obtains the visibility modulus. In the case of MIA analysis, which is integrating the squared visibility modulus, the integration over frequency performed over the squared monochromatic visibility values would be needed (cf. Wittkowski et al., 2006).

The expected stellar flux contribution f_c^{star} is computed for each spectral channel c of MIDI as

$$f_c^{\mathrm{star}} = 2\pi \frac{\Theta_{\mathrm{out}}^{\mathrm{star}}['']/2}{206265} \int_{v_{min}(c)}^{v_{max}(c)} \int_0^{R_{\mathrm{out}}^{\mathrm{star}}} I_v^{\mathrm{star}}(r)\ e^{-\tau(v)}\ r\ \mathrm{d}r\ \mathrm{d}v \tag{4.9}$$

The optical depth $\tau(v)$ is calculated based on tabulated absorption and scattering coefficients Q_{abs} and Q_{sca} of the two dust species i as

$$\tau(v) = \sum_i\ \tau^i(v_0)\ \frac{Q_{\mathrm{abs}}^i(v)\ +\ Q_{\mathrm{sca}}^i(v)}{Q_{\mathrm{abs}}^i(v_0)\ +\ Q_{\mathrm{sca}}^i(v_0)} \tag{4.10}$$

where v_0 corresponds to $\lambda_0 = 0.55\ \mu$m.

4.3.2 Defining synthetic values from the dust contribution

Monochromatic CLVs of the dust shell, after excluding the contribution of the central star, are computed with the ray-tracing method. This approach is described in detail in Ohnaka et al. (2006, 2007). The outermost model radius, where the intensity is set to 0, is defined by R_{dust} = 25 x R_{Phot}. The MIDI interferometric field of view is ∼250 mas. This corresponds to ∼ 25 times the expected photospheric angular diameter of S Ori ∼10 mas (Wittkowski et al., 2007), RR Aql ∼10 mas (Karovicova et al., 2009). However, it was verified that changing the outer model radius from 25 R_{Phot} to 50 R_{Phot} does not change the diameter results (<0.3%), and therefore can be omitted.

The expected dust visibility and flux contribution V_c^{dust} f_c^{dust} is computed in the same way as for the dust-free model atmosphere, but without the extinction term $\mathrm{e}^{-\tau(v)}$. The computation is again derived for each each spectral channel c of MIDI as

$$\mathrm{V}_c^{\mathrm{total}} = \frac{\int_{v_{min}(c)}^{v_{max}(c)} \int_0^{R_{\mathrm{out}}^{\mathrm{dust}}} I_v^{\mathrm{dust}}(r)\ J_0\ (\pi\ \Theta_{\mathrm{out}}^{\mathrm{star}}\ (B/\lambda))\ r\ \mathrm{d}r\ \mathrm{d}v}{\int_{v_{min}(c)}^{v_{max}(c)} \int_0^{R_{\mathrm{out}}^{\mathrm{dust}}} I_v^{\mathrm{dust}}(r)\ \mathrm{e}^{-\tau(v)}\ r\ \mathrm{d}r\ \mathrm{d}v} \tag{4.11}$$

$$f_c^{\mathrm{dust}} = 2\pi \frac{\Theta_{\mathrm{out}}^{\mathrm{dust}}['']/2}{206265} \int_{v_{min}(c)}^{v_{max}(c)} \int_0^{R_{\mathrm{out}}^{\mathrm{dust}}} I_v^{\mathrm{dust}}(r)\ r\ \mathrm{d}r\ \mathrm{d}v \tag{4.12}$$

The grain size was set to 0.1 μm. The modeled dust species consists of Al_2O_3 grains for $\lambda <$ 8 μm (Koike et al., 1995), for $\lambda > 8$ μm (Begemann et al., 1997), and silicates (Ossenkopf et al., 1992). The density distribution ρ(r) is described by a single power law with index p ($\rho(\mathrm{r}) \propto \mathrm{r}^p$). All radiative transfer models of the dust shell are calculated with an outer radius, so that the shell thickness is $R_{\mathrm{out}}\ /R_{\mathrm{in}} = 1000$.

4.4 Theoretical simulations

In this thesis, we performed a number of model simulations in order to investigate the visibility and photometry variations that are theoretically expected in the 8–13 μm wavelength range. Our theoretical investigation is divided into three parts. The first group of simulations models an atmosphere of the star mainly composed of silicate. The simulations in the second group describe the Al_2O_3 atmosphere, and the last group of simulation models an atmosphere composed of both dust species.

We based our simulations on a global model with several sets of parameters. The global model consists of radiative transfer models of the Al_2O_3 and silicate dust shells where the central source is described by a dust-free dynamic model atmosphere. The stellar atmospheric structure including the effects from atmospheric molecular layers is fully described by the choice of the specific model of the M series. We selected a grid of the ten M models including the 1st and 2nd cycle. The grid consists of M16n (model visual phase 0.60), M18 (0.75), M18n (0.84), M19n (0.90), M20 (0.05), M21n (0.10), M22 (0.25), M23n (0.30), M24n (0.40), M25n (0.50). For each of these 10 atmosphere models, whose SEDs are used as the central source, we calculated a computational grid of radiative transfer models of the dust shell. We investigated the effects of expected variations of the atmosphere model and the dust shell parameters during a pulsation cycle in order to interpret the observed photometry and visibility spectra of our three objects RR Aql, S Ori, and GX Mon. Lorenz-Martins & Pompeia (2000) have investigated the envelopes of 31 oxygen-rich AGB stars using the IRAS LRS spectra. Their sample also includes the Mira variables RR Aql, S Ori, and GX Mon. They classify the objects into three groups. The first group consist of stars whose IRAS LRS spectra can be modeled using silicate grains (RR Aql), the second group can be modeled using Al_2O_3 grains (S Ori), and the third group using the mix of silicate and Al_2O_3 grains (GX Mon).

The simulations 1-5 corresponds to typical parameters for stellar atmospheres with mainly

silicates in the dust shell. The parameters for these simulations are similar to those derived for RR Aql determined below in Sect. 5.3.5. The simulations 6-7 describe a stellar atmosphere with Al_2O_3 grains as a major component of the dust shell. The parameters are adopted from Wittkowski et al. (2007) (for the example of S Ori). The simulations 8-10 investigate atmosphere with a mix of silicate and Al_2O_3 grains. Tables 4.4, 4.5, 4.6 list the performed simulations including the phase of the model, the optical depth τ_V (Al_2O_3) and τ_V (silicate). The amount of dust of each species was characterized by the optical depths at a wavelength of 0.55 μm. The table lists also the inner boundary radii of the dust shell, $R_{\rm in}/R_{\rm Phot}$ (Al_4O_3) and $R_{\rm in}/R_{\rm Phot}$ (silicate). We used the inner boundary radii in units of the stellar photospheric radius $R_{\rm Phot}$ that is set to $R_{\rm Phot} = R_{1.04}$, the power-law indexes of the density distributions p (Al_2O_3), p (silicate), and the continuum photospheric angular diameter $\Theta_{\rm Phot}$. We assume a phase dependence of the angular photospheric diameter of about 20% (Thompson et al., 2002a; Ireland et al., 2004b). Figs. 4.3 - 4.17 show the results from the simulations. Each simulation compared two or more models, where one or more of the model parameters have been varied. The solid lines in the plots represent the global model, which is the sum of the attenuated stellar and dust contribution, represented respectively as dotted and dashed lines (Eq. 4.6 ans 4.7). The dashed-dotted lines in the visibility plot indicate the visibility based solely on the dust-free atmosphere model, i.e. $V_{\rm star}$ in Eq. 4.7.

4.4.1 Silicate-rich dust shell (Example of the oxygen-rich Mira variable RR Aql)

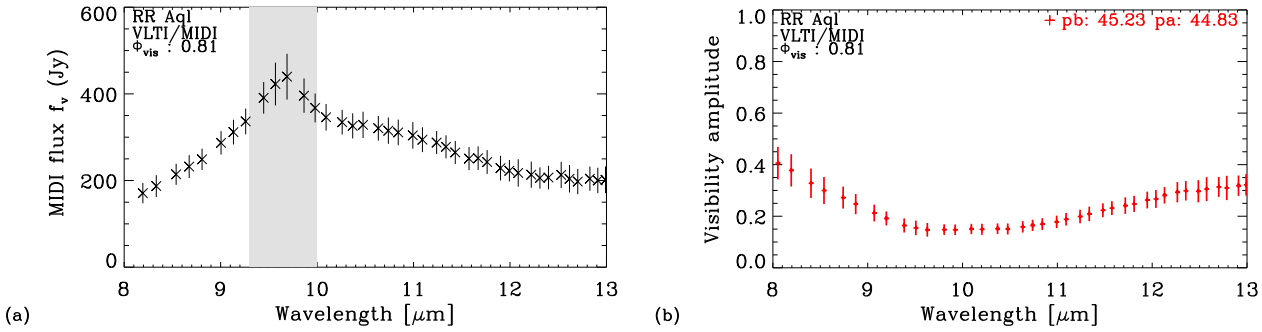

Figure 4.1: Flux (left) and visibility amplitude (right) in the wavelength range 8–13 μm for one of our MIDI observations of Mira variable RR Aql (see Chapter 5)

The visibility spectra contain information about the radial structure of the atmospheric molecular layers and the surrounding dust shells. The oxygen-rich Mira variable RR Aql, which is an example with silicate-rich dust shell from our sample of stars, is modeled in the following simulations. The visibility curves show a significant wavelength dependence with a steep decrease from 8 μm to $\sim$ 9.5 μm and a slow increase in the 9.5 μm to 13 μm range (Fig. 4.1). RR Aql is characterized by a typical drop in the visibility function $\sim$ 10 μm. Beyond $\sim$ 10 μm, the visibility increases again. The shape of the 8–13 μm flux spectrum with a maximum near 9.8 μm is known to be a characteristic silicate emission feature (e.g., Little-Marenin & Little, 1990; Lorenz-Martins & Pompeia, 2000). The corresponding drop in the visibility function between 8 μm and 9.5 μm is

a typical signature of a circumstellar dust shell that is dominated by silicate dust (Driebe et al. (c.f., e.g., 2008); Ohnaka et al. (c.f., e.g., 2008)).

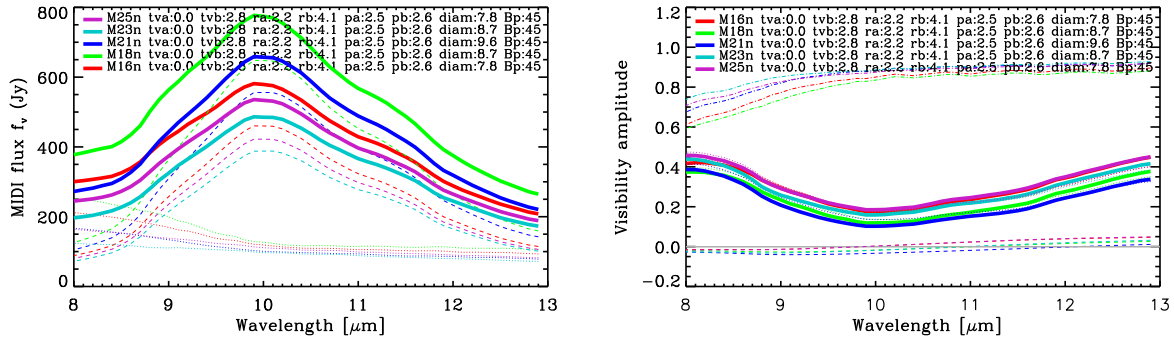

Figure 4.2: Simulation 0. Synthetic flux (left) and visibility amplitude (right) in the wavelength range 8–13 μm. The solid lines represent the global models, the dashed-dotted lines denote the unattenuated stellar contribution, the dotted lines denote the attenuated stellar contribution, and the dashed lines denote the dust shell contributions. This simulation compares five models consisting of the same dust shell parameters but different model atmospheres. The model atmosphere M16n ($\Phi_{\rm model}$ = 0.60) (red), the model M18n ($\Phi_{\rm model}$ = 0.84) (green) , the model M21n ($\Phi_{\rm model}$ = 0.10) (dark blue), the model M23n ($\Phi_{\rm model}$ = 0.30) (light blue), and the model M25n ($\Phi_{\rm model}$ = 0.50) (violet). The photospheric angular diameter is assumed to be larger at post-maximum phase than at minimum phase (9.6 mas compared to 7.8 mas). The projected baseline length is 45 m. For the exact model parameters, see Tab. 4.4. They describe variations around our best-fitting model for RR Aql.

Simulation 0

Simulation 0 introduces the selected models M16n ($\Phi_{\rm model}$ = 1 + 0.60), M18n ($\Phi_{\rm model}$ = 1 + 0.84), M21n ($\Phi_{\rm model}$ = 2 + 0.10), M23n ($\Phi_{\rm model}$ = 2 + 0.30), and M25n ($\Phi_{\rm model}$ = 2 + 0.50).

In simulation 0, we investigate the effect of model atmospheres at different pulsation phases which is shown in Fig. 4.2. We compared selected models covering 5 different pulsation phases over one full pulsation cycle. For all the models we applied the same dust shell parameters. The dust parameters were based on the average parameters (see Section 5.3.4 Tab. 5.3) of RR Aql derived in section 5.3.5. For the photometry the largest difference of $\sim$ 37% is seen around 10 μm, between model M18n and model M23n with less flux for the model after the maximum pulsation phase. All the models which used dust shell parameters show a clear difference between individual models. For the visibility however, the differences are less pronounced with a maximum difference of $\sim$10%. However, for the MIDI observations, the visibility measurements are more precise than the photometry, and therefore, in the following we focus mainly on the comparison of visibility functions. We mostly simulate model M21n at post-maximum pulsation phase ($\Phi_{\rm model}$ = 0.10) and model M23n or M24n at pre-minimum pulsation phase ($\Phi_{\rm model}$ = 0.30, and $\Phi_{\rm model}$ = 0.40). Model M21n proved to be the best fit to our RR Aql data (see Section 5.3.5 Table 5.3). The effective temperature of model M21n ($T_{\rm eff}$ = 2550 K) corresponds to the estimated effective temperature of RR Aql ($T_{\rm eff}$ = 2420 K) at the phase of our observation.

The following simulations 1 – 12 model the impact of a choice of a dynamic model atmosphere and various dust and shell parameters on the photometry and visibility spectra. Most of the simulations model spectra at minimum and maximum pulsation phase. Model M21n describing

the post-maximum phase is complemented with model M23n describing the pre-minimum phase with lower effective temperature (T_{eff} = 2230 K) and model M24n (T_{eff} = 2160 K).

Simulation 1

(Fig. 4.3) In simulation 1, we investigate the effect of model atmospheres at different pulsation phases and effective temperatures. We compared model M21n at a post-maximum pulsation phase ($\Phi_{model} = 0.10$) and model M23n at a pre-minimum pulsation phase ($\Phi_{model} = 0.30$), applying the same dust shell parameters for both models. The dust parameters are the same as in simulation 0, based on the results from the section 5.3.4. The projected baseline length was set to $B_p = 60$ m, which is the typical mean value of our MIDI observations. The overall shapes of the visibility spectra V_{total} (M21n) and V_{total} (M23n) are similar. The differences between the models are wavelength-dependent in the range of 4–10%. The shape of the photometry spectra are similar for both tested models f_{total} (M21n) and f_{total} (M23n). The largest difference of ~ 0.7 is seen around 10 μm, with less flux at minimum pulsation phase. Compared to the uncertainties of our MIDI measurements of $\sim$ 5–20% in the visibility spectra and of on average $\sim$ 20% in the photometric spectra (see Sect. 5.3), simulation 1 is consistent with our non-detection of visibility variations and a marginal detection of photometry variations.

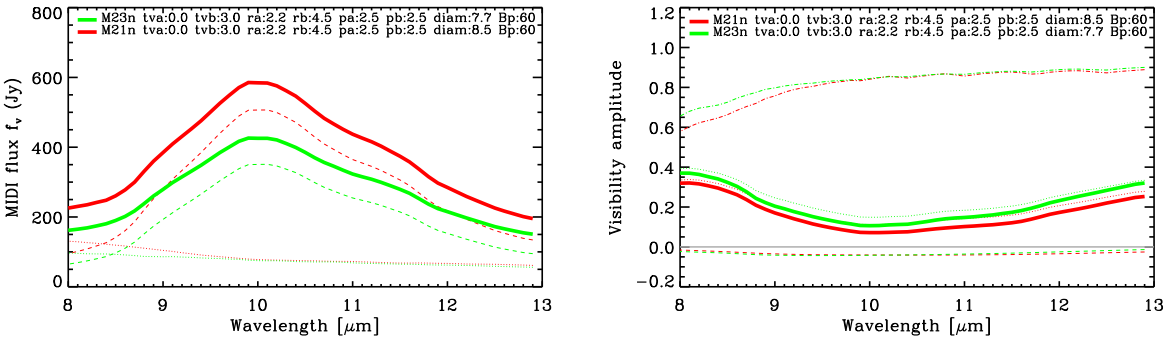

Figure 4.3: Simulation 1. This simulation compares two models consisting of the same dust shell parameters but different model atmospheres, the post-maximum model atmosphere M21n ($\Phi_{model} = 0.10$) (red) and the pre-minimum model atmosphere M23n ($\Phi_{model} = 0.30$) (green). The photospheric angular diameter is assumed to be 8.5 mas at the post-maximum phase compared to 7.7 mas at the minimum phase. The projected baseline length is 60 m.

Simulation 2

(Fig. 4.4) Compared to simulation 1, we adjusted the parameters according to the assumption that the outer layers of the atmosphere are cooler near minimum visual pulsation phase, and therefore more dust grains can form, and a higher molecular opacity can be expected. This theoretical assumption is consistent with mid-infrared interferometric observations (Wittkowski et al., 2007), where the observed data indicated more dust formation near minimum pulsation phase, with inner boundary radii of the dust shell located closer to the star. We increased the optical depth for model M23n. We also set a more extended dust shell after visual maximum for model M21n in comparison to the model M23n. This setting results in spectra with differences

Table 4.4: Model simulations. Each simulation compares two models that differ in one or more parameters. The differing parameters are marked by bold face.

Sim.	Model	$\Phi_{\rm vis}$	τ_V $Al(_2O_3)$ tva	τ_V (sil.) tvb	$R_{\rm in}/R_{\rm Phot}$ (Al_2O_3) ra	$R_{\rm in}/R_{\rm Phot}$ (sil.) rb	p (Al_2O_3) pa	p (sil.) pb	$\Theta_{\rm Phot}$ [mas] diam.	proj. bas. [m] B_p
0	**M25n**	**0.5**	0.0	2.8	2.2	4.1	2.5	2.6	**7.8**	45
	M23n	**0.3**	0.0	2.8	2.2	4.1	2.5	2.6	**8.7**	45
	M21n	**0.1**	0.0	2.8	2.2	4.1	2.5	2.6	**9.6**	45
	M18n	**0.8**	0.0	2.8	2.2	4.1	2.5	2.6	**8.7**	45
	M16n	**0.6**	0.0	2.8	2.2	4.1	2.5	2.6	**7.8**	45
1	**M21n**	**0.1**	0.0	3.0	2.2	4.5	2.5	2.5	**8.5**	60
	M23n	**0.3**	0.0	3.0	2.2	4.5	2.5	2.5	**7.7**	60
2	**M21n**	**0.1**	0.0	**3.0**	2.2	**4.5**	2.5	2.5	**8.5**	60
	M23n	**0.3**	0.0	**4.0**	2.2	**3.8**	2.5	2.5	**7.7**	60
3a	M21n	0.1	0.0	**3.0**	2.2	**4.5**	2.5	2.5	8.5	*60*
	M21n	0.1	0.0	**5.0**	2.2	**3.0**	2.5	2.5	8.5	*60*
3b	M21n	0.1	0.0	**3.0**	2.2	**4.5**	2.5	2.5	8.5	*40*
	M21n	0.1	0.0	**5.0**	2.2	**3.0**	2.5	2.5	8.5	*40*
3c	M21n	0.1	0.0	**3.0**	2.2	**4.5**	2.5	2.5	8.5	*25*
	M21n	0.1	0.0	**5.0**	2.2	**3.0**	2.5	2.5	8.5	*25*
3d	M21n	0.1	0.0	**3.0**	2.2	**4.5**	2.5	2.5	8.5	*15*
	M21n	0.1	0.0	**5.0**	2.2	**3.0**	2.5	2.5	8.5	*15*
4	M21n	0.1	**0.0**	3.0	2.2	4.5	2.5	2.5	8.5	60
	M21n	0.1	**0.6**	3.0	2.2	4.5	2.5	2.5	8.5	60
5	M21n	0.1	**0.0**	**3.0**	2.2	4.5	2.5	2.5	8.5	60
	M21n	0.1	**3.0**	**0.0**	2.2	4.5	2.5	2.5	8.5	60

in the range of 2-19% for the visibility values. The photometry differs again mostly around 10 μm with a maximum difference of 20%. Compared to simulation 1, the results are very similar, but with less differences in the photometry spectra. As in simulation 1, the results are consistent with our non-detection of visibility variations and a marginal detection of photometry variations within our measurement uncertainties (see Sect. 5.3).

Simulation 3

(Figs. 4.5 and 4.6) Here, we investigate the effect of different dust shell parameters (as in simulation 2), but keeping the M model constant. We used model M21n (phase 0.1), which is the best-fitting model to our RR Aql epochs (see Sect. 5.3.5) and also used a constant photospheric angular diameter. We compared two (silicate) dust models as in simulation 2, where in one model the optical depth is lower and the inner radius of the dust shell larger compared to the other model. These sets of model parameters lead to very similar results with visibility spectra almost overlapping, with a maximum difference of 4% for a projected baseline length of 60 m

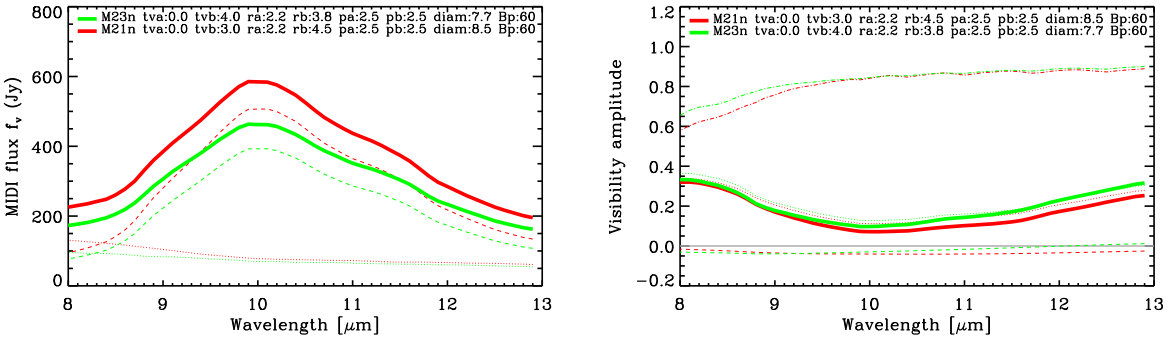

Figure 4.4: Simulation 2. As simulation 1 in Fig. 4.3, but for the parameters of simulation 2 comparing a post-maximum atmosphere model and a minimum model as in simulation 1, but where also the dust is assumed to be closer to the star with larger optical depth at the pre-minimum phase and farther from the star with lower optical depth at the post-maximum phase.

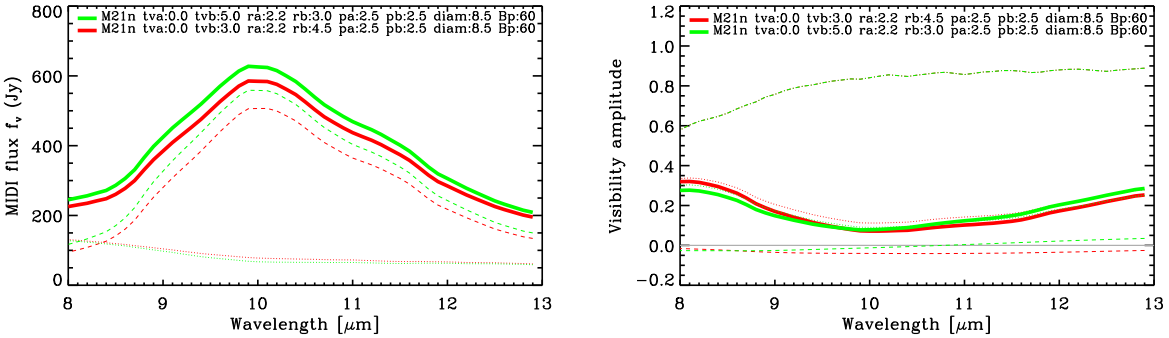

Figure 4.5: Simulation 3. As simulation 2 in Fig. 4.4, but where the atmosphere model is not varied.

(Fig. 4.5). The photometry spectra are also very similar with a maximum difference of 7%. Fig. 4.6 shows the visibility results for different projected baseline lengths of 40 m, 25 m, and 15 m. With projected baseline lengths of less than 60 m, the difference between the visibility values become more pronounced (10% difference beyond 10 μm with projected baseline lengths of 40 m and 25 m). This can be understood as the dust shell is over-resolved with a projected baseline length of 60 m, so that the visibility can not be sensitive to variations of the geometry of the dust shell. With a lower projected baseline length, the visibility values are located in the first lobe of the visibility function, and thus more sensitive to variations of the dust shell geometry. However, even with the lower projected baseline lengths of 15 m, the difference between individual models starts to be again less pronounced (<7%). In the wavelength range from 8 μm to $\sim$ 9 μm the dust is fully resolved with only baselines larger than $\sim$ 20 m and the visibility contribution of the dust reaches into the 2nd lobe of the visibility function.This indicates an optimum projected baseline length of $\sim$ 25–40 m to characterize the dust shell geometry for sizes as found for RR Aql.

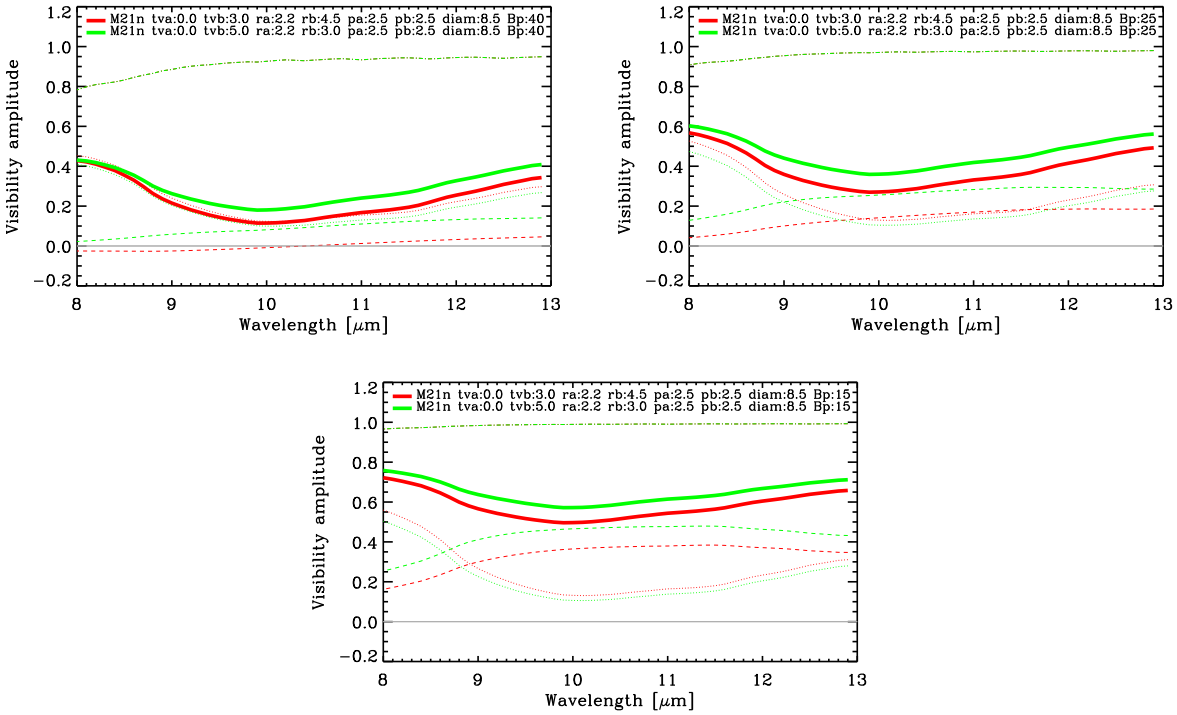

Figure 4.6: Simulation 3. As Fig. 4.5, but showing the visibility spectra for different projected baseline lengths of 40 m (top left), 25 m (top right), and 15 m (bottom).

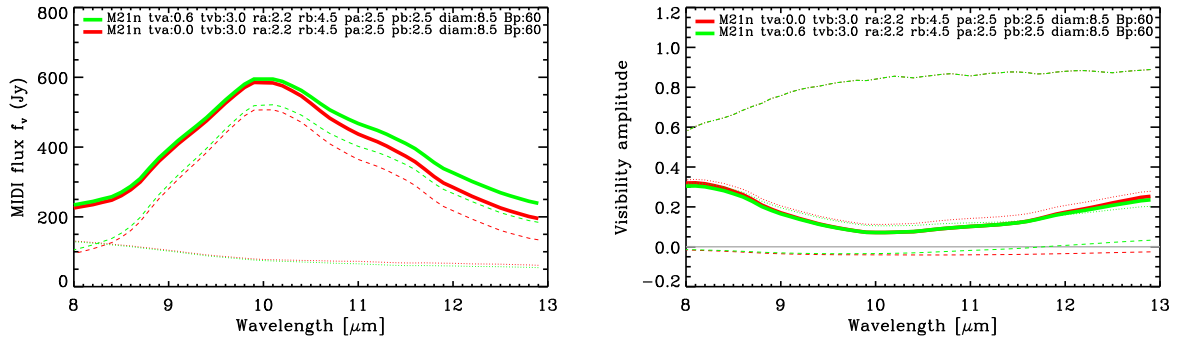

Figure 4.7: Simulation 4. Comparison of a model with a silicate shell only and a model that also includes an Al_2O_3 dust shell with lower optical depth. For the model parameters, see Tab. 4.4; For the description of the figure, see the caption of Fig. 4.3.

Simulation 4

(Fig. 4.7) Furthermore, we investigate the effect of adding small amounts of Al_2O_3 grains to a so far pure silicate dust shell. We examined 10% and 20% of Al_2O_3 grains. Fig. 4.7 shows the simulation with 20% of Al_2O_3 grains, showing that the addition of small amounts of Al_2O_3 grains leads to almost identical photometry and visibility spectra (differences <2%).

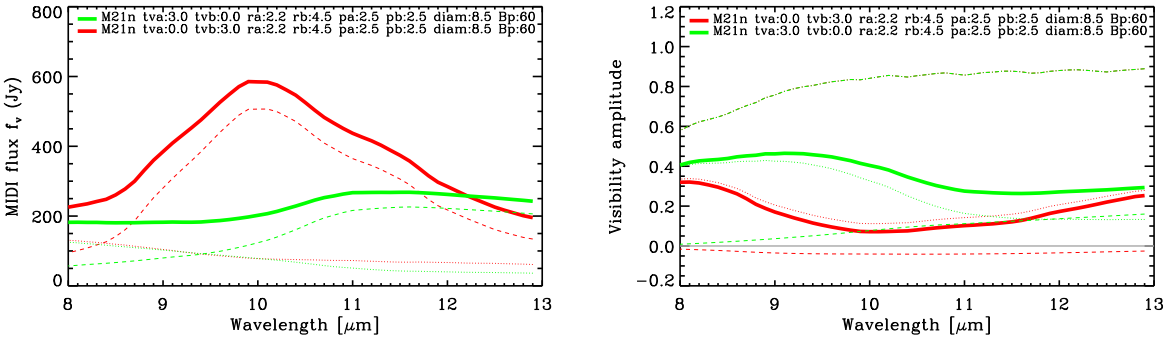

Figure 4.8: Simulation 5. Comparison of a model with a silicate dust shell only and a model with an Al_2O_3 dust shell only. For the model parameters, see Tab. 4.4; For the description of the figure, see the caption of Fig. 4.3.

Simulation 5

(Fig. 4.8) Here, we present the difference between a pure Al_2O_3 dust shell and a pure silicate dust shell. We used model M21n with dust shells of optical depth τ_V (Al_2O_3)=3 and τ_V (silicate)=0 versus τ_V(Al_2O_3)=0 and τ_V (silicate)=3. This simulation illustrates that silicate and Al_2O_3 dust shells lead to characteristically different shapes of the photometry and visibility spectra in the 8–13 μm wavelength range. In particular, it confirms that the feature near 10 μm is a characteristic signature for a silicate dust shell.

4.4.2 Al_2O_3-rich dust shell (Example of the oxygen-rich Mira variable S Ori)

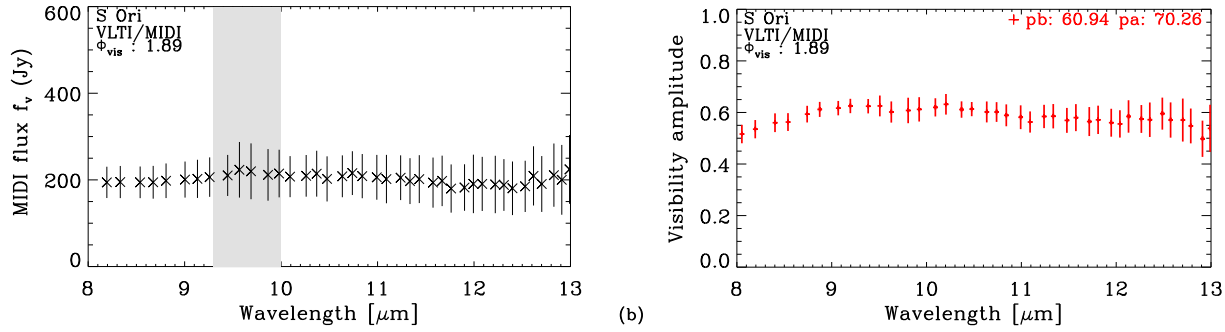

Figure 4.9: Flux (left) and visibility amplitude (right) in the wavelength range 8–13 μm for one of our MIDI observations of Mira variable S Ori (see Chapter 7).

The general shape of the visibility function of S Ori is characterized by a partially resolved stellar disc, including atmospheric molecular layers that are optically thick at mid-infrared wavelengths, surrounded by a spatially resolved, optically thin dust shell (Wittkowski et al., 2007). The visibility increases between ~8 - 9 μm and beyond ~ 9 - 10 μm the visibility flattens. This is because beyond ~9.5 μm radiation from the dust shell starts to represent a considerable part

of the total intensity, and the extinction of the stellar light by the dust shell becomes important. Compared to Mira variable RR Aql, S Ori does not exhibit any prominent silicate feature (Fig. 4.9). This broad spectrum and visibility function in the wavelength range 8–13 μm was interpreted as a dust shell consisting of Al_2O_3 dust (Wittkowski et al., 2007) or silicate and Al_2O_3 dust (Ohnaka et al., 2005). This indicates that silicate grains are not a main component of the dust shell.

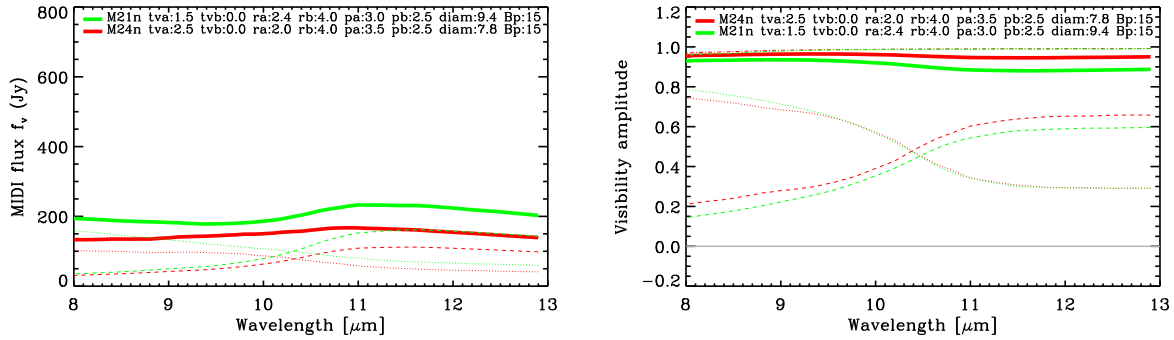

Figure 4.10: Simulation 6. This simulation compares two different model atmospheres, the post-maximum model atmosphere M21n ($\Phi_{\rm model} = 0.10$) (red) and the pre-minimum model atmosphere M24n ($\Phi_{\rm model} = 0.40$) (green), applying the dust shell parameters corresponding to the dust formation closer to the star during the minimum pulsation phase. The photospheric angular diameter is assumed to be 9.4 mas at post-maximum phase and 7.8 mas at minimum phase. The projected baseline length is 15 m.

Simulation 6

In simulation 6 (Fig. 4.10), we investigate the effect of model atmospheres at different pulsation phases simulating the atmosphere of Mira variable S Ori. We compared model M21n ($\Phi_{\rm model} = 0.10$) and model M24n ($\Phi_{\rm model} = 0.40$), applying the dust shell parameters based on the results in Wittkowski et al. (2007), showing more dust formation near minimum pulsation phase with the inner boundary radii of the dust shell located closer to the star. The angular diameter based on the work of Wittkowski et al. (2007) was set to 9.4 mas near minimum pulsation phase and 7.8 mas close the maximum pulsation phase. The projected baseline length was set for the first simulation to $B_p = 15$ m, which is a typical value of our MIDI observations. The overall shapes of the visibility spectra $V_{\rm total}$ (M21n) and $V_{\rm total}$ (M24n) are similar. The differences between the models are wavelength-dependent, and more pronounced beyond 10 μm. In comparison to the uncertainties of our MIDI measurements of $\sim$ 5–20% in the visibility spectra, the differences are $\sim$6% beyond 11 μm. The shape of the photometry spectra is almost the same for both tested models $f_{\rm total}$ (M21n) and $f_{\rm total}$ (M24n). The differences at 10 μm are $\sim$20%.

Simulation 7

(Fig. 4.11, 4.12, 4.13) Here, we keep the M models and dust shell parameters as in simulation 6, and we investigate the effect of different projected baseline lengths. Fig. 4.6 shows the visibility results for different projected baseline lengths of 30 m, 45 m, 60 m, 75 m, 90 m, and 105 m. With projected baseline lengths of less than 20 m, the difference between the visibility values become less

Table 4.5: Model simulations. Each simulation compares two models that differ in one or more parameters. The differing parameters are marked by bold face.

Sim.	Model	$\Phi_{\rm vis}$	τ_V $Al(_2O_3)$ tva	τ_V (sil.) tvb	$R_{\rm in}/R_{\rm Phot}$ (Al_2O_3) ra	$R_{\rm in}/R_{\rm Phot}$ (sil.) rb	p (Al_2O_3) pa	p (sil.) pb	$\Theta_{\rm Phot}$ [mas] diam.	proj. bas. [m] B_p
6a	M21n	0.1	**1.5**	**0.0**	**2.4**	**4.0**	**3.0**	**2.5**	**9.4**	**15**
	M24n	0.4	**2.5**	**0.0**	**2.0**	**4.0**	**3.5**	**2.5**	**7.8**	**15**
7a	M21n	0.1	1.5	0.0	2.4	4.0	3.0	2.5	9.4	**30**
	M24n	0.4	2.5	0.0	2.0	4.0	3.5	2.5	7.8	**30**
7b	M21n	0.1	1.5	0.0	2.4	4.0	3.0	2.5	9.4	**45**
	M24n	0.4	2.5	0.0	2.0	4.0	3.5	2.5	7.8	**45**
7c	M21n	0.1	1.5	0.0	2.4	4.0	3.0	2.5	9.4	**60**
	M24n	0.4	2.5	0.0	2.0	4.0	3.5	2.5	7.8	**60**
7d	M21n	0.1	1.5	0.0	2.4	4.0	3.0	2.5	9.4	**75**
	M24n	0.4	2.5	0.0	2.0	4.0	3.5	2.5	7.8	**75**
7e	M21n	0.1	1.5	0.0	2.4	4.0	3.0	2.5	9.4	**90**
	M24n	0.4	2.5	0.0	2.0	4.0	3.5	2.5	7.8	**90**
7f	M21n	0.1	1.5	0.0	2.4	4.0	3.0	2.5	9.4	**105**
	M24n	0.4	2.5	0.0	2.0	4.0	3.5	2.5	7.8	**105**

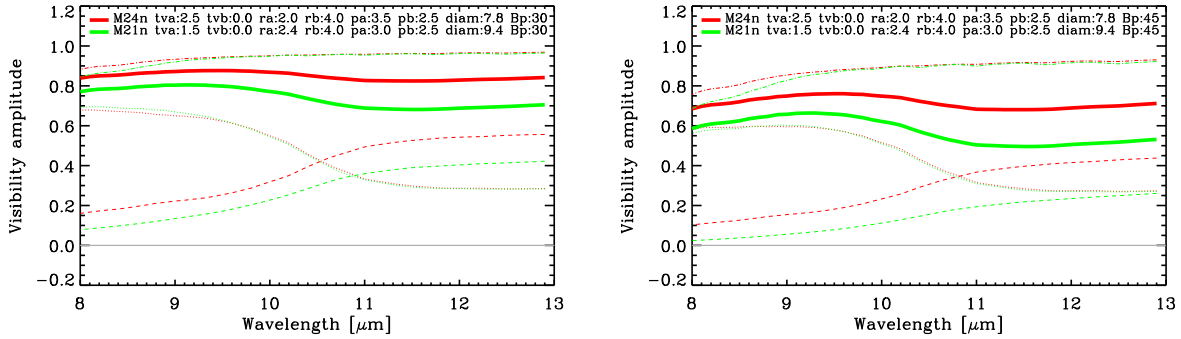

Figure 4.11: Simulation 7a,b. As Simulation 6 (Fig. 4.10), but showing the visibility spectra for different projected baseline lengths of 30 m (left), and 45 m (right).

pronounced (10% difference beyond 11 μm with projected baseline lengths of 15 m and 25 m). This can be understood as the star component is almost unresolved with a projected baseline length of 15 m, and therefore, the visibility is less sensitive to the variations. With larger projected baseline lengths, the star are more resolved, and thus more sensitive to variations of the dust shell geometry. Around 11 μm the difference is $\sim$ 15% (B_p=30 m), $\sim$ 0.7 (for B_p=45 m), $\sim$ 33% (for B_p=60 m), and $\sim$ 40% (for B_p=75 m). However, with projected baseline lengths greater than 90 m, the difference between individual models again starts to be less pronounced (with a maximum difference at 13μm of $\sim$ 40%). This indicates the optimum projected baseline length in order to characterize the dust shell geometry for the adopted angular diameters is $\sim$ 45–80 m

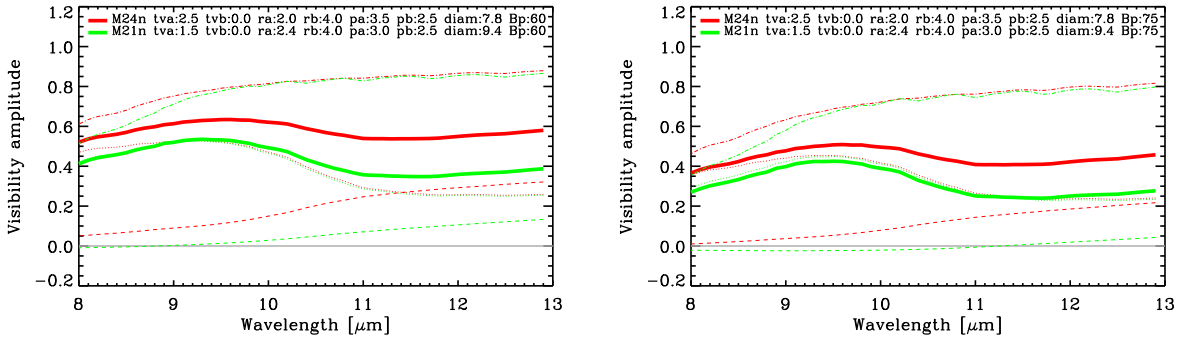

Figure 4.12: Simulation 7c,d. As Simulation 6 (Fig. 4.10), but showing the visibility spectra for different projected baseline lengths of 60 m (left), and 75 m (right).

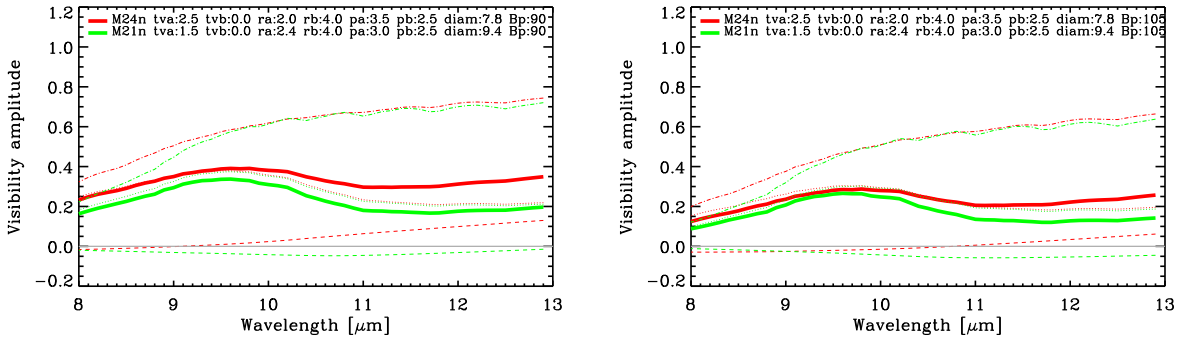

Figure 4.13: Simulation 7e,f. As Simulation 6 (Fig. 4.10), but showing the visibility spectra for different projected baseline lengths of 90 m (left), and 105 m (right).

4.4.3 Al_2O_3 + silicate -rich dust shell (Example of the oxygen-rich Mira variable GX Mon)

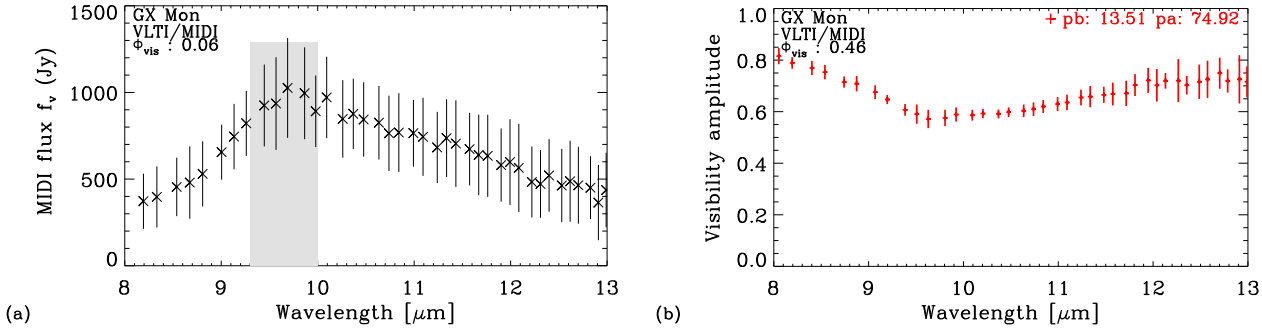

Figure 4.14: Flux (left) and visibility amplitude (right) in the wavelength range 8–13 μm for one of our MIDI observations of Mira variable GX Mon (see Chapter 8).

Fig . 4.14 shows that the general shape of the visibility and photometry function of GX Mon

is qualitatively similar to the Mira variable RR Aql, with typical silicate features present in both spectra, however, less pronounced. The visibility functions show a significant wavelength dependence with a steep decrease from 8 μm to ~9.5 μm, with a drop, and a slow increase in the 9.5 μm to 13 μm range. The photometry spectra show also the silicate feature, indicating presence of the silicate grains in the dust shell.

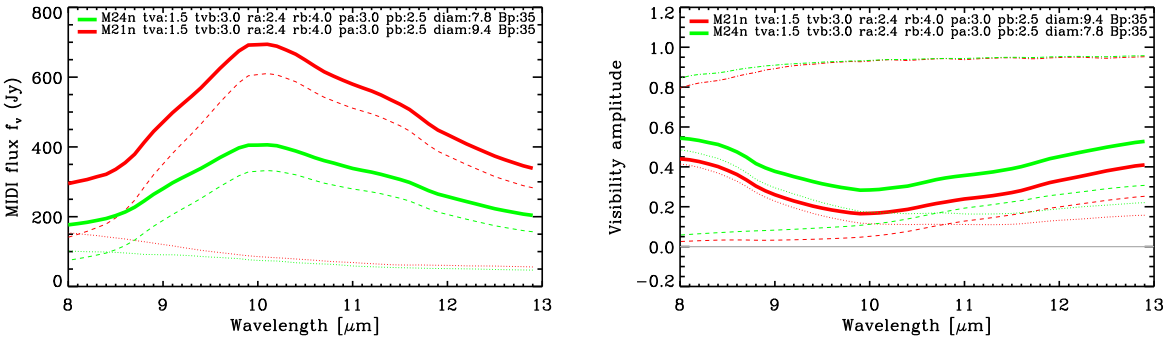

Figure 4.15: Simulation 8 The simulation compares two different model atmospheres, the post-maximum model atmosphere M21n ($\Phi_{\rm model} = 0.10$) (red) and the minimum model atmosphere M23n ($\Phi_{\rm model} = 0.30$) (green), using 1.5 of Al_2O_3 grains and τ_V (silicate) = 3.0 grains. The photospheric angular diameter is assumed to be 9.4 mas at post-maximum phase and 7.8 mas at minimum phase. The projected baseline length is 35 m.

Simulation 8

(Fig. 4.15) Here, we investigate an atmosphere with a mix of silicate and Al_2O_3 grains, typical for the atmosphere of the Mira variable GX Mon. The first simulation in this section shows model M21n and M24n with 1.5 of Al_2O_3 grains and 3.0 of silicate grains. The inner boundary radii and the power law index are set as for the simulation of the atmosphere of RR Aql. As mentioned before the angular photospheric diameter is assumed to be phase dependent. We adopt the values of the S Ori simulations. The projected baseline is set to 35 m.

Simulation 9

(Fig. 4.16) In simulation 9 we show the effect of the ratio of the two dust compounds, Al_2O_3 and silicate grains, for model M24n at pre-minimum pulsation phase (0.4). The inner boundary radii, the power law index, the angular photospheric diameter, and the projected baseline length are set to the same values as in simulation 8. We investigate a model with τ_V (Al_2O_3) = 3.0 and τ_V (silicate) = 0.7 grains, model with τ_V (Al_2O_3) = 3.0 and τ_V (silicate) = 1.5 grains, model with τ_V (Al_2O_3) = 3.0 and τ_V (silicate) = 3.0 grains, and model with τ_V (Al_2O_3) = 1.5 and τ_V (silicate) = 1.5 grains. Models with 3.0 of silicate grains do not vary significantly with an amount of Al_2O_3 grains (1.5 or 3.0). This is by contrast to the models with 3.0 of Al_2O_3 grains and different ratio of silicate grains. The different amount of silicate grains change significantly both, the visibility and photometry function, respectively. The largest difference is around 10μm.

The Table 4.7 lists the difference at ~ 10μm between models with a different ratio of the dust species (in %). The main difference is in the shape of the spectra as a functions the amount of

Table 4.6: Model simulations. Each simulation compares two models that differ in one or more parameters. The differing parameters are marked by bold face.

Sim.	Model	$\Phi_{\rm vis}$	τ_V $Al(_2O_3)$ tva	τ_V (sil.) tvb	$R_{\rm in}/R_{\rm Phot}$ (Al_2O_3) ra	$R_{\rm in}/R_{\rm Phot}$ (sil.) rb	p (Al_2O_3) pa	p (sil.) pb	$\Theta_{\rm Phot}$ [mas] diam.	proj. bas. [m] B_p
8	M21n	0.1	**1.5**	**3.0**	**2.4**	**4.0**	**3.0**	**2.5**	**9.4**	**35**
	M24n	0.4	**1.5**	**3.0**	**2.4**	**4.0**	**3.0**	**2.5**	**7.8**	**35**
9	M24n	0.4	**3.0**	**0.7**	2.4	4.0	3.0	2.5	7.8	35
	M24n	0.4	**3.0**	**1.5**	2.4	4.0	3.0	2.5	7.8	35
	M24n	0.4	**3.0**	**3.0**	2.4	4.0	3.0	2.5	7.8	35
	M24n	0.4	**1.5**	**3.0**	2.4	4.0	3.0	2.5	7.8	35
10	M21n	0.1	**3.0**	**0.7**	2.4	4.0	3.0	2.5	9.4	35
	M21n	0.1	**3.0**	**1.5**	2.4	4.0	3.0	2.5	9.4	35
	M21n	0.1	**3.0**	**3.0**	2.4	4.0	3.0	2.5	9.4	35
	M21n	0.1	**1.5**	**3.0**	2.4	4.0	3.0	2.5	9.4	35

Table 4.7: Model simulations. Each simulation compares two models that differ in the ration of the dust species. The last column lists the % difference between individual models.

	model dust ratio	model dust ratio	%difference $\sim 10\mu$m
visibility	τ_V (Al_2O_3) = 3.0 +	τ_V (Al_2O_3) = 3.0 +	47%
photometry	τ_V (silicate) = 3.0	τ_V (silicate) = 0.7	44%
visibility	τ_V (Al_2O_3) = 3.0 +	τ_V (Al_2O_3) = 3.0 +	30%
photometry	τ_V (silicate) = 3.0	τ_V (silicate) = 1.5	28%
visibility	τ_V (Al_2O_3) = 3.0 +	τ_V (Al_2O_3) = 1.5 +	$\sim$ overlap
photometry	τ_V (silicate) = 3.0	τ_V (silicate) = 3.0	4%

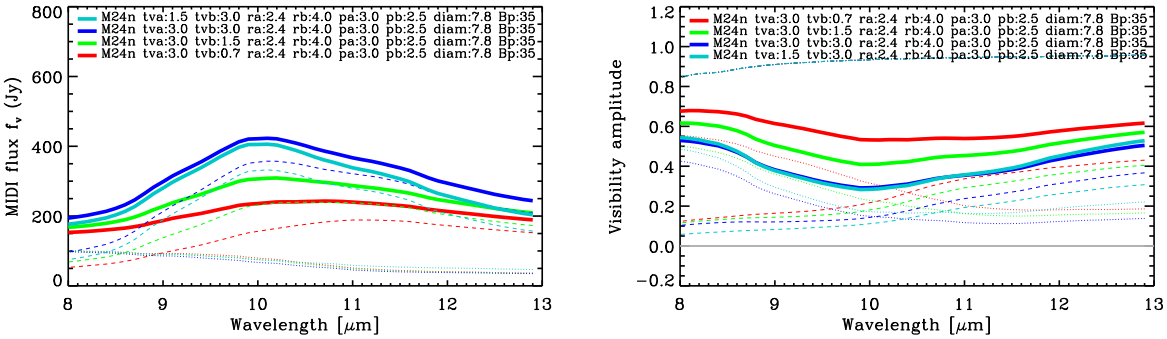

Figure 4.16: Simulation 9 The simulation compares four different sets of dust shell parameters using the minimum model atmosphere M24n ($\Phi_{\rm model} = 0.40$). The simulation shows τ_V (Al_2O_3) = 3.0 + τ_V (silicate) = 0.7 (light blue), τ_V (Al_2O_3) = 3.0 + τ_V (silicate) = 1.5 (violet), τ_V (Al_2O_3) = 3.0 + τ_V (silicate) = 3.0 (green), and τ_V (Al_2O_3) = 1.5 + τ_V (silicate) = 3.0 (red). The photospheric angular diameter is assumed to be 7.8 mas. The projected baseline length is 35 m. This ratio of the dust species corresponds to the observational photometry and visibility spectra of GX Mon quite well.

silicate.

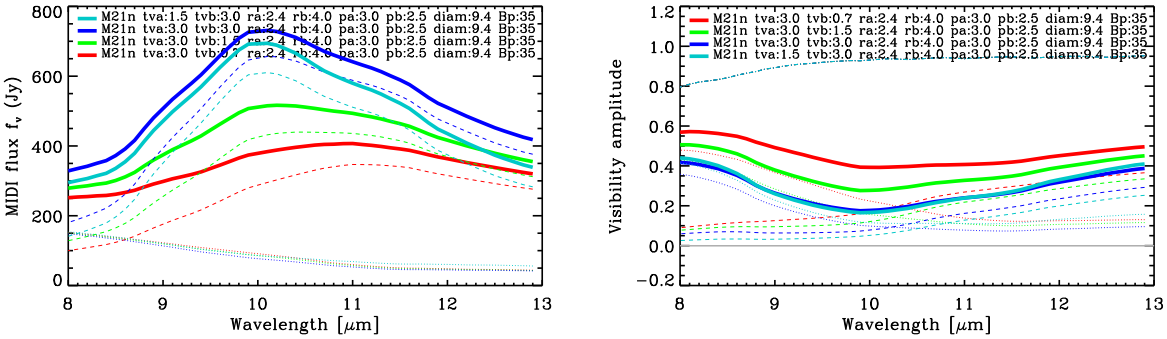

Figure 4.17: Simulation 10 The simulation compares four different sets of dust shell parameters using the pre-minimum model atmosphere M24n ($\Phi_{\rm model} = 0.40$). The simulation shows τ_V (Al_2O_3) = 3.0 + τ_V (silicate) = 0.7 (light blue), τ_V (Al_2O_3) = 3.0 + τ_V (silicate) = 1.5 (violet), τ_V (Al_2O_3) = 3.0 + τ_V (silicate) = 3.0 (green), and τ_V (Al_2O_3) = 1.5 + τ_V (silicate) = 3.0 (red). The photospheric angular diameter is assumed to be 9.6 mas. The projected baseline length is 35 m.

Simulation 10

(Fig. 4.17) Simulation 10 is the same as simulation 9 except that in this case we investigate model M21n at the post-maximum pulsation phase (0.1). The results are very similar to the results in Simulation 9, with the only difference being in the photometry function. The silicate feature for simulations with τ_V (Al_2O_3) = 3.0 + τ_V (silicate) = 3.0 is more pronounced than in the previous Simulation (maximum difference at 10μm of 48%). We conclude that the addition of a silicate dust shell with low optical depth compared to the Al_2O_3 dust shell affects strongly the features and shape of the photometry and visibility spectra.

Summarizing,
our model simulations based on the combination of a radiative transfer model of the dust shell with dynamic model atmospheres representing the central source predict rather small variations with phase at mid-infrared wavelengths. Our simulations indicate that detections of pulsation effects at mid-infrared wavelengths would in particular benefit from high accuracy additional photometric measurements, and from a well planned range of projected baseline lengths. The most suitable baseline lengths for RR Aql are $\sim$ 20–30 m, and for S Ori $\sim$ 45–80 m. These measurements would help us to distinguish models of different pulsation phases. We showed that for stars with a silicate dust chemistry, the addition of an Al_2O_3 dust shell with low optical depth compared to the silicate dust shell could not be detected. We also showed that for stars with an Al_2O_3 dust chemistry, the addition of a silicate dust shell with low optical depth, compared to the Al_2O_3 dust shell, affects the features and shape of the photometry and visibility spectra.

Chapter 5

MIDI Observations of RR AQL (silicate-rich dust shell)

5.1 Characteristics of RR Aql

RR Aql is an oxygen-rich Mira variable with spectral type M6e-M9 (Samus et al., 2004). RR Aql shows a strong silicate emission feature in its mid-infrared spectrum (Lorenz-Martins & Pompeia, 2000). In addition, it has relatively strong SiO, H_2O, and OH maser emission (Benson et al., 1990). Vlemmings & van Langevelde (2007) observed OH masers toward RR Aql at 5 epochs with the VLBA. Based on these observations, the distance to RR Aql is estimated to D = 633^{+214}_{-128} pc (HIPPARCOS distance D = 540 pc). van Belle et al. (2002) obtained with the Infrared Optical Telescope Array (IOTA) a K-band (λ=2.2 μm, $\Delta\lambda$=0.4 μm) angular size of $\Theta_{\rm UD}$ = 10.73 $\pm$ 0.66 mas at phase Φ = 0.48, an effective temperature $T_{\rm eff}$ = 2127 $\pm$ 111 K, and a bolometric flux $f_{\rm bol}$ = 78.4 $\pm$ 11.8 10^{-8} ergs $cm^{-2}s^{-1}$. Miyata et al. (2000) studied spectroscopically the dust around the star and obtained $F_{\rm dust}/F_{\rm star}$ at 10 μm of 1.49 $\pm$ 0.02. The mass loss rate of 9.1 10^{-7} $M_\odot$/year was estimated by Loup (1993). Ragland et al. (2006) measured the closure phase with IOTA in the H-band, and classified RR Aql as a target with no detectable asymmetries. The IRAS flux at 12 μm is 332 Jy. The light-curve in the V band varies from $\sim$8 at maximum light to $\sim$14 at minimum light. Whitelock et al. (2000) showed that the K magnitude of RR Aql varies from $\sim$0.0 at maximum light to $\sim$1.0 at minimum light. RR Aql is pulsating with a period of P = 394.78 days (Samus et al., 2004) and the Julian Date of the last maximum brightness is T_0 = 245 2875.4 (Pojmanski et al., 2005). The period of pulsation visually corresponds to recent values from the AAVSO[1] and AFOEV[2] databases. Figure 5.1 shows the visual light-curve of RR Aql based on values from the AAVSO and AFOEV databases as a function of Julian day and stellar phase.

[1] http://www.aavso.org
[2] http://cdsweb.u-strasbg.fr/afoev

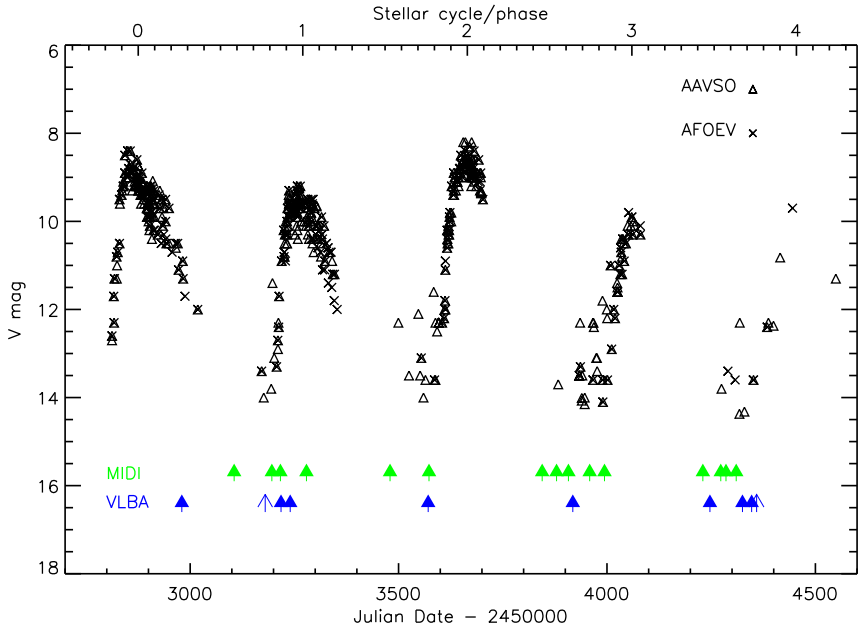

Figure 5.1: Visual light-curve of RR Aql based on data from the AAVSO and AFOEV databases as a function of Julian Date and stellar cycle/phase. The green arrows indicate the dates of our VLTI/MIDI observations. The blue arrows indicate the dates of our VLBA observations. Here, the full arrows denote observations of SiO maser emission and simple arrows observations of H_2O maser emission.

5.2 VLTI/MIDI Observations and data reduction

We obtained 57 spectrally-dispersed mid-infrared interferometric observations of RR Aql with the VLTI/MIDI instrument between Apr 9, 2004 and Jul 28, 2007. MIDI - the mid-infrared interferometric instrument (Leinert et al., 2004) combines the beams from two telescopes of the VLTI (Glindemann et al., 2003) and provides spectrally resolved visibilities in the 10 μm window (N-band, 8-13 μm). To obtain dispersed photometric and interferometric signals, we used the PRISM as a dispersive element with a spectral resolution R = $\Delta\lambda/\lambda \sim 30$. The beams were combined in *High_Sens* mode (HS). In this mode the photometric signal is observed after the interferometric signal.

The details of the observations and the instrumental settings are summarized in Table 5.1. The Table lists the epoch, the date, the time, the Julian Date (JD), the visual pulsation phase Φ_{vis}, the baseline configuration, the ground length of the configuration, the dispersive element, the beam combiner BC, the projected baseline length B_p, the position angle on the sky P.A. (deg. east of north), the DIMM seeing (at 500 nm), and the coherence time τ_0 (at 500 nm). All observations were executed in service mode using either the Unit Telescopes (UTs, 8.2m), or the Auxiliary Telescopes (ATs, 1.8m). The Figure 5.2 represents the *uv* coverage of our MIDI observations of RR Aql.

We merged the MIDI data into 15 epochs, with a maximum time-lag between individual observations of 5 days for each epoch (1.3% of the pulsation period). For technical problems we had to eliminate 2 epochs. The final 13 epochs are indicated by green arrows in Fig. 5.1 in comparison to the light-curve. The uncertainty in the allocation of the visual phase to our observations was estimated to ∼0.1. The blue arrows in Fig. 5.1 indicate our long-term VLBA monitoring of SiO

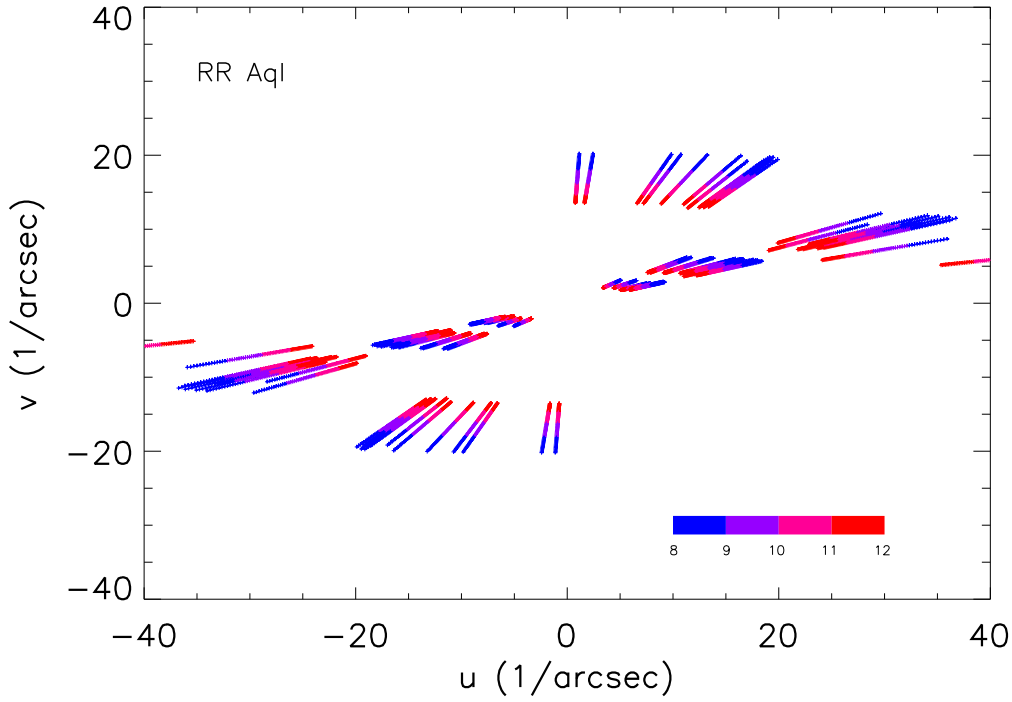

Figure 5.2: Coverage of the *uv* plane for the MIDI observations of RR Aql. Each point represents the UTs or ATs observations respectively over the wavelenght 8 to 13 μm.

and H_2O maser emission toward RR Aql, which will be presented in a forthcoming paper.

We used the MIA+EWS software package, version 1.6 (Jaffe, Koehler, et al[3]) for the MIDI data reduction. This package includes two different methods, an incoherent method (MPIA software package MIA) that analyzes the power-spectrum of the observed fringe signal, and a coherent integration method (EWS), which first compensates for optical path differences including both instrumental and atmospheric delays in each scan, and then coherently adds the fringes. We applied both methods to independently verify the data reduction results. The detector masks were calculated by the procedure of MIA, and were used for both the MIA and the EWS analysis. The obtained data reduction values correspond to each other, and we chose to use in the following the results derived from the EWS analysis, which offer error estimations.

To account for instrumental visibility losses and to determine the absolute flux values, calibrator stars with known flux and diameter values were observed immediately before or after the science target. Our main calibrators were HD 169916 (period P73, P75), HD 146051 (P77), and HD 177716 (P79). Calibrated science target visibility spectra were calculated using the instrumental transfer function derived from all calibrator data sets taken during the same night with the same baseline and instrumental mode as our scientific target. The number of available transfer function measurements depends on the number of calibrator stars observed per specific night including those calibrators observed by other programs (Tab. B.1). The errors of the transfer functions are given by the standard deviation of all transfer function measurements per night. To

[3]http://www.strw.leidenuniv.nl/∼nevec/MIDI

Table 5.1: VLTI/MIDI observation of RR Aql.

Epoch	DDMMYYYY	Time [UTC]	JD	Φ_{vis}	Config.	B	Disp. Elem.	BC	B_p [m]	PA [deg]	Seeing [″]	τ_0 [msec]
A	09042004	07:26	2453105	0.58	U2-U3	47m	Prism	HS	33.57	3.21	0.45	7.4
A	10042004	09:05	2453106	0.58	U2-U3	47m	Prism	HS	37.17	26.09	-1.00	7.8
A		09:52	2453106	0.58	U2-U3	47m	Prism	HS	39.86	33.48	0.64	8.2
B	09072004	08:25	2453196	0.81	U2-U3	47m	Prism	HS	45.23	44.83	0.47	4.8
C	28072004	08:09	2453215	0.86	U2-U3	47m	Prism	HS	42.54	41.57	1.36	1.0
C	29072004	02:05	2453216	0.86	U2-U3	47m	Prism	HS	37.83	28.16	1.66	1.0
C		03:33	2453216	0.86	U2-U3	47m	Prism	HS	42.84	39.49	0.75	2.3
C		04:55	2453216	0.86	U2-U3	47m	Prism	HS	45.99	44.67	1.04	1.6
C		06:33	2453216	0.86	U2-U3	47m	Prism	HS	46.16	45.71	3.38	0.5
C		07:04	2453216	0.86	U2-U3	47m	Prism	HS	45.32	44.92	2.68	0.7
C	01082004	00:12	2453219	0.87	U2-U3	47m	Prism	HS	33.76	6.86	0.73	3.1
D	18042005	10:30	2453479	1.53	U2-U4	89m	Prism	HS	88.37	81.72	0.76	3.5
D	19042005	07:53	2453480	1.53	U2-U4	89m	Prism	HS	61.36	76.41	0.83	2.3
E	20072005	03:51	2453572	1.76	U1-U4	130m	Prism	HS	119.63	59.78	0.71	1.9
E		06:16	2453572	1.76	U1-U4	130m	Prism	HS	128.64	63.28	0.81	1.6
E	22072005	05:10	2453574	1.77	U2-U3	47m	Prism	HS	45.65	44.12	1.00	1.4
E		07:56	2453574	1.77	U2-U3	47m	Prism	HS	44.44	43.96	1.11	1.2
F	18042006	09:38	2453844	2.45	D0-G0	32m	Prism	HS	28.99	70.01	1.08	2.1
F	19042006	08:32	2453845	2.46	D0-G0	32m	Prism	HS	24.74	65.81	0.80	6.0
F		09:21	2453845	2.46	D0-G0	32m	Prism	HS	28.21	69.32	0.78	6.3
G	21052006	05:53	2453877	2.54	E0-G0	16m	Prism	HS	10.94	62.10	0.56	4.0
G	25052006	06:35	2453881	2.55	A0-G0	64m	Prism	HS	53.17	67.77	0.55	5.1
G		08:46	2453881	2.55	A0-G0	64m	Prism	HS	63.93	72.67	0.44	6.7
H	18062006	03:58	2453905	2.61	D0-G0	32m	Prism	HS	21.37	61.34	1.29	1.5
H		04:41	2453905	2.61	D0-G0	32m	Prism	HS	25.09	66.21	1.27	1.6
H	18062006	05:39	2453905	2.61	D0-G0	32m	Prism	HS	29.05	70.06	1.00	2.1
H	20062006	05:49	2453907	2.61	A0-G0	64m	Prism	HS	59.89	70.81	1.05	3.9
H		06:33	2453907	2.61	A0-G0	64m	Prism	HS	63.00	72.15	0.88	4.5
H	21062006	07:08	2453908	2.62	E0-G0	16m	Prism	HS	16.00	72.76	1.01	2.2
H		09:36	2453908	2.62	E0-G0	16m	Prism	HS	13.21	70.37	0.77	2.9
H	23062006	03:20	2453910	2.62	E0-G0	16m	Prism	HS	9.84	58.42	0.76	3.9
H		04:07	2453910	2.62	E0-G0	16m	Prism	HS	11.97	64.86	0.67	4.4
I	08082006	05:12	2453956	2.74	A0-G0	64m	Prism	HS	61.41	72.62	1.02	2.3
I		05:57	2453956	2.74	A0-G0	64m	Prism	HS	56.88	71.58	1.10	2.2
I	09082006	06:39	2453957	2.74	A0-G0	64m	Prism	HS	50.33	69.49	1.47	1.5
I	10082006	03:07	2453958	2.74	D0-G0	32m	Prism	HS	31.37	72.03	1.43	2.6
I		04:31	2453958	2.74	D0-G0	32m	Prism	HS	31.65	72.90	1.67	2.5
I		05:45	2453958	2.74	D0-G0	32m	Prism	HS	28.72	71.74	1.43	3.2
I	11082006	02:44	2453959	2.74	D0-G0	32m	Prism	HS	30.76	71.51	1.43	2.3
I	13082006	04:05	2453961	2.75	E0-G0	16m	Prism	HS	15.94	72.90	0.91	1.9
I		04:56	2453961	2.75	E0-G0	16m	Prism	HS	15.26	72.56	0.63	2.7
I		05:52	2453961	2.75	E0-G0	16m	Prism	HS	13.76	71.07	0.60	2.8
J	14092006	01:01	2453993	2.83	E0-G0	16m	Prism	HS	15.82	72.29	0.85	2.3
J	16092006	02:15	2453995	2.84	A0-G0	64m	Prism	HS	62.86	72.85	0.95	1.6
J		03:13	2453995	2.84	A0-G0	64m	Prism	HS	58.12	71.90	1.68	0.9
K	09052007	08:53	2454230	3.43	D0-H0	64m	Prism	HS	61.43	71.46	1.12	1.3
L	22062007	03:50	2454274	3.54	G0-H0	32m	Prism	HS	21.96	62.20	1.17	1.0
L		05:29	2454274	3.54	G0-H0	32m	Prism	HS	29.30	70.26	1.21	0.9
M	03072007	07:25	2454285	3.57	E0-G0	16m	Prism	HS	15.51	72.73	1.07	2.8
M		07:37	2454285	3.57	E0-G0	16m	Prism	HS	15.31	72.59	0.75	3.9
M	04072007	04:42	2454286	3.57	G0-H0	32m	Prism	HS	29.28	70.24	1.59	1.0
M		06:30	2454286	3.57	G0-H0	32m	Prism	HS	31.98	72.83	1.51	1.1

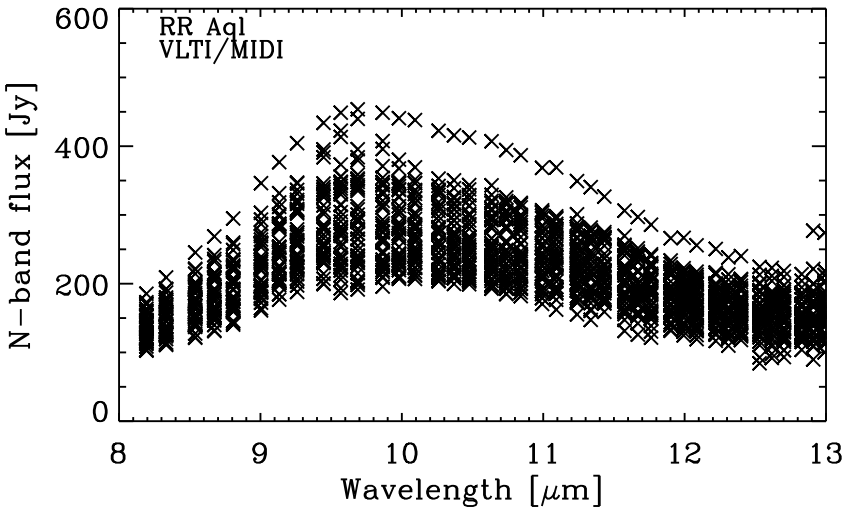

Figure 5.3: Calibrated RR Aql MIDI flux spectra as a function of wavelength. For clarity, the error bars are omitted in the plot.

estimate the uncertainty of the transfer function for nights when only one calibrator was available, we used typical values based on nights when many calibrator stars were observed. The final errors on the observed visibilities are mostly systematic, and include the error of the coherence factor of the science target and the calibrators, the adopted diameter errors, and the standard deviation of the transfer function over the night.

The photometric spectrum was calibrated with one or two calibrators, which were observed close on sky and in time compared to our science target. For most calibrator stars, absolutely calibrated spectra are available in Cohen et al. (1999). For those calibrators where the absolutely calibrated spectrum was not directly available, we used instead a spectrum of a calibrator with similar spectral type and similar effective temperature (see the instrument consortium's catalog[4]). The spectra of such calibrators were scaled with the IRAS flux at 12 μm to the level of our calibrator. In addition, we verified that our synthetic spectra obtained by this procedure are valid by scaling known spectra of two Cohen calibrators. In a few cases, when the atmospheric absorption was strongly affecting the spectra around 9.5μm, we used another similar calibrator instead of the main calibrator observed in the same night with the same level of flux. The ambient conditions for all the observations were carefully checked. If we were facing problems with clouds, constraints due to wind, significant differences in seeing, humidity, coherence time, and airmass between the science target and the corresponding calibrator, the photometry was omitted from the analysis. The detailed data calibration procedure can be found in Chapter 3, Sections 3.2, 3.4, and 3.5.

[4]http://www.ster.kuleuven.ac.be/∼tijl/MIDI_calibration/mcc.txt

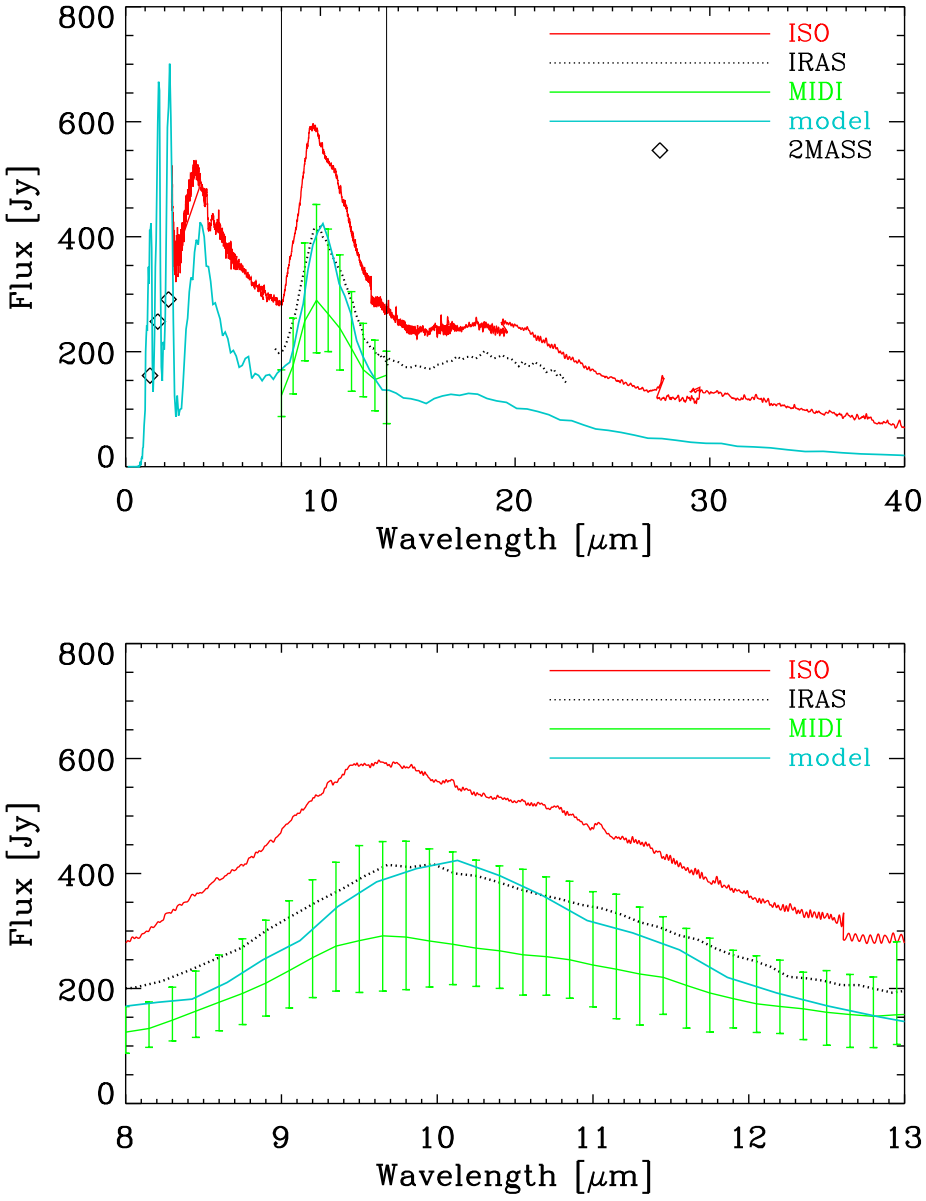

Figure 5.4: RR Aql flux spectrum as a function of wavelength from 2.4 μm to 40 μm (top). The lines represents the flux spectra from ISO-SWS observations covering wavelengths from 2.5 μm to $\sim$240 μm (solid red thick line), IRAS-LRS observations covering $\sim$ 7.7 μm to $\sim$ 23 μm (dotted thin black like), and the mean of our N-band MIDI measurements (solid thin green line). Here, the vertical bars span the maximum and minimum values measured. The diamond symbols denote 2MASS measurements at 1.25 μm, 1.65 μm, and 2.2 μm. The solid blue line indicates our atmosphere and dust shell model as explained in Sect. 5.3.5. The bottom plot shows an enlarged segment of the plot in the MIDI wavelength range of 8–13 μm.

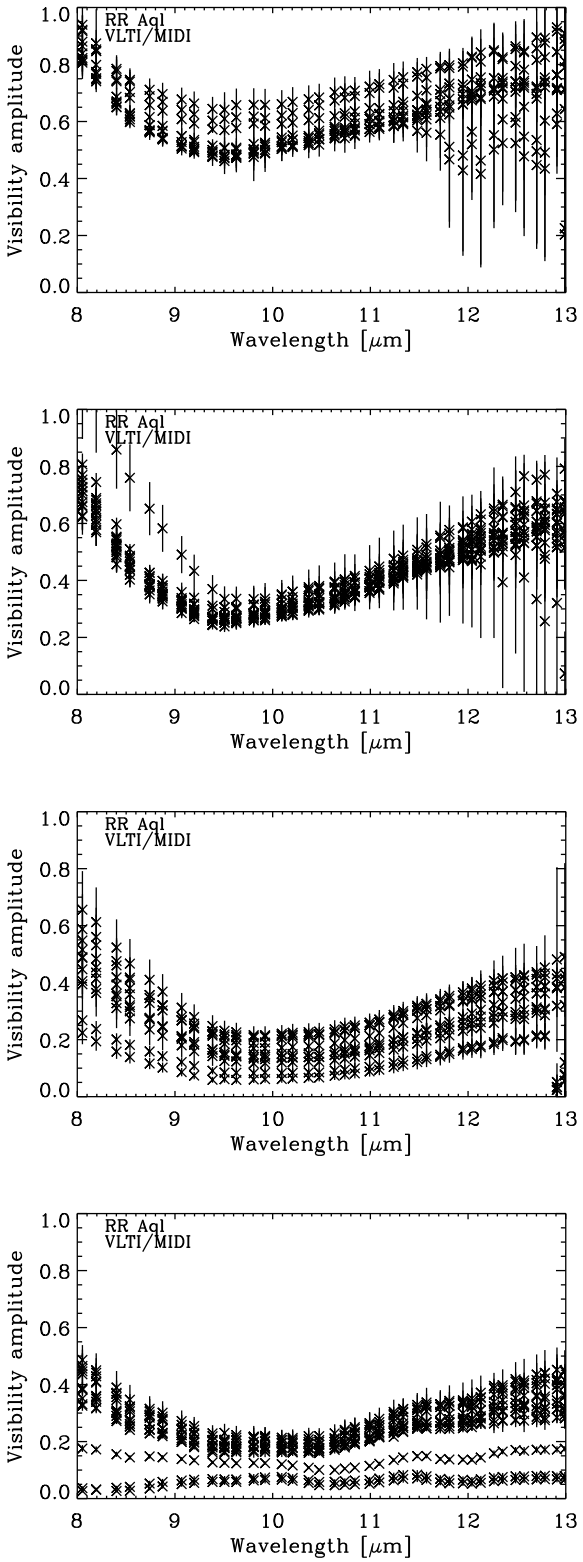

Figure 5.5: Calibrated RR Aql MIDI visibility amplitudes as a function of wavelength. (from top to bottom) Observations executed at projected baselines (pb) < 20 m, 20 m $<$ pb $<$ 35 m, 35 m $<$ pb $<$ 50 m, and pb > 50 m.

5.3 MIDI results

We observed RR Aql at different phases over 4 pulsation cycles in order to monitor the mid-infrared photometry and visibility spectra. Here, we present and discuss the general properties of the data, followed by an analysis of their variability as a function of phase and cycle in Sects. 5.3.1 and 5.3.2.

Figure 5.3 shows all obtained calibrated photometry spectra as a function of wavelength. The MIDI flux measurements show a consistent shape exhibiting an increase of the flux from $\sim$100–200 Jy at 8 μm to a maximum near 9.8 μm of $\sim$200–400 Jy, and a decrease towards 13 μm, where the flux values reach values of again $\sim$100–200 Jy. The level of the flux spectrum differs for individual measurements with a spread of $\sim$ 100–200 Jy. Figure 5.4 shows a comparison of the mean of our MIDI flux measurements to measurements obtained with the ISO and IRAS instruments. The shape of the flux curve is well consistent among the MIDI, ISO, and IRAS measurements. The level of the IRAS flux is within the range of our MIDI measurements. The level of the ISO flux is higher, which most likely can be explained by the post-maximum phase of 0.16 of the ISO observations (1997-05-03) compared to our minimum to pre-maximum phases. The difference between the MIDI and ISO flux level may also indicate a flux variation over different cycles. Figure 5.4 also includes a model description of our MIDI data, which will be explained below in Sect. 5.3.5.

Figure 5.5 shows all obtained calibrated visibility spectra, which are combined into four groups of different projected baseline lengths (B_p) of $B_p < 20$ m, 20 m $< B_p <$ 35 m, 35 m $< B_p <$ 50 m, and $B_p > 50$ m. The visibility curves show a significant wavelength dependence with a steep decrease from 8 μm to $\sim$ 9.5 μm and a slow increase in the 9.5 μm to 13 μm range. The shape and absolute scale of the visibility function depends on the length of the projected baseline where a longer baseline results in a lower and flatter curve.

As a first basic interpretation of the interferometric data, we computed for each data set and spectral channel the corresponding UD diameter and the Gaussian FWHM. This leads to a rough estimate of the characteristic size of the target at each wavelength. However, it should be mentioned that the true intensity distribution across the stellar disk is expected to be more complex than can be described by these elementary models. Fig. 5.3 shows for the example of epoch A the flux, the visibility amplitude, the corresponding UD diameter, and the corresponding Gaussian FWHM diameter as a function of wavelength. The shape of the UD diameter and Gaussian FWHM functions show a steep increase from 8 μm to $\sim$ 9.5 μm by a factor of 2. A plateau appears between $\sim$ 9.5 μm and 11.5 μm, and the values are nearly constant from $\sim$ 11.5 μm to 13 μm.

The shape of the 8–13 μm flux spectrum with a maximum near 9.8 μm is known to be a characteristic silicate emission feature (e.g. Little-Marenin & Little, 1990; Lorenz-Martins & Pompeia, 2000). The corresponding drop in the visibility function between 8 μm and 9.5 μm, and increase of the UD diameter and Gaussian FWHM has also been shown to be a typical signature of a circumstellar dust shell that is dominated by silicate dust (cf., e.g. Driebe et al., 2008; Ohnaka et al., 2008). The opposite trend, a brad spectrum and visibility function in the wavelength range 8–13 μm was interpreted as a dust shell consisting of Al_2O_3 dust (Wittkowski et al., 2007) or silicate and Al_2O_3 dust (Ohnaka et al., 2005).

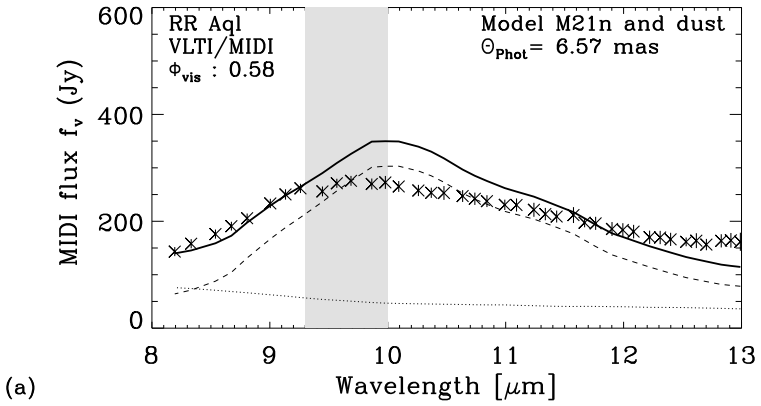
RR Aql
VLTI/MIDI
Φvis : 0.58
Model M21n and dust
ΘPhot= 6.57 mas
MIDI flux fν (Jy)
Wavelength [μm]

(a)

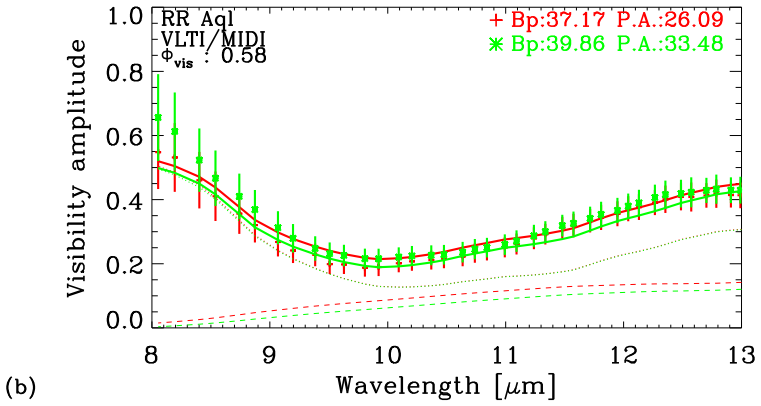
RR Aql
VLTI/MIDI
Φvis : 0.58
+ Bp:37.17 P.A.:26.09
✳ Bp:39.86 P.A.:33.48
Visibility amplitude
Wavelength [μm]

(b)

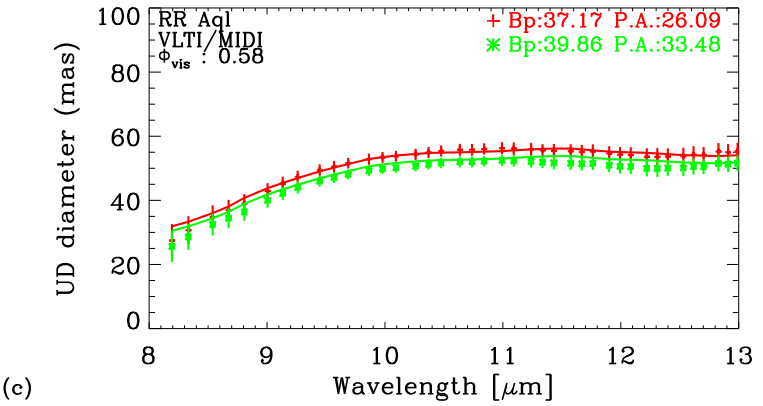
RR Aql
VLTI/MIDI
Φvis : 0.58
+ Bp:37.17 P.A.:26.09
✳ Bp:39.86 P.A.:33.48
UD diameter (mas)
Wavelength [μm]

(c)

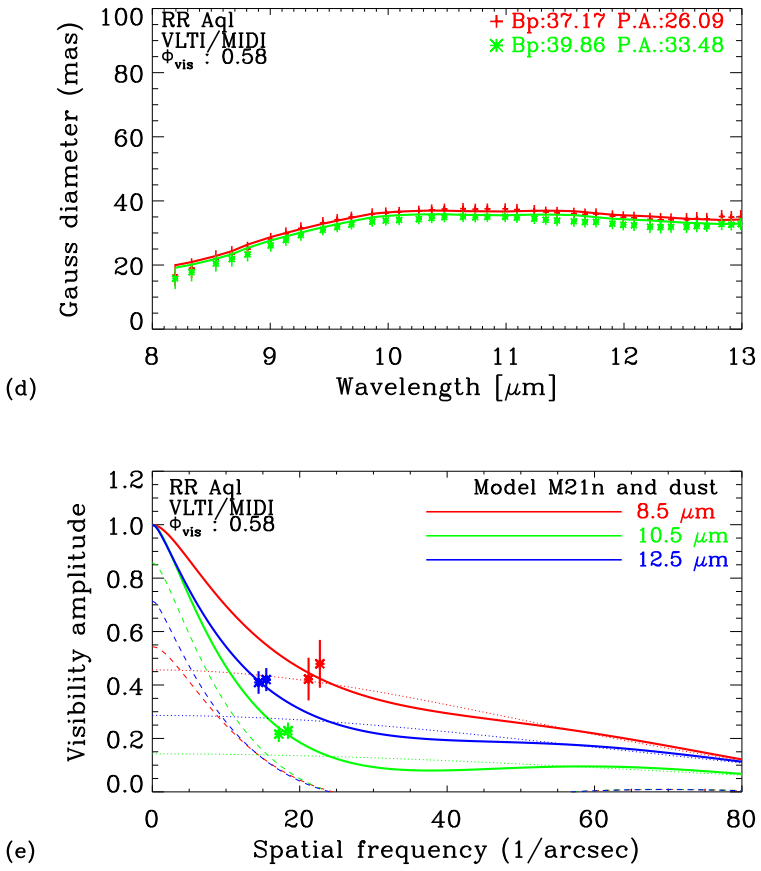

Figure 5.6: VLTI/MIDI interferometry at 8-13μm of RR Aql for the example of epoch A (stellar phase 0.58). The panels show (a) the flux, (b) the visibility amplitude, (c) the corresponding UD diameter, (d) the corresponding Gaussian FWHM diameter as a function of wavelength. The gray shade indicates the wavelength region around 9.5 μm that is affected by atmospheric absorption. Panel (e) shows the visibility amplitude as a function of spatial frequency for three averaged bandpasses of 8-9 μm, 10-11 μm, and 12-13 μm. The crosses with error bars denote the measured values. The solid lines indicate our best-fitting model, as described in Sect. 5.3.5. It consists of a combination of a dust-free dynamic model atmosphere representing the central star and a radiative transfer model representing the surrounding dust shell. The contributions of the stellar and dust components alone are indicated by the dotted and the dashed line, respectively.

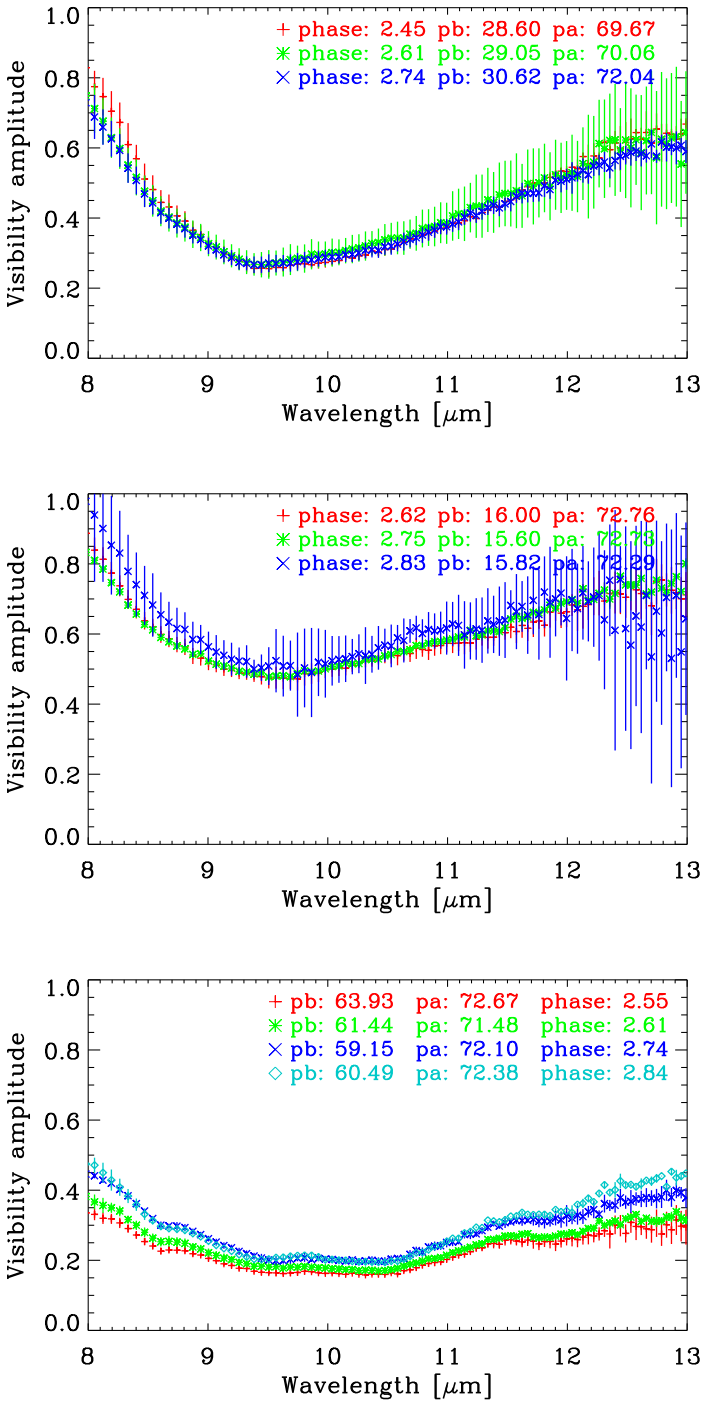

Figure 5.7: Calibrated MIDI visibility amplitudes for different pulsation phases within the same cycle to investigate intra-cycle visibility variations. Each line represents a different pulsation phase within the same cycle and is computed as an average of data obtained at the respective phase (± 0.15) and observed at similar projected baseline length (pb ± 10%) and position angle (PA ± 10%). The top panel shows the example of pulsation phases 0.45, 0.61, and 0.74 of cycle 2 observed with a projected baseline length of ∼ 29 m and a position angle of ∼70 deg. The middle panel shows the example of pulsation phases 0.62, 0.75, and 0.83 of cycle 2 observed with a projected baseline length of ∼ 16 m and a position angle of ∼72 deg. The bottom panel shows the example of pulsation phases 0.55, 0.61, 0.74 and 0.84 of cycle 2 observed with a projected baseline length of ∼ 61 m and a position angle of ∼72 deg. The error bars are computed as the standard deviation of the averaged visibilities.

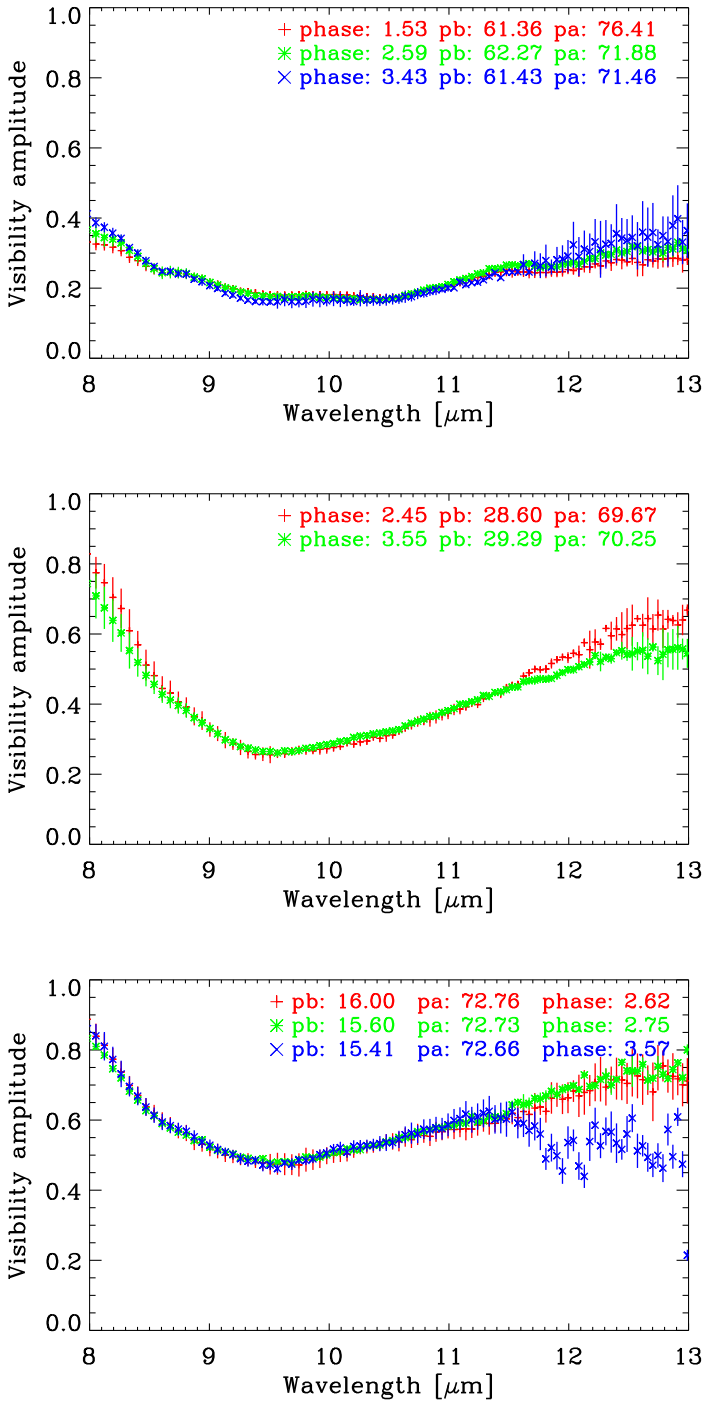

Figure 5.8: As Fig. 5.7, but for the same pulsation phase in consecutive pulsation cycles to investigate cycle-to-cycle visibility variations. The top panel shows the example of pulsation phase $\sim$ 0.5 in three consecutive cycles observed with a projected baseline length of $\sim$ 61 m and a position angle $\sim$75 deg. The middle panel shows the example of pulsation phase 0.5 in 2 consecutive cycles observed with a projected baseline length of $\sim$ 29 m and a position angle $\sim$70 deg. The bottom panel shows the example of pulsation phase 0.6 in 2 consecutive cycles observed with a projected baseline length of $\sim$ 16 m and a position angle $\sim$72 deg.

5.3.1 Visibility monitoring

We obtained a rich sample of MIDI data on RR Aql that cover a total of 4 pulsation cycles and pulsation phases between 0.45 and 0.85, i.e. minimum to pre-maximum phases (see Tab. 5.1 and Fig. 5.1). For many different pulsation cycles and phases we have obtained data at similar projected baseline lengths and position angles. This gives us a unique opportunity to meaningfully compare interferometric data obtained at different pulsation phases and cycles. Since the visibility depends on the probed point in the *uv* plane, and thus on the projected baseline length and position angle, visibility data at different pulsation phases can be directly compared only if they were obtained at the same, or very similar, point in the *uv* plane. For this reason, we have combined individual observations into groups of similar pulsation phases ($\Phi_{\rm vis} \pm 0.15$), projected baseline lengths ($B_p \pm 10$ %), and position angles (P.A. $\pm$ 10 %). The data within each group were averaged. The uncertainty of the averaged visibility curves was estimated as the standard deviation of the averaged visibilities.

Intra-cycle visibility monitoring

In order to investigate intra-cycle visibility variations we compared data observed at different pulsation phases within the same cycle. Fig. 5.7 shows three examples of calibrated visibility curves, where each line in the plots represents an average of a group of visibility data, as described above, (i.e. with similar B_p, P.A., and $\Phi_{\rm vis}$). The top panel shows an example of observations within the second pulsation cycle at phases 2.45, 2.61, and 2.74 obtained with $B_p \sim 30$ m and P.A. $\sim 70°$. The middle panel shows an example of observations at phases 2.62, 2.75, and 2.83 obtained with $B_p \sim 16$ m and P.A. $\sim 72°$. The bottom panel shows an example of observations at phases 2.55, 2.61, 2.74 and 2.84 obtained with $B_p \sim 61$ m and P.A. $\sim 72°$. The data do not show any evidence for intra-cycle visibility variations within the probed range of pulsation phases ($\sim 0.45 - 0.85$) and within our visibility accuracies of about 5–20%.

Cycle-to-cycle visibility monitoring

We compared data observed at similar pulsation phases of different, consecutive, cycles to investigate cycle-to-cycle visibility variations. Figure 5.8 shows three of these examples computed in the same way as shown in Fig. 5.7 of Sect. 5.3.1, but (top panel) for minimum phases of 1.53, 2.59, and 3.43 in three consecutive cycles obtained with a projected baseline length of ~ 62 m and P.A. $\sim 73°$, (middle panel) for minimum phases 2.43, and 3.55 of two consecutive cycles obtained with a projected baseline length of ~ 29 m, and P.A. $\sim 70°$, and (bottom panel) for post-minimum phases 2.62, 2.75, and 3.57 of two consecutive cycles obtained with a projected baseline length of ~ 16 m, and P.A. $\sim 72°$. Here, the phases of the different cycles differ by up to ~ 20%. However, we showed in Sect. 5.3.1 that there is no evidence for intra-cycle visibility variations, so that the chosen phases can well be compared for different cycles. As a result, Fig. 5.8 shows that our data do not exhibit any significant cycle-to-cycle visibility variation for minimum phases over 2–3 cycles within our visibility accuracies of $\sim$ 5–20%.

Deviations from circular symmetry

Most position angles varied around 40° or 70°. Only in two cases the P.A. is significantly different with values of 3° and 7°. However, in both cases the visibility data quality is poor. The

differential phases are close to zero within $\sim$10-20 deg, which is of the order of the calibration uncertainties that can be reached for MIDI differential phases (e.g. Ohnaka et al., 2008). Therefore these observations do not allow us to make any reliable conclusion regarding the possible presence or absence of an asymmetric intensity distribution.

Summarizing, our RR Aql MIDI data do not show an evidence of significant intra-cycle or cycle-to-cycle visibility variations within the examined phase coverage of $\sim$ 0.45–0.85 in 4 consecutive cycles (see Tab. 5.1 for details of the phase coverage) and within our visibility accuracies of $\sim$ 5–20%. The obtained mid-infrared interferometric observations imply either that the mid-infrared sizes of molecular and dusty layers of RR Aql do not significantly vary within our phase coverage, or that the conducted observations are not sufficiently sensitive to detect such variations. In addition, the good agreement of visibility data obtained at the same projected baseline lengths and position angles during several years also confirms the good data quality and credibility of the data reduction procedure.

5.3.2 *N*-band flux monitoring

In order to investigate the intra-cycle and cycle-to-cycle variability of our 8–13 μm flux spectra, we combined the data into groups of data obtained at similar pulsation phases ($\Phi_{\rm vis} \pm 0.15$). The data within each group were averaged. The uncertainty of the averaged photometry curves was estimated as the standard deviation of the averaged values.

Intra-cycle photometry monitoring

Fig. 5.9 shows three examples of a comparison of the MIDI calibrated flux spectrum at different pulsation phases of the same cycle. The top panel shows a comparison between phases 0.58 and 0.85 of cycle 0, the middle panel shows a comparison between phases 1.53 and 1.76 of cycle 1, and the bottom panel shows a comparison between phases 2.46 and 2.84 of cycle 2. The examples compare data taken at post-minimum and pre-maximum phases, i.e. with the largest separation in phase that is available in our dataset. The RR Aql flux values within the N-band are larger at the pre-maximum phases than at the post-minimum phases, corresponding to the lightcurve of the V-magnitude. The difference is most pronounced toward the silicate emission feature around 9.8 μm and smaller towards the edges of the MIDI bandpass at 8.0 μm and 13.0 μm. The differences correspond to up to 20%–35%, or about 1–2 standard deviations.

Cycle-to-cycle photometry monitoring

Fig. 5.10 shows a comparison of data observed at the same phase of consecutive pulsation cycles. The top panel shows a comparison between phases 1.76 and 2.74, i.e. phase 0.75 of cycles 1 and 2. The middle panel shows a comparison between phases 0.85 and 2.84, i.e phase 0.85 of cycle 0 and 2. The bottom panel shows a comparison between phases 2.55 and 3.56, i.e phase 0.55 of cycle 2 and 3. In the first two examples, the N-band fluxes are lower in cycle 2 compared to the same phase of (a) cycle 1 and (b) cycle 0 by up to $\sim$ 100 Jy, corresponding to about 30% or 1–2 standard deviations. As for the intra-cycle photometry variations discussed in the previous paragraph, the differences are most pronounced toward the silicate emission feature at 9.8 μm. This might indicate an irregularity of the variability cycle in the N-band. In the optical band the

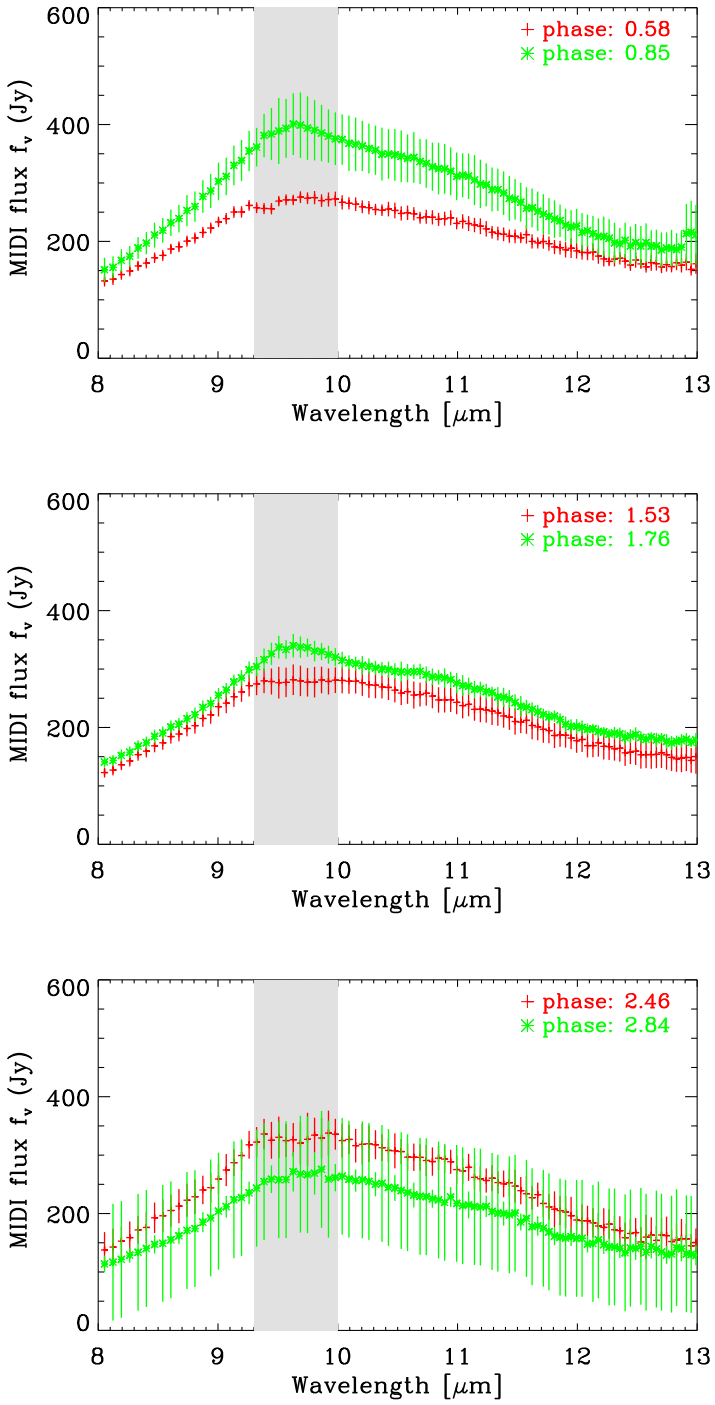

Figure 5.9: Calibrated MIDI flux spectrum for different pulsation phases within the same cycle to investigate intra-cycle photometry variations. Each line represents a different pulsation phase within the same cycle and is computed as an average of data obtained at the respective phase (± 0.15). The top panel shows the example of pulsation phases 0.58 and 0.85 of cycle 0. The middle panel shows the examples of phases 0.53 and 0.76 of cycle 1. The bottom panel shows the examples of phases 2.46 and 2.84 of cycle 2. The error bars are computed as the standard deviation of the averaged photometry curves. The gray shades denote zones that are affected by atmospheric absorption.

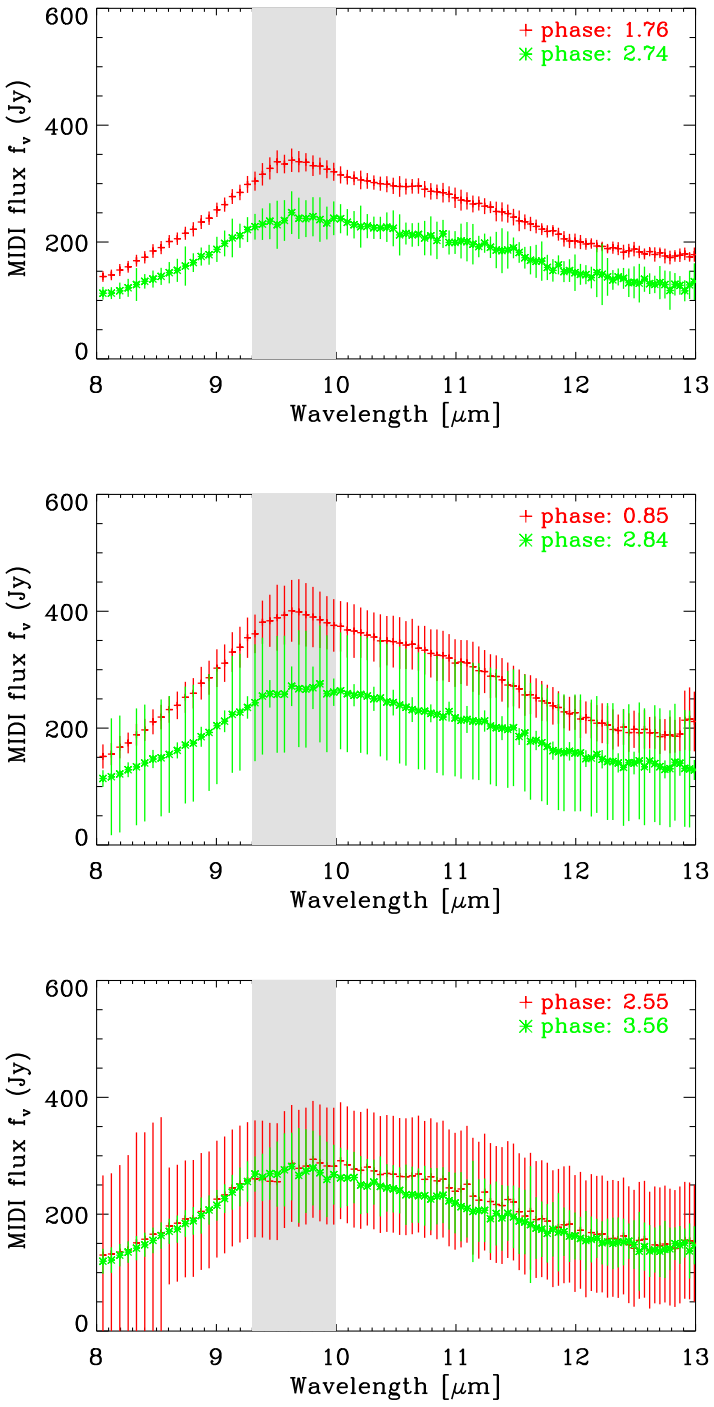

Figure 5.10: As Fig. 5.9, but for the same pulsation phase in consecutive pulsation cycles to investigate cycle-to-cycle photometry variations. The top panel shows the example of phase ~ 0.75 in cycles 1 and 2. The middle panel shows the example of phase ~ 0.85 of cycles 0 and 2. The bottom panel shows the example of phase ~ 0.55 of cycles 2 and 3.

Table 5.2: Best-fitting model parameters for each epoch of RR Aql observations

Epoch	$\Phi_{\rm vis}$	τ_V (sil.)	$R_{\rm in}/R_{\rm Phot}$ (sil.)	p (sil.)	$\Theta_{\rm Phot}$ [mas]
A	0.58	3.0 ± 0.9	4.5 ± 1.1	2.5 ± 0.4	6.6 ± 2.4
B	0.81	3.0 ± 0.7	4.5 ± 1.6	2.5 ± 0.5	7.1 ± 2.9
C	0.86	2.5 ± 0.8	5.0 ± 1.3	2.5 ± 0.5	8.0 ± 2.8
D	1.53	3.7 ± 0.6	3.2 ± 1.1	2.5 ± 0.5	6.7 ± 2.6
E	1.77	2.0 ± 0.8	4.5 ± 1.4	3.0 ± 0.4	8.0 ± 2.9
F	2.46	2.7 ± 0.8	4.6 ± 1.1	3.0 ± 0.5	7.7 ± 2.4
G	2.55	3.0 ± 0.6	3.4 ± 1.7	2.1 ± 0.6	7.2 ± 2.5
H	2.62	2.0 ± 0.8	4.5 ± 1.1	2.4 ± 0.5	8.5 ± 2.7
I	2.74	2.0 ± 0.9	4.0 ± 1.5	2.6 ± 0.5	8.5 ± 2.8
J	2.84	3.2 ± 0.7	3.0 ± 1.5	2.0 ± 0.6	7.2 ± 2.6
K	3.43	5.0 ± 0.8	3.0 ± 1.3	3.0 ± 0.5	7.3 ± 2.2
L	3.54	2.3 ± 0.9	5.0 ± 1.5	2.5 ± 0.4	8.2 ± 2.4
M	3.57	2.5 ± 0.7	4.5 ± 1.1	2.5 ± 0.4	7.5 ± 2.4

Table 5.3: Average model parameters for all epochs of RR Aql observations

Model	τ_V (Al_2O_3)	τ_V (silicate)	$R_{\rm in}/R_{\rm Phot}$ (silicate)	p (silicate)	$\Theta_{\rm Phot}$ [mas]
M21n	0.0	2.8 ± 0.8	4.1 ± 0.7	2.6 ± 0.3	7.6 ± 0.6

visual lightcurve clearly shows that the pulsation cycles are not perfectly symmetric (see Fig. 5.1).

Summarizing, our data exhibit a 1–2σ signature of intra-cycle as well as cycle-to-cycle flux variations at wavelengths of 8–13 μm, which are most pronounced toward the silicate emission feature at 9.8 μm. This indication is consistent with observations by Monnier et al. (1998), who reported on temporal variations in the mid-infrared spectra of late type stars. In particular, stars with a strong emission feature around 9.8 μm showed evident changes of the spectral profile. Considerable phase variation of the N-band spectra can as well be found in Alvarez & Plez (1998).

5.3.3 MIDI modeling

Here, we use an approach of an ad-hoc radiative transfer modeling of the dust shell where the central stellar source is described by readily available and established dust-free dynamic model atmosphere series, as introduced by Wittkowski et al. (2007) (Section 4.3). The dust shell surrounding the central star is modeled by the Monte Carlo radiative transfer code mcsim_mpi (Ohnaka et al., 2006) (Section 4.2). The radiative transfer model requires an assumption on the spectral energy distribution (SED) of the central stellar source. Since we expect the photosphere and molecular layers of RR Aql to be partly resolved with our MIDI baselines ($V^2 \sim 0.4$ for $\Theta =$ 10 mas, B = 120 m, $\lambda = 10\,\mu$m), we also need to model the intensity distribution across the atmospheric layers. For these purposes, we use the dust-free dynamic model atmospheres, based on self-excited pulsation models (P and M series), by Ireland et al. (2004b,a) and references therein as the currently best available option (Section 4.1).

The dust-free models describing the dynamic atmosphere of the central source were constructed to reproduce the M-type Mira prototypes *o* Cet and R Leo. In comparison to these Mira variables, RR Aql pulsates with a larger period of 394 days. The main sequence precursor mass of RR Aql is 1.16 $M/\mathrm{M}_{\odot}$ (Wyatt & Cahn, 1983), and its spectral type is M6e-M9 (Samus et al., 2004), versus M5-M9 (P series) and M6-M9.5 (M series). However, Tej et al. (2003) indicated that the spectral shape can be reproduced reasonably well even for stars with different pulsation periods. We assume that differences between the stellar parameters of the models designed to represent the prototypes o Cet and R Leo and the parameters of our science target RR Aql should not significantly influence the resulting model fit. Based on the stellar parameters we chose to use of the M series, the best avaiable models describing RR Aql's atmosphere.

5.3.4 MIDI model parameters

A clear silicate feature is identified in the spectra of RR Aql (see Fig. 5.4 and Sect. 5.3). RR Aql is one of 31 oxygen-rich stars studied by Lorenz-Martins & Pompeia (2000). The authors modeled the stars using Al_2O_3 and silicate grains and suggest that the dust chemistry of RR Aql contains silicate grains only. In this study we examined both of these two dust species, Al_2O_3 grains (Begemann et al., 1997; Koike et al., 1995) and silicates grains (Ossenkopf et al., 1992). The amount of dust is described by the optical depths at $\lambda_0 = 0.55$ μm. The grain size was set to 0.1 μm for all grains. We set the photospheric radius to the well-defined continuum photospheric radius at $\lambda = 1.04$ μm ($R_{\mathrm{Phot}} = R_{1.04}$). The density gradient was defined by a single power law $\rho(r) \propto r^{-p}$ with index p. The shell thickness was set to $R_{\mathrm{out}}/R_{\mathrm{in}} = 1000$.

The global model includes seven parameters. The radiative transfer model describing the circumstellar dust shell includes six parameters: the optical depths τ_V (Al_2O_3) and τ_V(silicate), the inner boundary radii $R_{\mathrm{in}}/R_{\mathrm{Phot}}$ (Al_2O_3) and $R_{\mathrm{in}}/R_{\mathrm{Phot}}$ (silicate), and the density gradients p_{A} (Al_2O_3) and p_{B} (silicate). The model of the P/M atmosphere series is a further parameter. Here, we used ten models covering one complete cycle of the M series: M16n (model visual phase Φ_{model}=0.60), M18 (0.75), M18n (0.84), M19n (0.90), M20 (0.05), M21n (0.10), M22 (0.25), M23n (0.30), M24n (0.40), and M25n (0.50).

We computed a grid of dust shell models for each of these M models including all combinations of optical depths τ_V (Al_2O_3) = 0.0, 0.1, 0.2, 0.5, 0.8; τ_V (silicate) = 2.0, 2.5, 3.0, 3.5, 4.0, 4.5, 5.0; $R_{\mathrm{in}}/R_{\mathrm{Phot}}$ (Al_2O_3) = 2.0, 2.5, 3.0; $R_{\mathrm{in}}/R_{\mathrm{Phot}}$ (silicate) = 2.5, 3.5, 4.5, 5.5, 6.5; p_{A} (Al_2O_3) = 2.0, 2.5, 3.0, 3.5; and p_{B} (silicate) = 2.0, 2.5, 3.0, 3.5.

In a first selection of suitable models, we compared the MIDI data of each epoch to our entire grid of models. The angular diameter Θ_{Phot} was the only free parameter. We weighted down the part of the photometric spectra around 9.5 μm, which is strongly affected by telluric absorption. Otherwise, the weight of each data point was given by the corresponding uncertainty. For each epoch we kept the best ∼30 models with lowest χ^2 values (Eq. 5.1). In a next step, a grid with finer steps around these parameters was computed. This procedure was repeated several times. The results of the automatic selection were visually inspected. We completed the selection with 10 models for each epoch which are in best agreement with the data.

The modeled visibilities $V_i^{\mathrm{mod}}(\lambda)$ were compared to the observed ones $V_i^{\mathrm{obs}}(\lambda)$. The discrep-

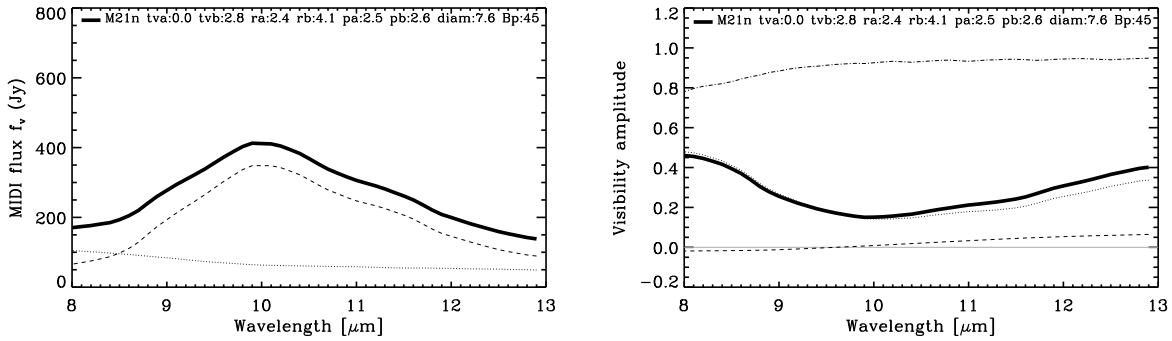

Figure 5.11: Model with average dust shell parameters for different epochs of our RR Aql observations (Table 5.3).

ancy was weighted with the mesurements errors $\sigma_{V_i^{\rm obs}}(\lambda)$ to obtain $\chi^2(\lambda)$.

$$\chi^2(\lambda) = \sum_{i=1}^{N} \Big(\frac{V_i^{\rm obs}(\lambda) - V_i^{\rm mod}(\lambda)}{\sigma_{V_i^{\rm obs}}(\lambda)}\Big)^2 \tag{5.1}$$

The $\chi^2(\lambda)$ was minimised using the Levenberg-Marquardt least-squares minimalisation algorithm.

5.3.5 MIDI model results

For each of the 13 epochs we found the best-fitting model parameters including the best-fitting set of dust parameters of the radiative transfer model together with the best-fitting model of the P/M series. We used the procedure outlined in Sect. 5.3.4.

Following Lorenz-Martins & Pompeia (2000), we have investigated dust shells including Al_2O_3 and/or silicate shells with different inner radii and density gradients. We obtained best fit results with a silicate shell alone, and the addition of an Al_2O_3 shell did not result in an improvement of the model fits. This result is consistent with Lorenz-Martins & Pompeia (2000) who classified RR Aql as a source that can be described with a silicate dust shell alone.

The best fitting parameters for each epoch are listed in Tab. 5.2. The table lists the epoch, the phase at the epoch, the optical depth τ_V, the inner boundary radius $R_{\rm in}/R_{\rm Phot}$, the density distribution p, and the continuum photospheric angular diameter $\Theta_{\rm Phot}$. Here, the dust shell parameters are those of the silicate dust shell. The errors of the dust shell parameters are derived as the standard deviation based on the find 10 best-fitting models (Tab 5.2). Table 5.3 lists the average model parameters of our different epochs. Figure 5.11 shows the models simulating the average parameters for our average pulsation phase of $\overline{\Phi_V} = 0.64 \pm 0.15$. The average phase of our observations is $\overline{\Phi_V} = 0.64 \pm 0.15$.

The best fitting model atmosphere was M21n ($T_{\rm model} = 2550\,{\rm K}$, $\Phi_{\rm Model}$=0.1) for all epochs. The difference between the average phase of our observation and the phase of the best fitting model atmosphere can most likely be explained by the different stellar parameters of RR Aql compared to those of the M series. It means that $T_{\rm eff}$ of RR Aql at the time of observation is similar to $T_{\rm eff}$ of model M21n, which has a different phase but whose basic parameters are also not exactly those of RR Aql.

Figure 5.3 includes, for the example of epoch A, the model flux and model visibility compared to the observed values. All the observational epochs can be find in appendix (Figs. C.1– C.7). For most epochs, the agreement between the models and the observed data is very good, in particular for the visibility spectra. The visibility spectra contain information about the radial structure of the atmospheric molecular layers and the surrounding dust shells. In the wavelength range from 8 μm to $\sim$ 9 μm the dust is fully resolved with baselines larger than $\sim$ 20 m and the visibility contribution of the dust reaches into the 2nd lobe of the visibility function. RR Aql is characterized by a partially resolved stellar disk including atmospheric layers, with a typical drop in the visibility function $\sim$ 10 μm, where the flux contribution of the silicate emission is highest and the flux contribution of the star relative to the total flux decreases. Beyond $\sim$ 10 μm, the spatially resolved radiation from the optically thin dust shell starts to be a notable part of the observed total flux. From $\sim$ 10 μm to 13 μm the dust contribution becomes nearly constant while the stellar contribution increases, and this results in a rebound of the visibility function. Photometry spectra also fit well. For some epochs, the models predict higher fluxes than observed near the silicate emission feature at $\sim$9.8 μm. Generally, our attempt of a radiative transfer model of the circumstellar dust shell that uses dynamical model atmosphere series to describe the central stellar source can very well reproduce the shape of both the visibility and the photometry spectra. Our model also resembles the shape of the full SED in the range of 1–40 μm (Fig. 5.4).

The obtained model parameters for the different epochs do not indicate any significant dependence on phase or cycle. This is consistent with the result from Sect. 5.3.1 that a direct comparison of visibility values of different phases or cycles did not show any variability within our uncertainties, and that the photometric values indicated only small variations of up to $\sim 2\,\sigma$. However, we cannot confirm or deny an eventual phase-dependence of the dust formation process that effects the 8–13 μm visibility and photometry values by less than our uncertainties of about 5–20% and 10–50%, respectively.

A silicate dust shell alone, i.e. without the addition of a Al_2O_3 dust shell, provides the best agreement with our data. The average optical depth of the silicate dust is τ_V(silicate)=2.8$\pm$0.8 at $\lambda = 0.55\,\mu$m (corresponding to 0.03 at $\lambda = 8\,\mu$m, 0.06 at $\lambda = 12\,\mu$m, and a maximum within 8–12 μm of 0.22 at $\lambda = 9.8\,\mu$m). The inner radius of the dust shell is $R_{\rm in}$=4.1$\pm$0.7 $R_{\rm Phot}$, and the power-law index of the density distribution is p=2.6$\pm$0.3. Wind models predict a power-law index of the density distribution of 2 at radii outward the dust formation zone. However, for radii close to the dust formation zone (r<$\sim$10 $R_\star$) a larger index is expected (cf, e.g., Fig. 6 in Wittkowski et al., 2007), which is consistent with our result.

The average photospheric angular diameter results in $\Theta_{\rm Phot}$=7.6$\pm$0.6 mas. This value is smaller than the K-band ($\lambda = 2.2\,\mu$m, $\Delta\lambda = 0.4\,\mu$m) UD diameter of $\Theta_{\rm UD}$=10.73$\pm$0.66 mas derived by van Belle et al. (2002) at a minimum phase of 0.48. This can most likely be explained by the different radius definitions. Our diameter is a photospheric angular diameter that has already been corrected for effects of molecular layers lying above the continuum photosphere using the prediction by the best-fitting model atmosphere, while the diameter by van Belle et al. (2002) is a broad-band uniform disk diameter that still contains contamination by molecular layers. It is known that broad-band UD diameters may widely overestimate the photospheric radius due to contamination by molecular layers lying above the photosphere (cf., e.g., Ireland et al., 2004b; Fedele et al., 2005; Wittkowski et al., 2007). With the parallax of $\pi = 1.58 \pm 0.40$ mas (Vlemmings & van Langevelde, 2007), our value for $\Theta_{\rm Phot}$ corresponds to a photospheric radius of $R_{\rm phot} = 520^{+230}_{-140}\,{\rm R}_\odot$. Together with the bolometric magnitude of RR Aql of $m_{\rm bol} = 3.71$ and $\Delta m_{\rm bol} = 1.17$ from Whitelock et al. (2000), our value for $\Theta_{\rm Phot}$ at $\overline{\Phi_V} \sim 0.64$ corresponds to an

effective temperature of $T_{\rm eff} \sim 2420 \pm 200$ K. This value is consistent with the effective temperature of the best fitting model atmosphere M21n, which is $T_{\rm eff}$=2550 K.

Figure 5.12 shows the full model SED in the range of 0.3–100 μm (top panel), 1–2.4 μm (middle panel0, and 8–13 μmm (bottom panel) including the model with the average parameters describing RR Aql (Tab. 5.3) (black line), with the stellar contribution (red line), dust emission (green line), and dust scattering (blue line).

5.4 Discussion

Our MIDI observations of RR Aql did not show significant variations of the 8–13 μm visibility within the examined pulsation phases between 0.45 and 0.85 within a total of 4 pulsation cycles, and showed only marginal variations of the 8–13 μm flux.

We have performed model simulations with expected variations of the pulsation phase of the innermost dust-free atmosphere model and of the parameters of the surrounding dust shells (Sec. 4.4.1). These model simulations show that visibility variations are indeed not expected for the parameters and observational settings of RR Aql at wavelengths of 8–13 μm within the uncertainties of our observations. Variations of the flux spectra may in some cases just be detectable. Thus, our observational result of a constant visibility and only slightly varying flux at wavelengths of 8–13 μm are consistent with, and not contradicting, theoretical expectations of a pulsating atmosphere.

Our model simulations indicate that detections of pulsation effects at mid-infrared wavelengths would in particular benefit from smaller uncertainties in the photometric spectrum compared to our current data. Also, a large range of projected baselines at each phase, for RR Aql in particular including baseline lengths around 20-30 m, would help us to distinguish models of different pulsation phases.

For our analysis, we have considered silicate (Ossenkopf et al., 1992) and Al_2O_3 (Begemann et al., 1997; Koike et al., 1995) dust species, following the work by Lorenz-Martins & Pompeia (2000), and have used fixed grain sizes of 0.1 μm. It is known that other dust species with a more complex gran size distributions may occur in the circumstellar environment of Mira variables (e.g., Höfner, 2008; Molster & Waters, 2003, , and references therein). We showed that a model including only a silicate dust shell can well reproduce the observed RR Aql visibility and flux spectrum at 8–13 μm. The addition of an Al_2O_3 dust shell with comparable low optical depth did not significantly improve the fit to our data. However, our model simulations have shown that our 8–13 μm visibility and flux values are not sensitive to the addition of an Al_2O_3 dust shell with low optical depth within our uncertainties. As a result, we can not exclude the presence of an inner Al_2O_3 dust shell in addition to the silicate dust shell. Woitke (2006) used dynamical models for dust-driven winds of oxygen-rich AGB stars including frequency-dependent radiative transfer and found that dust temperatures are strongly material-dependent. Two dust layers are formed in his dynamical models, almost pure glassy Al_2O_3 close to the star (r $> \sim 1.5$ $R_{\rm star}$) and the more opaque Fe-poor Mg-Fe-silicates further out at 4–5 $R_{\rm star}$.

The dust-free dynamic model atmospheres predict a significant dependence of the characteristics of the molecular layers on the stellar pulsation phase at near-infrared wavelengths (Ireland et al., 2004b,a). There are a few near-infrared interferometric observation, which detected a clear variation of the continuum angular diameters with pulsation phase (Thompson et al., 2002b; Perrin et al., 1999; Young et al., 2000b; Woodruff et al., 2004). Spectrally resolved near-infrared

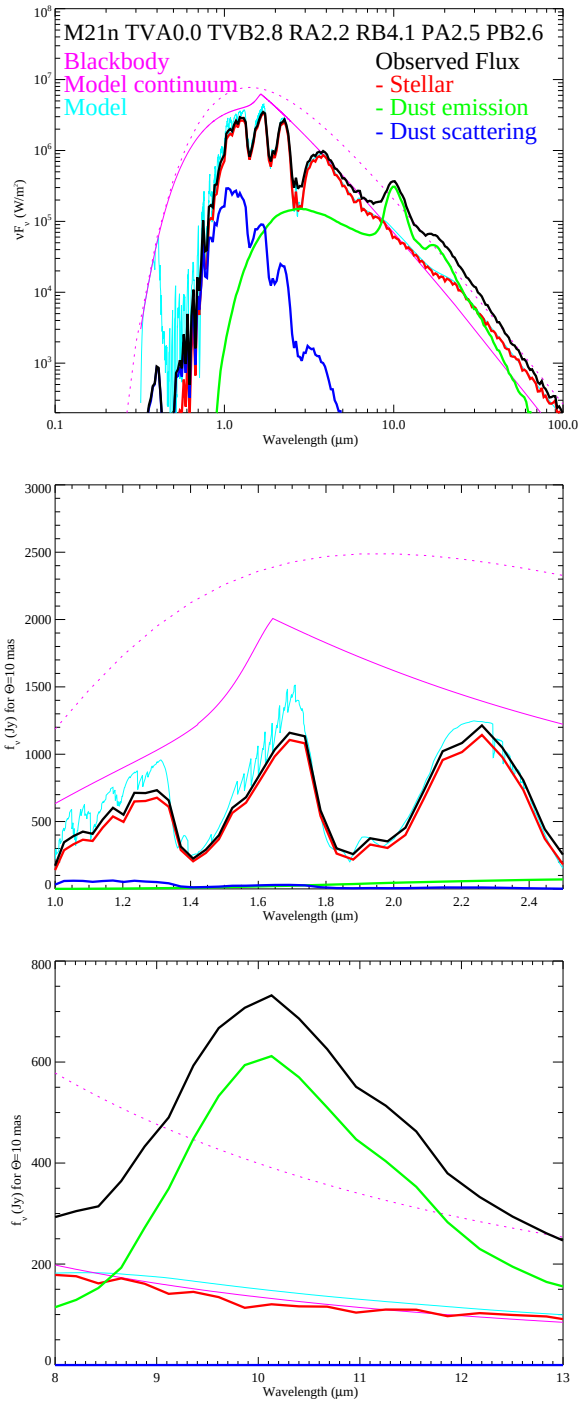

Figure 5.12: The top panel shows the full SED in the range of 0.3–100 μm, the middle panel shows the SED in the range 1–2.4 μm, and the bottom panel shows the SED in the range of 8–13 μm. The pink solid line represents model continuum, the pink dashed line describes the blackbody, the black line - the model with the average dust shell parameters describing RR Aql (Tab. 5.3), the red line - the stellar contribution of the model, the green line - dust emission, the blue line - dust scattering.

interferometric measurements at different phases, such as the AMBER observations by Wittkowski et al. (2008) but at more than one phase, promise to lead to stronger constraints of dynamic model atmospheres.

Our model simulations based on the combination of dynamic model atmospheres with a radiative transfer model of the dust shell predict only small variations with phase at mid-infrared wavelengths. The difference near a wavelength of 10 μm amounts to $\sim$5% for the visibility values and to $\sim$25% for the photometry values. These results lead to the suggestion that the stellar photosphere and overlying molecular layers pulsate, which is demonstrated by the diameter variations in the near-infrared, but that these pulsations can not be detected for RR Aql by our 8–13 μm interferometry within our uncertainties. In addition, our visibility uncertainties do not allow us to exclude variations of the geometry and optical depth of the dust shell as a function of pulsation phase as observed previously for other targets (Lopez et al.(1997). Possible explanations for the non-detection of a phase-dependence of the dust shell parameters in our study compared to the ISI observations include: (i) Longer baseline lengths in our study that often fully resolve the very extended silicate dust shell. (ii) Our limited phase coverage between minimum and pre-maximum (0.45–0.85) phases. Possible variations over the whole pulsation cycle can not be excluded.

The observed variability of the 8–13 μm flux at a significance level of 1–2σ may indicate variations of the stellar radiation re-emitted by the dust, and/or changes of the dust geometry or optical depth.

5.5 Summary and Conclusions

We have investigated the circumstellar dust shell and characteristics of the atmosphere of the oxygen-rich Mira variable RR Aql using mid-infrared interferometric observations. We have observed RR Aql with the VLTI/MIDI instrument at different pulsation phases in order to monitor the photometry and visibility spectra. A total of 57 observations were combined into 13 epochs covering 4 pulsation cycles between April 2004 and July 2007, and covering pulsation phases between minimum and pre-maximum phases (0.45–0.85).

We have modeled the observed data with an ad-hoc radiative transfer model of the dust shell using the radiative transfer code mcsim_mpi by Ohnaka et al. (2006). Hereby, we used a series of dust-free dynamic model atmospheres based on self-excited pulsation models (M series, Ireland et al., 2004b,a) to describe the intensity profile of the central source. This study represents the first comparison between interferometric observations and theoretical models over an extended range of pulsation phases covering several cycles.

Our main observational results are as follows: (i) The interferometric data do not show evidence for intra-cycle visibility variations. (ii) The data do not show evidence for cycle-to-cycle visibility variations. (iii) The 8–13 μm flux suggests intra-cycle and cycle-to-cycle photometry variations at a significance level of 1–2σ. Follow-up observations with higher accuracy using a dedicated photometric instrument, such as VISIR at the VLT, are needed to confirm this result.

These observational results can be explained by dynamic model atmospheres and variations of dust shell parameters. Simulations using different phases of the dynamic model atmosphere and different sets of dust shell parameters predict visibility variations that are lower or of the order of the observed visibility uncertainties (5-20 %). Model-predicted variations of the photometry spectra are largest around wavelengths of 10 μm with difference of up to $\sim$25% corresponding to up to 1–2σ.

The best-fitting model for our average pulsation phase of $\overline{\Phi_V} = 0.64 \pm 0.15$ includes a silicate dust shell with an optical depth of τ_V(silicate)=2.8±0.8, an inner radius of $R_{\rm in}$=4.1±0.7 $R_{\rm Phot}$, and a power-law index of the density distribution of p=2.6±0.3. The corresponding best-fitting atmosphere model of the series used to describe the central intensity profile is M21n ($T_{\rm model} = 2550\,{\rm K}$, $\Phi_{\rm model} = 0.1$) with a photospheric angular diameter of $\Theta_{\rm Phot}$=7.6±0.6 mas. The photospheric angular diameter corresponds to a photospheric radius of $R_{\rm phot} = 520^{+230}_{-140}\,{\rm R}_\odot$ and an effective temperature of $T_{\rm eff} \sim 2420 \pm 200\,{\rm K}$. The latter value is consistent with the effective temperature of the used model M21n. The combined model can well reproduce the shape and features of the observed photometry and visibility spectra of RR Aql, as well as the SED at 1–40 μm.

The addition of an Al_2O_3 dust shell did not improve the model fit. However, our model simulations show that the addition of an Al_2O_3 dust shell with low optical depth compared to the silicate dust shell could not be detected within our measurement uncertainty (Sec 4.4.1 Simulation 4). A description of the RR Aql dust shell with silicate grains alone is consistent with the results by Lorenz-Martins & Pompeia (2000).

We conclude that our RR Aql data can be described by a silicate dust shell surrounding a pulsating atmosphere, consistent with near-infrared observations of Mira variables. The effects of the pulsation on the mid-infrared flux and visibility values are expected to be less than about 25% and 20%, respectively, and are too low to be detected within our measurement uncertainties. Although the addition of an Al_2O_3 dust shell did not improve the model fit, our simulations also indicate that we can not exclude the presence of an inner Al_2O_3 dust shell with relatively low optical depth, which may be an important contributor to the dust condensation sequence.

Our modeling attempt of a radiative transfer model of the dust shell surrounding a dynamic dust-free model atmosphere provides constraints on the geometric extensions of atmospheric molecular and dust shells. It should be noted that it can not explain the mechanism by which the observed mass-loss is produced and the wind is driven. Newer models of M type, i.e. of oxygen-rich Miras, that include atmospheric dust (e.g. Ireland et al., 2008, ,Ireland, in preparation) typically predict very close to zero effective acceleration in high layers but, so far, no clear outward acceleration, i.e. no wind. Subtle details are being discussed that may overcome this shortcoming of dynamic models of M type Miras Höfner (2011). Future observations aiming at characterizing and constraing such new models of the mass-loss process and the wind driving mechanism at mid-infrared wavelengths would benefit from obtaining more precise photometry values using a dedicated instrument like VISIR at the VLT, the addition of shorter baselines to characterize the extension of the silicate dust shell, and a more complete coverage of the pulsation cycle. The addition of concurrent spectrally resolved near-infrared interferometry would be needed to more strongly constrain atmospheric molecular layers located close to the photosphere.

Chapter 6

AMBER Observations of RR AQL

6.1 VLTI/AMBER Observations and data reduction

6.1.1 The AMBER observations

The Very Large Telescope Interferometer (VLTI, Glindemann et al., 2003) of ESO's Paranal Observatory has been equipped with the infrared interferometric instruments AMBER and MIDI. AMBER is the near-infrared interferometric beam combiner (Petrov et al., 2007) operating in the J, H, and K-band covering the wavelength range 1.0 - 2.4 μm. AMBER combines the light of three telescopes, and thus allows to measure in addition to the three visibilities and three differential phases of the object also the closure phase. While the measured visibilities characterize the size and the shape of the object, the differential and closure phase are related to the possible deviation from the spherical symmetry of the object. Non-zero closure phase value (alternatively non 180deg) indicate the asymmetric features of the observed object. AMBER offers spectrally dispersed information in low (R$\sim$35), medium (R$\sim$1500), and high-resolution (R$\sim$12000). With the baselines which can reach 130m for the Unit Telescopes (UTs, 8.2m), and 200m for the Auxiliary Telescopes (ATs, 1.8m) the AMBER instrument is able to resolve features up to 2 mas.

In this chapter we present interferometric observations which were obtained with the AMBER instrument in medium spectral resolution mode (R$\sim$ 1500), using three Unit Telescopes (UTs) on 09/09/2006 (Julian day 245 3988). The observations are summarized in Table 6.1, which lists the name of the star and calibrators, the wavelength range, the time, the projected baseline lengths (B_p) and the position angle (PA_p) on sky. The detector integration time (DIT) was 50 ms, the air-mass about 1.1, the optical seeing about 1.2 arcsec and the coherence time about 2.1 msec. The date of observation corresponds to a visual phase Φ_{vis}= 2.82, with an uncertainty of about 0.1. In addition to the science target RR Aql, the two calibration stars 70 Aql and ψ $_{01}$ Aqr, as well as the check star λ Aqr, were observed close in time. We have used λ Aqr as a check star to confirm the reliability of the instruments. The adopted limb-darkened diameters of 70 Aql and ψ $_{01}$ Aqr are Θ_{LD} =3.18$\pm$0.037 mas and Θ_{LD} =2.18$\pm$0.025 mas respectively (Merand, Borde at al, 2005).

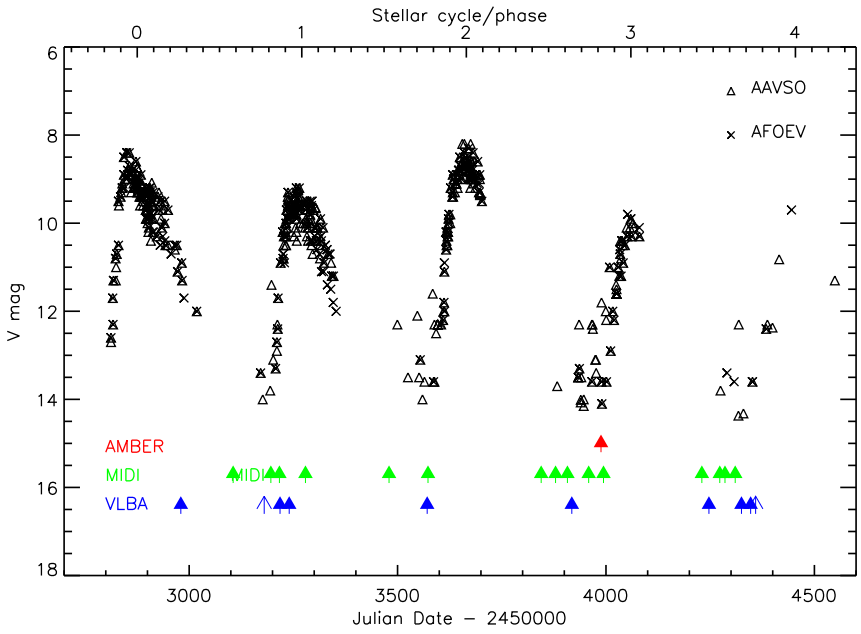

Figure 6.1: Visual light-curve of RR Aql based on data from the AAVSO and AFOEV databases as a function of Julian Date and stellar cycle/phase. The red arrow indicate the dates of our VLTI/AMBER observations. The green arrows indicate the dates of our VLTI/MIDI observations. The blue arrows indicate the dates of our VLBA observations. Here, the full arrows denote observations of SiO maser emission and simple arrows observations of H_2O maser emission.

Table 6.1: RR Aql - observations with the AMBER instrument

Target	Purpose	Wavelenght range[μm]	Time [UTC]	B_p [m] U1-U2/ U2-U3/U3-U1	PA_p deg
70 Aql	Calibrator(K5 II)		1:53-2:06	53.1/44.5/96.8	27.4/41.9/34.0
RR Aql	Science target	2.12-2.20	2:34-2:47	55.6/46.5/101.4	33.4/45.5/38.7
RR Aql	Science target	2.12-2.20	3:00-3:09	56.1/46.6/102.1	34.0/45.9/39.4
70 Aql	Calibrator(K5 II)		3:28-3:37	55.9/46.6/101.9	33.6/45.7/39.1
λ Aqr	Check star(M2 III)	2.19-2.27	3:59-4:08	54.0/44.9/98.1	25.4/39.9/32.0
ψ_{01} Aql	Calibrator(K1 III)		4:27-4:36	54.5/45.3/99.0	25.7/40.1/32.2

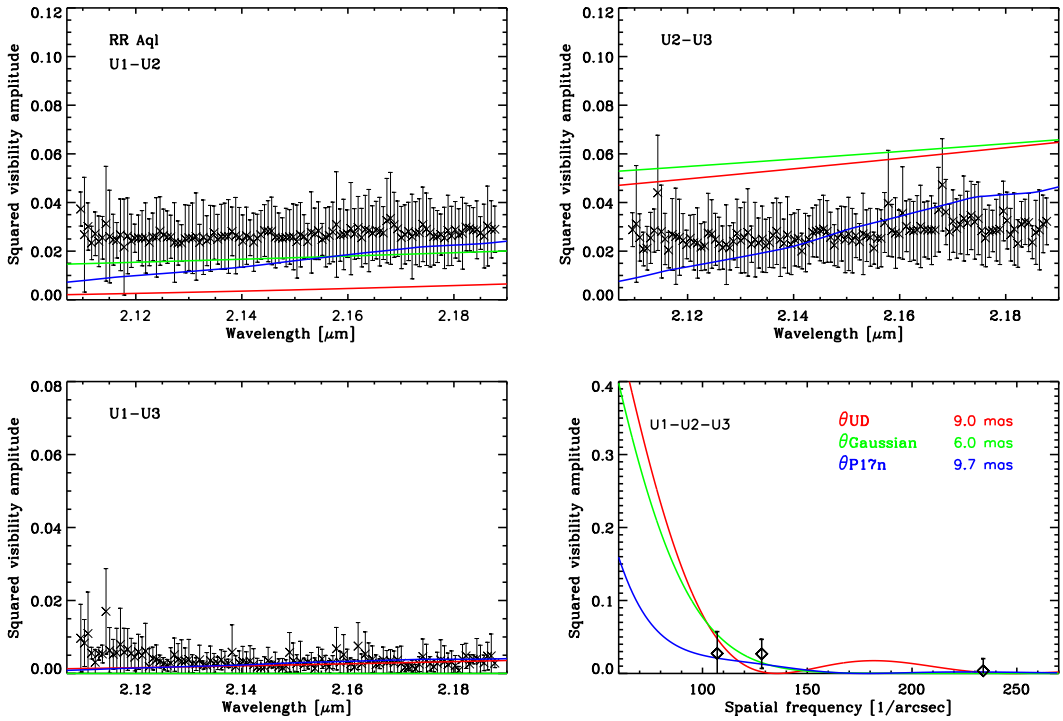

Figure 6.2: Measured visibility data of RR Aql compared to models of a UD (red line), of a Gaussian profile (green line), and of the P17n atmosphere model (blue line).

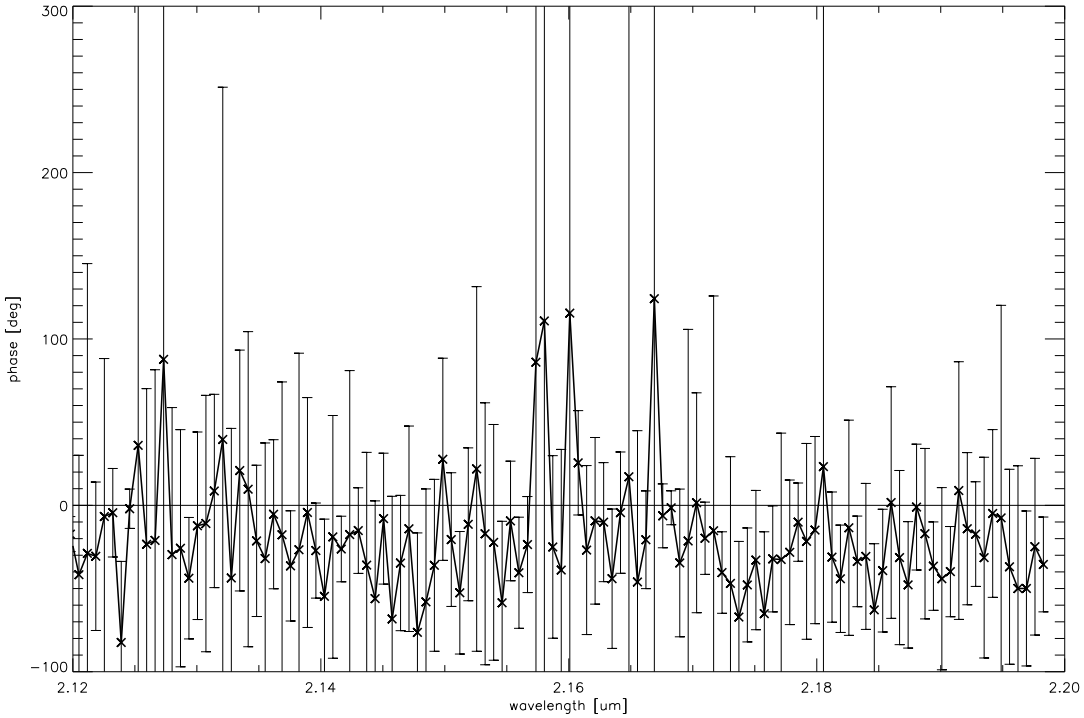

Figure 6.3: RR Aql Closure phase signal as a function of wavelength.

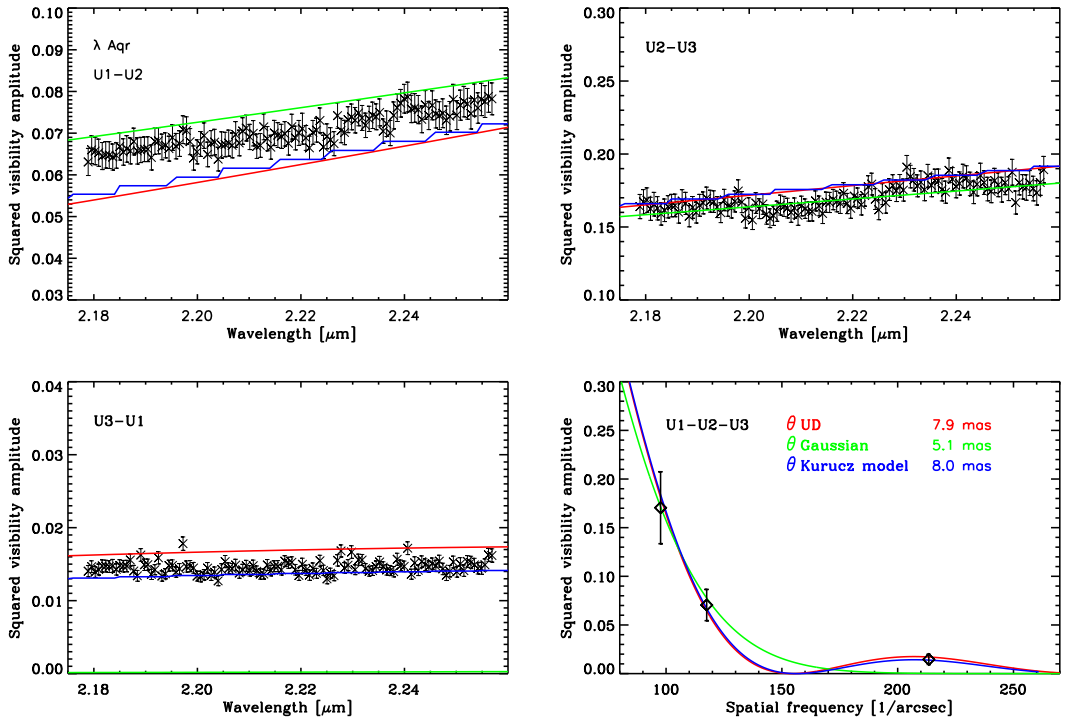

Figure 6.4: Measured visibility data of the check star 70 Aql compared to models of a UD (red line), of a Gaussian disk (green line), and of the P17n atmosphere model (blue line).

6.2 The AMBER data reduction and modeling

For the AMBER data reduction we used the *Amdlib* package (version 2.1) with the yorick interface (provided by the Amber consortium and the Jean-Marie Mariotti Center).
We obtained several days of observations in the scope of this program, however for technical reasons and conditions issues, the data were of very poor quality and had to be dropped out for all but one observation. Absolute wavelength calibration was performed by correlating the raw spectra with a model of the atmospheric transmission with the same spectral resolution.
The selection criteria were varied and the impact on the result was checked. For the frame selection criteria and averaging, we vary the best frames based on the piston for: 50%, 60%, 70%, 80%, 90%, and the best fringe S/N of all frames for: 20%, 30%, 40%. All the differences were carefully monitored.
We calibrated both science targets and the check star with each calibrator data file using the same settings. We verified that the results did not lead to significant systematic dependence on the selection criteria. Except for the higher S/N where the errors bars get lower, but the results stay rather stable. The best selection criteria are: manual shift 2, piston: 90%. In the final selection we included 20% of all frames.

6.3 Results

Figures 6.2 and 6.4 show our measured squared visibilities as a function of wavelength/spatial frequency. We compared the visibility data to the best fitting models of a uniform disk (UD), a Gaussian disk with a constant diameter and also to stellar atmospheres models. For RR Aql, we used the complete self-excited dynamic model atmospheres of Mira stars by Ireland et al. (2004b,a) (Section 4.1). These models include the effect from molecular layers that lie above the continuum-forming photosphere. Out of the available phase and cycle combinations of the M and P series, the best fit to our measured AMBER visibility data its obtained with the model P17n. We estimate a continuum photospheric angular diameter of $\Theta_{\rm Phot}$= 9.9 ± 2.4 mas, based on an average of those models where | Φ_{vis} - Φ_{model} | < 0.1. The determined UD angular diameter of $\Theta^{\rm UD}_{\rm Phot}$= 9.0 ± 1.8 mas, and Gaussian FWHM of $\Theta^{\rm Gauss}_{\rm Phot}$= 6.0 ± 1.5 mas. The closure phase values are noisy (see Figure 6.3), and they do not allow us to confirm or deny possible asymmetric brightness distribution across the stellar surface. For λ Aqr we used an ATLAS 9 model atmosphere (Kurucz, 1993). Note that the spectral resolution of the ATLAS 9 data is 0.01 m, compared to $\sim$ 0.0015 of our observations.

6.4 Discussion and Conclusion

The observations with UTs resulted in a low data quality showing very low transfer function values. Low transfer function values can be caused by UTs vibrations which lower instrumental visibilities. At phase Φ_V=2.82 we determined the near-infrared continuum photospheric angular diameter to $\Theta_{\rm Phot}$= 9.9 ± 2.4 mas, we determined a UD angular diameter of $\Theta^{\rm UD}_{\rm Phot}$= 9.0 ± 1.8 mas, and a Gaussian FWHM of $\Theta^{\rm Gauss}_{\rm Phot}$= 6.0 ± 1.5 mas. In comparison, van Belle et al. (2002) estimated a UD diameter in the K-band ($\lambda = 2.2\,\mu$m, $\Delta\lambda = 0.4\,\mu$m) of $\Theta^{\rm UD}_{\rm Phot}$=10.73±0.66 mas at a minimum phase of 0.48. The diameters were derived at different pulsation phases, and they are within the range of the derived uncertainties. The photospheric angular diameter estimated from our MIDI observations of $\Theta_{\rm Phot}$=7.6±0.6 mas at an average pulsation phase of $\overline{\Phi_V} = 0.64 \pm 0.15$ is smaller than the near-infrared continuum photospheric angular diameter derived from the AMBER data. The difference is within the 1 sigma uncertainty, and can most likely be explained by the different phases and the use of different model atmospheres to estimate the photospheric angular diameter from the data.

Chapter 7

MIDI Observations of S ORI (Al_2O_3-rich dust shell)

The Mira variable S Ori was analyzed and modeled in the same way as described in Chapter 5.

7.1 Characteristics of S ORI

The stellar parameters of the star in this paragraph are adopted from Wittkowski et al. (2007). S Ori is an oxygen-rich Mira variable star with spectral type M6.5e-M9.5e and V magnitude 7.2-14.0 (Samus et al., 2004). S Ori's period appears to vary in a seemingly sinusoidal fashion between about 400 and 450 days over about the past 100 years (Templeton et al.(2005). The mean period is P = 420.0 days. Our observation epochs correspond to the latest period P $\sim$ 430 days. This value is corresponding with the AAVSO[1] and AFOEV[2] data for the cycle of our observations, as well as for the most recent $\sim$5 cycles using P = 430 days and a Julian Date of last maximum brightness T_0 = 2 453 190 days. Figure 7.1 shows the visual light-curve of S Ori as a function of Julian Date and stellar phase based on these values. Also indicated are the dates/epochs of our VLTI observations. The distance to S Ori, as for many Mira stars, is not well known. van Belle et al. (2002) have estimated the distance to S Ori to 480 pc $\pm$ 120 pc based on a calibration of the period-luminosity relationship by Feast et al. (1989), and we adopt this value. The near-infrared K-band UD angular diameter Θ_{UD}^{K} of S Ori has been measured by van Belle et al. (1996), Millan-Gabet et al. (2005), and by Boboltz & Wittkowski (2005) to values between 9.6 mas and 10.5 mas at different phases. Diameter measurements of S Ori at other wavelengths have so far not been reported. S Ori exhibits SiO and OH maser emission (Benson et al. 1990), while a detection of H_2O maser toward S Ori has not been reported. The maps of the SiO maser emission in Boboltz & Wittkowski (2005) are the first toward S Ori. They derived average distances and standard deviations of the SiO maser spots from the center of their distribution at phase 0.73 of 9.4 $\pm$ 1.4 mas and 8.8 $\pm$ 1.7 mas for the 43.1 GHz and 42.8 GHz transitions, respectively. Sloan & Price (1998) report on a relatively low dust-emission coefficient (Dec, the total emission of the dust to the total emission of the star in the wavelength range 7.7–14.0 μm). The mass loss rate of 2.2 10^{-7} $M_\odot$/year was estimated by Young (1995).

[1] http://www.aavso.org
[2] http://cdsweb.u-strasbg.fr/afoev

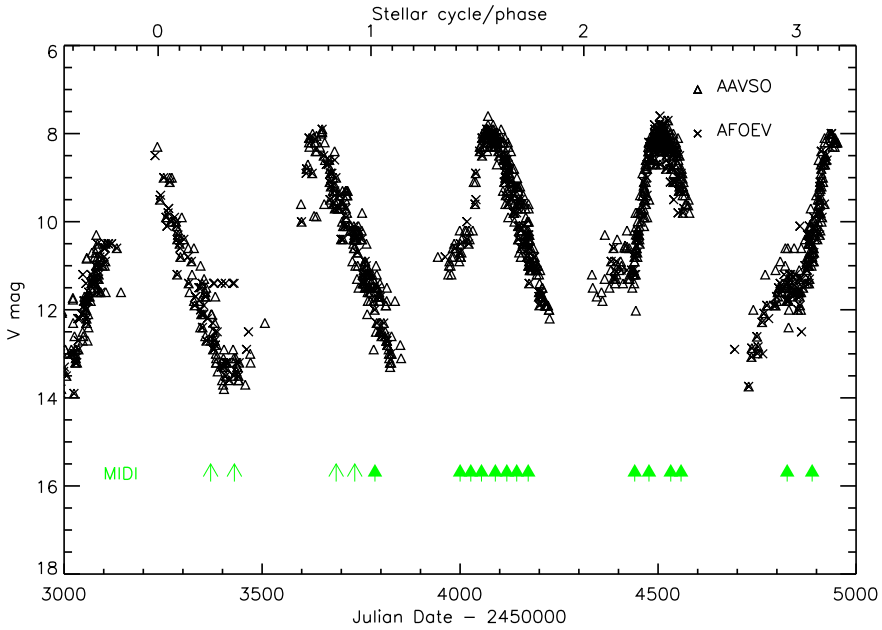

Figure 7.1: Visual light-curve of S Ori based on data from the AAVSO and AFOEV databases as a function of Julian Date and stellar cycle/phase. The green arrows indicate the dates of our VLTI/MIDI observations. The full arrows indicate our observations and the simple arrows indicate observations by Wittkowski et al. (2007)

7.2 VLTI/MIDI Observations and data reduction

We obtained 48 spectrally-dispersed mid-infrared interferometric observations of S Ori with the MIDI instrument. The observations were obtained between Feb 16, 2006 and Mar 14, 2009. These observations are follow up of 7 MIDI observations between Dec 31, 2004 and Dec 30, 2005 (Wittkowski et al., 2007). In order to obtain dispersed photometric and interferometric signals, we used the PRISM as a dispersive element with a spectral resolution R = $\Delta\lambda/\lambda \sim 30$. For most observations the beams were combined in *Sci_Phot* (SP) mode, complemented by several observations in the *High_Sens* (HS) mode. In the *Sci_Phot* mode beam splitters record the interferograms and the photometric spectra simultaneously, while in the *High_Sens* mode the photometric signal is observed after the interferometric signal.

The details of the observations and the instrumental settings are summarized in Table 7.1. The Table lists the epoch, the date, the time, the Julian Date (JD), the visual pulsation phase Φ_{vis}, the baseline configuration, the ground length of the configuration, the dispersive element, the beam combiner BC, the projected baseline length B_p, the position angle on the sky PA (deg. east of north), the DIMM seeing (at 500 nm), and the coherence time τ_0 (at 500 nm). We obtained observations mostly at pre-maximum and post-maximum pulsation phases ($\Phi_{\rm vis} = 0.90$–1.20) All observations were executed in service mode using different configuration of the Auxiliary Telescopes (ATs, 1.8m) in contrast to the previous observations by Wittkowski et al. (2007) acquired with UTs. Figure 7.2 indicates the *uv* coverage of our S Ori observations.

We merged the MIDI data into 14 epochs, with a maximum time-lag between individual observations of 8 days for each epoch (1.9% of the pulsation period). For technical problems we had to eliminate 6 observations. Fig. 7.1 indicates the observational epochs in comparison

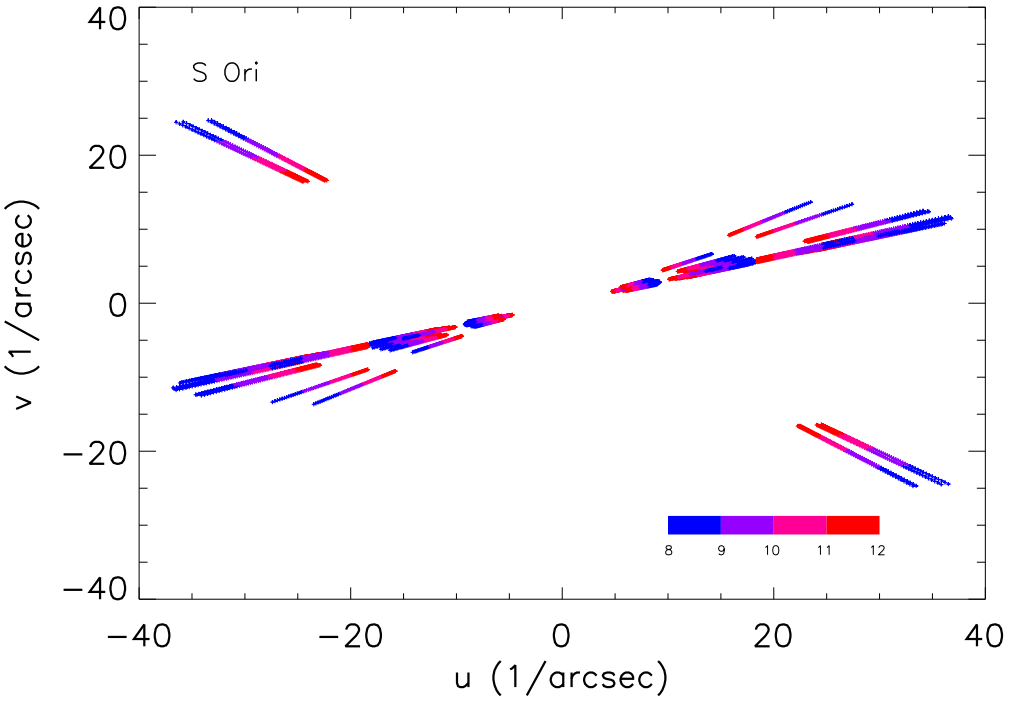

Figure 7.2: Coverage of the *uv* plane for the MIDI observations of S Ori. Each point represents the observations with ATs over the wavelength 8 to 13 μ.

to the light-curve. The full arrows indicate our observations and the simple arrows indicate observations by Wittkowski et al. (2007) The uncertainty in the allocation of the visual phase to our observations was estimated to ∼0.1.

We applied the same data reduction methods as for Mira variable RR Aql. For more details see Section 5.2 The calibration of S Ori data was as well proceeded in the same manner as for RR Aql (Section 5.2). Our main calibrators were Sirius (P80), HD25025 (P76/78), and HD 50778 (P74). Table B.2 lists calibrator stars observed per specific night including those calibrators observed by other programs.

7.3 MIDI results

As well as for Mira variable RR Aql we aimed to monitor the mid-infrared photometry and visibility spectra of S Ori. Here, we present and discuss the general properties of the data. We investigate and analyze the variability of the data as a function of phase and cycle in Sects. 7.3.1 and 7.3.2. We observed S Ori over 5 pulsation cycles. For comparison with the observations in Wittkowski et al. (2007) (simple arrows), the phase of our observations (full arrows) begins at 1.39 see Fig. 7.1). Our observations are mostly obtained at pre-maximum and post-maximum pulsation phases ($\Phi_{\rm vis} = 0.90$–1.20) except first two observations obtained at phases 1.38 and 1.40. 4 observational epochs in Wittkowski et al. (2007) cover phases 0.42, 0.55, 1.16, and 1.27.

Figure 7.4 shows all obtained calibrated photometry spectra as a function of wavelength. Most

Table 7.1: VLTI/MIDI observation of S Ori.

Epoch	DDMMYYYY	Time [UTC]	JD	Φ_{vis}	Config.	B	Disp. Elem.	BC	B_p [m]	PA [deg]	Seeing [″]	τ_0 [msec]
A	16022006	03:29	2453783	1.38	E0-G0		Prism	HS	12.77	71.93	0.93	4.8
A	22022006	00:17	2453789	1.40	E0-G0		Prism	HS	15.98	72.45	1.61	1.5
B	21092006	09:22	2454000	1.89	K0-G0		Prism	HS	60.94	70.26	-1.00	1.1
C	17102006	07:32	2454026	1.95	H0-D0		Prism	SP	60.34	69.90	1.02	2.4
C	17102006	08:43	2454026	1.95	H0-D0		Prism	SP	63.93	72.49	0.79	2.4
C	18102006	08:58	2454027	1.95	E0-G0		Prism	SP	16.00	72.88	0.88	2.4
C	19102006	07:05	2454028	1.95	E0-G0		Prism	SP	14.64	68.85	8.49	2.4
C	20102006	09:20	2454029	1.95	D0-G0		Prism	SP	31.61	73.30	0.41	4.8
C	14112006	05:44	2454054	2.01	D0-G0		Prism	SP	30.28	70.02	0.68	2.9
D	17122006	02:21	2454087	2.09	H0-G0		Prism	SP	25.94	64.85	1.02	2.7
D	17122006	04:56	2454087	2.09	H0-G0		Prism	SP	31.99	72.79	1.18	2.3
D	19122006	01:31	2454089	2.09	K0-G0		Prism	SP	45.13	59.80	1.02	4.6
D	19122006	04:46	2454089	2.09	K0-G0		Prism	SP	63.97	72.74	0.55	8.4
D	21122006	06:30	2454091	2.10	H0-G0		Prism	SP	28.59	73.10	0.63	5.9
E	11012007	02:57	2454112	2.15	E0-G0		Prism	SP	15.96	72.30	1.41	2.5
E	11012007	04:49	2454112	2.15	E0-G0		Prism	SP	14.83	73.33	1.34	3.2
E	13012007	03:45	2454114	2.15	E0-G0		Prism	SP	15.46	74.35	0.70	5.9
E	17012007	01:36	2454118	2.16	E0-G0		Prism	SP	15.22	70.19	1.36	1.7
E	18012007	04:55	2454119	2.16	H0-G0		Prism	SP	27.65	72.82	1.26	1.9
E	19012007	01:58	2454120	2.17	H0-G0		Prism	SP	31.38	71.43	0.94	2.5
E	20012007	04:48	2454121	2.17	H0-D0		Prism	SP	55.14	72.79	0.87	4.1
E	21012007	04:19	2454122	2.17	H0-D0		Prism	SP	58.22	73.23	0.72	5.4
F	10022007	00:54	2454142	2.22	H0-D0		Prism	SP	63.69	72.17	0.89	3.9
F	11022007	00:35	2454143	2.22	E0-G0		Prism	SP	15.79	71.68	1.21	3.2
F	12022007	01:08	2454144	2.22	H0-G0		Prism	SP	31.99	72.71	1.10	3.6
G	12032007	23:44	2454172	2.29	E0-G0		Prism	SP	15.93	73.14	1.25	2.6
G	12032007	02:07	2454172	2.29	E0-G0		Prism	SP	12.30	71.46	0.87	3.5
G	14032007	00:07	2454174	2.29	K0-G0		Prism	SP	62.32	73.41	0.88	2.8
H	02122007	06:53	2454437	2.91	H0-D0		Prism	SP	62.08	73.43	0.89	2.1
H	10122007	02:41	2454445	2.92	H0-D0		Prism	SP	50.63	64.00	1.43	1.9
I	29122007	02:55	2454464	2.97	H0-D0		Prism	SP	61.12	70.36	0.94	2.7
I	10012008	01:48	2454476	3.00	E0-G0		Prism	SP	14.85	69.32	0.80	5.9
I	11012008	01:32	2454477	3.00	H0-G0		Prism	SP	29.02	68.59	0.87	5.4
I	11012008	04:12	2454477	3.00	H0-G0		Prism	SP	31.16	73.42	0.90	6.2
I	12012008	01:50	2454478	3.00	E0-G0		Prism	SP	15.07	69.84	1.30	4.7
I	12012008	03:49	2454478	3.00	E0-G0		Prism	SP	15.83	73.27	1.54	4.0
J	06032008	00:31	2454532	3.13	H0-D0		Prism	SP	62.61	73.39	0.91	3.8
J	06032008	01:11	2454532	3.13	H0-D0		Prism	SP	59.51	73.35	0.94	3.6
J	06032008	01:29	2454532	3.13	H0-D0		Prism	SP	57.62	73.15	0.88	3.7
J	13032008	00:29	2454539	3.14	H0-G0		Prism	SP	30.41	73.43	-1.00	2.1
K	01042008	00:24	2454558	3.19	H0-G0		Prism	SP	26.24	72.28	0.85	2.2
L	25122008	06:00	2454826	3.81	A0-G1		Prism	SP	72.97	123.81	0.84	4.7
L	25122008	06:21	2454826	3.81	A0-G1		Prism	SP	68.68	126.70	0.91	4.2
L	31122008	03:34	2454832	3.83	H0-E0		Prism	SP	47.78	72.17	0.84	5.5
L	31122008	04:09	2454832	3.83	H0-E0		Prism	SP	47.95	72.95	0.76	6.2
M	26022009	01:57	2454889	3.96	A0-G1		Prism	SP	72.09	124.37	0.75	6.0
M	26022009	02:12	2454889	3.96	A0-G1		Prism	SP	69.08	126.42	0.85	5.4
M	04032009	00:20	2454895	3.97	E0-H0		Prism	SP	47.62	73.22	1.28	3.3

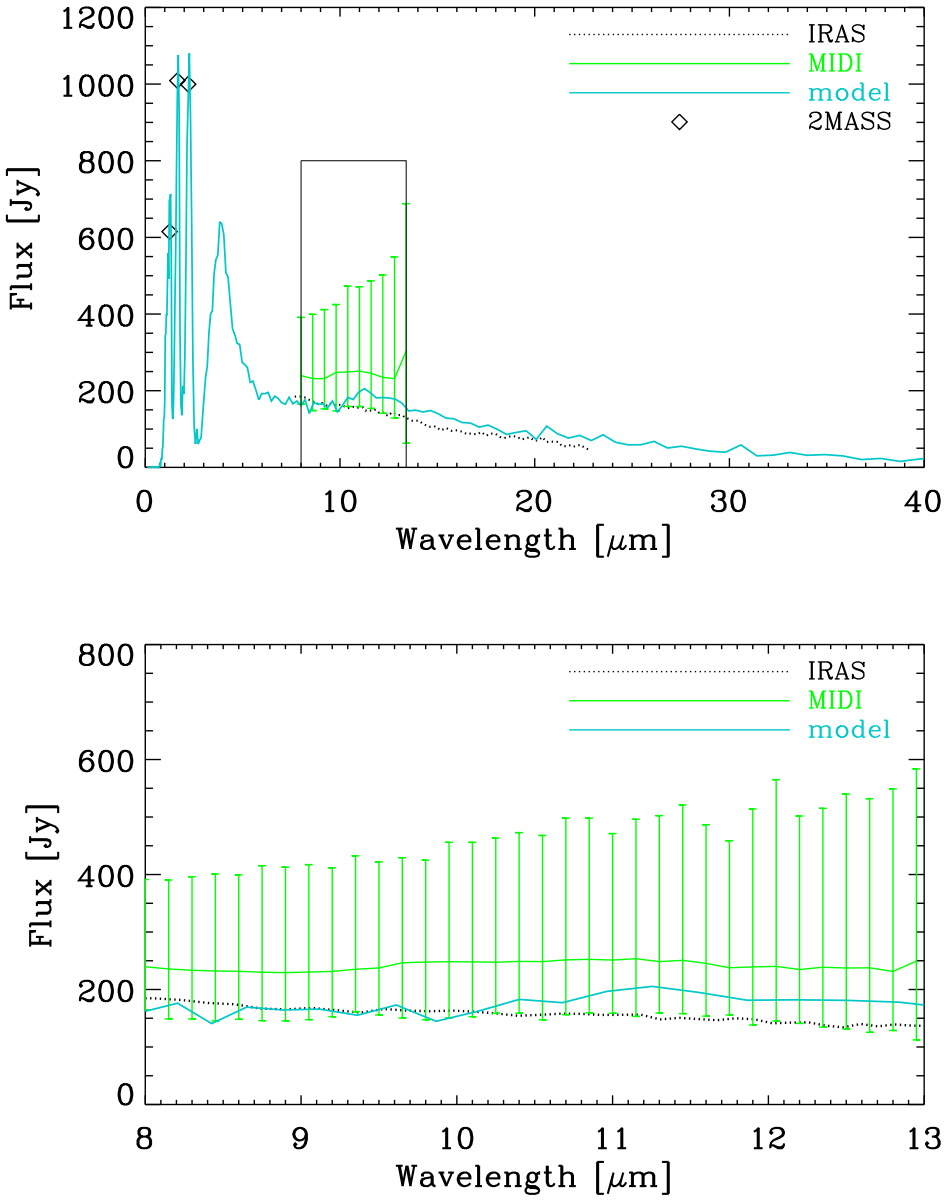

Figure 7.3: S Ori flux spectrum as a function of wavelength from 2.4 μm to 40 μm (top). The lines represents the flux spectra from IRAS-LRS observations covering wavelengths from $\sim$ 7.7 μm to $\sim$ 23 μm (dotted thin black like), and the mean of our N-band MIDI measurements (solid thin green line). Here, the vertical bars span the maximum and minimum values measured. The diamond symbols denote 2MASS measurements at 1.25 μm, 1.65 μm, and 2.2 μm. The solid blue line indicates our atmosphere and dust shell model as explained in Sect. 7.3.4. The bottom plot shows an enlarged segment of the plot in the MIDI wavelength range of 8–13 μm.

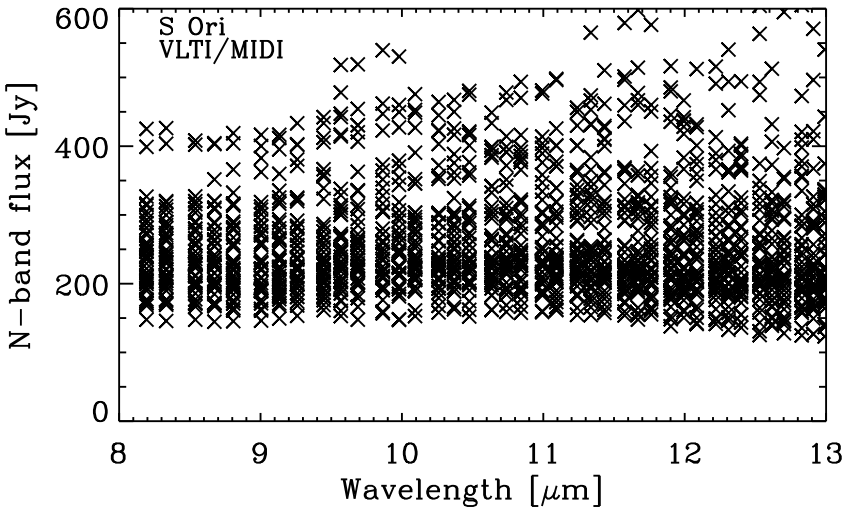

Figure 7.4: Calibrated S Ori MIDI flux spectra as a function of wavelength. For clarity, the error bars are omitted in the plot.

of the MIDI flux measurements show a flat shape. The majority of the values falls into the range of $\sim$ 130–450 Jy. The level of the flux spectrum differs for individual measurements with a spread of $\sim$ 300–350 Jy. Figure 7.3 shows a comparison of the mean of our MIDI flux measurements to measurements obtained with the IRAS instruments. The shape of the flux curve is well consistent between the MIDI and IRAS measurements. The level of the IRAS flux is within the range of our MIDI measurements. The difference between the MIDI and IRAS flux level may indicate a flux variation during the pulsation cycles. Figure 7.3 also includes a model description of our MIDI data, which will be explained latter in the text (Sect. 7.3.4).

Figure 7.5 shows all obtained calibrated visibility spectra, which are combined into four groups of different projected baseline lengths (pb) of pb $<$ 20 m, 20 m $<$ pb $<$ 35 m, 35 m $<$ pb $<$ 50 m, and pb $>$ 50 m. The visibility curves do not show a strong wavelength dependence. The visibility increases between $\sim$ 8-9 μm, and beyond $\sim$ 9-10 μm visibility curves flattens. The shape and absolute scale of the visibility function does not significantly depend on the length of the projected baseline. A broad spectrum and visibility function in the wavelength range 8–13 μm is interpreted as a dust shell consisting of Al_2O_3 dust (Wittkowski et al., 2007) or silicate and Al_2O_3 dust (Ohnaka et al., 2005).

As well as for RR Aql we computed for each data set and spectral channel the corresponding UD diameter and the Gaussian FWHM. As previously mentioned, these values are leading to the first rough estimate of the characteristic size of the target at each wavelength. Fig. 7.6 shows for the example of epoch B the flux, the visibility amplitude, the corresponding UD diameter, and the corresponding Gaussian FWHM diameter as a function of wavelength. A quasi-constant equivalent UD diameter is roughly twice the continuum photospheric size. Beyond $\sim$ 9-10 μm a equivalent UD diameter increases.

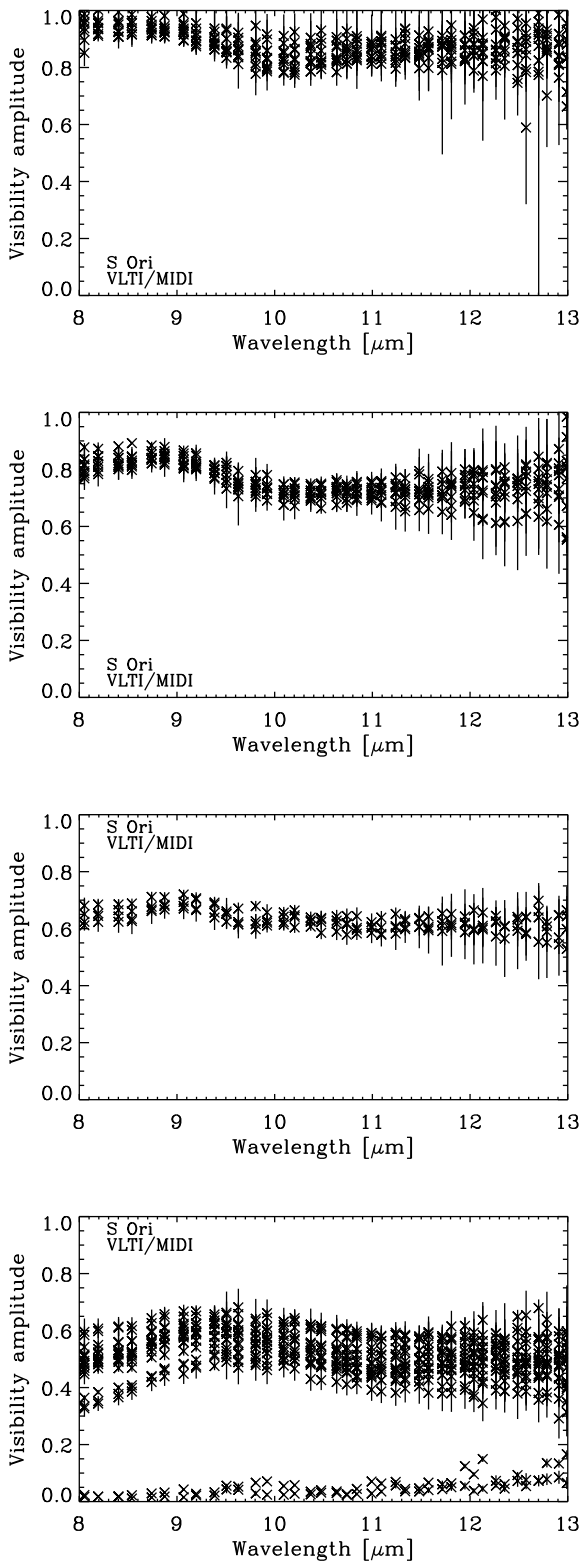

Figure 7.5: Calibrated S Ori MIDI visibility amplitudes as a function of wavelength. (from top to bottom) Observations executed at projected baselines (pb) < 20 m, 20 m $<$ pb $<$ 35 m, 35 m $<$ pb $<$ 50 m, and pb > 50 m.

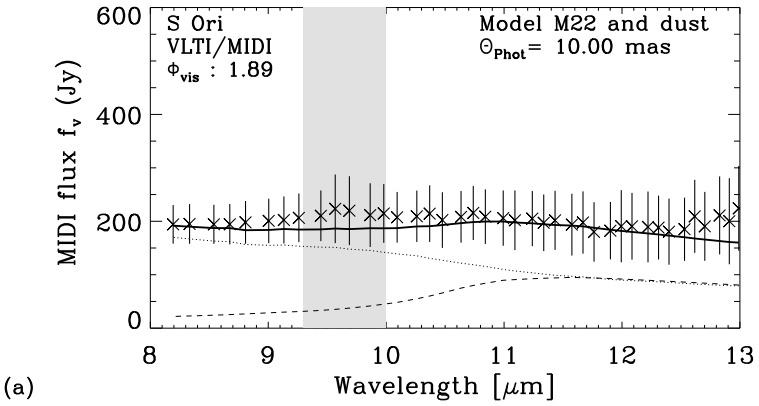
S Ori
VLTI/MIDI
Φvis : 1.89
Model M22 and dust
ΘPhot= 10.00 mas
MIDI flux fν (Jy)
Wavelength [μm]

(a)

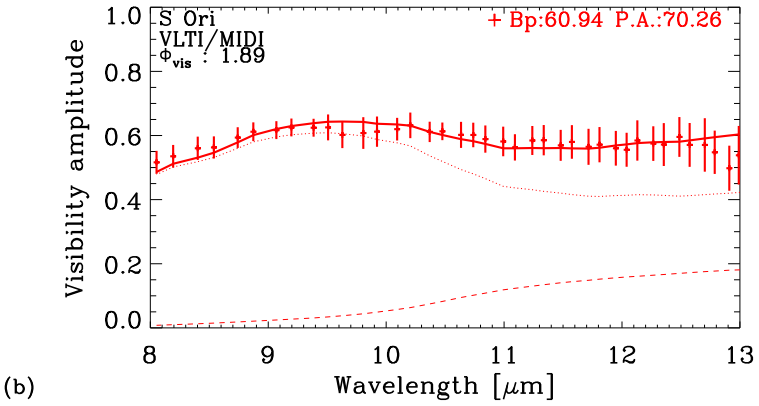
S Ori
VLTI/MIDI
Φvis : 1.89
+ Bp:60.94 P.A.:70.26
Visibility amplitude
Wavelength [μm]

(b)

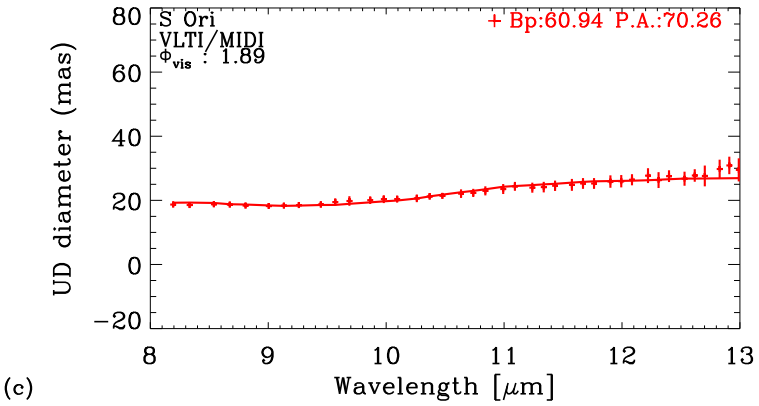
S Ori
VLTI/MIDI
Φvis : 1.89
+ Bp:60.94 P.A.:70.26
UD diameter (mas)
Wavelength [μm]

(c)

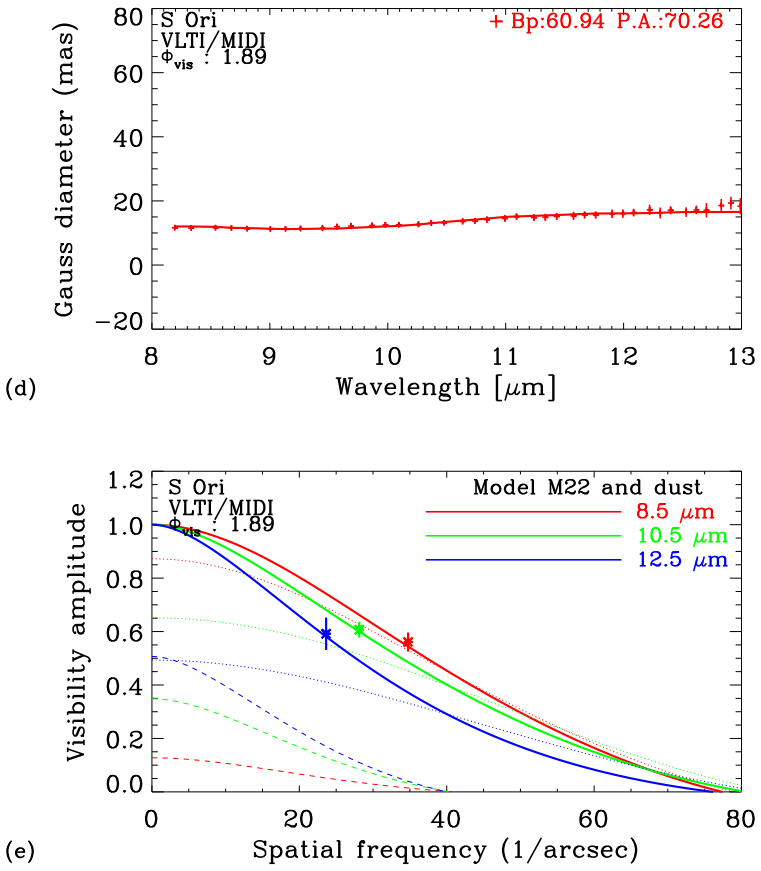

Figure 7.6: VLTI/MIDI interferometry at 8-13μm of S Ori for the example of epoch B (stellar phase 1.89). The panels show (a) the flux, (b) the visibility amplitude, (c) the corresponding UD diameter, (d) the corresponding Gaussian FWHM diameter as a function of wavelength. The gray shade indicates the wavelength region around 9.5 μm that is affected by atmospheric absorption. Panel (e) shows the visibility amplitude as a function of spatial frequency for three averaged bandpasses of 8-9 μm, 10-11 μm, and 12-13 μm. The crosses with error bars denote the measured values. The solid lines indicate our best-fitting model, as described in Sect. 7.3.4. The model consists of a radiative transfer model describing the surrounding dust shell where the central star is represented by a dust-free dynamic model atmosphere. The contributions of the stellar and dust components alone are indicated by the dotted and the dashed line, respectively.

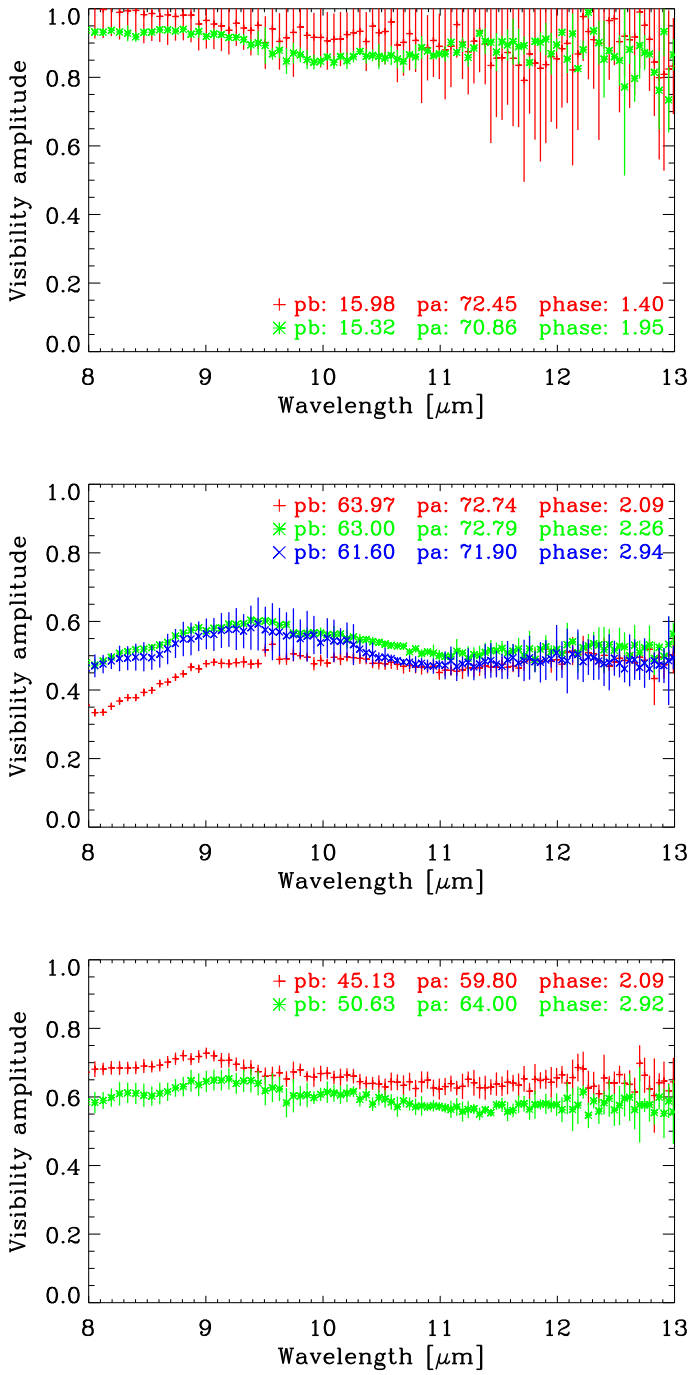

Figure 7.7: Calibrated MIDI visibility amplitudes for different pulsation phases within the same cycle to investigate intra-cycle visibility variations. Each line represents a different pulsation phase within the same cycle and is computed as an average of data obtained at the respective phase (± 0.15) and observed at similar projected baseline length (pb ± 10%) and position angle (PA ± 10%). The top panel shows the example of pulsation phases 0.40, and 0.95 of cycle 1 observed with a projected baseline length of ∼ 15 m and a position angle of ∼71 deg. The middle panel shows the example of pulsation phases 0.09, 0.26, and 0.94 of cycle 2 observed with a projected baseline length of ∼ 63 m and a position angle of ∼72 deg. The bottom panel shows the example of pulsation phases 0.09, and 0.92 of cycle 2 observed with a projected baseline length of ∼ 47 m and a position angle of ∼62 deg. The error bars are computed as the standard deviation of the averaged visibilities.

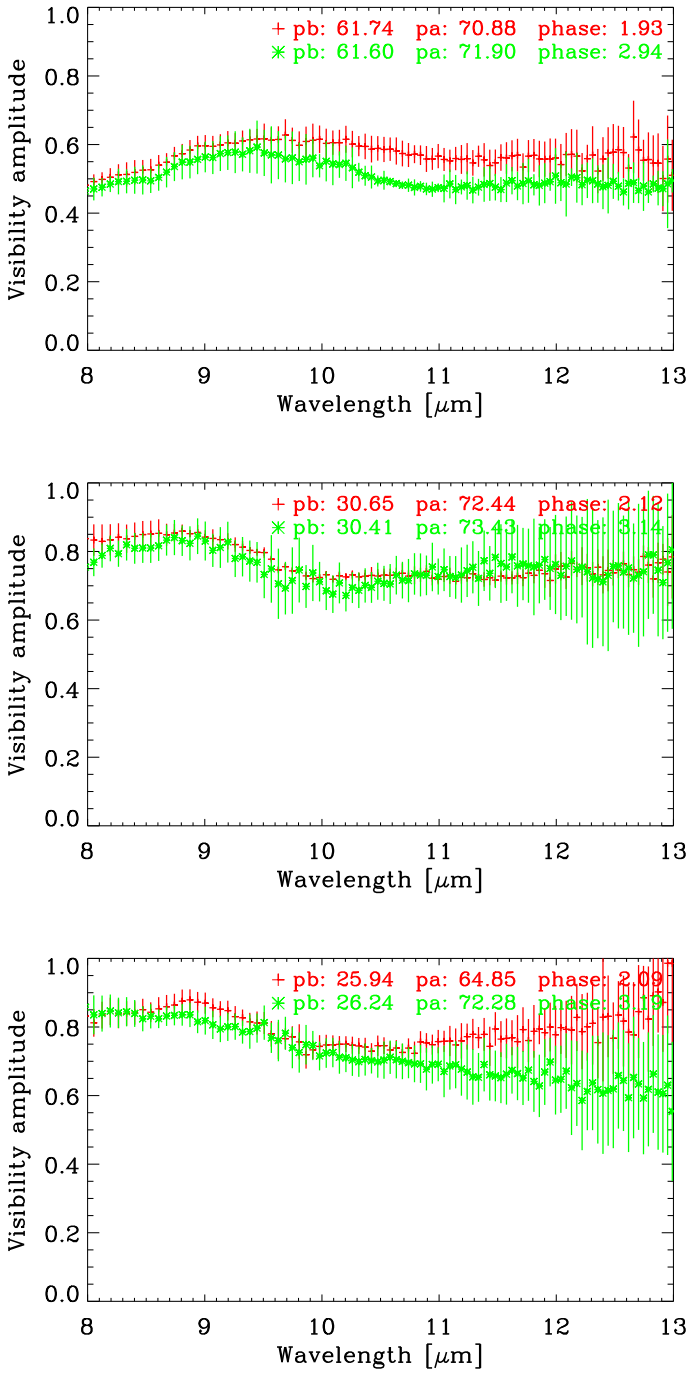

Figure 7.8: As Fig. 7.7, but for the same pulsation phase in consecutive pulsation cycles to investigate cycle-to-cycle visibility variations. The top panel shows the example of pulsation phase $\sim$ 0.93 in two consecutive cycles observed with a projected baseline length of $\sim$ 61 m and a position angle $\sim$71 deg. The middle panel shows the example of pulsation phase 0.13 in 2 consecutive cycles observed with a projected baseline length of $\sim$ 30 m and a position angle $\sim$73 deg. The bottom panel shows the example of pulsation phase 0.14 in 2 consecutive cycles observed with a projected baseline length of $\sim$ 26 m and a position angle $\sim$68 deg.

7.3.1 Visibility monitoring

The MIDI data on S Ori cover a total of 5 pulsation cycles covering mostly pre-maximum and post-maximum pulsation phases ($\Phi_{vis} = 0.90$–1.20) (see Tab. 7.1 and Fig. 7.1). We again obtained data at similar projected baseline lengths and position angles which gives us an opportunity to compare interferometric data obtained at different pulsation phases and cycles. We have as well as for RR Aql combined individual observations into groups of similar pulsation phases ($\Phi_{vis} \pm 0.15$), projected baseline lengths (pb $\pm$ 10 %), and position angles (PA $\pm$ 10 %). The data within each group were averaged. The uncertainty of the averaged visibility curves was estimated as the standard deviation of the averaged visibilities.

Intra-cycle visibility monitoring

In this section, we compared data observed at different pulsation phases within the same cycle. Our observations, however, cover mostly pre-maximum and post-maximum pulsation phases ($\Phi_{vis} = 0.90$–1.20). Fig. 7.7 shows three examples of calibrated visibility curves, where each line in the plots represents an average of a group of visibility data, as described above, (i.e. with similar pb, PA, and Φ_{vis}). The top panel shows an example of observations within the first pulsation cycle at phases 1.40, and 1.95 obtained with pb $\sim$ 15 m and PA $\sim 71°$. The middle panel shows the example of second pulsation cycle with pulsation phases 2.09, 2.26, and 0.94 observed with a projected baseline length of $\sim$ 63 m. The bottom panel shows an example of observations at phases 2.09, and 2.92 obtained with pb $\sim$ 47 m and PA $\sim 62°$. The data as well as for RR Aql (see Sections 5.3.1) do not show any evidence for intra-cycle visibility variations within the probed range of pulsation phases (mostly pre-maximum and post-maximum pulsation phases $\Phi_{vis} = 0.90$–1.20, see Tab. 7.1) and within our visibility accuracies of about 5–20%.

Cycle-to-cycle visibility monitoring

In order to investigate cycle-to-cycle visibility variations, we also compared data observed at similar pulsation phases of different, consecutive, cycles. Figure 7.8 shows three of these examples. The values were computed in the same way as shown in Fig. 7.7 of Sect. 7.3.1. The top panel shows visibilities at maximum pulsation phases of 1.93, and 2.94 in two consecutive cycles obtained with a projected baseline length of $\sim$ 61 m and PA $\sim 71°$. The middle panel shows visibilities at post-maximum phases of 2.12, and 3.14 obtained with a projected baseline length of $\sim$ 30 m and PA $\sim 73°$. The bottom panel shows also visibilities at post-maximum phases of 2.09, and 3.19 obtained with a projected baseline length of $\sim$ 26 m and PA $\sim 68°$. In the last example the phases differ more then 10%, however, the previous section (7.3.1) shows no intra-cycle visibility variations for this difference of phase, and therefore the observations can be compared. The data (Fig. 7.8) again do not show any significant cycle-to-cycle visibility variation within our visibility accuracies of $\sim$ 5–20%.

Deviations from circular symmetry

Except 4 observations observed with the P.A. $\sim 125°$, all our observations were obtained with the P.A. $\sim 70°$ (see Tab. 7.1. Unfortunately, the quality of the data do not allow us to confirm or deny possible presence of an asymmetric intensity distribution.

Summarizing,
the obtained MIDI data on S Ori do not exhibit any significant intra-cycle or cycle-to-cycle visibility variations in 5 consecutive cycles (see Tab. 7.1 for details of the phase coverage) and within our visibility accuracies of $\sim$ 5–20%. The S Ori observations show good agreement of visibility data obtained at the same projected baseline lengths and position angles. This again confirms the good data quality and credibility of the data reduction procedure.

7.3.2 *N*-band flux monitoring

To investigate the intra-cycle and cycle-to-cycle variability of our 8–13 μm flux spectra, the data were again combined into groups of data obtained at similar pulsation phases ($\Phi_{\rm vis} \pm 0.15$). The data within each group were averaged. The uncertainty of the averaged photometry curves was estimated as the standard deviation of the averaged values.

Intra-cycle photometry monitoring

Fig. 7.9 shows three examples of a comparison of the MIDI calibrated flux spectrum at different pulsation phases of the same cycle. The top panel shows a comparison between phases 1.39 and 1.94 of cycle 1, the middle panel shows pulsation phases 2.26, 2.16, 2.08 and 2.94 of cycle 2,and the bottom panel shows a comparison between phases 3.14, 3.62, and 3.96 of cycle 3. The S Ori flux values do not show any significant flux variation with the pulsation phase, except of the observations at phase 2.94 (the middle panel). The differences correspond to up to 40%–50%, or about 0.5–1 standard deviations. All the examples exhibit quite large standard deviations that do not allow us to make any reliable conclusions.

Cycle-to-cycle photometry monitoring

Fig. 7.10 shows a comparison of data observed at the same phase of consecutive pulsation cycles. The top panel shows a comparison between phases 1.94, 2.94, and 3.96, i.e. phase 0.95 of cycles 1, 2 and 3. The middle panel shows phases 2.16 and 3.14, i.e. phase 0.15 of cycle 2 and 3. The bottom panel shows a comparison between phases 2.26 and 1.39, i.e phase $\sim$ 0.32 of cycle 1 and 2. As for the intra-cycle photometry variations discussed in the previous paragraph, the differences between phases in the last comparison is more than 10%, but since the observations did not show any significant intra-cycle variations we included the observations in the cycle-to-cycle comparison. The data again exhibit large spread and do not allow us to confirm or deny photometry variations of S Ori.

Summarizing,
the data do not show any considerable phase variation of the *N*-band spectra within the examined phase coverage (mostly obtained at pre-maximum and post-maximum pulsation phases, $\Phi_{\rm vis} = 0.90$–1.20). .

7.3.3 MIDI model parameters

The best model parameters were derived in the same manner as for the previous oxygen-rich Mira variable RR Aql. Here, we only recall the main points, and we list modified parameters. For more details see Section 5.3.4.

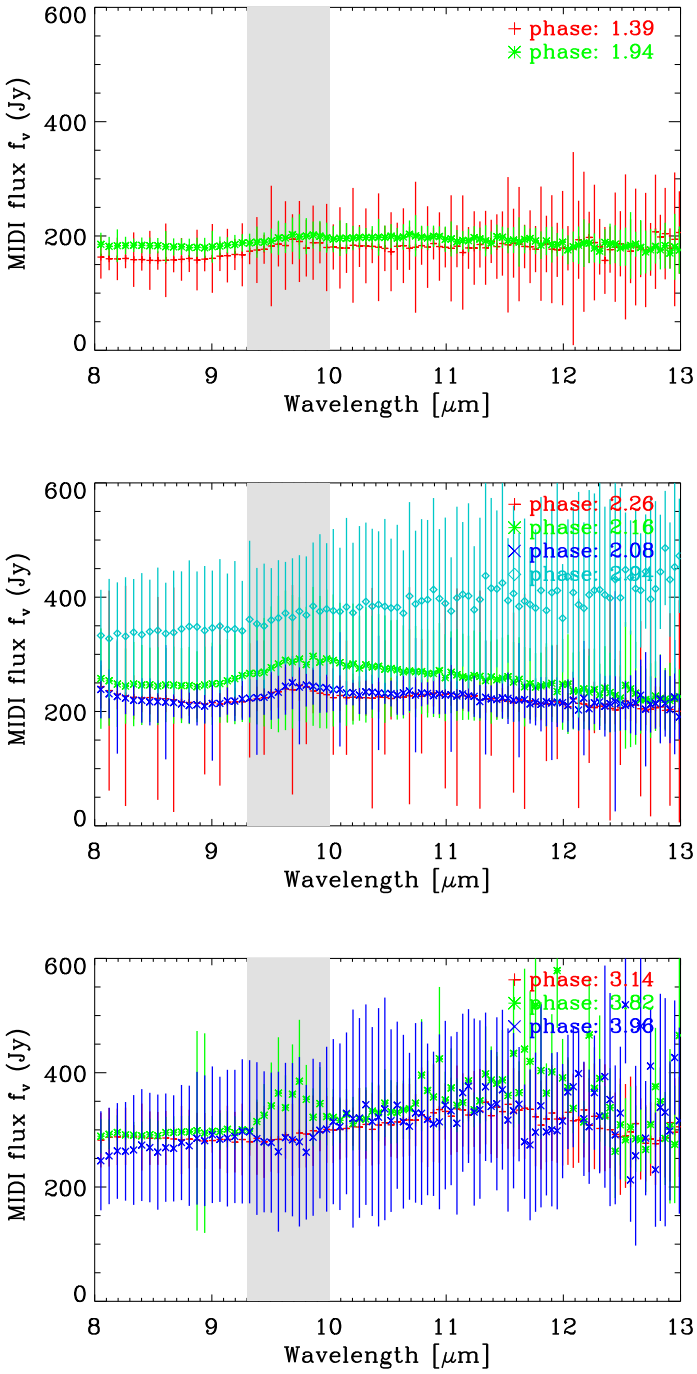

Figure 7.9: Calibrated MIDI flux spectrum for different pulsation phases within the same cycle to investigate intra-cycle photometry variations. Each line represents a different pulsation phase within the same cycle and is computed as an average of data obtained at the respective phase (± 0.15). The top panel shows the example of pulsation phases 0.39 and 0.94 of cycle 1. The middle panel shows the example of pulsation phases 0.26, 0.16, 0.08 and 0.94 of cycle 2. The bottom panel shows the examples of phases 0.14, 0.62 and 0.96 of cycle 3. The error bars are computed as the standard deviation of the averaged photometry curves. The gray shades denote zones that are affected by atmospheric absorption.

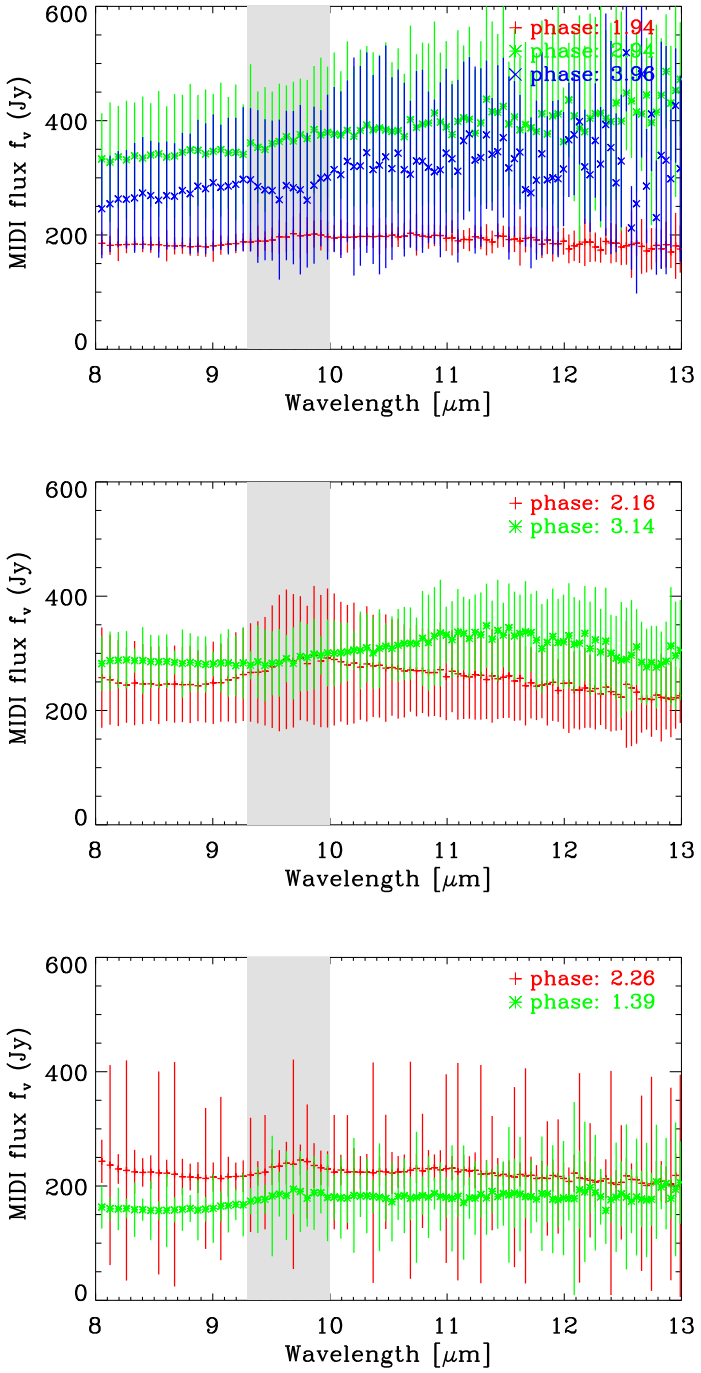

Figure 7.10: As Fig. 7.9, but for the same pulsation phase in consecutive pulsation cycles to investigate cycle-to-cycle photometry variations. The top panel shows the example of phase ~ 0.95 in cycles 1, 2 and 3. The middle panel shows the example of phase ~ 0.15 in cycles 2 and 3. The bottom panel shows the example of phase ~ 0.32 of cycles 1 and 2.

Table 7.2: Best-fitting model parameters for each epoch of S Ori observations

Epoch	$\Phi_{\rm vis}$	Model	$\Phi_{\rm mod}$	τ_V (Al_2O_3)	$R_{\rm in}/R_{\rm Phot}$ (Al_2O_3)	p (Al_2O_3)	$\Theta_{\rm Phot}$ [mas]
A	0.40	M24n	0.40	2.5	2.0	2.4	8.5
B	1.89	M22	0.25	1.0	1.8	3.3	10.0
C	1.95	M21n	0.10	1.4	2.3	3.7	8.8
D	2.01	M21n	0.10	1.5	2.4	3.0	8.9
E	2.10	M22	0.25	1.4	1.8	3.0	10.5
F	2.16	M23n	0.30	1.1	2.2	3.6	10.1
G	2.22	M23n	0.30	1.2	1.8	2.7	10.1
H	2.29	M25n	0.50	1.2	1.8	2.5	8.5
I	2.91	M22	0.25	1.4	1.7	3.0	10.2
J	3.00	M22	0.25	1.2	1.8	2.5	11.1
K	3.13	M25n	0.50	2.4	1.5	3.0	9.0
L	3.19	M23n	0.30	1.8	2.2	2.5	10.9
M	3.82	M22	0.25	1.4	1.7	2.9	10.8
N	3.96	M25n	0.50	1.5	2.1	2.5	8.7

Table 7.3: Average model parameters for all epochs of S Ori observations

Model	τ_V (Al_2O_3)	τ_V (silicate)	$R_{\rm in}/R_{\rm Phot}$ (Al_2O_3)	p (Al_2O_3)	$\Theta_{\rm Phot}$ [mas]
M22	1.5 ± 0.5	0.0	1.9 ± 0.3	2.9 ± 0.4	9.7 ± 1.0

As well as for RR Aql we used ten models covering one complete cycle of the M series: M16n (model visual phase $\Phi_{\rm model}$=0.60), M18 (0.75), M18n (0.84), M19n (0.90), M20 (0.05), M21n (0.10), M22 (0.25), M23n (0.30), M24n (0.40), and M25n (0.50). The M models were complemented with six parameters describing the circumstellar dust shell: the optical depths τ_V (Al_2O_3) and τ_V(silicate), the inner boundary radii $R_{\rm in}/R_{\rm Phot}$ (Al_2O_3) and $R_{\rm in}/R_{\rm Phot}$ (silicate), and the density gradients $p_{\rm A}$ (Al_2O_3) and $p_{\rm B}$ (silicate).

S Ori do not exhibit any prominent silicate feature. This indicates that the surrounding dust shell do not include silicate as a main component (see Fig. 7.3 and Sect. 7.3). Lorenz-Martins & Pompeia (2000) suggest that the dust chemistry of S Ori contains only Al_2O_3 grains. However, for modeling we used both dust species Al_2O_3 grains (Begemann et al., 1997; Koike et al., 1995) and silicates grains (Ossenkopf et al., 1992). The grain size was again set to 0.1 μm for all grains.

We computed a grid of models including all combinations of optical depths τ_V (Al_2O_3) = 1.0, 1.5, 1.8, 2.1, 2.4, 2.7, 3.0; τ_V (silicate) = 0.0, 0.2, 0.5, 0.8, 1.0; $R_{\rm in}/R_{\rm Phot}$ (Al_2O_3) = 1.5, 2.0, 2.5, 3.0; $R_{\rm in}/R_{\rm Phot}$ (silicate) = 2.5, 3.5, 4.5, 5.5, 6.5; $p_{\rm A}$ (Al_2O_3) = 2.0, 2.5, 3.0, 3.5; and $p_{\rm B}$ (silicate) = 2.0, 2.5, 3.0, 3.5. The angular diameter $\Theta_{\rm Phot}$ was the only free parameter. The selection of the probed parameters is based on Wittkowski et al. (2007).

We remind that we weighted down the part of the photometric spectra around 9.5 μm, which is strongly affected by telluric absorption. The weight of all other data points was given by the corresponding uncertainty. Selection of the best fitting models follow the same way as in the previous chapter (4.1 Section 5.3.4).

7.3.4 MIDI model results

We found the best-fitting model parameters for all 14 epochs separately. For each epoch we found the phase of the dust-free dynamical model atmosphere represented by the M model and the set of dust parameters of the radiative transfer model (Sect. 7.3.3).

We have investigated dust shells including Al_2O_3 and/or silicate shells with different inner radii and density gradients. The best fit results were obtained with a Al_2O_3 shell without a contribution of silicate in the dust shell. Our result is consistent with previous investigations of Wittkowski et al. (2007) and Lorenz-Martins & Pompeia (2000). The best fitting parameters for each epoch are listed in Tab. 7.2. The table lists the epoch, the phase at the epoch, the optical depth τ_V, the inner boundary radius $R_{\rm in}/R_{\rm Phot}$, the density distribution p, and the continuum photospheric angular diameter $\Theta_{\rm Phot}$. Since the best fitting models are without any contribution of silicates the Table list only parameters of Al_2O_3 dust shell.

The agreement between the models and the observed data is in general very good. Figure 7.6 shows the example of epoch B, and includes the model flux and model visibility compared to the observed values. All the observational epochs can be find in appendix (Figs. D.1– D.7). The observations of S Ori show a partially resolved stellar disk including atmospheric molecular layers that are optically thick at the wavelength range 8–13 μm. The disk is surrounded by a spatially resolved, optically thin dust shell. Beyond 9 μm spatially resolved, optically thin radiation from the dust shell starts to take more important part of the total intensity, and together with extinction of the stellar light by the dust shell, spatially resolved radiation from the dust shell overtake the measured intensity at the longest wavelengths ($\sim$ 12–13 μm).

The shape of both the visibility and the photometry spectra of S Ori can be very well reproduced by the combination of the radiative transfer model describing the circumstellar dust shell were the central source is represented by the dynamical model atmospheres.

In the selection process we choose the best fitting model between 10 models with lowest χ^2. Among these models we selected the best model for each epoch. It should be mentioned that in the final selection of the best model and the dust shell parameters there are a few models that fir equally well. Figure 7.11 shows an example of two models describing the data well. Model M18 describe the atmosphere where the less dust is created further from the star, and model M22 is describing the atmosphere with more dust is formed closer to the star.

Note, that most of the model phases are shifted ahead towards the visual phases of our observations. It has been shown that the mid-infrared flux might still increase well beyond the visual maximum Wittkowski et al. (2007).

Models parameters determined in the way described above, do not indicate any significant dependence of the dust formation on phase or cycle. However, it should be note, that our phase coverage is mainly limited to the pre-maximum and post-maximum pulsation phases, and therefore we cannot confirm or deny an eventual phase-dependence of the dust formation process that effects the 8–13 μm visibility and photometry values over the full pulsation cycle. Table 7.3 lists the average dust shell parameters for our different epochs. Figure 7.12 shows the model simulating the average parameters for our average pulsation phase of $\overline{\Phi_V} = 0.00 \pm 0.33$. The average M model cannot be determined since almost every epoch is represented by different M model. For general interpretation of S Ori data we chose model M22. The results show that a dust shell consisting only of Al_2O_3 without the addition of silicate, corresponds the best with our S Ori data. This result is in agreement with previous study by Wittkowski et al. (2007) and Lorenz-Martins & Pompeia (2000).

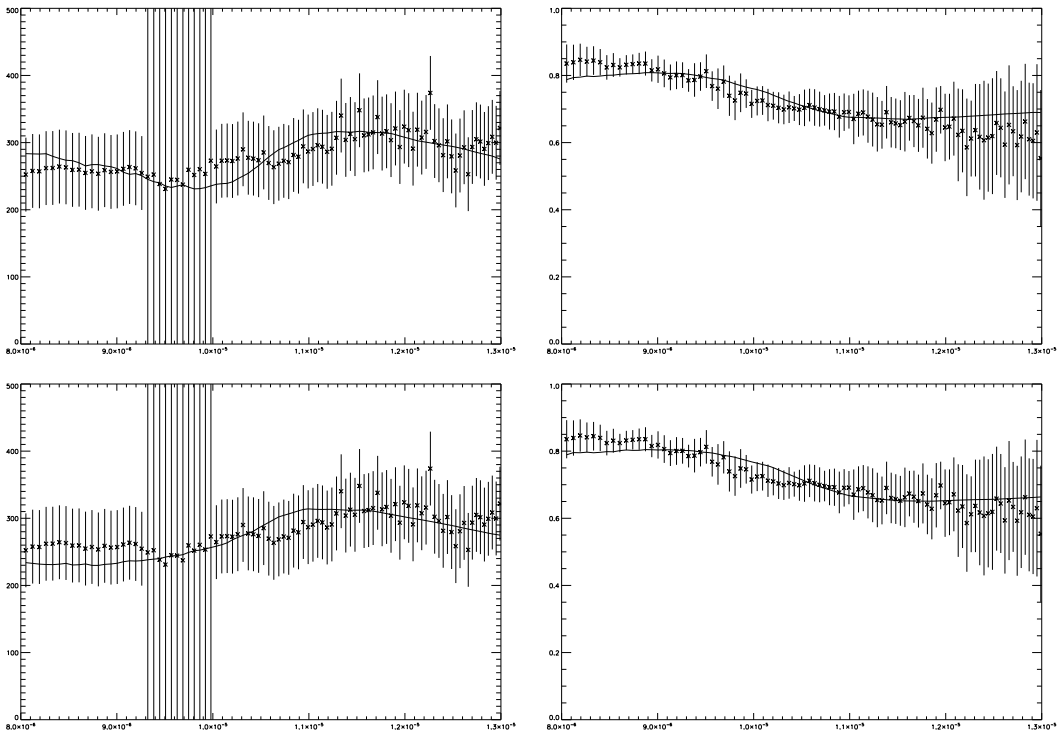

Figure 7.11: Comparison of two different models describing the same data (01/04/2008). The top panel shows model M18 ($\Phi_{\rm model} = 0.75$) with dust shell parameters tva 1.6, tvb 0.0, ra 2.6, and pa 2.5. The bottom panel shows model M22 ($\Phi_{\rm model} = 0.25$) with dust shell parameters tva 2.4, tvb 0.0. ra 2.0, and pa 2.5. The pulsation phase of the observations ($\Phi_{\rm obs} = 3.19$), the projected baseline length is 26 m, and position angle 72 deg.

Figure 7.13 shows the simulation of the full SED in the range of 0.3–100 μm including the model with the average parameters.

The average optical depth of the Al_2O_3 dust is $\tau_V(Al_2O_3)$=1.5±0.5 at $\lambda = 0.55\,\mu$m (corresponding to 0.04 at $\lambda = 8\,\mu$m, 0.29 at $\lambda = 12\,\mu$m, and a maximum within 8–12 μm of 0.30 at $\lambda = 11.8\,\mu$m). The inner radius of the dust shell is $R_{\rm in} = 1.9\pm0.3\,R_{\rm Phot}$, and the power-law index of the density distribution is $p = 2.9\pm0.4$. The average photospheric angular diameter results in $\Theta_{\rm Phot} = 9.7\pm1.0$ mas. This value corresponds to the K-band ($\lambda = 2.2\,\mu$m, $\Delta\lambda = 0.4\,\mu$m) values of UD diameter $\Theta_{\rm UD}$ between 9.6 mas and 10.5 mas measured by van Belle et al. (1996), Millan-Gabet et al. (2005), and Boboltz & Wittkowski (2005). Our average photospheric angular diameter derived from observations mostly obtained at pre-maximum and post-maximum pulsation phases ($\Phi_{\rm vis} = 0.90$–1.20) also corresponds well to the diameters derived from the previous S Ori interferometric observations (Wittkowski et al., 2007) of 9.0 mas ($\Phi_{\rm V}$=0.42), 7.92 mas ($\Phi_{\rm V}$=0.55), 9.66 mas ($\Phi_{\rm V}$=1.16), and 9.48 mas ($\Phi_{\rm V}$=1.27).

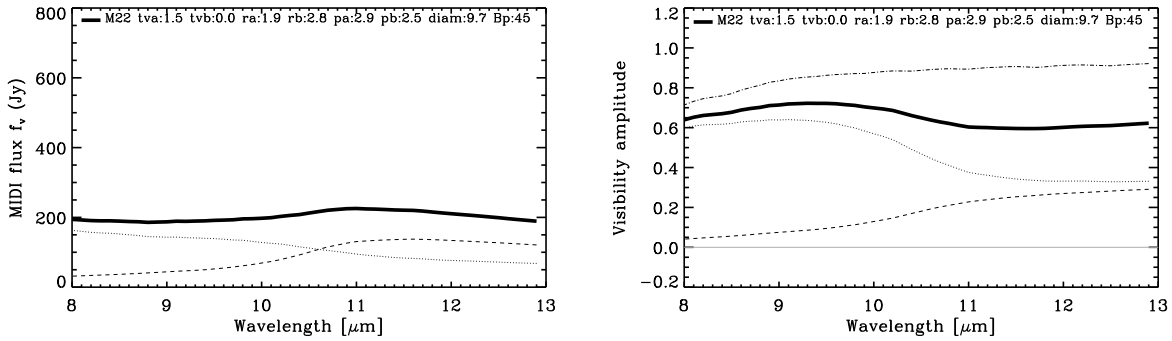

Figure 7.12: Model with average dust shell parameters for different epochs of our S Ori observations (Table 7.3).

7.4 Summary, Conclusions and Discussion

We have observed the oxygen-rich Mira variable S Ori with the VLTI/MIDI instrument in order to investigate the circumstellar dust shell and characteristics of the atmosphere including the continuum photosphere and overlying molecular layers. We obtained a total of 48 observations which were combined into 14 epochs covering 5 pulsation cycles between Feb 16, 2006 and Mar 14, 2009. We monitored the photometry and visibility spectra covering mostly pre-maximum and post-maximum pulsation phases ($\Phi_{\rm vis} = 0.90$–1.20).

We have modeled the observed data with an ad-hoc radiative transfer model of the dust shell using the radiative transfer code mcsim_mpi by Ohnaka et al. (2006). We used a series of dust-free dynamic model atmospheres based on self-excited pulsation models (M series, Ireland et al., 2004b,a) to describe the intensity profile of the central source. This study represents a continuation of the previous study by Wittkowski et al. (2007) of comparison between interferometric observations of S Ori and theoretical models over different pulsation phases covering several cycles.

Our MIDI observational results of S Ori are as follows: (i) The interferometric data covering mostly pre-maximum and post-maximum pulsation phases ($\Phi_{\rm vis} = 0.90$–1.20) do not show evidence for intra-cycle visibility variations. (ii) The data do not show evidence for cycle-to-cycle visibility variations. (iii) The 8–13 μm flux exhibits large spread and do not allow us to confirm or deny photometry variations in the examined range of phases. This results needed to be confirmed by higher accuracy follow-up observations using a dedicated photometric instrument, such as VISIR at the VLT.

Summarizing, the data do not show visibility variations, however, due to the limited phase coverage possible variations over the whole pulsation cycle can not be excluded.

We conclude, that the radiative transfer model with the dust-free dynamic model atmosphere representing the central source can well reproduce the shape and features of the observed photometry and visibility spectra of S Ori, as well as the SED at 1–40 μm. The observational results can be well explained by simulations with variations of dust shell parameters and dynamic model atmospheres. For our analysis, we have considered Al_2O_3 (Begemann et al., 1997; Koike et al., 1995) and silicate (Ossenkopf et al., 1992) dust species, following the work by Lorenz-Martins & Pompeia (2000), and have used fixed grain sizes of 0.1 μm. We showed that a model including only an Al_2O_3 dust shell can well reproduce the observed S Ori visibility and flux spectrum at 8–13 μm. The addition of a silicate dust shell with comparable low optical depth did not improve

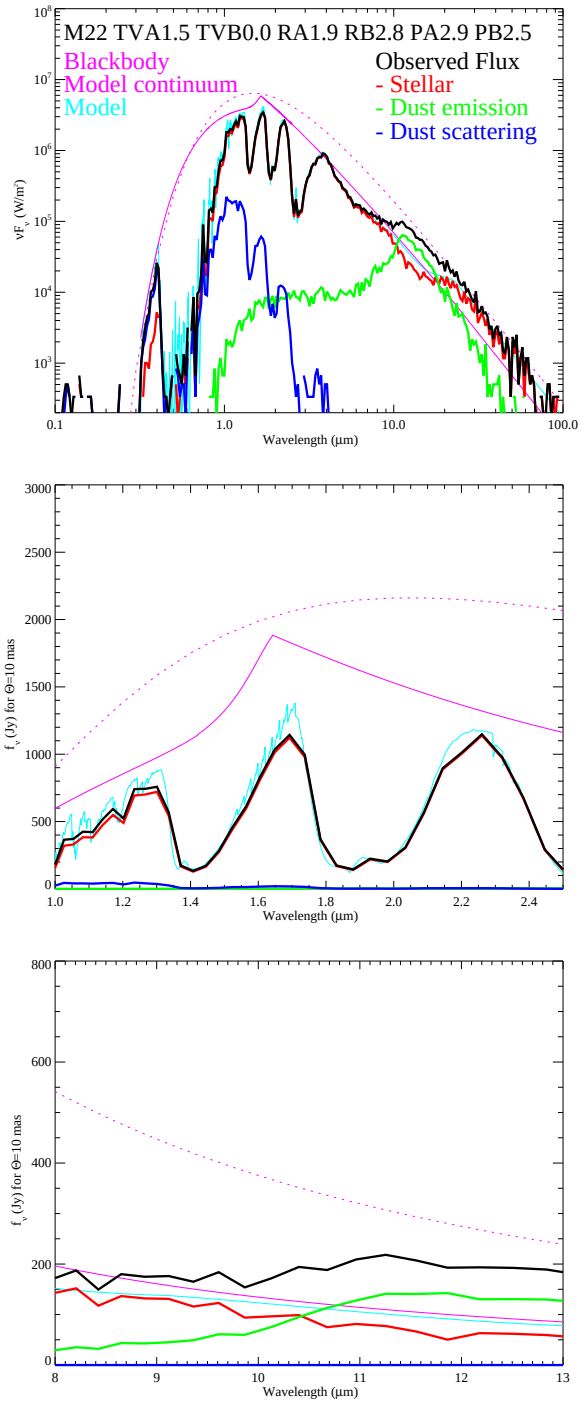

Figure 7.13: The top panel shows the full SED in the range of 0.3–100 μm, the middle panel shows the SED in the range 1–2.4 μm, and the bottom panel shows the SED in the range of 8–13 μm. The pink solid line represents model continuum, the pink dashed line describes the black-body, the black line - the model with the average dust shell parameters describing S Ori (Tab. 7.3), the red line - the stellar contribution of the model, the green line - dust emission, the blue line - dust scattering.

the fit to our data. A description of the S Ori dust shell with Al_2O_3 grains alone is consistent with the results of Lorenz-Martins & Pompeia (2000).

Simulations using pre-maximum and post-maximum phases of the dynamic model atmosphere and different sets of dust shell parameters predict considerable visibility variations that are higher then our observed visibility uncertainties (5-20 %) only for baseline range from 45 to 80 m. Model-predicted variations of the photometry spectra are lower or within our observed photometry uncertainties (40-50 %).

The best-fitting model for our average pulsation phase of $\overline{\Phi_V} = 0.00 \pm 0.33$ includes the Al_2O_3 dust shell with an optical depth of $\tau_V(Al_2O_3)$=1.5±0.5, the inner radius of $R_{\rm in}$=1.9±0.3 $R_{\rm Phot}$, and the power-law index of the density distribution of p=2.9±0.4. The average atmosphere model of the series that is used to describe the central intensity profile is M22 ($T_{\rm model} = 2330$ K, $\Phi_{\rm model} = 0.25$), and the photospheric angular diameter is $\Theta_{\rm Phot}$=9.7±1.0 mas.

Chapter 8

MIDI Observations of GX MON (Al_2O_3 + silicate-rich dust shell)

The Mira variable GX Mon was analyzed and modeled in the same way as described in Chapter 5.

8.1 Characteristics of GX Mon

The oxygen-rich Mira variable GX Mon is not very well investigated. The light curve of GX Mon is not monitored owing to tis relatively faint V magnitude, and therefore the visual phase of GX Mon is not well known. GX Mon is a star with spectral type M9 and V magnitude 13.2 – <17.0 (Samus et al., 2004). The mean pulsation period is uncertain, estimated to P = 527.0 days. The distance toward GX Mon is as well not well known. Olivier et al. (2001) estimated a distance of 700 pc based on the period-luminosity relationship by Feast et al. (1989). Justtanont et al. (1994) derived a distance of 740 pc from modeling the CO J = 1 – 0 and 2 – 1 lines. In our study, we adopt a mean value, and estimate the uncertainty to 25%, i.e. we use d =720±185 pc. Diameter measurements of GX Mon have so far not been reported. GX Mon exhibits SiO, H_2O (Kim 2010), and OH maser emission. A mass loss rate of 5.4 10^{-7} $M_\odot$/year was estimated by Loup (1993).

8.2 VLTI/MIDI Observations and data reduction

We obtained 40 spectrally-dispersed mid-infrared interferometric observations of GX Mon with the MIDI instrument at the VLTI. The observations were obtained between Feb 16, 2006 and Apr 1, 2008. We used the PRISM as a dispersive element with a spectral resolution R = $\Delta\lambda/\lambda \sim 30$. The beams were combined mostly using the *Sci_Phot* (SP) mode (see Tab. 8.1).

Table 8.1 lists the epoch, the date, the time, the Julian Date (JD), the visual pulsation phase Φ_{vis}, the baseline configuration, the ground length of the configuration, the dispersive element, the beam combiner BC, the projected baseline length B_p, the position angle on the sky PA (deg. east of north), the DIMM seeing (at 500 nm), and the coherence time τ_0 (at 500 nm). All observations were executed in service mode using different configuration of the Auxiliary

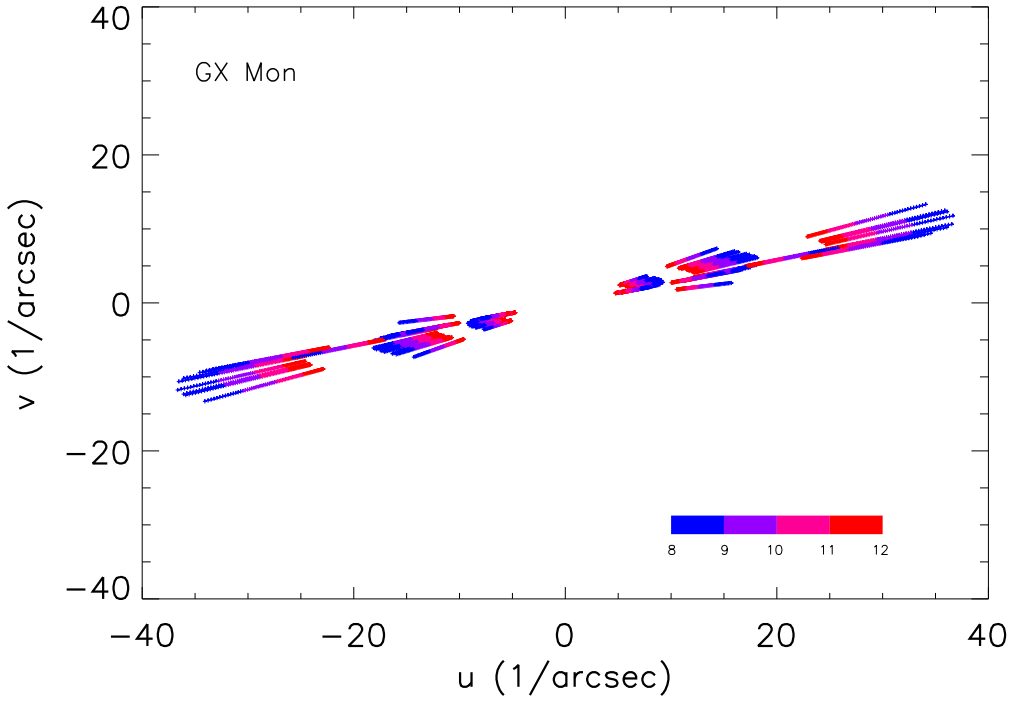

Figure 8.1: Coverage of the *uv* plane for the MIDI observations of GX Mon. Each point represents the observations with ATs over the wavelength 8 to 13 μ.

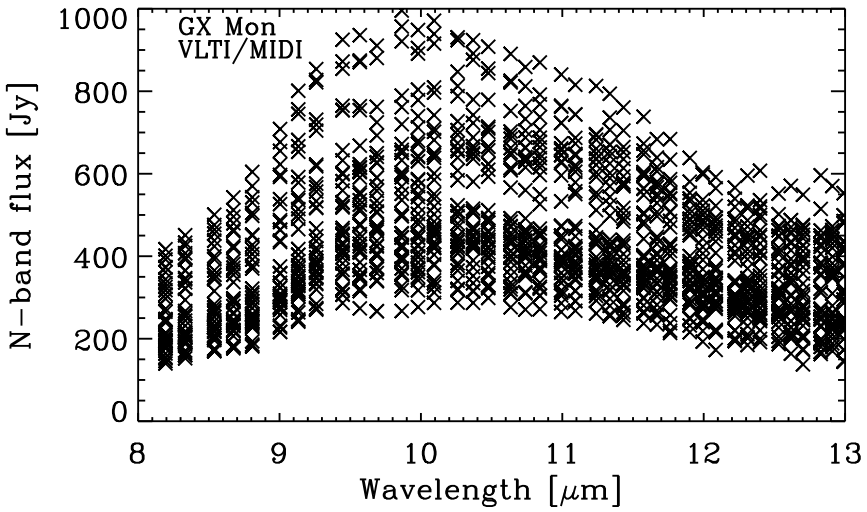

Figure 8.2: Calibrated GX Mon MIDI flux spectra as a function of wavelength. For clarity, the error bars are omitted in the plot.

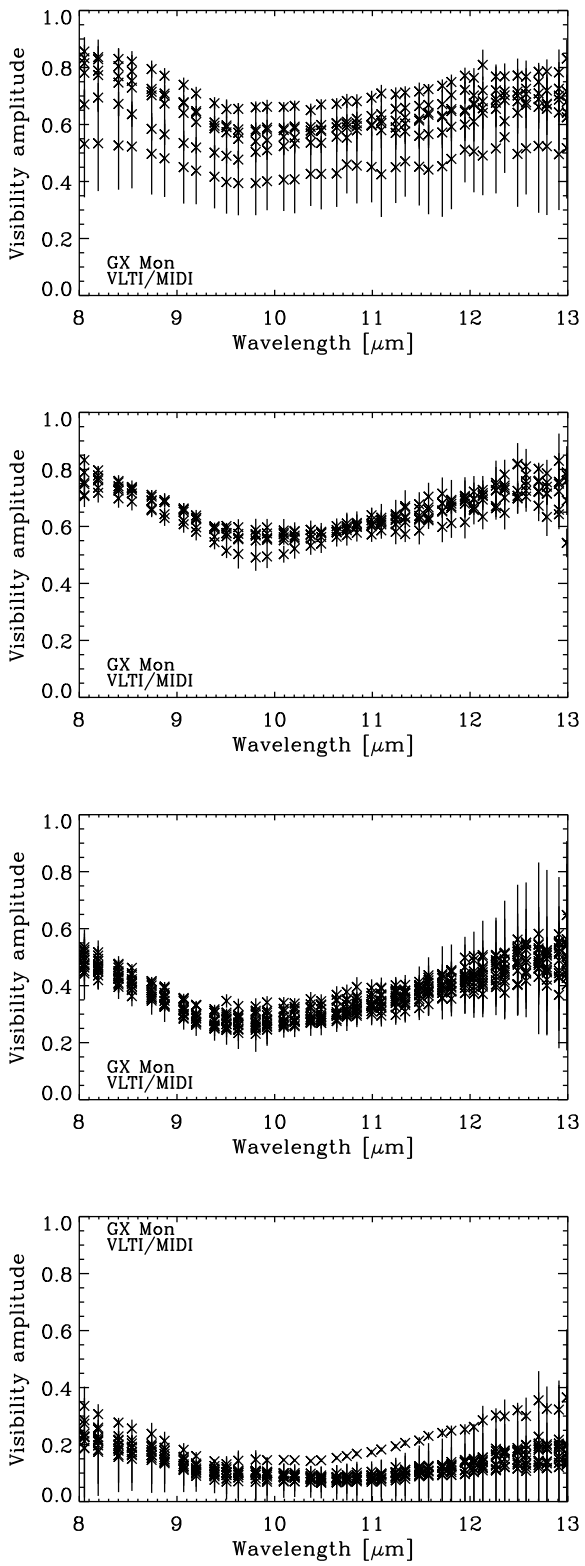

Figure 8.3: Calibrated GX Mon MIDI visibility amplitudes as a function of wavelength. (top left) Observations executed at projected baselines (pb) < 20 m, (top right) 20 m $<$ pb $<$ 35 m, (bottom left) 35 m $<$ pb $<$ 50 m, and (bottom right) pb > 50 m.

Telescopes (ATs, 1.8m). The Figure 8.1 represents the *uv* coverage of our MIDI observations of GX Mon.

The MIDI data were merged into 12 epochs, with a maximum time-lag between individual observations of 11 days (∼2% of the pulsation period). For technical problems we had to eliminate 5 observations. Since the light-curve of GX Mon is not currently documented we indicated our first observation to the 0.0 phase in order to compare the observations within the pulsation cycle.

As in previous section for S Ori we applied the same data reduction and calibration methods. Our main calibrators were Sirius (P80), HD25025 (P76/78), and HD 50778 (P74). For more details see Section 5.2. Table B.3 lists calibrator stars observed per specific night including those calibrators observed by other programs.

8.3 MIDI results

We observed GX Mon over different (however uncertain phases) of stellar pulsation. We as well monitored the mid-infrared photometry and visibility spectra as a function of phase. The analysis of the data and investigation of their variability is following the same way as in Sections 5.3.1 and 5.3.2.

Figure 8.2 shows all obtained calibrated photometry spectra as a function of wavelength. The MIDI flux measurements show a consistent shape which exhibits an increase of the flux from ∼100–400 Jy at 8 μm to a maximum near 9.8 μm of ∼300–1000 Jy, and a decrease towards 13 μm, where the flux values reach values of ∼100–500 Jy. The level of the flux spectrum differs for individual measurements with a spread of ∼ 500–600 Jy. The photometry spectra are very similar with the photometry spectra of RR Aql.

Figure 8.4 shows a comparison of the mean of our MIDI flux measurements to measurements obtained with the IRAS instrument. The shape of the flux curve is well consistent among the MIDI and IRAS measurements. The level of the IRAS flux is within the range of our MIDI measurements. Figure 8.4 also includes a model description of our MIDI data, which will be explained below in Sect. 8.3.4.

Figure 8.3 shows all obtained calibrated visibility spectra, which are combined into four groups of different projected baseline lengths (pb) of pb $<$ 15 m, 15 m $<$ pb $<$ 25 m, 25 m $<$ pb $<$ 35 m, and pb $>$ 35 m. The shape of the visibility spectra is also very similar to the shape of the visibility spectra of RR Aql. The visibility curves show a significant wavelength dependence with a steep decrease from 8 μm to ∼ 9.5 μm, and a slow increase in the 9.5 μm to 13 μm range. The shape and absolute scale of the visibility function, as well as for RR Aql, depends on the length of the projected baseline, where observations at longer baselines result in lower and flatter curves.

Figure 8.3 shows for the example of epoch E the flux, the visibility amplitude, the corresponding UD diameter, and the corresponding Gaussian FWHM diameter as a function of wavelength. The shape of the UD diameter and Gaussian FWHM functions show a steep increase from 8 μm to ∼ 9.5 μm by a factor of 1.5. A plateau appears between ∼ 9.5 μm and 11.5 μm, and the values stay nearly constant from ∼ 11.5 μm to 13 μm.

The shape of the flux spectra between 8–13 μm displays a maximum near 9.8 μm. The visibility curves show a drop in the visibility function between 8 μm and 9.5 μm with a corresponding increase of the UD diameter and Gaussian FWHM. These features indicate a presence of the silicate dust in the surrounding shell (e.g. Little-Marenin & Little, 1990; Lorenz-Martins & Pompeia, 2000; Driebe et al., 2008; Ohnaka et al., 2008).

Table 8.1: VLTI/MIDI observation of GX Mon.

Epoch	DDMMYYYY	Time [UTC]	JD	Φ_{vis}	Config.	B	Disp. Elem.	BC	B_p [m]	PA [deg]	Seeing [″]	τ_0 [msec]
A	16022006	04:39	2453783	'0.00'	E0-G0		Prism	SP	13.99	64.87	0.70	6.6
B	18032006	01:30	2453813	'0.06'	E0-G0		Prism	HS	15.60	70.07	1.15	5.2
C	18102006	08:14	2454027	'0.46'	E0-G0		Prism	SP	13.51	74.92	0.88	2.4
C	11112006	07:59	2454051	'0.51'	H0-D0		Prism	SP	62.26	74.22	0.70	4.0
D	14122006	03:56	2454084	'0.57'	E0-G0		Prism	SP	12.15	74.51	1.10	1.6
D	14122006	06:25	2454084	'0.57'	E0-G0		Prism	SP	15.95	73.30	0.91	1.9
D	16122006	04:51	2454086	'0.57'	H0-G0		Prism	SP	28.84	74.90	1.08	2.4
D	17122006	07:11	2454087	'0.58'	H0-G0		Prism	SP	31.62	71.03	1.05	2.6
D	19122006	03:10	2454089	'0.58'	K0-G0		Prism	SP	43.80	73.80	0.58	7.9
D	20122006	05:45	2454090	'0.58'	K0-G0		Prism	SP	63.21	73.77	0.92	3.6
E	11012007	03:32	2454112	'0.62'	E0-G0		Prism	SP	15.05	74.68	1.14	3.3
E	11012007	05:23	2454112	'0.62'	E0-G0		Prism	SP	15.90	71.48	0.99	4.1
E	13012007	03:45	2454114	'0.63'	E0-G0		Prism	SP	15.46	74.35	0.70	5.9
E	18012007	03:34	2454119	'0.64'	H0-G0		Prism	SP	31.18	74.18	0.93	2.6
E	18012007	05:14	2454119	'0.64'	H0-G0		Prism	SP	31.44	70.61	1.02	2.3
E	19012007	02:31	2454120	'0.64'	H0-G0		Prism	SP	28.49	74.94	0.66	3.5
E	19012007	04:53	2454120	'0.64'	H0-G0		Prism	SP	31.77	71.44	1.39	1.7
E	21012007	02:46	2454122	'0.64'	H0-D0		Prism	SP	59.49	74.76	0.83	4.1
F	09022007	01:04	2454141	'0.68'	H0-G0		Prism	SP	28.22	74.95	1.04	2.4
F	09022007	04:18	2454141	'0.68'	H0-G0		Prism	SP	30.47	68.83	0.69	3.8
F	10022007	01:16	2454142	'0.68'	H0-D0		Prism	SP	58.35	74.87	0.78	4.4
F	10022007	03:09	2454142	'0.68'	H0-D0		Prism	SP	63.93	72.19	1.18	3.1
F	11022007	00:54	2454143	'0.68'	E0-G0		Prism	SP	14.06	74.93	0.77	5.1
F	11022007	02:36	2454143	'0.68'	E0-G0		Prism	SP	15.96	73.21	0.96	6.6
F	12022007	01:27	2454144	'0.68'	H0-G0		Prism	SP	30.10	74.68	0.79	4.6
G	10122007	03:50	2454445	'1.26'	H0-D0		Prism	SP	44.49	73.93	1.92	1.4
H	29122007	03:57	2454464	'1.29'	H0-D0		Prism	SP	57.28	74.92	0.78	3.2
H	10012008	02:52	2454476	'1.31'	E0-G0		Prism	SP	13.78	74.93	0.92	4.8
H	11012008	02:24	2454477	'1.32'	H0-G0		Prism	SP	25.72	74.80	0.59	7.7
H	12012008	02:40	2454478	'1.32'	E0-G0		Prism	SP	13.62	74.92	0.80	7.7
H	13012008	07:10	2454479	'1.32'	H0-G0		Prism	SP	26.45	80.27	0.60	8.3
I	22022008	02:46	2454519	'1.40'	H0-D0		Prism	SP	63.35	71.14	1.29	2.2
J	06032008	02:02	2454532	'1.42'	H0-D0		Prism	SP	63.09	70.83	0.87	3.8
J	06032008	02:39	2454532	'1.42'	H0-D0		Prism	SP	60.75	68.66	1.09	3.0
J	13032008	02:32	2454539	'1.43'	H0-G0		Prism	SP	29.45	67.21	0.96	5.3
J	14032008	02:50	2454540	'1.44'	E0-G0		Prism	SP	14.12	65.29	0.63	7.3
K	28032008	01:16	2454554	'1.46'	E0-G0		Prism	SP	15.12	68.41	1.16	2.3
K	01042008	00:43	2454558	'1.47'	H0-G0		Prism	SP	30.87	69.51	0.69	2.8
K	01042008	01:26	2454558	'1.47'	H0-G0		Prism	SP	28.96	66.45	0.92	2.1
K	01042008	02:03	2454558	'1.47'	H0-G0		Prism	SP	26.71	62.90	0.82	2.3

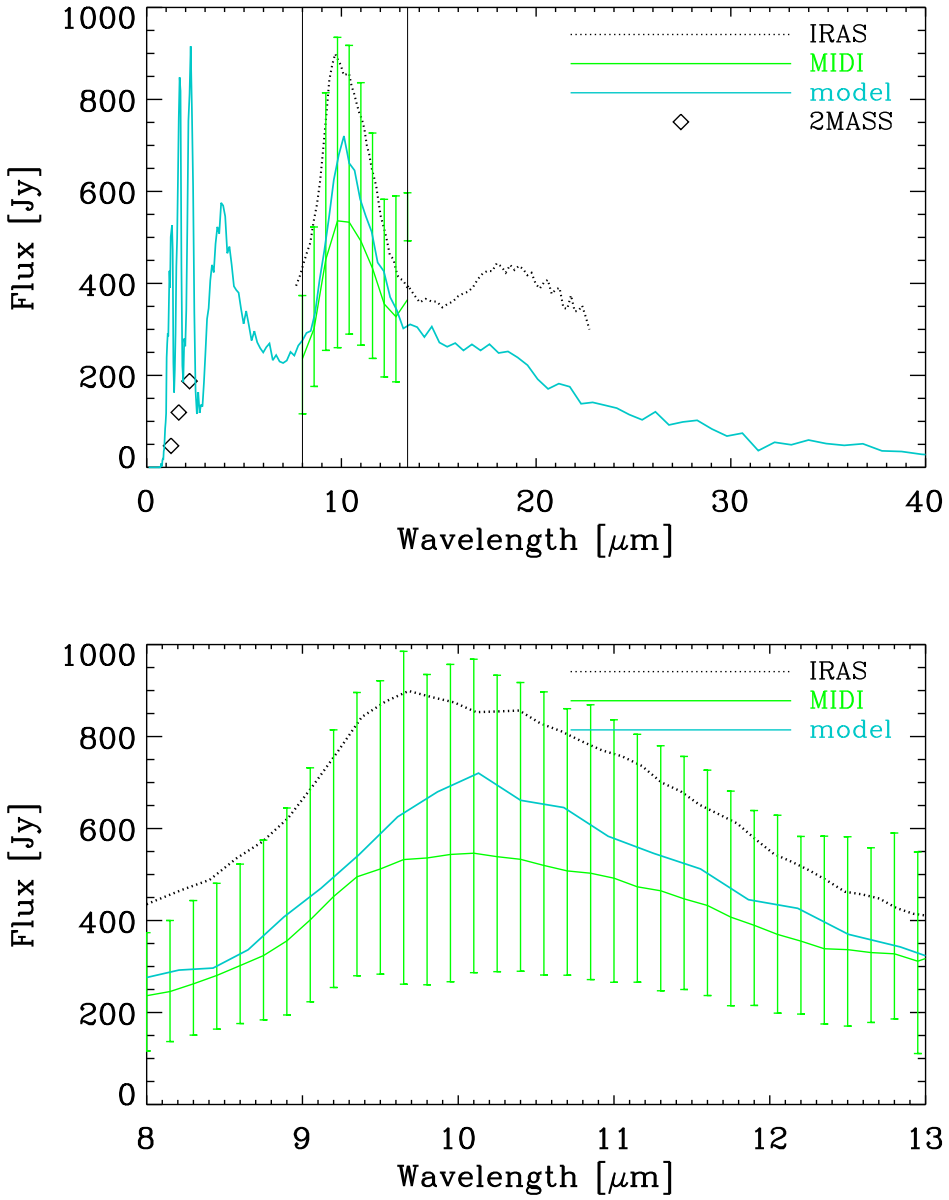

Figure 8.4: GX Mon flux spectrum as a function of wavelength from 2.4 μm to 40 μm (top). The lines represents the flux spectra from IRAS-LRS observations covering wavelengths from $\sim$ 7.7 μm to $\sim$ 23 μm (dotted thin black like), and the mean of our N-band MIDI measurements (solid thin green line). Here, the vertical bars span the maximum and minimum values measured. The diamond symbols denote 2MASS measurements at 1.25 μm, 1.65 μm, and 2.2 μm. The solid blue line indicates our atmosphere and dust shell model as explained in Sect. 8.3.4. The bottom plot shows an enlarged segment of the plot in the MIDI wavelength range of 8–13 μm.

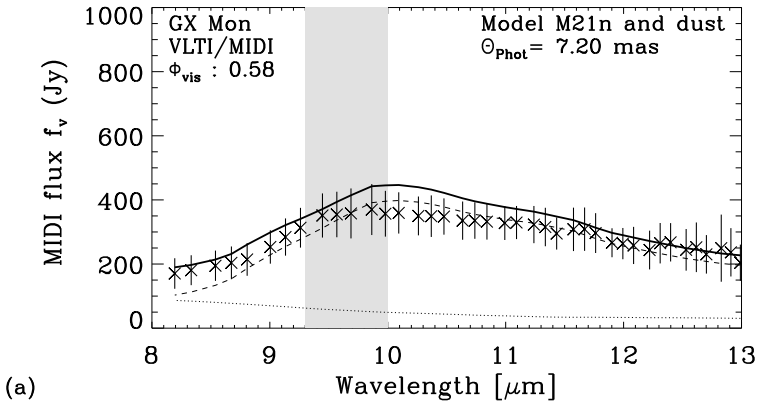
GX Mon
VLTI/MIDI
Φvis : 0.58
Model M21n and dust
ΘPhot= 7.20 mas
MIDI flux fν (Jy)
Wavelength [μm]

(a)

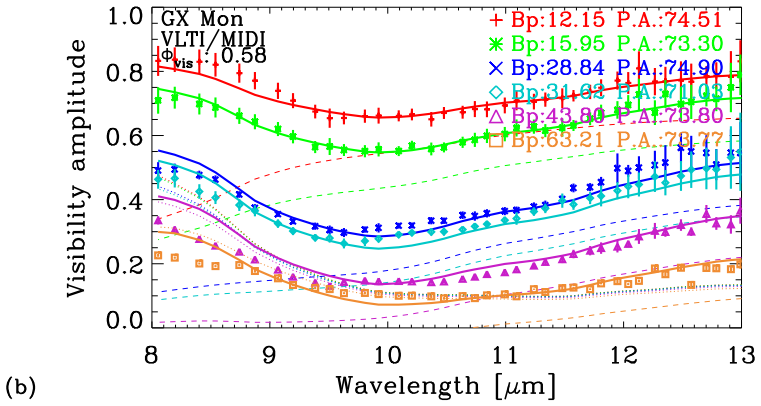
GX Mon
VLTI/MIDI
Φvis : 0.58
+ Bp:12.15 P.A.:74.51
✳ Bp:15.95 P.A.:73.30
× Bp:28.84 P.A.:74.90
◇ Bp:31.62 P.A.:71.03
△ Bp:43.80 P.A.:73.80
□ Bp:63.21 P.A.:73.77
Visibility amplitude
Wavelength [μm]

(b)

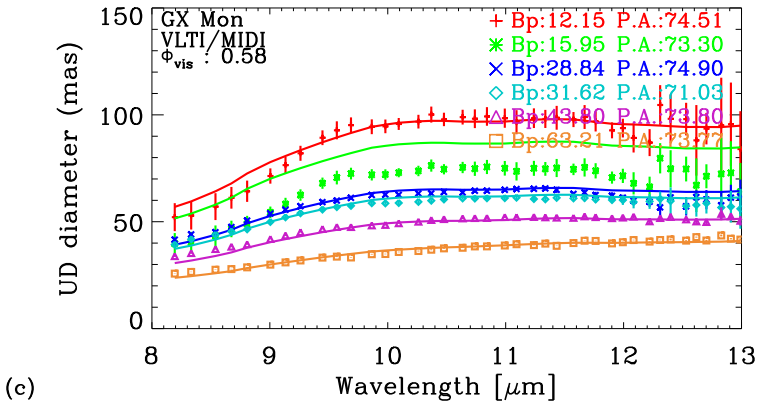
GX Mon
VLTI/MIDI
Φvis : 0.58
+ Bp:12.15 P.A.:74.51
✳ Bp:15.95 P.A.:73.30
× Bp:28.84 P.A.:74.90
◇ Bp:31.62 P.A.:71.03
△ Bp:43.80 P.A.:73.80
□ Bp:63.21 P.A.:73.77
UD diameter (mas)
Wavelength [μm]

(c)

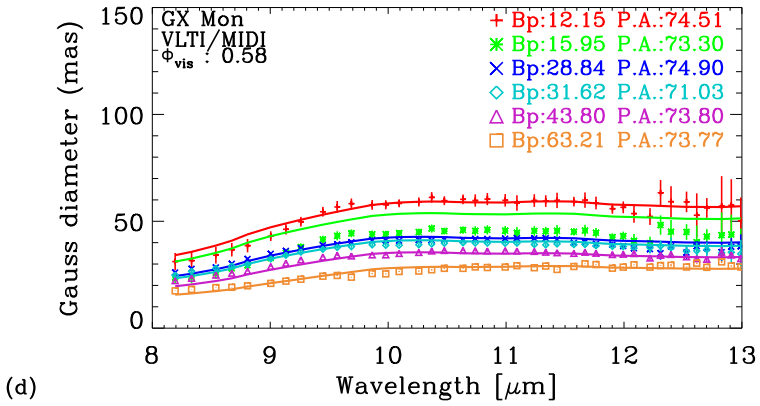

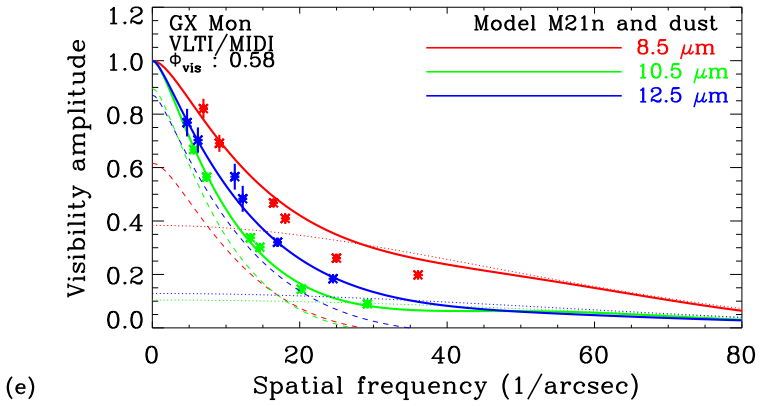

Figure 8.5: VLTI/MIDI interferometry at 8-13μm of GX Mon for the example of epoch E. The panels show (a) the flux, (b) the visibility amplitude, (c) the corresponding UD diameter, (d) the corresponding Gaussian FWHM diameter as a function of wavelength. The gray shade indicates the wavelength region around 9.5 μm that is affected by atmospheric absorption. Panel (e) shows the visibility amplitude as a function of spatial frequency for three averaged bandpasses of 8-9 μm, 10-11 μm, and 12-13 μm. The crosses with error bars denote the measured values. The solid lines indicate our best-fitting model, as described in Sect. 8.3.4. The model consists of a radiative transfer model describing the surrounding dust shell where the central star is represented by a dust-free dynamic model atmosphere. The contributions of the stellar and dust components alone are indicated by the dotted and the dashed line, respectively.

As previously mentioned, since the light-curve of GX Mon is not know, we set the phase 0.0 to our first observation. Therefore, assign phases are used only for relative comparison between observations in the pulsation cycle(s). In the following sections the phases are indicated between quotes as 'phase'.

8.3.1 Visibility monitoring

With the pulsation period P=527 days our MIDI data on GX Mon cover 2 pulsation cycles.

As well as in Section 5.3.1 we combined individual observations into groups of similar pulsation phases ($\Phi_{\rm vis} \pm 0.15$), projected baseline lengths (pb $\pm$ 10 %), and position angles (PA $\pm$ 10 %). The data within each group were as well as for the previous stars averaged, and the uncertainty of the averaged visibility curves was estimated as the standard deviation of the averaged visibilities.

Intra-cycle visibility monitoring

Figure 8.6 shows two examples of calibrated visibility curves within the same cycle (see Section 8.3.1). The top panel shows an example of observations within the 0 pulsation cycle at phases 0.54, and 0.68 obtained with pb $\sim$ 62 m and PA $\sim$ 73°. The bottom panel shows an example of observations at phases 0.57, and 0.68 obtained with pb $\sim$ 30 m and PA $\sim$ 72°. The data do not exhibit any evidence for intra-cycle visibility variations (compare to Sections 5.3.1 and 7.3.1).

Cycle-to-cycle visibility monitoring

We investigated cycle-to-cycle visibility variations. Figure 8.7 shows three of these examples computed in the same way as in Section 5.3.1. The top panel shows phases of '1.45', and '0.46' in two consecutive cycles obtained with a projected baseline length of $\sim$ 14 m and PA $\sim$ 70°, the middle panel shows phases '0.54', and '1.41' of two cycles obtained with a projected baseline length of $\sim$ 62 m, and PA $\sim$ 72°, and the bottom panel shows phases '0.57', and '1.47' of two cycles obtained with a projected baseline length of $\sim$ 29 m, and PA $\sim$ 69°. The phases in the middle panel slightly differ, but as well as in case of RR Aql and S Ori (see Sections 5.3.1 and 7.3.1) we showed that the selected phases can be well compared, since there is no evidence for intra-cycle visibility variations (see Section 8.3.1). The observations also show no significant cycle-to-cycle visibility variation within our visibility accuracies ($\sim$ 5–20%).

Deviations from circular symmetry

All our observations were obtain with position angles between 60° and 75°. Therefore, our observations do not allow us to investigate the deviation from circular symmetry of GX Mon.

Summarizing,
the GX Mon MIDI data, as well as previously investigated Mira variables RR Aql and S Ori (Sections 5.3 and 7.3), do not show an evidence of significant intra-cycle or cycle-to-cycle visibility variations within our visibility accuracies (of $\sim$ 5–20%). However, it is important to note again, that the indicated pulsation phases are only relative since they cannot be related to any visual pulsation phase. The data as well as previous targets show a good agreement of visibility data obtained at the same projected baseline lengths.

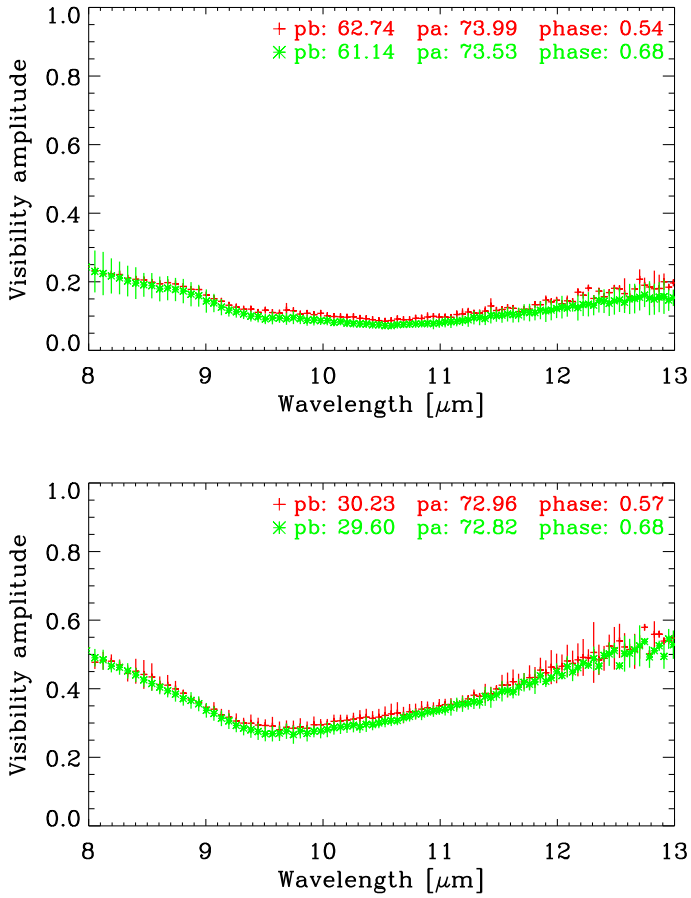

Figure 8.6: Calibrated MIDI visibility amplitudes for different pulsation phases within the same cycle to investigate intra-cycle visibility variations. Each line represents a different pulsation phase within the same cycle and is computed as an average of data obtained at the respective phase (± 0.15) and observed at similar projected baseline length (pb ± 10%) and position angle (PA ± 10%). The top panel shows the example of pulsation phases 0.54, and 0.68 of cycle 0 observed with a projected baseline length of ∼ 62 m and a position angle of ∼73 deg. The bottom panel shows the example of pulsation phases 0.57, and 0.68 of cycle 0 observed with a projected baseline length of ∼ 30 m and a position angle of ∼72 deg. The error bars are computed as the standard deviation of the averaged visibilities.

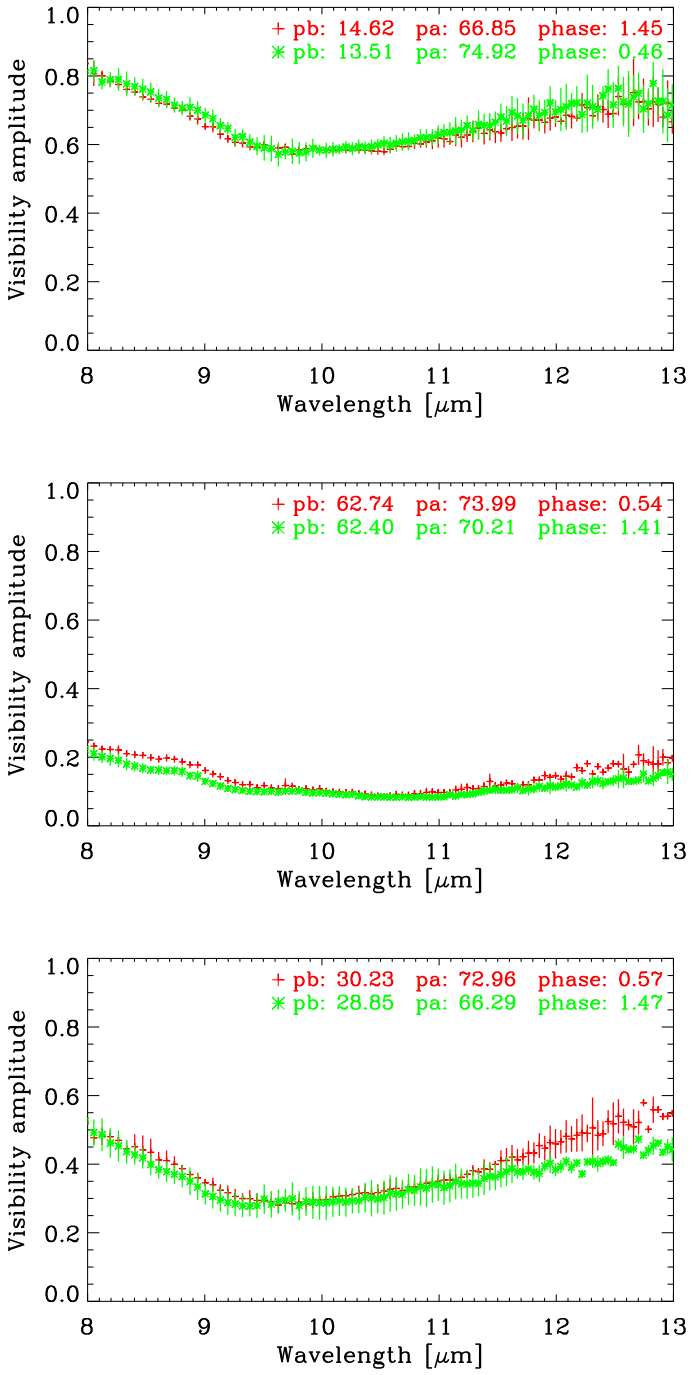

Figure 8.7: As Fig. 8.6, but for the same pulsation phase in consecutive pulsation cycles to investigate cycle-to-cycle visibility variations. The top panel shows the example of pulsation phase $\sim$ '0.45' in two consecutive cycles observed with a projected baseline length of $\sim$ 14 m and a position angle $\sim$70 deg. The bottom panel shows the example of pulsation phase '0.5' in two consecutive cycles observed with a projected baseline length of $\sim$ 62 m and a position angle $\sim$72 deg.

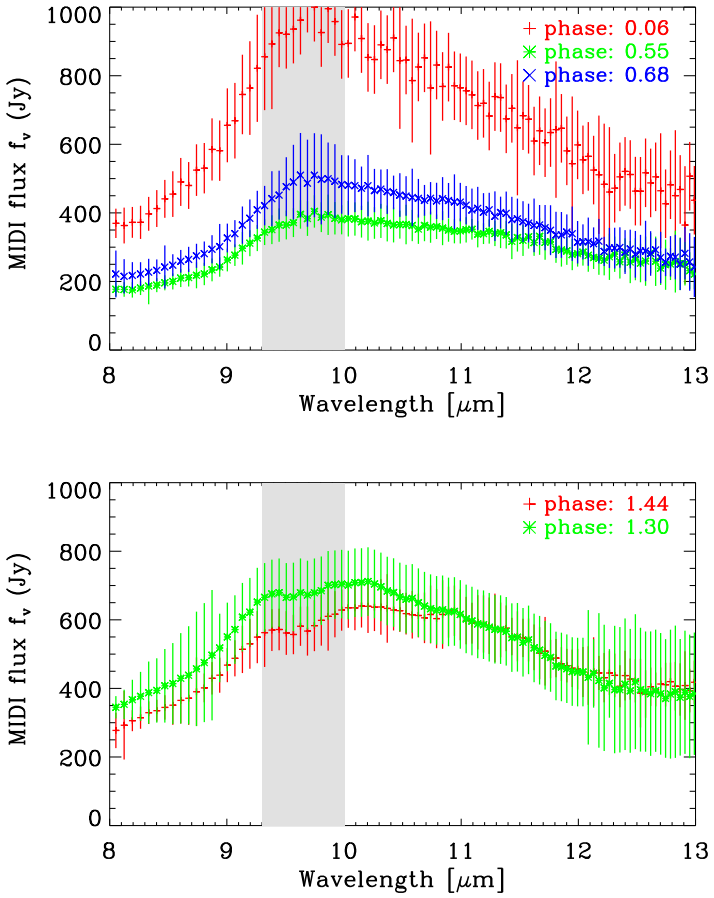

Figure 8.8: Calibrated MIDI flux spectrum for different pulsation phases within the same cycle to investigate intra-cycle photometry variations. Each line represents a different pulsation phase within the same cycle and is computed as an average of data obtained at the respective phase ($\pm$ 0.15). The top panel shows the example of pulsation phases '0.06', '0.55' and '0.68' of cycle 0. The bottom panel shows the examples of phases '1.44' and '1.30' of cycle 1. The error bars are computed as the standard deviation of the averaged photometry curves. The gray shades denote zones that are affected by atmospheric absorption.

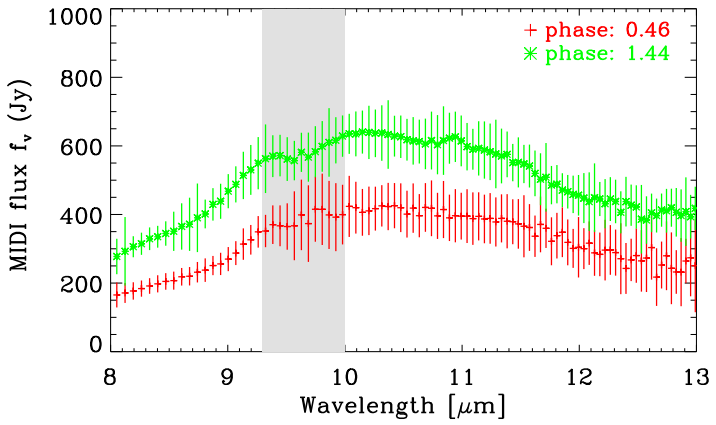

Figure 8.9: As Fig. 8.8, but for the same pulsation phase in consecutive pulsation cycles to investigate cycle-to-cycle photometry variations. The panel shows the example of phase $\sim$ '0.45' in cycles 0 and 1.

8.3.2 *N*-band flux monitoring

This Section describes the investigations of the intra-cycle and cycle-to-cycle variability of the 8–13 μm flux spectra. For detail approach of the photometry monitoring see Section 5.3.2.

Intra-cycle photometry monitoring

Figure 8.8 shows two examples of a comparison of the MIDI calibrated flux spectra at different pulsation phases of the same cycle. The top panel shows a comparison between phases '0.06', '0.55' and '0.68' of cycle 0, and the bottom panel shows a comparison between phases '1.44' and '1.30' of cycle 1. The first plot shows comparison of the largest separation in the phase that is available in our data-set. The GX Mon flux values within the N-band are larger at the post-maximum phases than at the minimum and post-minimum phases. The differences are as well as for RR Aql (Section 5.3.2) most pronounced toward the silicate emission feature around 9.8 μm, and less pronounced toward the edges of the MIDI bandpass at 8 μm and 13 μm. The differences correspond to up to 50%–55%, or about 4–5 standard deviations.

Cycle-to-cycle photometry monitoring

Figure 8.9 shows a comparison of data observed at the same phase of consecutive pulsation cycles. The panel shows a comparison between phases '0.46' and '1.44', i.e. phase '0.45' of cycles 0 and 1. The N-band flux is lower in cycle 1 compared to the same phase of the 0 cycle by up to $\sim$ 250 Jy, corresponding to about 25% or 2–3 standard deviations. The differences are also most pronounced toward the silicate emission feature at 9.8 μm. As mentioned in the Section 5.3.2 many visual light-curves show that the pulsation cycles are not perfectly symmetric in the V-band. This could imply possible variations in the N-band as well. The data might indicate an irregularity of the cycle in the N-band of GX Mon (Fig. 5.10). However, due to the lack of data point, the data do not allow us to make any reliable conclusion. In addition, the GX Mon data cannot be compare with a visual light-curve in the optical band.

Table 8.2: Best-fitting model parameters for each epoch of GX Mon observations

Ep.	$\Phi_{\rm mod}$	Model	$\Phi_{\rm mod}$	τ_V (Al_2O_3)	τ_V (sil.)	$R_{\rm in}/R_{\rm Phot}$ (Al_2O_3)	$R_{\rm in}/R_{\rm Phot}$ (sil.)	p (Al_2O_3)	p (sil.)	$\Theta_{\rm Phot}$ [mas]
A	*0.00*	M21n	0.10	1.5	3.0	2.0	4.8	3.5	2.5	9.1
B	*0.06*	M21n	0.10	1.3	3.4	1.8	4.8	3.0	2.5	10.5
C	*0.46*	M25n	0.50	1.4	3.0	2.3	4.8	3.3	2.5	7.3
D	*0.51*	M21n	0.10	2.5	3.0	2.4	4.5	3.0	2.5	7.2
E	*0.57*	M21n	0.10	1.8	3.0	2.5	4.6	2.5	2.5	7.2
F	*0.62*	M21n	0.10	1.8	3.0	2.4	4.3	3.5	2.5	7.5
G	*0.68*	M21n	0.10	1.2	3.0	1.8	4.8	2.5	2.5	7.5
H	*1.26*	M23n	0.30	2.8	4.8	1.8	4.8	2.5	2.5	10.0
I	*1.31*	M23n	0.30	3.1	3.0	1.7	4.8	2.5	2.5	10.6
J	*1.40*	M21n	0.10	2.2	3.0	1.8	4.4	2.5	2.5	9.5
K	*1.42*	M21n	0.10	1.7	3.0	2.6	4.4	2.5	2.5	8.8
L	*1.47*	M21n	0.10	2.1	2.7	2.2	4.6	2.5	2.5	8.8

Table 8.3: Average model parameters for all epochs of GX Mon observations

Model	$\Phi_{\rm mod}$	τ_V (Al_2O_3)	τ_V (silicate)	$R_{\rm in}/R_{\rm Phot}$ (Al_2O_3)	$R_{\rm in}/R_{\rm Phot}$ (silicate)	p (Al_2O_3)	p (silicate)	$\Theta_{\rm Phot}$ [mas]
M21n	0.10	1.9 ± 0.6	3.2 ± 0.5	2.1 ± 0.3	4.6 ± 0.2	2.8 ± 0.4	2.5 ± 0.0	8.7 ± 1.3

Summarizing,
our data exhibit a 4–5σ intra-cycle and 2–3σ cycle-to-cycle flux variations at wavelengths of 8–13 μm. The variations are most pronounced toward the silicate emission feature at 9.8 μm. Our averaged data indicate a flux variations in the N-band, however, for clear conclusions, further observational data would be required.

8.3.3 MIDI model parameters

The modeling approach follow the same steps as for the previous stars (for more details see Section 5.3.4 and 7.3.3).

GX Mon show a pronounced silicate feature in photometry and visibility spectra. This indicates that silicate is one of the component of the dust shell (see Fig. 8.4 and Sect. 8.3). For the modeling of the atmosphere of the Mira variable GX Mon we again used both dust species, Al_2O_3 grains (Begemann et al., 1997; Koike et al., 1995) and silicate grains (Ossenkopf et al., 1992) following the work by Lorenz-Martins & Pompeia (2000) who suggested that the dust surrounding GX Mon contains both Al_2O_3 and silicate grains, respectively. The grain size set to 0.1 μm for all grains

We computed a grid of models including six parameters describing the circumstellar dust shell. The models consists of the M series: M16n (model visual phase $\Phi_{\rm model}$=0.60), M18 (0.75), M18n (0.84), M19n (0.90), M20 (0.05), M21n (0.10), M22 (0.25), M23n (0.30), M24n (0.40), and M25n (0.50) including all combinations of optical depths τ_V (Al_2O_3) = 0.0, 0.2, 0.5, 0.8, 1.5; τ_V (silicate) = 2.5, 3.0, 3.5, 4.0, 4.5, 5.0; $R_{\rm in}/R_{\rm Phot}$ (Al_2O_3) = 2.0, 2.5, 3.0; $R_{\rm in}/R_{\rm Phot}$ (silicate) = 2.5, 3.5, 4.5, 5.5, 6.5; $p_{\rm A}$ (Al_2O_3) = 2.0, 2.5, 3.0, 3.5; and $p_{\rm B}$ (silicate) = 2.0, 2.5, 3.0, 3.5. Where

τ_V (Al_2O_3) and τ_V(silicate) are the optical depths, R_{in}/R_{Phot} (Al_2O_3) and R_{in}/R_{Phot} (silicate) the inner boundary radii, and p_A (Al_2O_3) and p_B (silicate) the density gradients. The angular diameter Θ_{Phot} was the only free parameter.

8.3.4 MIDI model results

As well as for the previous stars we found or each of the 12 epochs the best-fitting model parameters. The parameters again include, the phase of the dust-free dynamical model atmosphere, represented by the M model, and the set of the dust shell parameters of the radiative transfer model. The examined parameters are listed in Section 8.3.3.

GX Mon is classified by Lorenz-Martins & Pompeia (2000) as an oxygen-rich star that can be described with a combination of a silicate and Al_2O_3 dust shell. We have investigated dust shells including Al_2O_3 and silicate dust shells with different inner radii and density gradients. In accordance with Lorenz-Martins & Pompeia (2000) we obtained best-fit results with a combination of the silicate and Al_2O_3 dust shell.

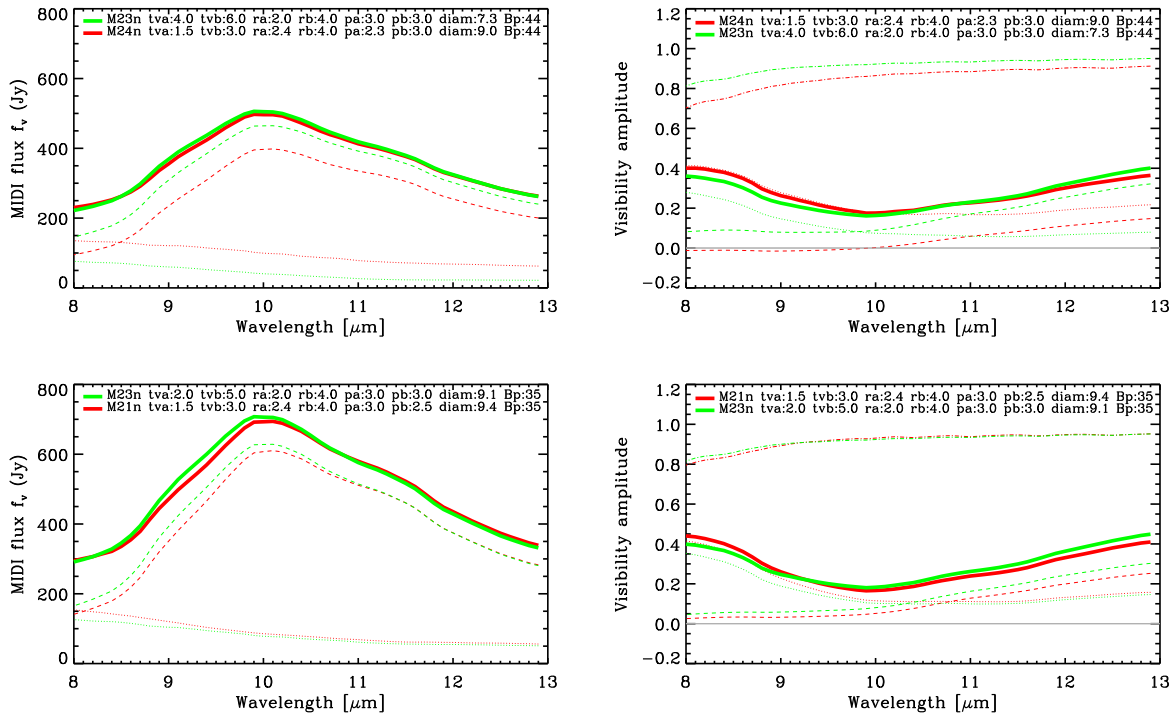

Figure 8.10: Simulation compare the same model atmospheres M23n ($\Phi_{model} = 0.30$) with two sets of dust shell parameters. The first set is describing the epoch 1 (top panel) and 2 (bottom panel) of observations by Wittkowski (private communication). The second set of dust shell parameters show parameters derived by our simulations describing the same data.

The best-fitting parameters for each epoch are listed in Table 8.2. The table lists the epoch, the phase at the epoch, the optical depth τ_V, the inner boundary radii R_{in}/R_{Phot}, the density distribution p, and the continuum photospheric angular diameter Θ_{Phot}. The best-fitting model atmosphere was most frequently M21n (Φ_{Model}=0.1).

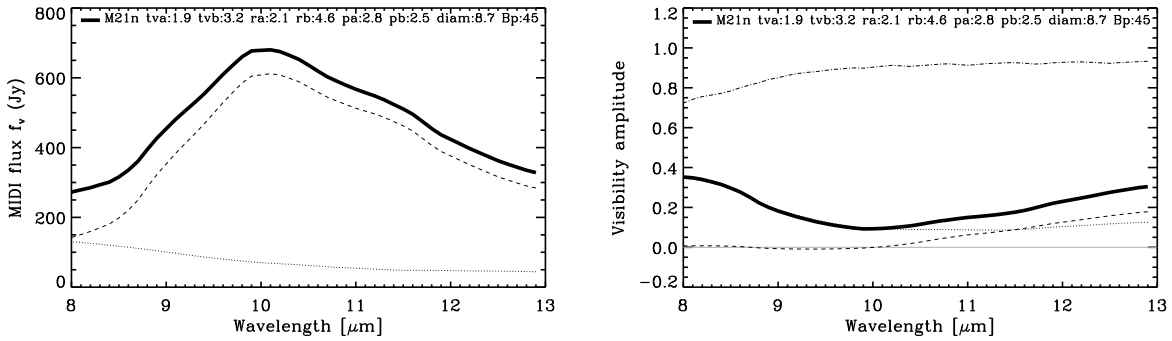

Figure 8.11: Model with average dust shell parameters for different epochs of our GX Mon observations (Table 8.3).

Figure 8.3 includes, for the example of epoch E, the model flux and model visibility compared to the observed values. All the observational epochs can be find in appendix (Figs. E.1– E.6). The agreement between the models and the observed data is as well as for the previous stars very good. The shape of the visibility and the photometry spectra is very similar to the spectra of RR Aql. In the wavelength range from 8 μm to $\sim$ 9 μm the dust is fully resolved with baselines larger than $\sim$ 45 m, and the visibility contribution of the dust reaches into the 2nd lobe of the visibility function. GX Mon is characterized as well as RR Aql by a partially resolved stellar disk including atmospheric layers, with a typical drop in the visibility function $\sim$ 10 μm, where the flux contribution of the silicate emission is highest, and the flux contribution of the star relative to the total flux decreases.

Beyond $\sim$ 10 μm, the spatially resolved radiation from the optically thin dust shell is considerable part of the observed total flux. From $\sim$ 10 μm to 13 μm the dust contribution becomes nearly constant while the stellar contribution increases, this results in an increase of the visibility function. The results show that the shape of both the visibility and the photometry spectra can be very well reproduce by the combination of the radiative transfer model describing the circumstellar dust shell and the dynamical model atmospheres representing the central source.

As already mentioned, the visual phase of GX Mon is not known, however, the mean pulsation period was estimated to P = 527.0 days (Samus et al., 2004), our data therefore cover more then a full pulsation cycle. We can conclude that the obtained model parameters for the different epochs do not indicate any significant dependence on cycle.

However, as for the AGB stars RR Aql and S Ori we cannot confirm or deny eventual phase-dependence of the dust formation process that affects the 8–13 μm visibility and photometry values by less than our uncertainties of about 5–20% and 10–50%, respectively.

Table 8.3 lists the average model parameters of our different epochs. Figure 8.11 shows the model simulating the average parameters. The dynamic model atmosphere M21n ($\Phi_{\rm model} = 0.1$) resulted for most of the epochs as the best-fitting M model. An Al_2O_3 dust shell with combination of a silicate dust shell, provides the best agreement with our data.

The average optical depth of the Al_2O_3 dust shell is $\tau_V(Al_2O_3)$=1.9±0.6, the average optical depth of the silicate dust is τ_V(silicate)=3.2±0.5 at $\lambda = 0.55\,\mu$m. The inner radius of the Al_2O_3 dust shell is $R_{\rm in}(Al_2O_3)$=2.1±0.3 $R_{\rm Phot}$, the inner radius of the silicate dust shell is $R_{\rm in}$(silicate)=4.6±0.2 $R_{\rm Phot}$and the power-law index of the density distribution is $p(Al_2O_3)$=2.8±0.4,

p(silicate)=2.5±0.0. The average photospheric angular diameter results in $\Theta_{\rm Phot}$=8.7±1.3 mas.

Figure 8.12 shows the simulation of the full SED in the range of 0.3–100 μm including the model with the average parameters.

8.4 Summary, Conclusions and Discussion

We obtained a total of 40 observations of GX Mon with the VLTI/MIDI instrument. The observations were combined into 12 epochs covering 2 pulsation cycles between Feb 16, 2006 and Apr 1, 2008. We investigated the circumstellar dust shell and characteristics of the atmosphere that consists of the continuum photosphere and overlying molecular layers, and we monitored the photometry and visibility spectra.

As well as for the Mira variables RR Aql and S Ori we have modeled the observed data of GX Mon with an ad-hoc radiative transfer model of the dust shell using the radiative transfer code mcsim_mpi by Ohnaka et al. (2006). We again used a series of dust-free dynamic model atmospheres based on self-excited pulsation models (M series, Ireland et al., 2004b,a) to describe the intensity profile of the central source.

Our MIDI observational results of GX Mon are as follows: (i) The interferometric data do not show evidence for intra-cycle visibility variations. (ii) The data do not show evidence for cycle-to-cycle visibility variations. (iii) The 8–13 μm flux exhibits a 4–5σ signature of intra-cycle as well and 2–3σ cycle-to-cycle flux variations. The variations are most pronounced toward the silicate emission feature at 9.8 μm. Our averaged data indicate a flux variations in the wavelength range 8–13 μm, however for clear conclusions, further observational data with higher accuracy would be required.

Summarizing, the precise visual phase of GX Mon is not known, however, the data do not show visibility variations over investigated period (P = 527.0 days) within our uncertainties.

The shape and features of the observed photometry and visibility spectra of GX Mon, as well as the SED at 1–40 μm can be well reproduce by the combination of the radiative transfer model describing the dust shell and the dust-free dynamic model atmosphere representing the central source. The shape of the visibility and photometry function is typical for AGB stars surrounded by dust shells that include silicates or silicates and Al_2O_3 (Lorenz-Martins & Pompeia, 2000). For our analysis, we have considered Al_2O_3 (Begemann et al., 1997; Koike et al., 1995) and silicate (Ossenkopf et al., 1992) dust species, following the work by Lorenz-Martins & Pompeia (2000). The grain sizes were fixed to 0.1 μm. We conclude that a model including a combination of an Al_2O_3 dust shell and a silicate dust shell can well reproduce the observed GX Mon visibility and flux spectra at 8–13 μm. This conclusion is consistent with the results by Lorenz-Martins & Pompeia (2000). The observational results can be well explained by simulations with variations of dust shell parameters and dynamic model atmospheres. The data clearly shows signature of an Al_2O_3 dust shell with an inner boundary at $\sim$ 2.1 stellar radii and a silicate dust shell with an inner boundary at $\sim$ 4.6 stellar radii. The data do not show any phase-dependent formation of the dust within our investigated phases. However, as for the AGB stars RR Aql and S Ori we cannot confirm or deny eventual phase-dependence of the dust formation process that effects the 8–13 μm visibility and photometry values over the full pulsation cycle.

The average model includes the Al_2O_3 dust shell with an optical depth of $\tau_V(Al_2O_3)$=1.9±0.6, the silicate dust is τ_V(silicate)=3.2±0.5, the inner radius of $R_{\rm in}(Al_2O_3)$=2.1±0.3 $R_{\rm Phot}$, the inner radius of the silicate dust shell is $R_{\rm in}$(silicate)=4.6±0.2 $R_{\rm Phot}$, and the power-law index of the den-

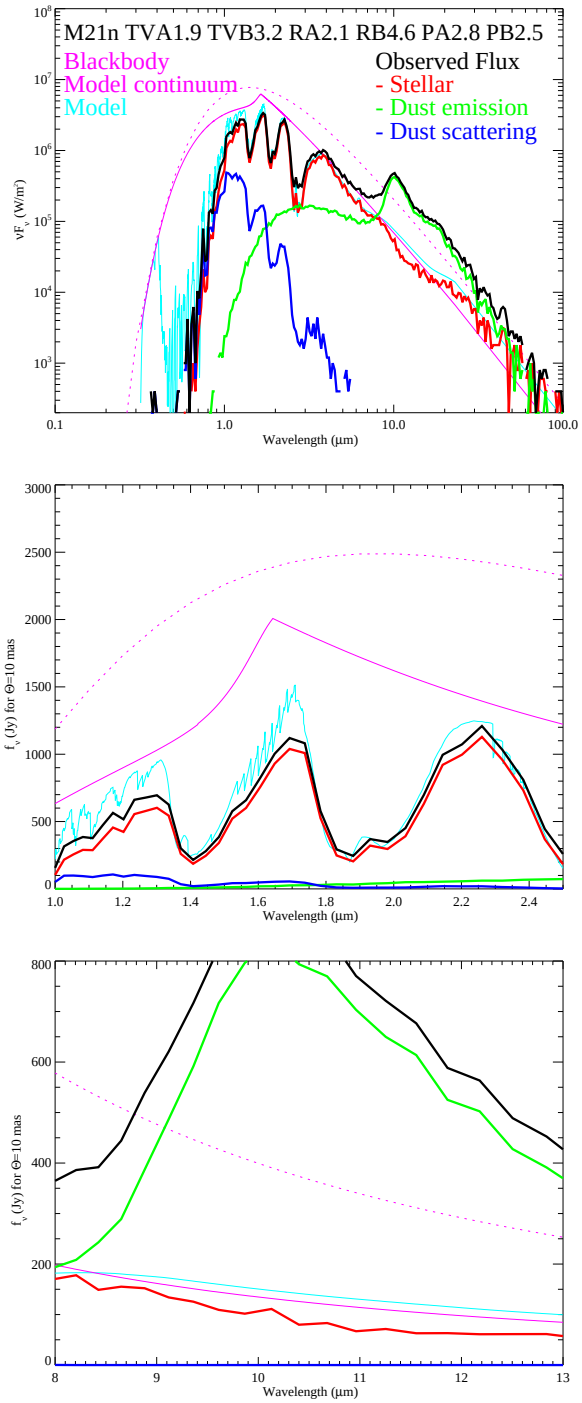

Figure 8.12: The top panel shows the full SED in the range of 0.3–100 μm, the middle panel shows the SED in the range 1–2.4 μm, and the bottom panel shows the SED in the range of 8–13 μm. The pink solid line represents model continuum, the pink dashed line describes the black-body, the black line - the model with the average dust shell parameters describing GX Mon (Tab. 8.3), the red line - the stellar contribution of the model, the green line - dust emission, the blue line - dust scattering.

sity distribution of $p(Al_2O_3)$=2.8±0.4 and p(silicate)=2.5±0.0. The average atmosphere model of the series that is used to describe the central intensity profile is M21n ($T_{\rm model}$ = 2550 K, $\Phi_{\rm model}$ = 0.10) with the photospheric angular diameter of $\Theta_{\rm Phot}$=8.7±1.3 mas. Simulations showed that the data can be generally described using 20–25% of Al_2O_3 grains compare to silicate grains.

Chapter 9

MIDI Observations of R CNC (Al_2O_3-rich dust shell)

The Mira variable R Cnc was analyzed and modeled in the same way as described in in Chapter 5.

9.1 Characteristics of R Cnc

The stellar parameters of the star in this paragraph are adopted from Wittkowski, Boboltz, Karovicova, in preparation. R Cnc is a Mira variable star with spectral type M6e–M9e, V magnitude 6.07–11.80 and period 362 days (Samus et al., 2009). We use a distance of $d = 283 \pm 40$ pc from Whitelock et al. (2000) based on their period-luminosity relation. They derive a small A_V value of 0.07; in this paper we use A_V=0 and include the uncertainty in the errors. Figure 9.1 shows the visual light-curve of R Cnc, where our 4 epochs of observations are indicated. Here, we use a last Julian date of visual maximum of 2454720 and a period of 370 days based on the cycles covering our observations. The assignment of visual phases to the dates of observation is uncertain to about 0.1. The light-curve includes data from the AAVSO[1] and AFOEV[2], and ASAS data. Our epochs correspond to one pre-minimum and one minimum phase in two consecutive cycles. The mass loss rate of 0.2 10^{-7} $M_\odot$/year was estimated by Young (1995).

9.2 VLTI/MIDI Observations and data reduction

Table 9.1 shows an overview of the R Cnc data that we obtained with the different instruments and modes, including the VLTI/MIDI instrument (8–13 μm with spectral resolution $R \sim 30$). Furthermore, we obtained data with the VLTI/AMBER instrument in the low resolution mode (LR HK, 1.46 – 2.54 μm, R ∼30) and MR modes (MR H, 1.54 – 1.82 μm, R ∼1500; MR K 2.1 μm, 1.93 – 2.28 μm, R ∼1500; MR K 2.3 μm, 2.13 – 2.47 μm, R ∼1500), SiO and H_2O maser observations with the VLBA, and $JHKL$ photometry at the SAAO. All the observations were grouped into 4 epochs, two of which include concurrent MIDI, AMBER, SAAO, and VLBA data; and two further epochs include AMBER data only. In this chapter we describe mainly

[1] http://www.aavso.org
[2] http://cdsweb.u-strasbg.fr/afoev

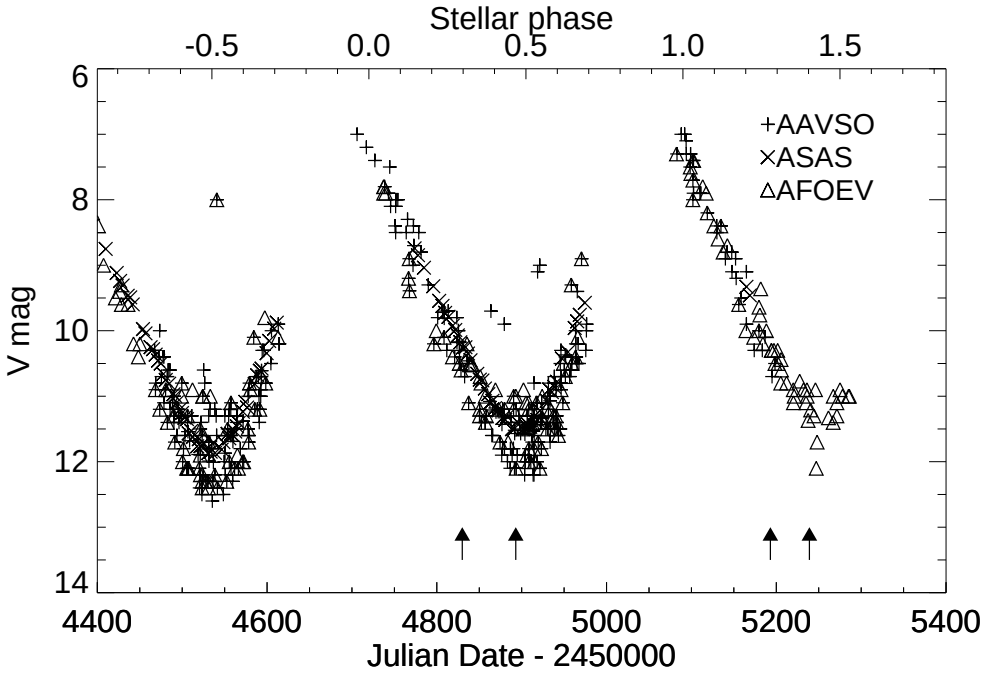

Figure 9.1: Visual light-curve of R Cnc based on data from the AAVSO, AFOEV, and ASAS databases as a function of Julian Date and stellar cycle/phase. The arrows indicate the epochs of our observation.

the VLTI/MIDI observations. The details of the other observations and their data reduction are described in Wittkowski, Boboltz, Karovicova, in preparation.

The spectrally-dispersed mid-infrared interferometric observations of R Cnc were obtained with the MIDI instrument on Dec 23 and Dec 30 2008 accompanied by observations on Feb 25, Mar 1, and Mar 3. We used the PRISM as a dispersive element with a spectral resolution R = $\Delta\lambda/\lambda \sim 30$. We obtained 9 observations in two observational epochs.

The details of the VLTI/MIDI observations and the instrumental settings are summarized in Table 9.2. The Table lists the epoch, the date, the time, the Julian Date (JD), the visual pulsation phase Φ_{vis}, the baseline configuration, the ground length of the configuration, the dispersive element, the beam combiner BC, the projected baseline length B_p, the position angle on the sky PA (deg. east of north), the DIMM seeing (at 500 nm), and the coherence time τ_0 (at 500 nm). All observations were executed in service mode using the Auxiliary Telescopes (ATs, 1.8m).

A maximum time-lag between individual observations is 7 days (1.9% of the pulsation period). The arrows in Figure 9.1 indicate our observations in comparison to the light-curve. The uncertainty in the allocation of the visual phase to our observations was estimated to ∼0.1. Fig. 9.2 shows the *uv* coverage with two groups of perpendicular observations of R Cnc.

The data reduction and calibration was proceeded in the same way as for the previous stars (see Section 5.2). Our main calibrators were Sirius, and HD 81797. Table B.4 lists calibrator stars observed per specific night including those calibrators observed by other programs.

Table 9.1: Overview of our R Cnc observations.

Epoch 1 (23 Dec - 10 Jan, $\Delta\Phi$=0.06):	
23 Dec 2008	MIDI
25 Dec 2009	SAAO Photometry
27 Dec 2009	SAAO Photometry
29 Dec 2008	AMBER LR HK
29 Dec 2008	AMBER MR K 2.3 μm
30 Dec 2008	AMBER MR K 2.1 μm
30 Dec 2009	MIDI
31 Dec 2009	SAAO Photometry
04 Jan 2009	VLBA, SiO maser
10 Jan 2009	VLBA, H_2O maser
Epoch 2 (25 Feb - 3 Mar, $\Delta\Phi$=0.02):	
25 Feb 2009	MIDI
27 Feb 2009	VLBA, SiO maser
01 Mar 2009	MIDI
01 Mar 2009	AMBER MR K 2.3 μm
02 Mar 2009	SAAO Photometry
03 Mar 2009	SAAO Photometry
03 Mar 2009	AMBER MR K 2.1 μm
03 Mar 2009	MIDI
Epoch 3 (27 Dec 2009):	
27 Dec 2009	AMBER MR H
Epoch 4 (11 Feb 2010):	
11 Feb 2010	AMBER MR K 2.3 μm

Table 9.2: VLTI/MIDI observation of R Cnc.

Epoch	DDMMYYYY	Time [UTC]	JD	Φ_{vis}	Config.	B	Disp. Elem.	BC	B_p [m]	PA [deg]	Seeing [″]	τ_0 [msec]
A	25122008	07:04	2454826	4.94	A0-G1		Prism	HS	84.87	110.94	0.96	3.9
A	25122008	08:18	2454826	4.94	A0-G1		Prism	HS	71.91	110.72	1.76	2.1
A	31122008	04:46	2454832	4.96	H0-E0		Prism	HS	40.29	76.96	0.99	4.9
A	31122008	05:59	2454832	4.96	H0-E0		Prism	HS	46.27	75.16	0.70	7.3
B	26022009	02:48	2454889	5.10	A0-G1		Prism	HS	85.91	111.11	0.53	8.7
B	26022009	02:58	2454889	5.10	A0-G1		Prism	HS	84.64	110.90	0.62	7.4
B	26022009	04:14	2454889	5.10	A0-G1		Prism	HS	71.28	110.77	0.77	6.3
B	03032009	02:05	2454894	5.11	E0-H0		Prism	HS	46.74	74.83	1.11	3.2
B	04032009	00:37	2454895	5.12	E0-H0		Prism	HS	40.15	76.99	0.81	5.2

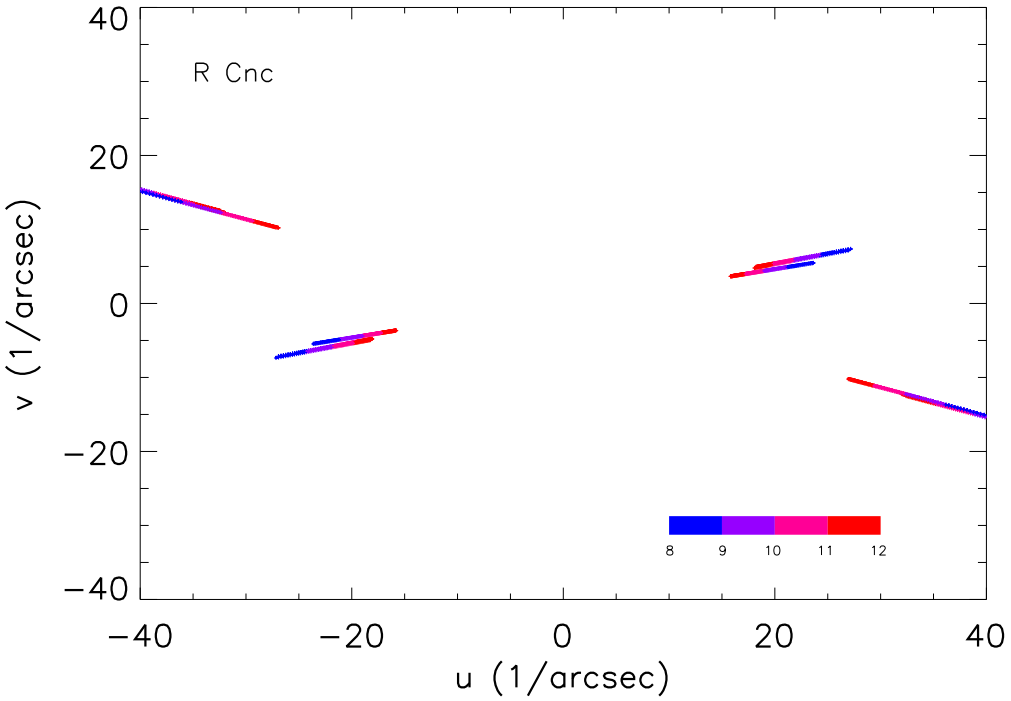

Figure 9.2: Coverage of the *uv* plane for the MIDI observations of R Cnc. Each point represents the observations with ATs over the wavelength 8 to 13 μ.

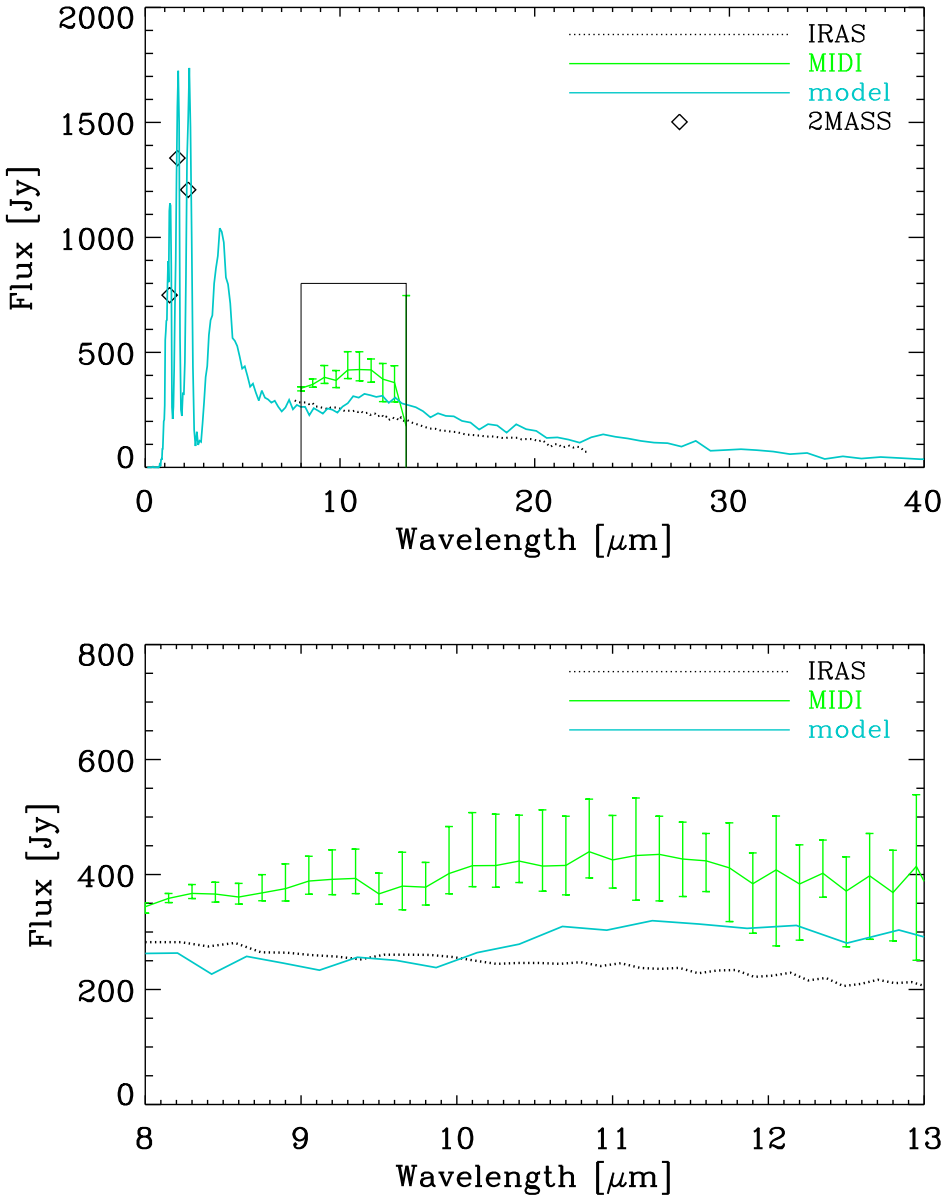

Figure 9.3: R Cnc flux spectrum as a function of wavelength from 2.4 μm to 40 μm (top). The lines represents the flux spectra from IRAS-LRS observations covering wavelengths from $\sim$ 7.7 μm to $\sim$ 23 μm (dotted thin black like), and the mean of our N-band MIDI measurements (solid thin green line). Here, the vertical bars span the maximum and minimum values measured. The diamond symbols denote 2MASS measurements at 1.25 μm, 1.65 μm, and 2.2 μm. The solid blue line indicates our atmosphere and dust shell model as explained in Sect. 9.3.2. The bottom plot shows an enlarged segment of the plot in the MIDI wavelength range of 8–13 μm.

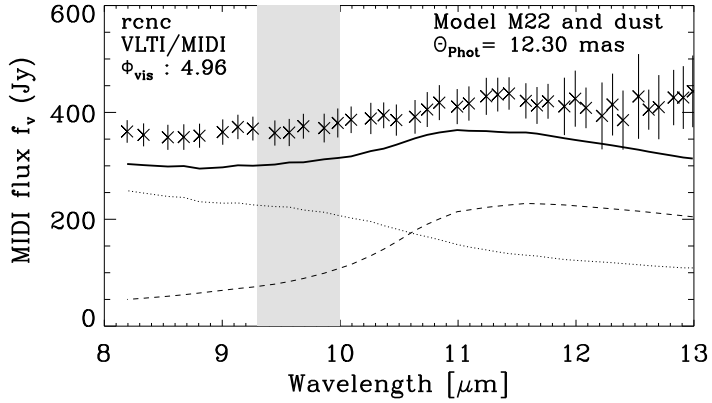
rcnc
VLTI/MIDI
Φvis : 4.96
Model M22 and dust
ΘPhot= 12.30 mas
MIDI flux fν (Jy)
Wavelength [μm]

(a)

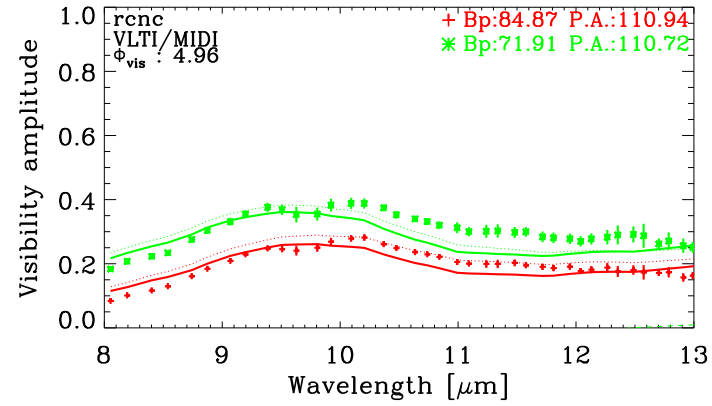
rcnc
VLTI/MIDI
Φvis : 4.96
+ Bp:84.87 P.A.:110.94
✳ Bp:71.91 P.A.:110.72
Visibility amplitude
Wavelength [μm]

(b)

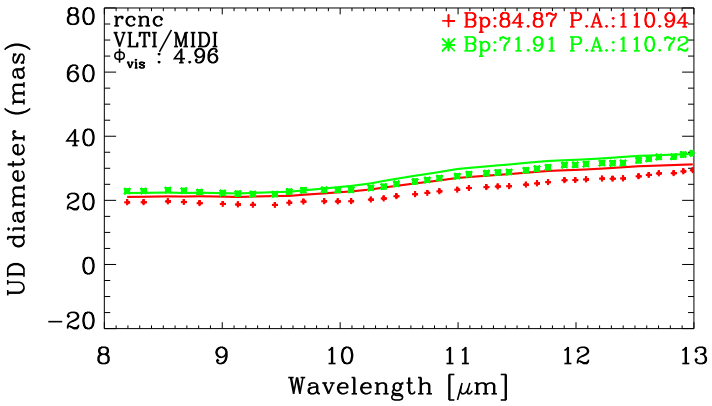
rcnc
VLTI/MIDI
Φvis : 4.96
+ Bp:84.87 P.A.:110.94
✳ Bp:71.91 P.A.:110.72
UD diameter (mas)
Wavelength [μm]

(c)

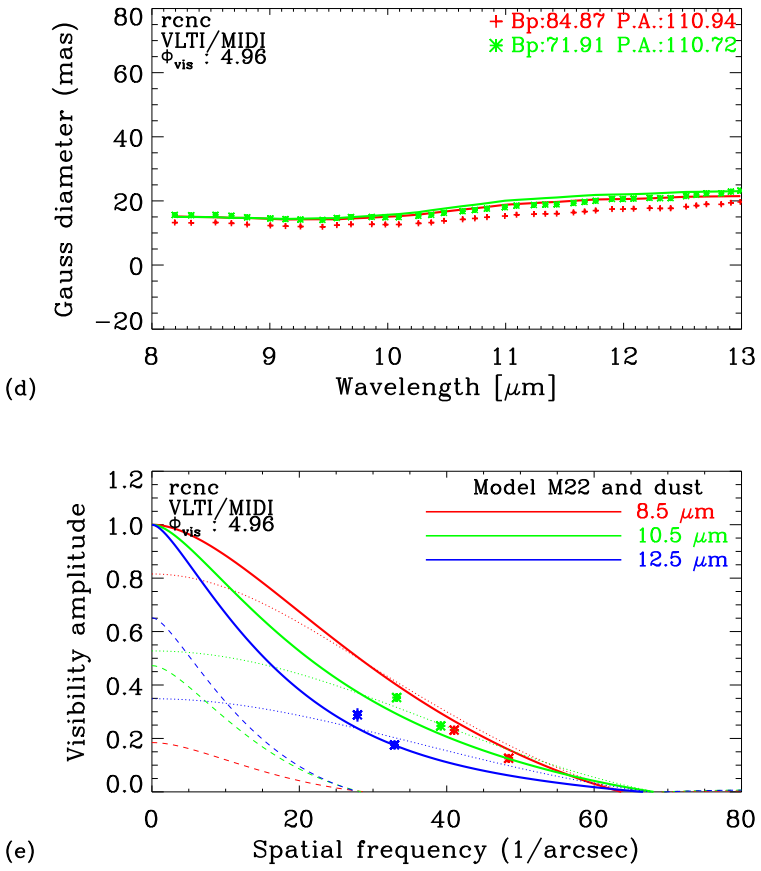

Figure 9.4: VLTI/MIDI interferometry at 8-13μm of R Cnc for the example of epoch A (stellar phase 4.96). The panels show (a) the flux, (b) the visibility amplitude, (c) the corresponding UD diameter, (d) the corresponding Gaussian FWHM diameter as a function of wavelength. The gray shade indicates the wavelength region around 9.5 μm that is affected by atmospheric absorption. Panel (e) shows the visibility amplitude as a function of spatial frequency for three averaged bandpasses of 8-9 μm, 10-11 μm, and 12-13 μm. The crosses with error bars denote the measured values. The solid lines indicate our best-fitting model, as described in Sect. 9.3.2. The model consists of a radiative transfer model describing the surrounding dust shell where the central star is represented by a dust-free dynamic model atmosphere. The contributions of the stellar and dust components alone are indicated by the dotted and the dashed line, respectively.

9.3 MIDI results

The calibrated photometry spectra as a function of wavelength show a rather flat shape. The photometry increases between $\sim$ 8-9.8 μm, and beyond $\sim$ 10 μm photometry curves flattens. The majority of values fall into the range of $\sim$400–600 Jy. The level of the flux spectrum differs for individual measurements with a spread of $\sim$ 50–150 Jy.

The visibility spectra of R Cnc do not exhibit a very strong wavelength dependence. The visibilities are rather flat and similar to the visibility functions of S Ori. The visibility functions increase between $\sim$ 8-9 μm, and beyond $\sim$ 9-10 μm flattens. The shape and absolute scale of the visibility functions as well as for S Ori do not significantly depend on the length of the projected baseline.

The equivalent UD diameter and the Gaussian FWHM is quasi-constant between $\sim$ 8-9.8 μm, and increases beyond $\sim$ 10 μm.

Deviations from circular symmetry

We obtained two groups of perpendicular observations in the *uv* plane acquired with P.A. $\sim 110\,^\circ$, and P.A. $\sim 75\,^\circ$ (see Tab. 9.2). Unfortunately, the quality of the data does not allow us to confirm or deny the possible presence of an asymmetric intensity distribution.

9.3.1 MIDI model parameters

As well as the previous Mira variables presented in this thesis the modeling of R Cnc followed the same modeling approach (see Section 5.3.4).

R Cnc shows rather broad spectra and visibility functions in the wavelength range 8–13 μm without a significant silicate feature. Lorenz-Martins & Pompeia (2000) classified R Cnc to the same group as S Ori, and suggested that the circumstellar dust shell contains only Al_2O_3 grains without a contribution of silicates. We modeled the R Cnc dust shell using both dust species, Al_2O_3 grains (Begemann et al., 1997; Koike et al., 1995) and silicates grains (Ossenkopf et al., 1992). The grain size was set to 0.1 μm for all grains.

We computed a grid of models including six parameters describing the circumstellar dust shell. The models consists of the M series: M16n (model visual phase $\Phi_{\rm model}$=0.60), M18 (0.75), M18n (0.84), M19n (0.90), M20 (0.05), M21n (0.10), M22 (0.25), M23n (0.30), M24n (0.40), and M25n (0.50) including all combinations of optical depths τ_V (Al_2O_3) = 1.0, 1.5, 1.8, 2.1, 2.4, 2.7, 3.0; τ_V (silicate) = 0.0, 0.2, 0.5, 0.8, 1.0; $R_{\rm in}/R_{\rm Phot}$ (Al_2O_3) = 1.5, 2.0, 2.5, 3.0; $R_{\rm in}/R_{\rm Phot}$ (silicate) = 2.5, 3.5, 4.5, 5.5, 6.5; $p_{\rm A}$ (Al_2O_3) = 2.0, 2.5, 3.0, 3.5; and $p_{\rm B}$ (silicate) = 2.0, 2.5, 3.0, 3.5. Where τ_V (Al_2O_3) and τ_V(silicate) is the optical depths, $R_{\rm in}/R_{\rm Phot}$ (Al_2O_3) and $R_{\rm in}/R_{\rm Phot}$ (silicate) the inner boundary radii, and $p_{\rm A}$ (Al_2O_3) and $p_{\rm B}$ (silicate) the density gradients. The angular diameter $\Theta_{\rm Phot}$ was the only free parameter.

The selection of best-fitting models follow the same way as in the previous chapters (eg. 4.1 Section 5.3.4).

Table 9.3: Best-fitting model parameters for each epoch of R Cnc observations

Epoch	$\Phi_{\rm vis}$	Model	$\Phi_{\rm mod}$	τ_V (Al_2O_3)	$R_{\rm in}/R_{\rm Phot}$ (Al_2O_3)	p (Al_2O_3)	$\Theta_{\rm Phot}$ [mas]
A	4.95	M22	0.25	1.5	2.0	2.5	12.3
B	5.11	M22	0.25	1.2	2.4	2.5	12.3

Table 9.4: Average model parameters for all epochs of R Cnc observations

Model	τ_V (Al_2O_3)	τ_V (silicate)	$R_{\rm in}/R_{\rm Phot}$ (Al_2O_3)	p (Al_2O_3)	$\Theta_{\rm Phot}$ [mas]
M22	1.35 ± 0.2	0.0	2.2 ± 0.3	2.5 ± 0.0	12.3 ± 0.0

9.3.2 MIDI model results

We found the best-fitting model parameters for both epochs including the phase of the dust-free dynamical model atmosphere represented by the M model and the set of the dust shell parameters of the radiative transfer model (Sect. 9.3.1).

We have investigated dust including Al_2O_3 and/or silicate shells with different inner radii and density gradients. The best fit results were obtained with an Al_2O_3 shell without a contribution of silicate in the dust shell. Our result is consistent with the previous study by Lorenz-Martins & Pompeia (2000). The best-fitting parameters for each epoch are listed in Table 9.3. The table lists the epoch, the phase at the epoch, the optical depth τ_V, the inner boundary radius $R_{\rm in}/R_{\rm Phot}$, the density distribution p, and the continuum photospheric angular diameter $\Theta_{\rm Phot}$. Since the best fitting models are without any contribution of silicates the Table list only parameters of Al_2O_3 dust shell.

The quality of the data is for 3 observations quite poor, nevertheless, the agreement between the models and the observed data is in general very good. We show that the shape of both the visibility and the photometry spectra of R Cnc can be very well reproduced by the combination of the radiative transfer code describing the circumstellar dust shell with the dynamical model atmospheres representing the central intensity profile. Figure 9.4 shows the example of epoch A, and includes the model flux and model visibility compared to the observed values. Both observational epochs can be find in appendix (Fig. F.1). Observations of R Cnc show a partially resolved stellar disk including atmospheric molecular layers that are optically thick at the wavelength range 8–13 μm. The disk is surrounded by a spatially resolved, optically thin dust shell. Beyond 9 μm spatially resolved, optically thin radiation from the dust shell starts to be a considerable part of the total intensity, and together with extinction of the stellar light by the dust shell, spatially resolved radiation from the dust shell overtake the measured intensity at the longest wavelengths ($\sim$ 12–13 μm).

Table 9.4 lists the average dust shell parameters for both epochs. Figure 9.5 shows the models simulating the average parameters. The average M model is represented by model M22. The results show that the dust shell consisting only of Al_2O_3 without the addition of silicate, corresponds the best with our R Cnc data. This result is in accordance with the investigations by Lorenz-Martins & Pompeia (2000).

The average optical depth of the Al_2O_3 dust is $\tau_V(Al_2O_3)$=1.35±0.2 at $\lambda = 0.55\,\mu$m (corresponding to 0.04 at $\lambda = 8\,\mu$m, 0.29 at $\lambda = 12\,\mu$m, and a maximum within 8–12 μm of 0.30 at

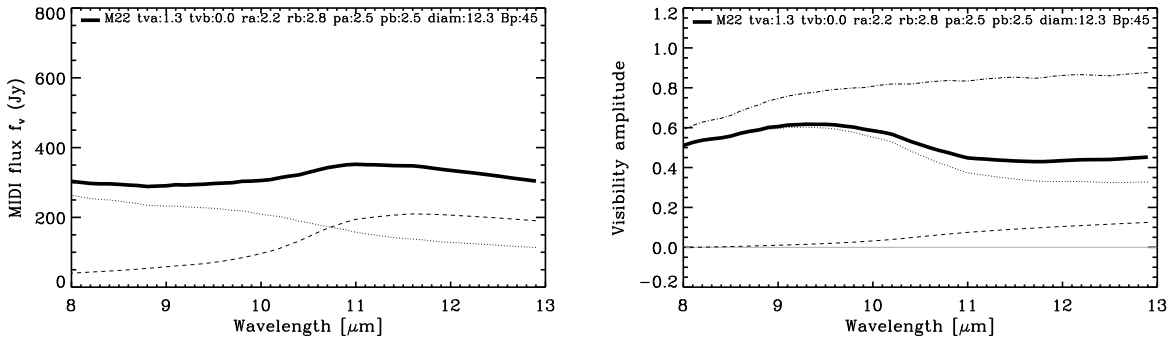

Figure 9.5: Model with average dust shell parameters for different epochs of our R Cnc observations (Table 9.4).

$\lambda = 11.8\,\mu$m). The inner radius of the dust shell is $R_{\rm in}$=2.2±0.3 $R_{\rm Phot}$, and the power-law index of the density distribution is p=2.5±0.0. The average photospheric angular diameter results in $\Theta_{\rm Phot}$=12.3±0.0 mas.

Figure 9.6 shows the simulation of the full SED in the range of 0.3–100 μm including the model with the average parameters.

9.4 Summary, Conclusions and Discussion

We have observed the oxygen-rich Mira variable R Cnc with the VLTI/MIDI instrument. We obtained 9 observations combined into 2 epochs. The observations were acquired on Dec 23 and Dec 30 2008 accompanied by observations on Feb 16, Feb 25, Mar 1, and Mar 3, 2008 and Mar 14, 2009. We have modeled the observed data with an ad-hoc radiative transfer model of the dust shell using the radiative transfer code mcsim_mpi by Ohnaka et al. (2006). We used a series of dust-free dynamic model atmospheres based on self-excited pulsation models (M series, Ireland et al., 2004b,a) to describe the intensity profile of the central source. We conclude that the combination of the models can well reproduce the shape and features of the observed photometry and visibility spectra of R Cnc, as well as the SED at 1–40 μm. We have considered Al_2O_3 (Begemann et al., 1997; Koike et al., 1995) and silicate (Ossenkopf et al., 1992) dust species with fixed grain sizes of 0.1 μm. We showed that a model including only an Al_2O_3 dust shell can well reproduce the observed visibility and flux spectra at 8–13 μm. The addition of a silicate dust shell with comparable low optical depth did not improve the fit to our data. Our results are consistent with the results by Lorenz-Martins & Pompeia (2000). The average model includes an Al_2O_3 dust shell with the optical depth of $\tau_V(Al_2O_3)$=1.35±0.2, the inner radius of $R_{\rm in}$=2.2±0.3 $R_{\rm Phot}$, and the power-law index of the density distribution of p=2.5±0.0. The average atmosphere model is M22 ($T_{\rm model}$ = 2330 K, $\Phi_{\rm model}$ = 0.25) with the photospheric angular diameter of $\Theta_{\rm Phot}$=12.3±0.0 mas.

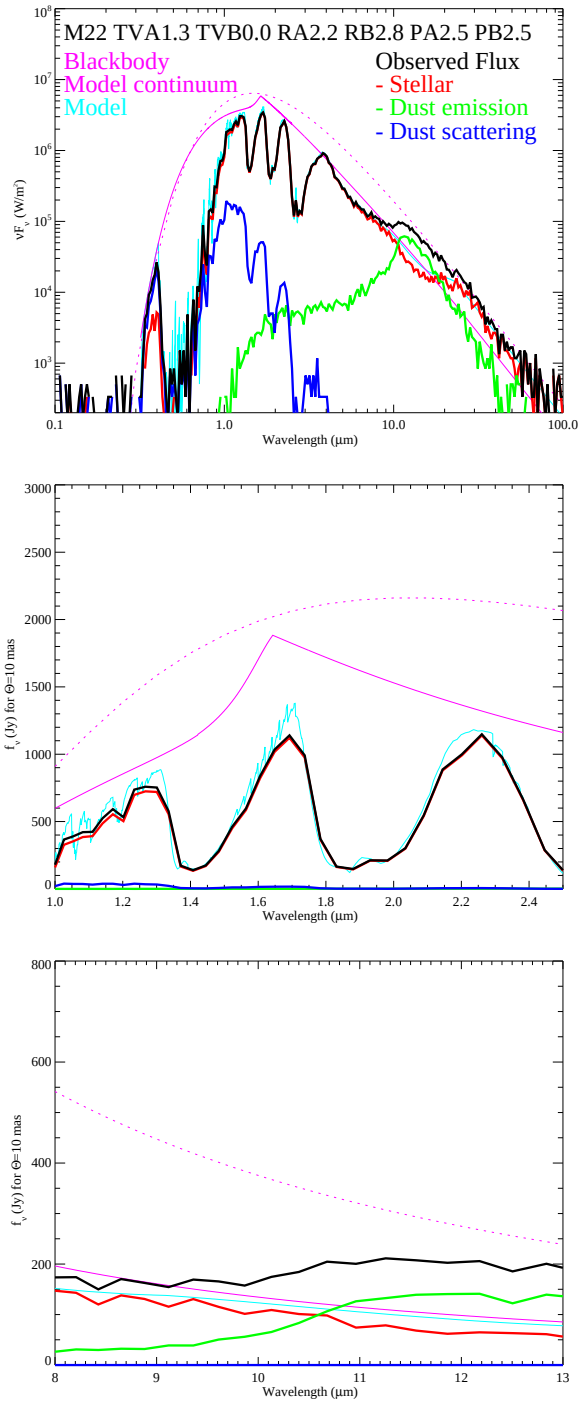

Figure 9.6: The top panel shows the full SED in the range of 0.3–100 μm, the middle panel shows the SED in the range 1–2.4 μm, and the bottom panel shows the SED in the range of 8–13 μm. The pink solid line represents model continuum, the pink dashed line describes the black-body, the black line - the model with the average dust shell parameters describing R Cnc (Tab. 9.4), the red line - the stellar contribution of the model, the green line - dust emission, the blue line - dust scattering.

Table 9.5: VLTI/AMBER observations

Date	JD 2450000+	Phase Vis.	Mode	Baseline m	P.A. deg
2008-12-29	4830.21	0.30	LR HK	14.04/28.07/42.11	-76.7
2008-12-29	4830.24	0.30	LR HK	15.13/30.24/45.37	-75.7
2008-12-29	4830.28	0.30	MR K 2.3	15.90/31.78/47.68	-73.7
2008-12-30	4831.29	0.30	MR K 2.1	16.00/31.98/47.98	-72.8
2008-12-30	4831.33	0.30	MR K 2.1	15.69/31.35/47.04	-69.5
2009-03-01	4892.11	0.46	MR K 2.3	15.95/31.88/47.82	-73.4
2009-03-01	4892.17	0.46	MR K 2.3	15.59/31.15/46.74	-69.0
2009-03-03	4894.13	0.47	MR K 2.1	15.98/31.94/47.92	-71.7
2009-12-27	5193.33	1.28	MR H	15.81/31.59/47.39	-70.2
2010-02-11	5239.20	1.40	MR K 2.3	15.89/31.75/47.64	-70.8

9.5 Observations with VLTI/AMBER, VLBA, and SAAO JHKL photometry

In the following sections we briefly introduce our other observations of R Cnc. We also show some preliminary results. Detailed description of the observations, used methods, and accomplished results can be find in Wittkowski, Boboltz, Karovicova, in preparation.

9.6 VLTI/AMBER observations

Table 9.5 shows observations on the R Cnc obtained with the VLTI/AMBER instrument. The table lists the the date of the observations, the Julian Date (JD), the visual pulsation phase Φ_{vis}, the mode, the baseline length (B_p), and the position angle (P.A.).

9.6.1 Modeling of the VLTI/AMBER data

We compared the visibility data to the best-fitting models of a uniform disk (UD), a Gaussian profile with a constant diameter and also to stellar atmospheres models. For R Cnc, we used the complete self-excited dynamic model atmospheres of Mira stars by Ireland et al. (2004b,a) (Section 4.1). These models include the effect from molecular layers that lie above the continuum-forming photosphere.

We estimate a continuum photospheric angular diameter of $\Theta_{\rm Phot}$= 12.0 ± 2.4 mas that corresponds with photospheric angular diameter of $\Theta_{\rm Phot}$= 12.3 ± 2.4 mas derived from our MIDI observations of R Cnc. The models M11, M20, P12 are also in good agreement with the best fitting model M22 obtain with the MIDI analysis.

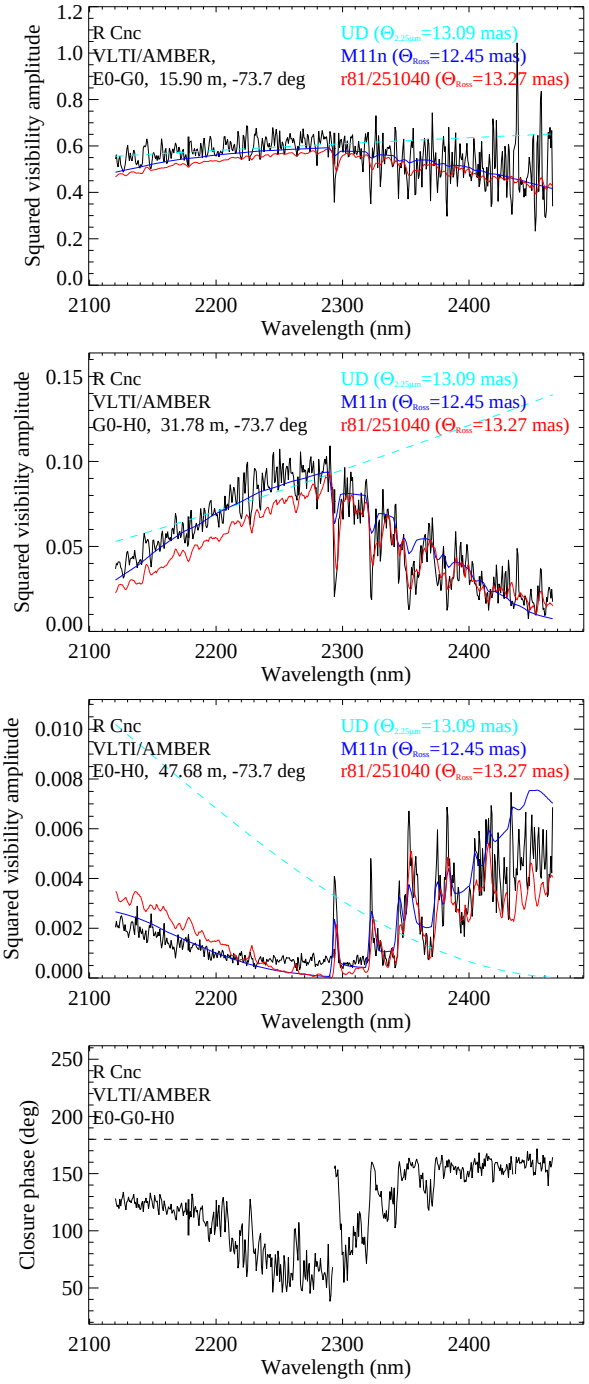

Figure 9.7: R Cnc visibility values obtained in AMBER MR K 2.3 μm mode on 2008-12-29 (epoch 1), compared to best-fitting models from the P/M and the new model series from Ireland et al. (2004b,a, 2008).

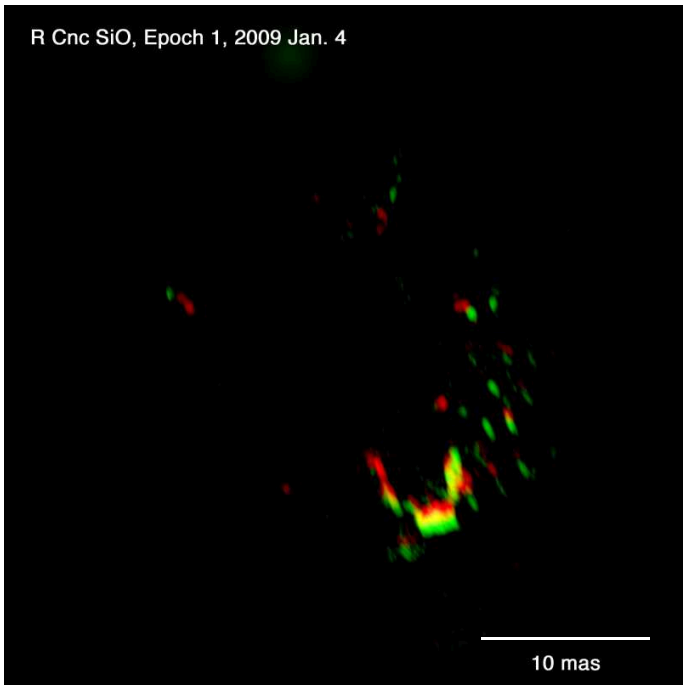

Figure 9.8: Images of the SiO masers from the first VLBA epoch. Red indicates the 42.8 GHz transition and green the 43.1 GHz transition. The two overlaps are indicated in yellow.

9.6.2 VLTI/AMBER closure phases and shaping processes

The non zero closure phase values (see Figure 9.7) indicate an asymmetric brightness distribution across the stellar surface.

9.6.3 VLBA observations

Figures 9.8 and 9.9 show the images of the SiO masers from the two VLBA epochs. Red indicates the 42.8 GHz transition and green the 43.1 GHz transition. The two overlaps are indicated in yellow. Not much overlap can be seen in the second epoch. However, there were significant changes, especially in the 42.8 GHz shell from the first epoch to the second one.

9.6.4 SAAO JHKL photometry

9.6.5 Parameters of R Cnc

Table 9.7 lists the parameters of R Cnc derived from our observations. Here, the Rosseland angular diameter $\Theta_{\rm Ross}$ is derived from the comparison of the AMBER data to the dynamic model atmospheres and the bolometric flux $f_{\rm bol}$ from the integration of the SAAO photometry and using the sun as the zero point. Then the effective temperature is computed from $\Theta_{\rm Ross}$ and $f_{\rm bol}$, the Rosseland radius $R_{\rm Ross}$ from $\Theta_{\rm Ross}$ and the adopted distance, and the luminosity from R and $T_{\rm eff}$.

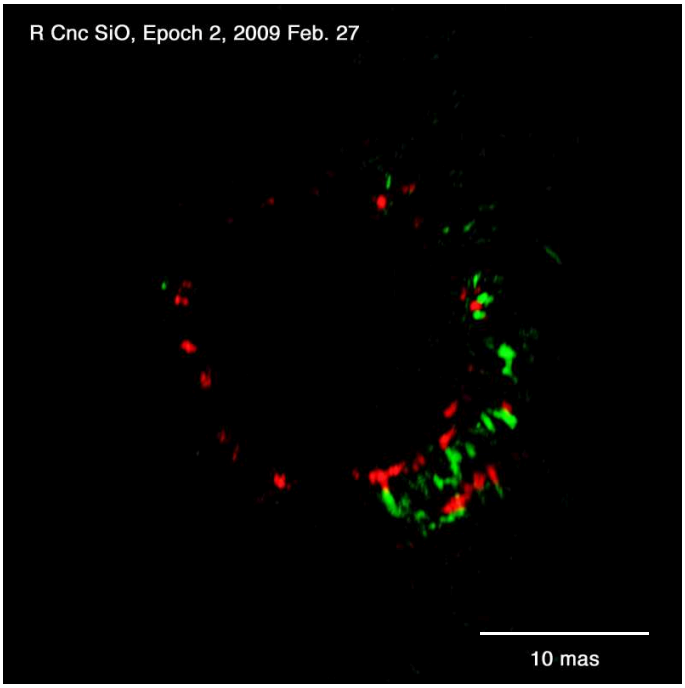

Figure 9.9: Images of the SiO masers from the second VLBA epoch. Red indicates the 42.8 GHz transition and green the 43.1 GHz transition. The two overlaps are indicated in yellow.

Table 9.6: SAAO JHKL photometry

Date	JD	Phase	J	H	K	L	$m_{\rm bol}$	$f_{\rm bol}$
	2450000+	Vis.	mag	mag	mag	mag	mag	10^{-9} W/m^{-2}
2008-12-25	4825.43	0.28	0.815	-0.215	-0.688	-1.119	2.51	2.52
2008-12-25	4825.50	0.28	0.806	-0.212	-0.676	-1.095	2.51	2.52
2008-12-27	4827.50	0.29	0.838	-0.205	-0.665	-1.112	2.53	2.47
2008-12-31	4831.45	0.30	0.866	-0.155	-0.652	-1.063	2.56	2.40
2009-03-02	4892.41	0.46	1.280	0.225	-0.328	-0.89:	2.95	1.68
2009-03-03	4893.41	0.47	1.444	0.468	-0.213	-0.909	3.12	1.44

Table 9.7: Results

Ep.	$\Phi_{\rm Vis}$	$\Theta_{\rm Ross}$	$f_{\rm bol}$	$T_{\rm eff}$	$R_{\rm Ross}$	L	$\Theta_{\rm SiO,42.8GHz}$	$\Theta_{\rm SiO,43.1GHz}$
		mas	10^{-9} W/m^{-2}	K	R$_\odot$	L$_\odot$	mas	mas
1	0.30	13.3 ± 1.7	2.40 ± 0.12	2526 ± 195	405 ± 130	3.78 ± 0.38	23	28
2	0.46	13.4 ± 0.9	1.56 ± 0.12	2260 ± 120	408 ± 100	3.59 ± 0.28		
3	1.28	13.5 ± 1.0	/	/	411 ± 105	/	/	/
4	1.40	12.7 ± 1.1	/	/	387 ± 105	/	/	/

Chapter 10

Outlook

The project presented in this thesis brought several interesting results, and determined the required accuracy for future infrared interferometric observations of evolved stars. It was shown that for answering crucial questions, it is necessary to obtain accurate photometric observations together with interferometric observations. These interferometric observations should be obtained using well considered projected baseline lengths. In the following section, further steps are outlined that may provide additional and/or more precise information about the atmospheres of evolved stars.

10.1 Further infrared interferometric observations using MIDI & AMBER at the VLTI

In this thesis I have analyzed results of multi-epoch observations of the oxygen-rich stars RR Aql, S Ori, GX Mon, and R Cnc. Similar multi-epoch observations have been conducted at the VLTI for the oxygen-rich stars R Aql, R Aqr, W Hya, R Hya, R Leo, U Her, R Dor and the carbon-rich stars V Aql, T Sgr, U Hya, and V Hya (PI: Lopez, PI: Quirrenbach). Some of the data has already been reduced and analyzed. For the oxygen-rich stars R Aql, R Aqr, W Hya, R Hya, and the carbon-rich star V Hya the data was modeled using Fully Limb-Darkened Disk (FDD) or FDD + Gaussian geometrical models (Zhao-Geisler - private communication). O-rich stars of this sample show a moderate to low diameter decrease from 8 to 10 μm and a strong diameter increase from 10 to 12 μm similar to RR Aql and GX Mon investigated in this thesis. For providing sufficient opacities and inner boundary radii and their dependence on the pulsation phase/cycle, one would need to apply dynamic atmospheric models (Ireland et al., 2004b,a) complemented by an ad-hoc radiative transfer model of the dust shell as used in this study (Wittkowski et al., 2007). A detailed comparison of all multi-epoch observations of oxygen-rich stars will give more extensive insights in the physical processes taking place in the pulsating stellar atmospheres of oxygen-rich Mira stars.

In order to obtain high quality results, future observations should be be carefully planned using the most beneficial baseline configurations based on the model simulations (4.4). In Section 4.2 the most suitable baseline lengths for individual stars are introduced to precisely determine the optical depths, inner boundary radii, and density gradient of individual dust species. One of the further steps will be as well to simulate the mid-infrared data with dust species showing a more

complex grain size distribution using the DUSTY code. The DUSTY code can estimate the mass-loss rate as well. It is known, that other dust species may occur in the stellar atmosphere. The characteristics of the dust species can be crucial in many respects. The kind of grains sufficient to support dust-driven winds in oxygen-rich stars is still under intense investigation. The problem of finding grains that can drive the mass loss close enough to the star has yet to be solved. For example, the iron content of the initial silicate seems to be a critical parameter affecting the observable properties, and therefore the wind driven mechanism (Woitke, 2006). Höfner (2008) demonstrated, that winds of M-type AGB stars can be driven by radiation pressure on micron-sized Fe-free silicate grains. New, more detailed observations in a range of baseline lengths corresponding to the regions where it is possible to distinguish between individual models will give clues whether the results predicted by theory are consistent with observation. However, with the additional dust species and grain sizes in the models also geometrically increase the required time for computation and finding the adequate set of parameters.

10.1.1 Image reconstruction

At present, interferometric imaging is still an observational challenge. To obtain full characteristic of the structure of a star's atmosphere, one would need to observe the star at all wavelengths at good *uv* coverage. In particular, for temporally varying AGB stars one would need to observe the target at many different pulsation phases covering the full pulsation cycle. Moreover since the cycles are not entirely periodic it is advisable to follow the star over several consecutive cycles (however one or two epochs would already provide important insight). Fulfilling all these requirements is very ambitious as telescope time is very costly. Unlike radio interferometric observations offering many telescopes, infrared interferometric observations are determined by a fairly small number of telescopes simultaneously processing the incoming light from the source, and thus limited by sampling in the spatial plane. In spite of the complexity of the scientific goal, most recent studies using the infrared interferometric instrument AMBER showed that it is now feasible to use imaging to study complex features of Mira variable stars. Aperture synthesis techniques with AMBER, which offer newly additional baselines that are more suited for imaging studies than the ones previously used, have succeeded for the first time in reconstructing images of an AGB star T Lep at each of several spectral channels at low resolution mode (Le Bouquin et al., 2009). The study showed reconstructed images that confirmed the general picture of a central star partially obscured by the surrounding molecular shell of changing opacity in the spectral domain $\lambda = 1.5 - 2.4$ μm. The data showed the shell becoming optically thin at 1.7 μm, with corresponding emission appearing as a ring circling the star. This observations demonstrated the first direct evidence of the spherical morphology of the molecular shell. This result is just a first step in the direction of infrared interferometric imaging. One of the further aims will be to conduct similar observations complemented simultaneously by mid-infrared (MIDI) and radio observations covering several pulsation phases (at medium and high resolution). This scientific goal will be more feasible with the second generation instrumentation (e.g. MATISSE instrument see bellow) which will offer, compared to the first generation, the capability of using simultaneously up to four telescopes. Careful planning of the projected baseline lengths along with concurrent observations in various bands will overcome the limitation of infrared interferometry in incomplete sampling of the aperture plane.

10.2 Further analysis of the RR Aql data

10.2.1 Further near-infrared interferometric observations at the VLTI/AMBER

We have recently obtained VLTI/AMBER observations of RR Aql in the H and K bands at several different baseline configurations. The observations were obtained in medium spectral resolution mode (R$\sim$1500) at pulsation phase 0.4. The observations were obtained on 06/06/2010 using baseline configuration H0-E0-G0, on 11/06/2010 using configuration D0-I1-H0 and G1-I1-A0, and on 17/06/2010 using configuration K0-I1-A0 and K0-I1-G1. These new near-infrared observations will be crucial for a new estimate of the continuum angular diameter of RR Aql. Previous observations conducted on 08/09/2006 with UTs resulted in low data quality and show very low visibilities. The observations were also conducted in the medium resolution, and only in the K band. We determined the near-infrared continuum photospheric angular diameter $\Theta_{\rm Phot}$= 9.9 $\pm$ 2.4 mas. The new observations using the ATs will confirm the estimate or determine a new estimate of the diameter. Spectrally resolved near-infrared AMBER observations will be compared to dynamic model atmospheres. The dynamic models predict wavelength-dependent radii caused by molecular layers that lie above the continuum-forming photosphere (Wittkowski et al., 2008). In addition, the new near-infrared observations are complemented by simultaneous MIDI observations obtained on 17/06/2010 using baselines A0-I1 and K0-G1.

Thus far, all the observations were obtained at medium spectral resolution and had rather large error bars. As a further step it would be beneficial to obtain a high S/N and high-precision visibility spectrum of the full K-band in medium resolution mode, and in addition, a high-resolution visibility spectrum at 2.172 μm. This band will provide a high-precision estimate of the continuum layer near 2.2 μm, and it will as well cover the Brγ line. It has been measured that Mira stars may show Brγ emission at post-maximum visual phases e.g., for χ Cyg by Wallace & Hinkle (1997); for U Crt by Lançon & Wood (2000), which most likely originates from the shock front.

10.3 Future scientific goals in the field of AGB stars

Future scientific goals for AGB stars could be specially addressed to:

- The shaping mechanism during the evolution from the AGB to the planetary nebulae phase.

The transition sources of post-AGB (PAGB) stars and planetary nebulae (PNe) present a great diversity of morphologies, such as bipolar with thick equatorial disks collimating the PAGB wind. Among others, it is still not well understood how (almost) spherically symmetric AGB stars evolve toward the asymmetric PN leaving the central star as a white dwarf (Balick & Frank, 2002). Various observations reveal that many AGB stars already show asymmetric brightness distribution. The shaping processes leading to the asymmetric brightness distribution may include large-scale photospheric convection leading to only a few, very large, starspots (Schwarzschild, 1975; Freytag & Höfner, 2008), external torques of a close or merging binary companion, possibly connected with episodic dust formation events, the emergence of magnetic fields, or the interaction of slow and fast winds (e.g. Balick & Frank, 2002; Kwok, 2008). Most recently, AMBER closure phase measurements of several AGB stars have revealed wavelength-dependent deviations from 0/180 deg., indicating different morphologies of the shells at different wavelength, (Wittkowski et al., in preparation). Therefore, the aim is to use the VLTI abilities to detect departures

from spherical symmetry, complemented by spectroscopic observations. This could help to find correlations between the asymmetries and other physical characteristics. These investigations would help to determine for what type of AGB and PAGB stars these asymmetric structures appear first.

- Investigation of mixed chemistry in AGB stars.

The analysis of the envelopes can help to distinguish differences between carbon and oxygen-rich type stars. PNe are usually classified as C-rich with polycyclic aromatic hydrocarbons features (PAH) or O-rich with amorphous silicate features. A minority of stars show mixed a chemistry of PAHs and silicate features. One proposed explanation is that the star becomes C-rich due to the third dredge-up, while the O-rich gas is trapped in a disk during the intensive mass loss phase. Observations can detect if the mixed chemistry implies that the dust was stored in a disk (VLTI). These disks can be created by rotation or an orbiting companion. Spectroscopy can detect possible rotation by broadening photospheric absorption lines as well as to study amorphous dust features, crystalline dust features, emission features of Polycyclic Aromatic Hydrocarbons, and (in the highest spectroscopic resolution) even molecular bands (MATISSE instrument see below).

- The detailed atmospheric stratification and chemical composition of evolved stars.

The chemical composition of evolved stars can be easily detected from the observed spectra which provides detailed information about the molecules present in the atmosphere. It can probe abundances, temperature, kinematics, and density. The data taken in different metallicity environments (Spitzer) allow us to study how the metallicity can affect the gas and dust composition of the star. Combining these data, one could investigate whether the dust type can be connected to certain physical or/and morphological characteristics.

10.4 Radio interferometric observations at the VLBA

One of the further steps will be to compare the mid-infrared MIDI data with our concurrent radio interferometric observations. The presented data (RR Aql, S Ori, GX Mon, and R Cnc) are a part of an ongoing program of long-term simultaneous observations of a sample of evolved stars by the VLTI instruments, and the radio interferometric instruments VLBA (The Very Long Baseline Array), and MERLIN. VLBA is a system of ten radio telescopes, each with a dish 25 meters in diameter which stretch across the United States. VLBA is operated by the National Astronomy Observatory (NRAO) at wavelengths 0.7 - 90 cm. MERLIN is the Multi-Element Radio Linked Interferometer Network, an array of seven radio telescopes distributed around Great Britain, with separations of up to 217 km. It operates at frequencies ranging from 151 MHz to 24 GHz. At 5 GHz, the resolution of MERLIN is better than 50 milliarcseconds. MERLIN is operated by the University of Manchester as a National Facility of the Science and Technology Facilities Council (STFC).

Different pulsating layers and their relative position across pulsating cycles can be ideally probed by time series of concurrent multiwavelength observations. The extended CSE display one or more of the three most common maser molecules: SiO, H_2O, and OH. The stellar atmosphere is populated by SiO masers and further out at larger distances of the stellar wind region lie the masing molecules H_2O and OH. The different distances for relative positions of maser

molecules are based on the abundances of the particular maser species, and on the excitation temperature. Radio interferometry is capable of providing complementary information to the infrared interferometric measurements about the spatial structure and kinematics of the maser spots. The velocity structure of the maser spots could indicate a radial gas expansion or contraction at certain pulsation stellar phase. The radial maser distribution could give a sign of asymmetric gas distribution. Furthermore, full-polarization images and direct map of magnetic field in the stellar atmosphere appearing close to the star can be obtained. We refer to previous results of one of our star S Ori at four epochs presented by Wittkowski et al. (2007).

10.5 Future high resolution facilities

10.5.1 Forthcoming facilities at the VLTI

PRIMA - the Phase-Referenced Imaging and Micro-arcsecond Astrometry is the new high resolution instrument at the VLTI. PRIMA (currently under commissioning) will significantly enhance the VLTI capabilities. Infrared interferometry is limited in sensitivity by the atmospheric turbulences. Integration time has to be very short to 'freeze' the fringe pattern. The PRIMA facility will provide simultaneous interferometric observations of two objects: a bright guide star near a fainter object (separated by up to 1 arcmin). The brighter of the two objects is used as a reference for stabilizing the fringes and for the correction of the atmospheric disturbances. This will allow a longer integration time. Thanks to the ability to combine phase referencing with adaptive optics, PRIMA will increase the sensitivity of VLTI instruments and thus will give access to the observations of many faint objects within a few tens of arcseconds from bright stars. Increasing the limiting magnitude is particularly important for observations of faint objects with the AMBER instrument. PRIMA will thus offer an opportunity to observe a large sample of fainter objects (AGB stars in the Magellanic Clouds) and help to determine the size, shape, inclination and clumpiness of these sources.

MATISSE - the Multi AperTure Mid-Infrared SpectroScopic Experiment is a mid-infrared spectro-interferometer operating in the N, L, M, and Q band. The instrument will combine the light beams of up to 4 Unit/Auxiliary Telescopes of the VLTI (Lagarde et al., 2006; Lopez et al., 2006). Thanks to the ability of combination of light beams from more then two telescopes, it will allow closure phase measurements. In comparison with the current mid-infrared instrument MIDI at the VLTI, MATISSE further offers the L, M, and Q mid-infrared bands. It additionally provides the possibility to perform simultaneous observations in separate bands, tracing different regions with characteristic physical and chemical conditions. The instrument will also offer interferometric spectroscopic measurements with different spectroscopic resolutions in the range of R = 30–1000. It will allow a fundamental analysis of the composition of gases and dust grains in various environments. Along with spectroscopy, MATISSE will provide first high-resolution image reconstruction (on angular scales of 10–20 mas) in the entire mid-infrared (more telescopes offer better *uv* coverage). Thus in summary, MATISSE will extend the astrophysical potential of AMBER and MIDI at the VLTI being an efficient instrument for image reconstruction. This will among others allow to investigate the asymmetric brightness distribution of AGB stars.

GRAVITY is one of the forthcoming VLTI instruments assisted with adaptive optics. It operates in near-infrared and it is designed for precision narrow-angle astrometry and interferometric phase referenced imaging of faint objects. In comparison with the present goal for PRIMA, it

will push the astrometric accuracy for narrow angle astrometry with the VLTI by a factor of 10. GRAVITY as well as MATISSE will utilize the unique 2" field of view of the VLTI concept. GRAVITY thus offers the combination of sensitivity and accuracy in no competing worldwide facility standards. It will allow to observe obscured targets (OH/IR) which are too faint in the V band to be observed with current instruments.

All presented capabilities will enable us to address directly a number of fundamental scientific issues that are nowadays at the top of the list of challenges for future astronomical high resolution instrumentation.

10.5.2 Infrared interferometric observations at the LBT

One of the challenging technical projects of present astronomical research is the construction of the Large Binocular Telescope (LBT). The LBT represents a new era of observational astronomy. The design and observational technology of the instrument have overcome several limitations. LBT will be the worlds largest single telescope in the next several years. It is located on the 3190 m high Mount Graham in Arizona. LBT was built by members of an international consortium consisting of the University of Arizona, the Arcetri Astrophysical Observatory (Florence), MPIA (Heidelberg), the MPI for Radioastronomy (Bonn), the University of Cologne, and other US-American institutes. The LBT joins two hyperbolic mirrors with 8.4 m diameter, each on a single common mount. The separation of the outer rims of both primary mirrors, the "baseline" relevant for interferometry, is 23 meters. The light waves reflected off both primary mirrors are superimposed coherently (in phase) to create an interferometric pattern. By combining the light beams coming from both 8.4 m mirrors the instrument can achieve the same resolving power as a single 23 m mirror. This will be accomplished by the complex LINC-NIRVANA instrument (Herbst et al., 2003; Ragazzoni et al., 2003), which combines adaptive optics (AO) and optical interferometry. The distortion of the flat wavefront of light coming from the object is measured in LINC-NIRVANA over the total field of view of both primary mirrors using several wavefront sensors. The image of a reference star will be analyzed up to 1000 times per second. This information is used to continually deform two small flexible mirrors installed in the light path so that the wavefront reflected off them becomes flat and the image of the reference star (and thus of all objects within the field of view) always keeps the maximum image sharpness achievable by an 8.4 m mirror. The LINC-NIRVANA instrument is working at wavelengths between 0.6 and 2.4 μm (optical to near infrared), and delivers true images in the Fizeau interferometric mode. It is complemented by MegaMIR - The Megapixel Mid-infrared Instrument, which is a proposed Fizeau-mode camera in mid-infrared and provides a full field of view. This relatively wide field of view offers a big advantage over the interferometry done at the Very Large Telescope, and will allow observations of highly complex and faint sources.

10.5.3 Infrared interferometric observations at the ISI

The ISI array at U.C. Berkeley is currently developing a new digital spectrometer-correlator system which is being built in collaboration with the Center for Astronomy Signal Processing and Electronics Research (CASPER). The new correlator uses high-speed digital signal processing of the heterodyne signals and the $\sim$3 GHz band will be divided into 64 spectral channels giving a spectral resolution of $\sim$600000 (although the upper and lower sidebands will overlap). This new system will obtain visibility measurements on-and-off individual molecular spectral lines in order

to trace the distribution of gases in extended stellar atmospheres. The stellar continuum will also be observed without confusion due to the molecular gases, allowing more precise determinations of the continuum sizes and features than have been seen before in the 11 μm region. Testing of the system is underway and spectroscopic-interferometry observations will be conducted in 2011 (Wishnov - private communication).

The future aim is to study the evolution of the spectral signatures during the pulsation cycle and to understand the relationships between the stellar pulsation and the opacity changes in the CSE. This research field is now enhanced by the new unique capability of the ISI/spectrometer-correlator system. It allows visibilities to be measured at the frequencies of molecular spectral lines. This will determine the location of molecules relative to the stellar continuum. The spatial distribution of various molecules will help map the temperature and density profile of an extended stellar atmosphere. These studies will help identify the formation processes of various molecules and will resolve questions regarding the presence, composition, temperature, and opacity of atmospheric layers.

Future goals will be to answer the following questions: What is the temperature gradient surrounding these stars? What are the radial distributions of different molecular species and does this vary during the luminosity cycle? What are the velocities of the various gases? What is the measurable influence of shocks on molecular spectral lines and visibilities? How do the locations of various species like H_2O compare to the locations of masers in CSEs?

10.6 VISIR spectroscopy

Our model simulations indicated that detections of pulsation effects at mid-infrared wavelengths would, in particular, benefit from smaller uncertainties in the photometric spectrum compared to our current data. Therefore additional independent photometric observations would certainly help to determine optimal model and dust shell parameters describing the stellar atmosphere. The aim is to observe our targets with the VLT spectrometer and imager for the mid–infrared (VISIR) located at the Cassegrain focus of UT3. VISIR provides diffraction-limited imaging at high sensitivity in the N band, and in addition, it features a long-slit spectrometer with a range of spectral resolutions between 150 and 30000. Using high resolution spectroscopy of emission lines in the mid-infrared, a map of gas dynamics could be obtained. With reliable flux measurements we could precisely calibrate MIDI flux values. As well as for MIDI observations of our variable targets, several epochs of VISIR observations would be convenient for proper conclusions.

10.7 Comparison with other multi-epoch observations of evolved stars

10.7.1 Comparison with multi-epoch observations of carbon-rich stars

The goal of this thesis was to help to understand the role of stellar pulsation and its connection to dust formation, and mass loss process. All presented conclusions are based entirely on oxygen-rich Mira variable stars. A further aim is to compare multi-epoch observations of O-rich AGB stars to multi-epoch observations of C-rich stars (in particular observations conducted at the VLTI). This comparison study will show the differences between stars with diverse dust chemistry over

their pulsation periods. The physical properties of the outer atmosphere of carbon stars and their variations over pulsation cycles have not yet been well studied. So far the only observations of C-rich stars R Scl and V Oph with the MIDI instrument was presented by Sacuto et al. (2011) and Ohnaka et al. (2007). Ohnaka et al. (2007) modeled V Oph using a dust shell, consisting of amorphous carbon (AMC) (85%) and SiC (15%), with a multi-dimensional Monte Carlo code (Ohnaka et al., 2006), complemented by a polyatomic molecular layer, consisting of C_2H_2 and HCN, where the opacities of these molecules were calculated with an appropriate band model assuming local thermodynamic equilibrium (LTE). For a better understanding of the physical processes responsible for molecule and dust formation close to the star, it is necessary as for the oxygen-rich stars, to compare the data to dynamic model atmospheres (Sacuto et al., 2011; Mattsson et al., 2010; Paladini et al., 2009). This modeling is crucial for identification of individual components and their relative contribution to the emission across the stellar atmosphere and circumstellar envelope. Sacuto et al. (2011) modeled the data using a self-consistent dynamic model atmosphere to discuss the dynamic picture deduced from the observations. Other multi-epoch observations have been already conducted for the carbon-rich stars V Aql, T Sgr, U Hya, and V Hya. Multi-epoch data for V Hya has been compared to the equivalent UD and FDD diameters (Zhao-Geisler - private communication).

10.7.2 Comparison with multi-epoch observations of red supergiants

In our program, we have also obtained multi-epoch observations of the red supergiant AH Sco between 12/04/2004 and 04/07/2007. Red supergiant stars (RSGs) represent a similar phase in stellar evolution as AGB stars, but for stars with high masses later exploding as a supernovae. Atmospheres of red supergiants, as well as atmospheres of AGB stars, become very extended and cool, even though they are not a prior supported by large amplitude pulsations as low-mass stars. RSG can exhibit very strong mass-loss rates of up to 10^4 $M_\odot$ /yr. In comparison with low-mass AGB stars, the atmospheric structure of red supergiants is not yet understood to the same detail. It is very important to study the evolution phase of the strong mass-loss process and to understand further stellar evolution of RSG stars. For the understanding of the mass-loss process and further evolution of massive stars toward supernovae, it is crucial to obtain the atmospheric intensity profile. Our visibility data will be compared to new available atmosphere models. The goal is to investigate whether the atmospheres of higher mass stars are significantly different compared to stars with lower masses. Tsuji (2000) previously confirmed the presence of water in these early M supergiant stars and suggested a possible presence of a gaseous component not as hot as the chromosphere but warmer than the cool expanding envelope. Recent studies of RSG Betelgeuse (α Orionis) with MIDI at the VLTI were reported by Perrin et al. (2007). The results confirmed the MOLsphere model (a molecular shell, the MOLsphere) (Tsuji, 2000), and brought evidence for more constituents and for the presence of species participating in the formation of dust grains in the atmosphere of the star, i.e. well below the distance at which the dust shell is detected. We believe that our investigations will bring more information and will help for general understanding of mass loss in red supergiant stars.

All the data will further improve our general understanding of the processes leading to the fundamental mass-loss process occurring during the last stage of stellar evolution. The data will be also used to constrain and refine the complete models of the stars and surrounding environment.

Chapter 11

Conclusions

This thesis presented multi-epoch interferometric observations of evolved stars on the Asymptotic Giant Branch (AGB). We observed the stars over several pulsating cycles using the near-infrared AMBER and mid-infrared MIDI instruments at the Very Large Telescope Interferometer (VLTI) of the European Southern Observatory located on Cerro Paranal in Chile. We obtained multi-epoch MIDI observations of the oxygen-rich Mira variables RR Aql (13 epochs), S Ori (14 epochs), GX Mon (12 epochs), and R Cnc (2 epochs) and individual AMBER observations of RR Aql and R Cnc. We have investigated the circumstellar dust shell and characteristics of the atmosphere. The presented data are modeled using basic models of uniform disks and Gaussian profiles. The AMBER data, along with the basic models, were modeled using the dust-free self-excited dynamic model atmospheres including the continuum forming photosphere and overlying molecular layers (Ireland et al., 2004b,a). In addition to the basic models, the MIDI data were fitted to a combination of a radiative transfer model of the circumstellar dust shell and a dust-free dynamic model atmospheres based on self-excited pulsation model representing the central stellar intensity profile. The dust shell is modeled using the radiative transfer code, mcsim_mpi (Ohnaka et al., 2006). The data are compared to the best modeling approach currently available.

The observations were acquired at many various projected baselines lengths and position angles allowing us to meaningfully compare the data observed with the *same* projected baselines lengths and position angles, and to monitor the photometry and visibility spectra over the pulsation cycle(s) of the stars.

The investigation provided the following conclusions:
(i) The obtained interferometric data of all oxygen-rich Mira variable stars do not show evidence of intra-cycle visibility variations within our uncertainties (5%–20%) and within our examined phase coverage (RR Aql phase coverage mostly $\Phi_{\rm vis} \sim 0.45$–0.85, S Ori ~ 0.90–1.20, GX Mon $\sim$ '0.25'–'0.65', and R Cnc) ~ 0.95–1.10. (ii) The data also do not show evidence of cycle-to-cycle visibility variations. (iii) The data exhibit intra-cycle and cycle-to-cycle photometry variations at 8–13 with a significance of 1–5σ. However, the photometry data exhibit large uncertainties, therefore, based on our observations the photometry variations cannot be confirmed. Follow-up observations with higher accuracy using a dedicated photometric instrument, such as VISIR at the VLT, are needed to confirm this result.

This study represented the first comparison between interferometric observations and a combination of a radiative transfer modeling of the dust shell with dynamic models describing the central intensity profile over an extended range of pulsation phases covering several cycles. Our study shows that the photometric and visibility spectra for all stars can be well described by the combination of the models. We found, for all the epochs, the best fitting models consisting of a dynamic model atmosphere, and dust shells parameters including the optical depth of the dust shell, the inner boundary radius, the power-law index of the density distribution, and the photospheric angular diameter. We examined two dust species, Al_2O_3 and silicate grains, with fixed grain sizes of 0.1 μm.

We showed that the optically thin dust shell of RR Aql can be well modeled using silicate grains alone, with the silicate inner boundary radii of 4–5 photospheric radii. The addition of an Al_2O_3 dust shell did not improve the model fit. However, the model simulations indicate that the presence of an inner Al_2O_3 dust shell with low optical depth compared to the silicate dust shell can not be excluded. The results show that the dust shell of GX Mon can be well modeled using a combination of Al_2O_3 and silicate dust grains, with the Al_2O_3 inner boundary radii of 2–2.5 and the silicate inner boundary radii of 4–5 photospheric radii. The dust shell of S Ori and R Cnc can be well modeled using only Al_2O_3 dust grains without a contribution of silicates, with the inner boundary radii of 2–2.5 radii. Our results are consistent with the results by Lorenz-Martins & Pompeia (2000) based on IRAS data.

Our results together with the mass loss rates adopted from the literature may imply the following dust condensation sequence: R Cnc with Al_2O_3 dust chemistry ($\dot{M}$ of 0.2 10^{-7} $M_\odot$/year), S Ori with Al_2O_3 dust chemistry ($\dot{M}$ of 2.2 10^{-7} $M_\odot$/year), GX Mon with Al_2O_3 and silicate dust chemistry ($\dot{M}$ of 5.4 10^{-7} $M_\odot$/year), and RR Aql with silicate dust chemistry ($\dot{M}$ of 9.1 10^{-7} $M_\odot$/year). These results would point in the direction of hypothesis suggested by Little-Marenin & Little (1990) and Blommaert et al. (2006) that the dust content of stars with low mass-loss rates is dominated by Al_2O_3 grains while the dust content of stars with high mass-loss rates will predominantly exhibit substantial amount of silicates.

We performed model simulations using variations of model phase and dust shell parameters in order to investigate the expected variability of our mid-infrared photometric and interferometric data. The simulations confirmed that significant intra-cycle and cycle-to-cycle visibility variations are not expected at mid-infrared wavelengths within our uncertainties. The effects to the pulsation on the mid-infrared flux and visibility values are expected to be less than 25% and 20%, respectively, and are too low to be detected within the measurement uncertainties.

The results from the project will allow refinements and enhancements of state-of-the-art dynamic model atmospheres and radiative transfer modeling codes, as well as new models describing the mass-loss process and the wind driving mechanism. Future observations aiming at characterizing and constraining such new models would benefit from obtaining more precise photometry values using a dedicated instrument such as VISIR at the VLT, the addition of most suitable baselines derived by our simulations, and a more complete phase coverage of the pulsation cycle. Additional concurrent spectrally resolved near-infrared interferometry would be also needed to stronger constrain atmospheric molecular layers located close to the photosphere.

Appendix A

Instrument project for AMBER: Selection of the 'Star of the month'

This section describes the Instrument Operation Team (IOT) project, selecting a spectrophotometric calibrator 'star-of-the-month' for the AMBER instrument. The aim is to find 6 to 8 standard spectrophotometric calibrators covering the full observing period. These calibrators will be observed at the beginning of each night, and therefore they should be uniformly distributed over the Right Ascension (RA) range from 0h to 24h. The spectrophotometric calibrators ('stars-of-the-month') have to fulfill several constrains in order to obtain a reliable response from the instrument. These constrains include:

- -10 < Declination (DEC) < -40
- uniform spread of RA from 0h to 24h
- unresolved by the AMBER instrument, vis > 0.9
- $3 < \mathrm{K}_{mag} < 4$
- well referenced star (Simbad)
- ideally already observed with the VLTI

In addition to the introduced selection criteria the calibrator stars should not exhibit any significant observational features. The calibrators should be non-variable single stars, not a binary, without infrared excess or peculiar spectrum, etc. The star should not be resolved by the AMBER instrument. Instrumental visibility is calculated from the known diameter using model of the UD. For the computation of the visibility the longest of the VLTI's baselines (200 m) is used. The limit for the K_{mag} is between 3 to 4. The calibrator stars cannot be too bright. Such stars would be also too large, and they would not be unresolved by AMBER. The fringe tracker FINITO will be used for all the observations. The obtained data will be trended over time. The stars will be observed at a low resolution with the same instrumental setup and the same integration time etc. Otherwise it would not be possible to determine whether possible modulations are caused by the instrument effect or the physical star's undergoing processes. The advantage is to chose

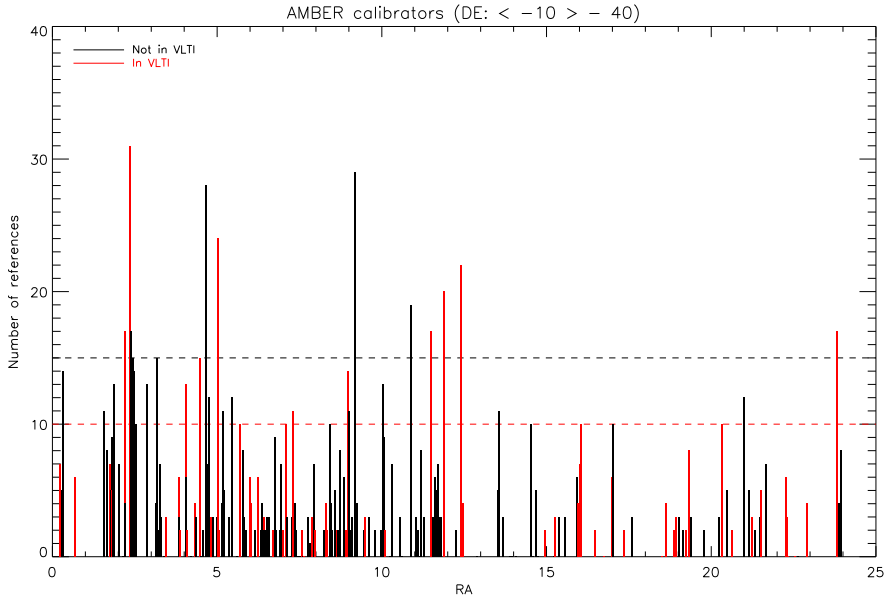

Figure A.1: The histogram of the number of references (Simbad) as a function of RA. The calibrator stars previously observed with the VLTI AMBER instrument are indicated in red lines. The histogram shows two thresholds: 15 references (black dashed line) and 10 references for stars already observed by the AMBER instrument (red dashed line). The calibrators are selected by the Declination Coordinates -10 < DE < -40.

calibrators with existing AMBER measurements. The star with well documented interferometric observations can be employ for cross-calibration.

Since no catalog of calibrator stars has been established for the AMBER instrument, the list of potential 'stars of the month' is compiled from two catalogs of calibrator stars: Catalog of calibrator stars for Long Baseline Stellar Interferometry (LBSI) Borde et al. +, Catalog of interferometric calibrator for near-IR observations with baselines up to 200 m Merand et al. + (2005). Both cataloges are well suited for AMBER. The latter catalog is an update of the Borde catalog for shortest baseline which was created from the Cohen catalog (C99) (15). Primary objects were selected from IRAS PSC objects with criteria of flux including flux > 1 Jy at 25 μm. Spectral types and luminosity classes between A0-G9 and II-IV; K0-M0 and III-V. Variable stars as well as carbon and emission-line stars were rejected from the selection. Some of the selection criteria were later relaxed and some appended, for example rejection of spectroscopic binaries and fast rotators. The selected stars must have an entry in Simbad with collected photometry data.

The calibrator star candidates were chosen using the selection criteria described above. 224 stars fulfill the constrains. These stars are shown in the Figure A.1. The histogram shows the number of references in Simbad as a function of RA. The stars previously observed with the AMBER instrument are showed in red. The threshold is set to a minimum of 15 references for calibrators not previously observed with AMBER (black dashed line), and 10 references for calibrators observed with AMBER (red dashed line). The preference is given to the calibrators previously observed with the instrument. The final selection consists of 8 stars fulfilling all the requirements. Table A.1 lists the acronym of the calibrator, RA, DEC, K_{mag}, the number of references, previous VLTI observations, visibility, and the diameter.

Table A.1: The 'star of the month' selection

calibrator star	RA	DE	K_{mag}	Ref.	VLTI	vis.	diam. [mas]
HR 693	02 22 05.0	-17 39 43.8	3.28	31	yes	0.95	1.21
HD 38054	05 42 14.5	-17 31 49.4	3.17	10	yes	0.95	1.31
HD 99923	11 29 37.5	-28 01 50.1	3.85	17	yes	0.97	1.00
HR 4558	11 54 42.5	-25 42 50.0	3.06	20	yes	0.96	1.13
HD 108110	12 25 18.4	-27 44 56.4	3.16	22	yes	0.96	1.14
HR 5973	16 03 54.7	-24 43 34.7	3.11	10	yes	0.95	1.29
HD 193302	20 20 51.9	-35 40 25.2	3.52	10	yes	0.96	1.08
HD 223428	23 49 31.6	-15 51 40.6	3.21	17	yes	0.96	1.11

Appendix B

MIDI Calibrators

The calibrators of the MIDI observations used for this study are shown in this appendix. Calibrated science target visibility spectra were calculated using the instrumental transfer function derived from the transfer functions of all available calibrator data sets. The number of available transfer function measurements depends on the number of calibrator stars observed per specific night, including calibrators observed by other programs. The Tables B.1– B.4 show all calibrators taken during the same night with the same baseline and instrumental mode as our scientific targets RR Aql, GX Mon, S Ori, and R Cnc. The Tables list: the identification of the calibrator, the spectral type, the Limb-Darkened angular diameter Θ_{LD} [mas], the effective temperature T_{eff} in K, the flux at 12 μm in Jy, the Cohen replacement for calibrators where the absolutely calibrated spectrum was not directly available, and the days of observations.

Table B.1: Main MIDI calibrators

Name	Spectral Type	Θ_{LD} [mas]	T_{eff} [K]	F_{12} [Jy]	Cohen replacement	days of observations
HD 169767	G9III	2.15±0.01	4787	8.19	HD 61935	18042005
HD 187642	A7V	3.31±0.02	7544	32.99		18062006, 14092006
HD 216386	M2III	7.58±0.03	3710			23062006, 08082006, 09082006, 14092006
HD 169916	K1IIIb	3.99±0.02	4730	29.55		09042004, 29072004, 01082004, 18042005, 19042005,20072005, 22072005, 16092006, 03072007, 04072007
HD 67582	K3III	2.30±0.01	4247	8.95		09042004
HD 220704	K4III	3.44±0.02	4089			22072005
HD 211416	K3III	5.99±0.06		56.12		23062006, 10082006, 13082006
HD 168723	K0III-IV	2.91±0.01	4930	16.23		10042004, 19042005
HD 122451	B1III	2.58±0.13		11.42		18042005, 19042005
HD 146051	M0.5III	10.03±0.10		142.85		18042006, 19042006, 25052006, 18062006, 20062006, 21062006, 23062006, 11082006
HD 218594	K1III	3.19±0.01	4500			22072005
HD 9053	M0IIIa	7.44±0.37		69.75		14092006, 16092006
HD 124897	K1.5III	20.03±0.08	4325	713.73	HD 220009	22062007, 03072007, 04072007
HD 189577	M4III	5.44±0.05	3726	47.51	HD 112213	23062006
HD 187076	M2II	7.80±0.39		102.0		21062006, 22062007, 04072007
HD 176411	K1III	2.20±0.01	4820	8.71	HD 16815	10042004
HD 178345	K0II	2.49±0.01	4619	10.70		01082004
HD 152786	K3III	6.88±0.04	4116	76.06	HD 98262	09042004, 23062006
HD 189319	M0III	5.94±0.03	3931	55.24		23062006
HD 81797	K3II-III	9.14±0.05	4189	149.72	HD 10380	09042004, 10042004, 19042006, 25052006
HD 139997	K5III	3.67±0.02	3996	18.91	HD 59381	10042004
HD 151249	K5III	5.52±0.02	3954	44.27		25052006, 20062006, 23062006
HD 4128	K0III	5.23±0.03	4871	51.71		18062006, 08082006, 09082006, 11082006
HD 142804	M1III	2.82±0.02	3726	11.38	HD 95578	18042005, 19042005
HD 107446	K3.5III	4.427±0.02	4139	30.81	HD 10380	10042004, 21022005
HD 165135	K0III	3.47±0.02	4850	20.17	HD 4128	09042004, 09072004, 28072004
HD 206778	K2Ib	7.59±0.05	4242	83.97	HD 188603	21062006, 23062006, 08082006, 09082006, 10082006, 11082006, 13082006, 14092006, 16092006, 04072007
HD 161892	K2III	3.84±0.02	4557	22.90	HD 85503	29072004
HD 37160	K0IIIb	2.20±0.02		9.37		19042005
HD 213009	G7III	2.11±0.01	4932	8.99		22072005
HD 134505	G8III	2.51±0.01	5046	12.95	HD 23249	09042004, 01082004
HD 157236	K5III	2.51±0.01	4007	9.99	HD 133774	19042005
HD 160668	K5III	2.26±0.01	4134	7.93	HD 126927	19042005, 22072005
HD 123139	K0IIIb	5.34±0.02	4804	54.71		28072004, 18042006, 19042006, 25052006, 21062006, 03072007
HD 188512	G8IV	2.07±0.01	5161	8.63	HD 23249	09072004, 01082004, 18042005, 20072005
HD 82668	K5III	7.13±0.08		72.37		09052007, 22062007
HD 120404	K7III	2.96±0.02	3838	11.59	HD 80493	18042005
HD 152885	M1III	2.89±0.03	3726	11.68	HD 196917	10042004, 19042005
HD 168454	K3IIIa	5.87±0.03	4321	58.95	HD 224889	25052006, 23062006, 10082006, 22062007, 04072007
HD 102461	K5III	2.98±0.01	3885	12.60		09052007
HD 50778	K4III	3.90±0.02	4049	23.27	HD 20644	21022005
HD 129456	K5III	3.37±0.01	4275	19.73	HD 130694	10042004
HD 177716	K1IIIb	3.75±0.02	4523	25.41		09072004, 28072004, 09052007
HD 152820	K5III	2.63±0.01	3947	9.22	HD 151249	20072005
HD 150052	K5	2.47±0.12		8.86		18042005, 19042005, 20072005
HD 150798	K2II-III	8.91±0.05	4305	132.43		21062006, 23062006, 10082006, 13082006
HD 167618	M3.5III	11.67±0.04	3612	201.52	HD 127093	21062006, 11082006, 09052007, 22062007, 03072007, 04072007

Table B.2: Main MIDI calibrators

Name	Spectral Type	Θ_{LD} [mas]	T_{eff} [K]	F_{12} [Jy]	Cohen replacement	days of observations
HD107446	K3.5III	4.427±0.021	4139	30.692	HD9138	22022006
HD89388	K3IIa	5.181±0.025	4163	42.77		16022006
HD12929	K2-IIIab	6.9±0.074		78.229		10012008, 11012008
HD25025	M0.5IIIb	8.74±0.088		108.883		16022006, 22022006, 21092006, 17102006, 18102006, 19102006, 20102006, 14112006, 17122006, 19122006, 21122006, 11012007, 13012007, 17012007, 18012007, 19012007, 20012007, 21012007, 10022007, 11022007, 12022007, 12032007, 14032007
HD45348	F0II	6.869±0.027	7779	167.597		17012007
HD224935	M3III	7.245±0.029	3584	81.948	HD127093	19102006, 02122007
HD4128	K0III	5.227±0.029	4871	51.712		21092006
HD81797	K3II-III	9.142±0.045	4189	157.703	HD83425	19122006, 21122006, 13012007, 18012007, 20012007, 21012007, 11022007, 12032007, 02122007, 11012008, 12012008, 06032008, 13032008, 01042008, 25122008, 31122008, 26022009, 04032009
HD48915	A1V	6.088±0.03	9889	193.074		22022006, 21092006, 02122007, 10122007, 29122007, 10012008, 11012008, 12012008, 06032008, 13032008, 01042008, 25122008, 31122008, 26022009, 04032009
HD167618	M3.5III	11.665±0.043	3612	201.522	HD127093	06032008
HD206778	K2Ib	7.59±0.046	4242	99.216	HD31767	18102006
HD29139	K5III	20.398±0.087	3885	644.882	HD1632	18102006, 20102006, 13012007, 17012007, 18012007, 19012007, 21012007
HD20720	M3/M4III	10.138±0.036	3596	153.428	HD127093	18102006, 19102006, 21122006
HD120323	M4.5III	13.248±0.062	3388	240.845	HD127093	13012007, 20012007, 21012007, 10022007, 11022007, 14032007, 13032008, 01042008
Kappamat		100.0±0.0001		0.1		17102006
HD18884	M1.5IIIa	12.275±0.0049	3744	218.473		17122006, 19122006, 21122006, 11012007, 13012007, 17012007, 18012007, 19012007, 20012007, 21012007

Table B.3: Main MIDI calibrators

Name	Spectral Type	Θ_{LD} [mas]	T_{eff} [K]	F_{12} [Jy]	Cohen replacement	days of observations
HD89388	K3IIa	5.181±0.025	4163	42.77		16022006
HD12929	K2-IIIab	6.9±0.074		78.229		10012008, 11012008
HD25025	M0.5IIIb	8.74±0.088		108.883		16022006, 18032006, 18102006, 11112006, 14122006, 16122006, 17122006, 19122006, 20122006, 11012007, 13012007, 18012007, 19012007, 21012007, 09022007, 10022007, 11022007, 12022007
HD81797	K3II-III	9.142±0.045	4189	157.703	HD83425	11112006, 14122006, 16122006, 19122006, 13012007, 18012007, 21012007, 09022007, 11022007, 11012008, 12012008, 06032008, 13032008, 28032008, 01042008
HD20720	M3/M4III	10.138±0.036	3596	153.428	HD127093	18102006, 16122006
HD167618	M3.5III	11.665±0.043	3612	201.522	HD127093	06032008
HD206778	K2Ib	7.59±0.046	4242	99.216	HD31767	18102006
HD29139	K5III	20.398±0.087	3885	644.882	HD1632	18102006, 14122006, 16122006, 13012007, 18012007, 19012007, 21012007
HD48915	A1V	6.088±0.03	9889	193.074		18032006, 10122007, 29122007, 10012008, 11012008, 12012008, 13012008, 22022008, 06032008, 13032008, 14032008, 28032008, 01042008
HD120323	M4.5III	13.248±0.062	3388	240.845	HD127093	13012007, 21012007, 09022007, 10022007, 11022007, 13032008, 14032008, 01042008
HD18884	M1.5IIIa	12.275±0.0049	3744	218.473		17122006, 19122006, 20122006, 11012007, 13012007, 18012007, 19012007, 21012007

Table B.4: Main MIDI calibrators

Name	Spectral Type	Θ_{LD} [mas]	T_{eff} [K]	F_{12} [Jy]	Cohen replacement	days of observations
HD81797	K3II-III	9.142±0.045	4189	157.703	HD83425	25122008, 31122008, 26022009, 03032009, 04032009
HD48915	A1V	6.088±0.03	9889	193.074		25122008, 31122008, 26022009, 04032009

Appendix C

RR Aql epochs 1 – 13

In the following all the observational epochs are presented. The plots show VLTI/MIDI interferometric observations of RR Aql at 8-13μm. The panels show (a) the flux, (b) the visibility amplitude, (c) the corresponding UD diameter, (d) the corresponding Gaussian FWHM diameter as a function of wavelength. Panel (e) shows the visibility amplitude as a function of spatial frequency for three averaged bandpasses of 8-9 μm, 10-11 μm, and 12-13 μm. The gray shade indicates the wavelength region around 9.5 μm that is affected by atmospheric absorption. The epoch of observations and the stellar phase is indicated in the panel (a). The crosses with error bars denote the measured values. The solid lines indicate our best-fitting model, as described in Sect. 5.3.5. It consists of a combination of a radiative transfer model describing the surrounding dust shell and a dust-free dynamic model atmosphere representing the central star. The contributions of the stellar and dust components alone are indicated by the dotted and the dashed line, respectively. The best fitting M model and dust shell parameters for each epoch together with projected baseline length (B_p) and position angle (P.A.) are listed below the panel (e). Symbols and colors correspond to the individual observations.

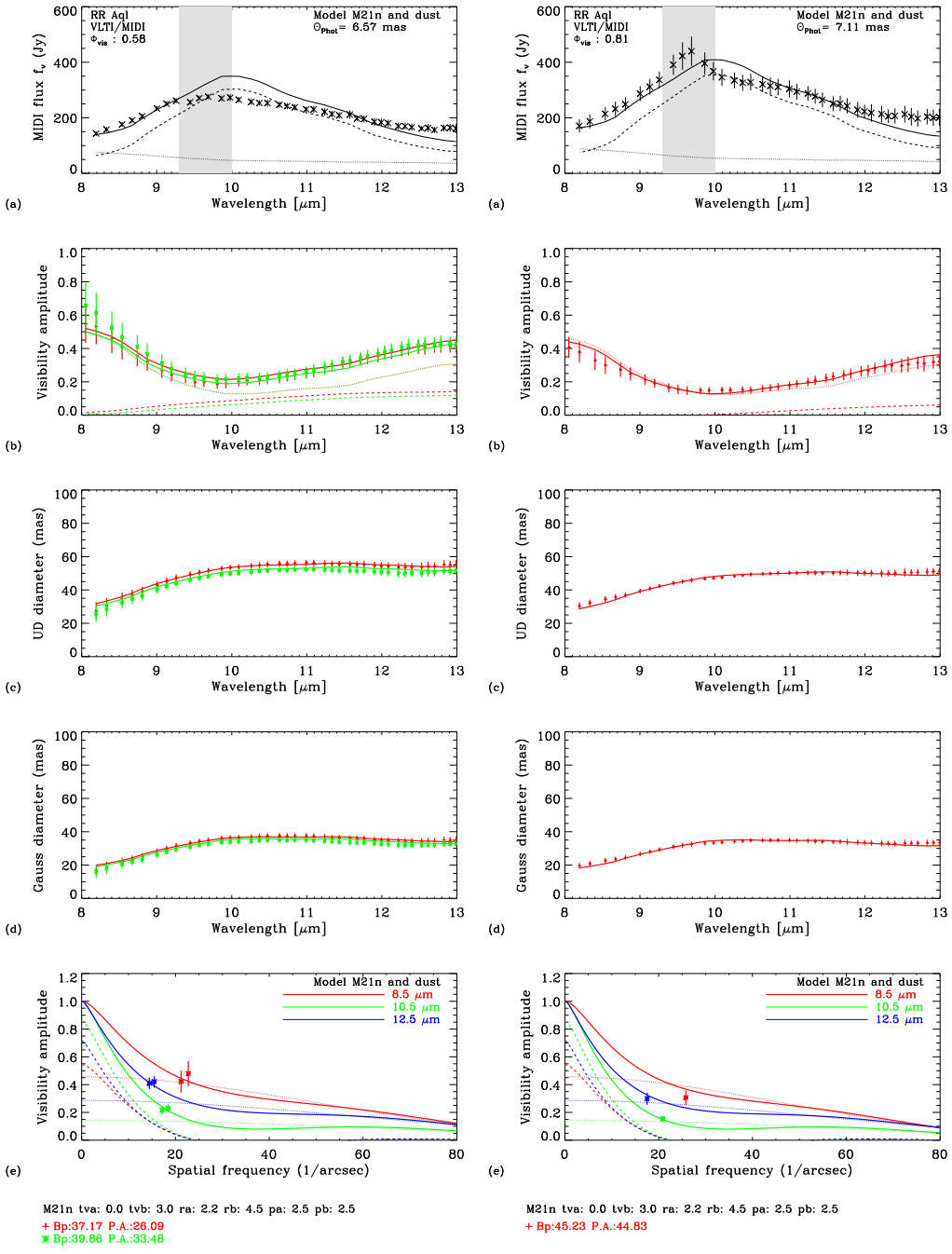

Figure C.1: RR Aql epoch A (left) and epoch B (right)

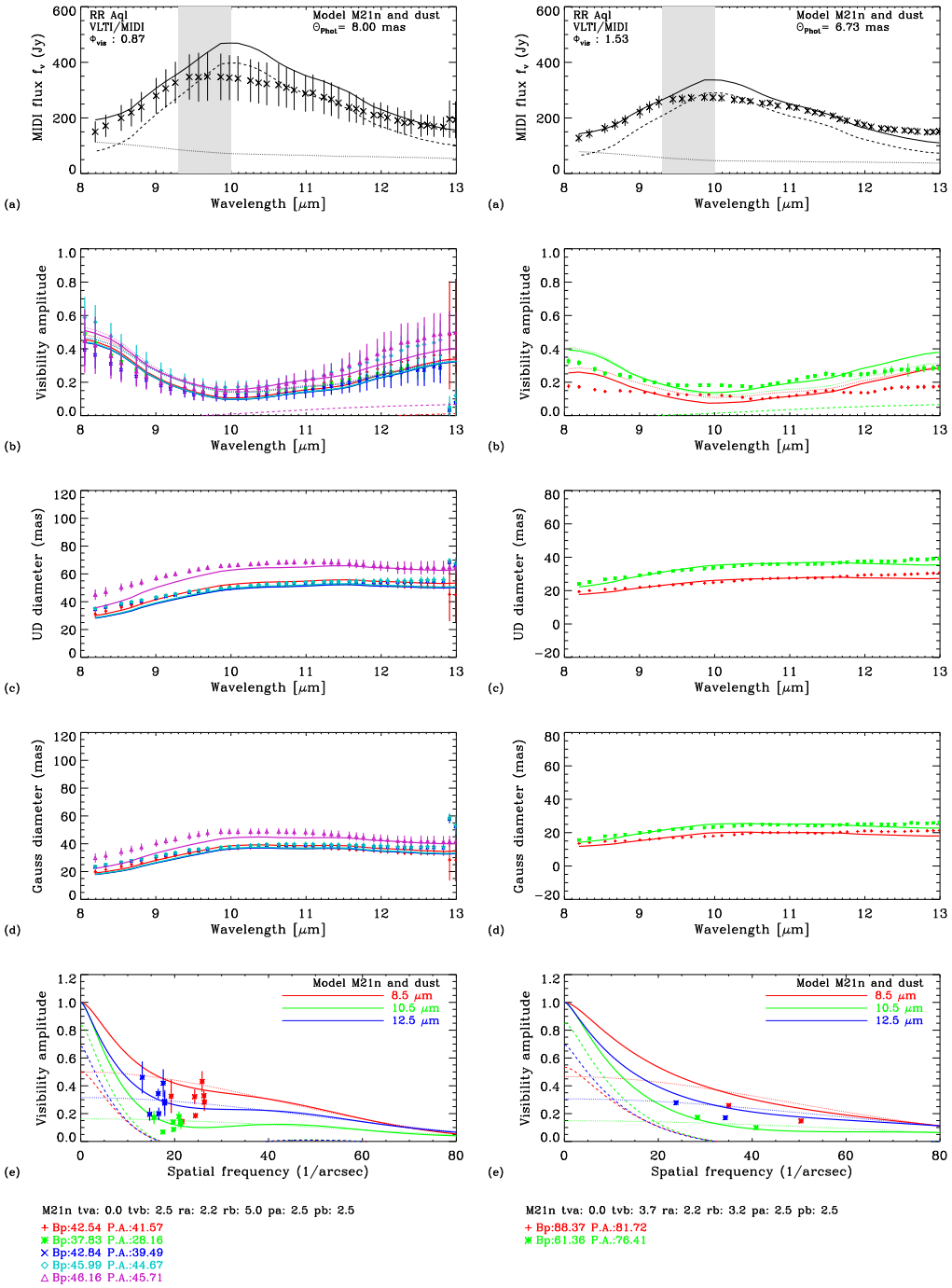

Figure C.2: RR Aql epoch C (left) and epoch D (right)

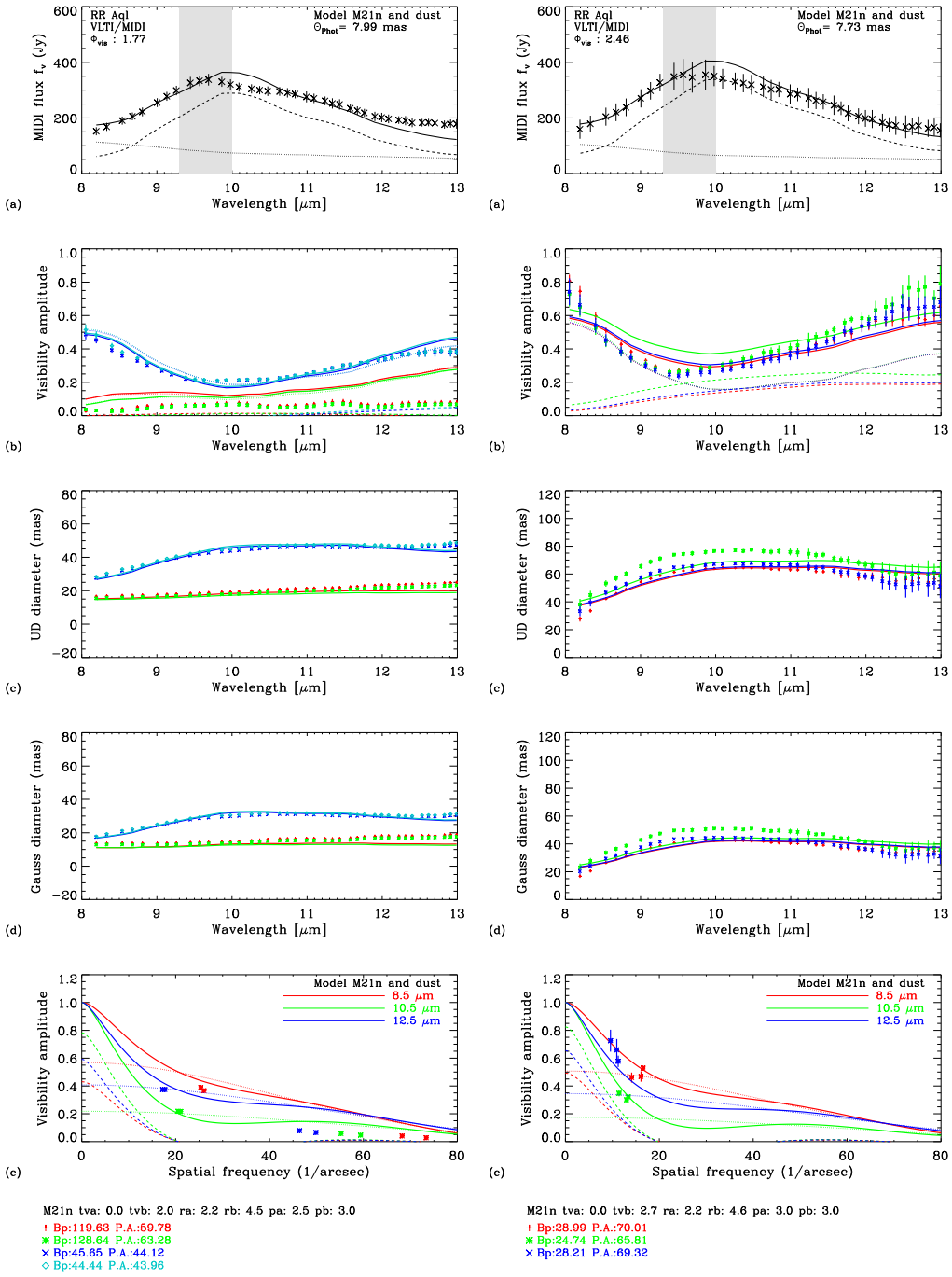

Figure C.3: RR Aql epoch E (left) and epoch F (right)

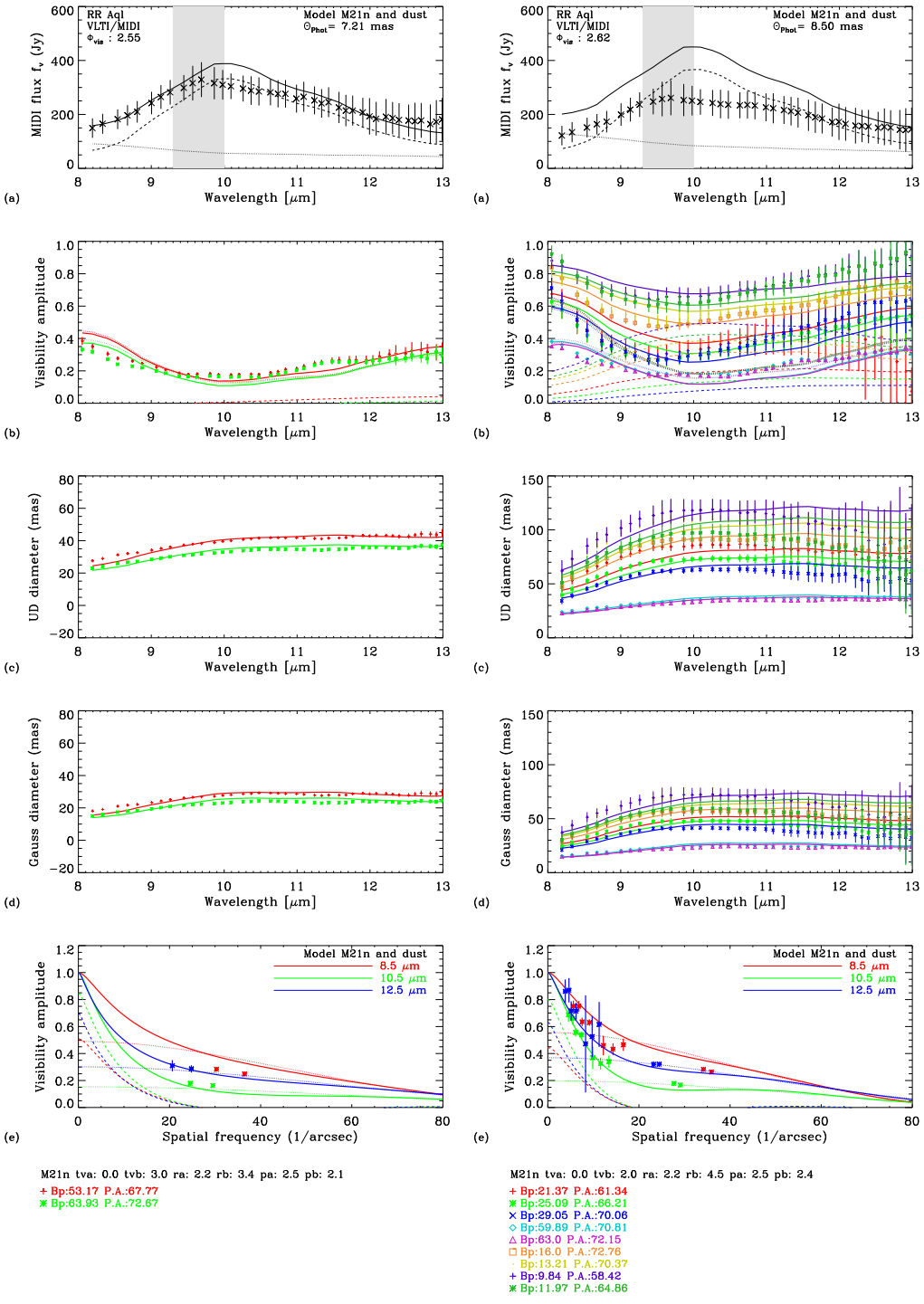

Figure C.4: RR Aql epoch G (left) and epoch H (right)

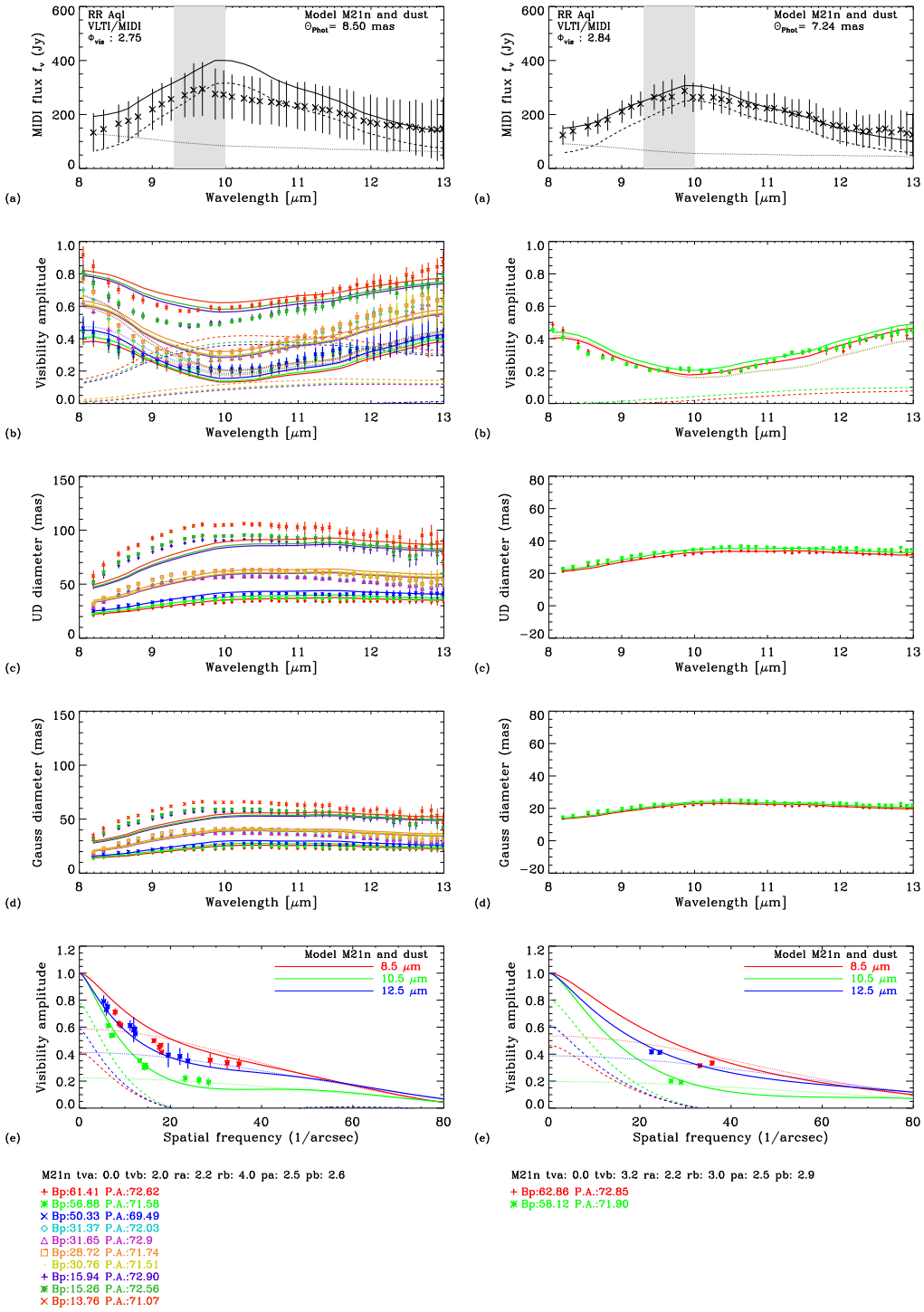

Figure C.5: RR Aql epoch I (left) and epoch J (right)

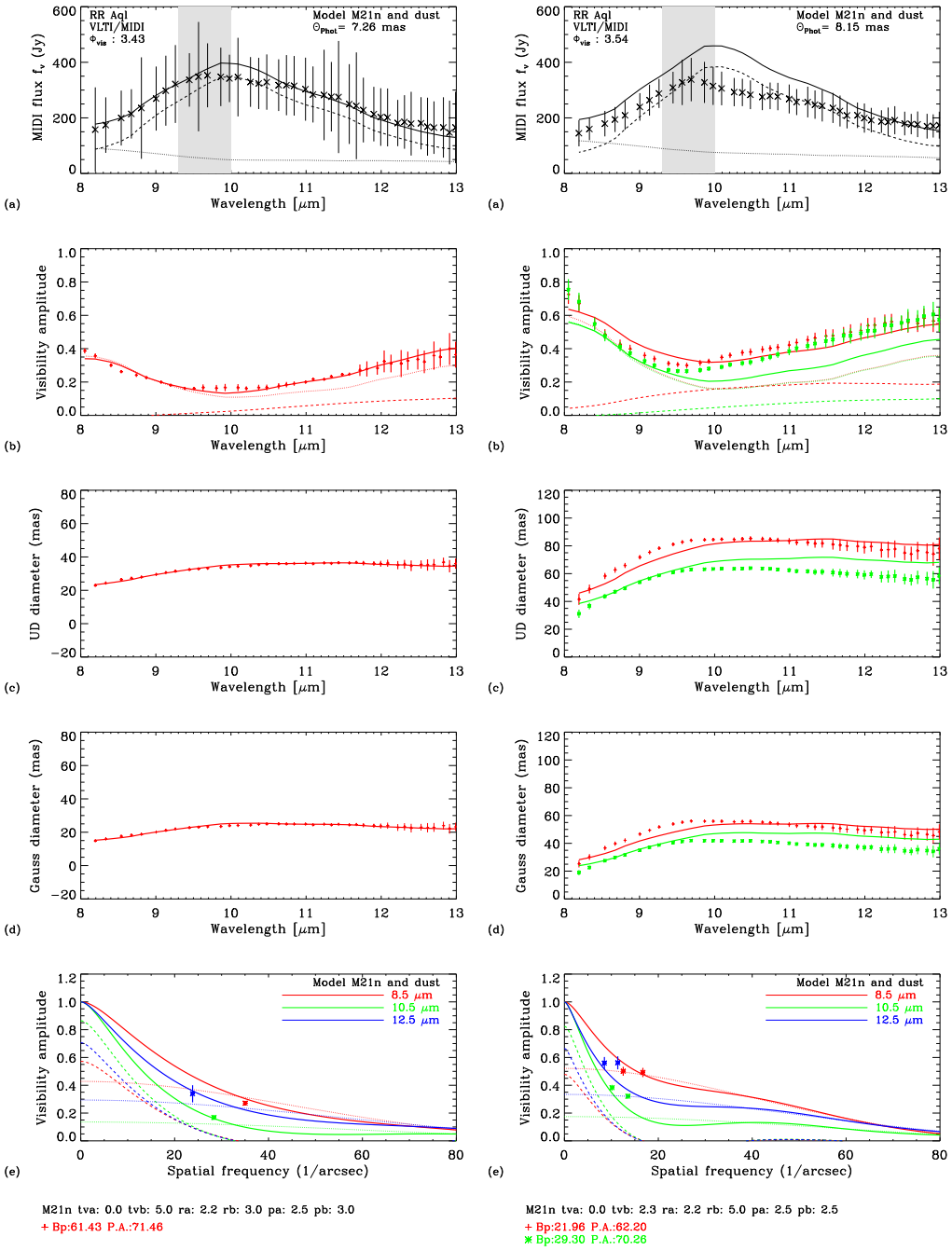

Figure C.6: RR Aql epoch K (left) and epoch L (right)

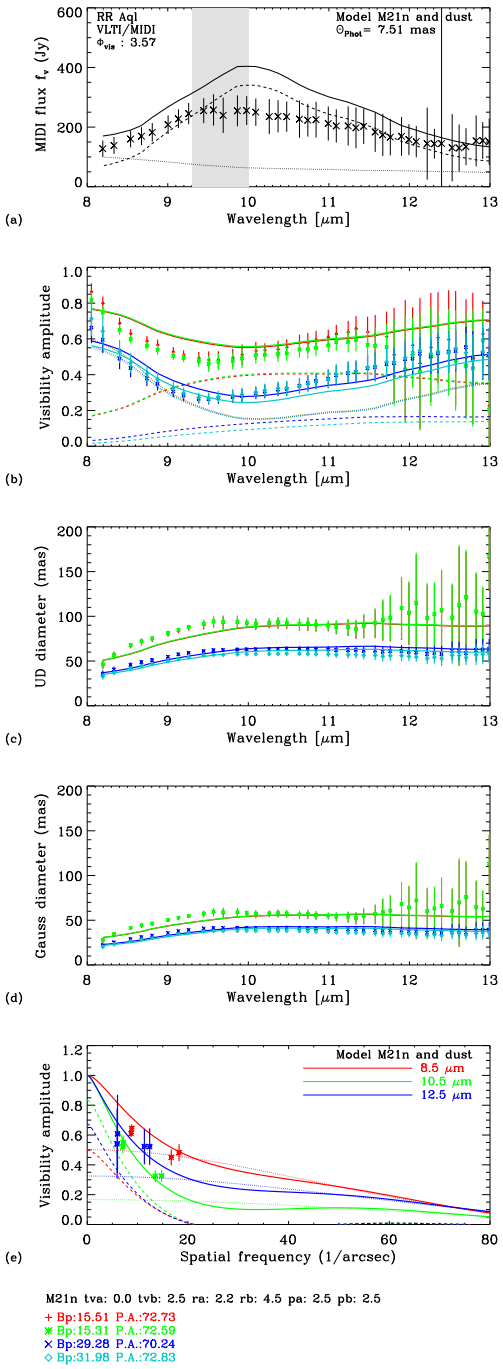

Figure C.7: RR Aql epoch M

Appendix D

S Ori epochs 1 – 14

In the following all the observational epochs are presented. The plots show VLTI/MIDI interferometric observations of S Ori at 8-13μm. The panels show (a) the flux, (b) the visibility amplitude, (c) the corresponding UD diameter, (d) the corresponding Gaussian FWHM diameter as a function of wavelength. Panel (e) shows the visibility amplitude as a function of spatial frequency for three averaged bandpasses of 8-9 μm, 10-11 μm, and 12-13 μm. The gray shade indicates the wavelength region around 9.5 μm that is affected by atmospheric absorption. The epoch of observations and the stellar phase is indicated in the panel (a). The crosses with error bars denote the measured values. The solid lines indicate our best-fitting model, as described in Sect. 7.3.4. It consists of a combination of a radiative transfer model describing the surrounding dust shell and a dust-free dynamic model atmosphere representing the central star. The contributions of the stellar and dust components alone are indicated by the dotted and the dashed line, respectively. The best fitting M model and dust shell parameters for each epoch together with projected baseline length (B_p) and position angle (P.A.) are listed below the panel (e). Symbols and colors correspond to the individual observations.

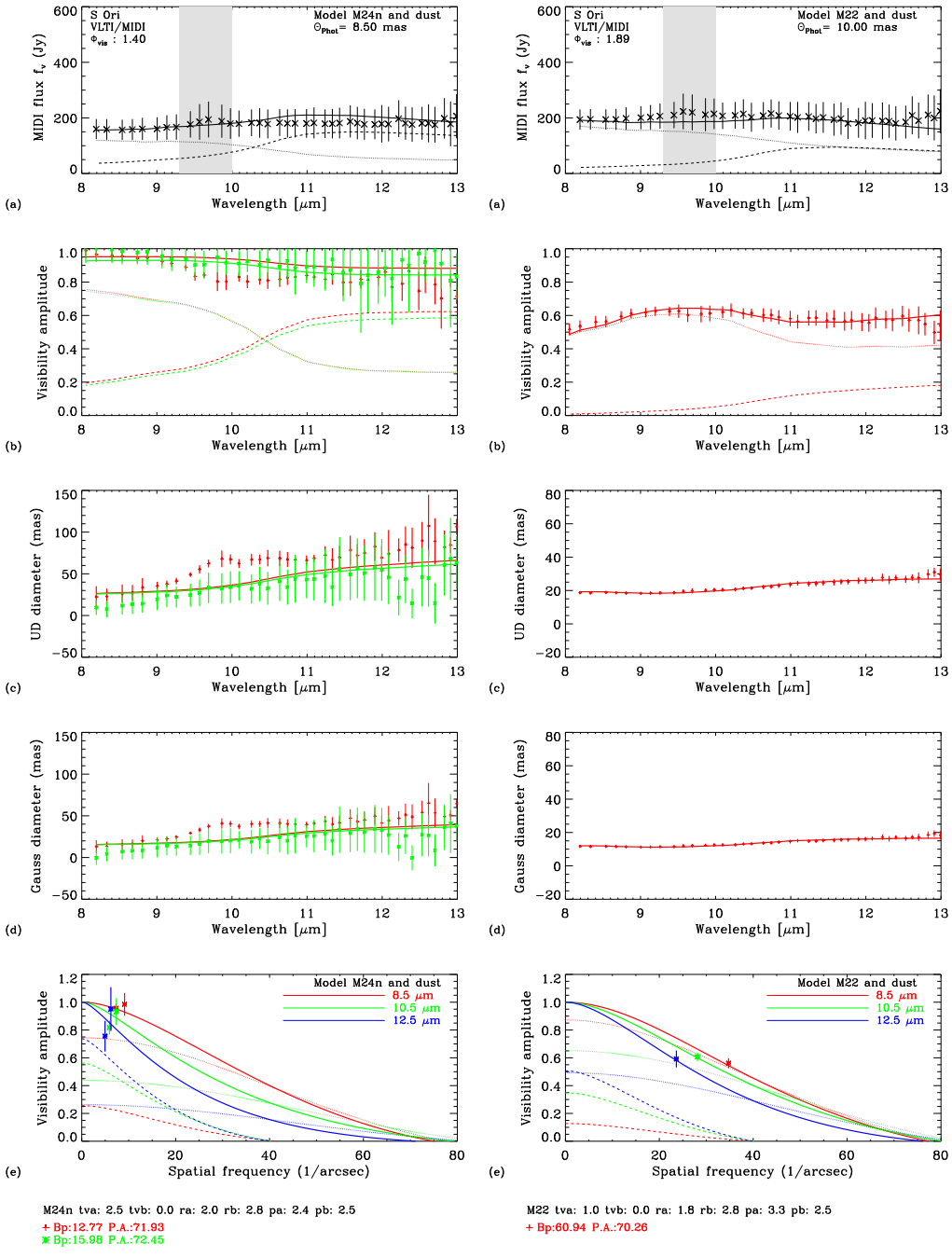

Figure D.1: S Ori epoch A (left) and epoch B (right)

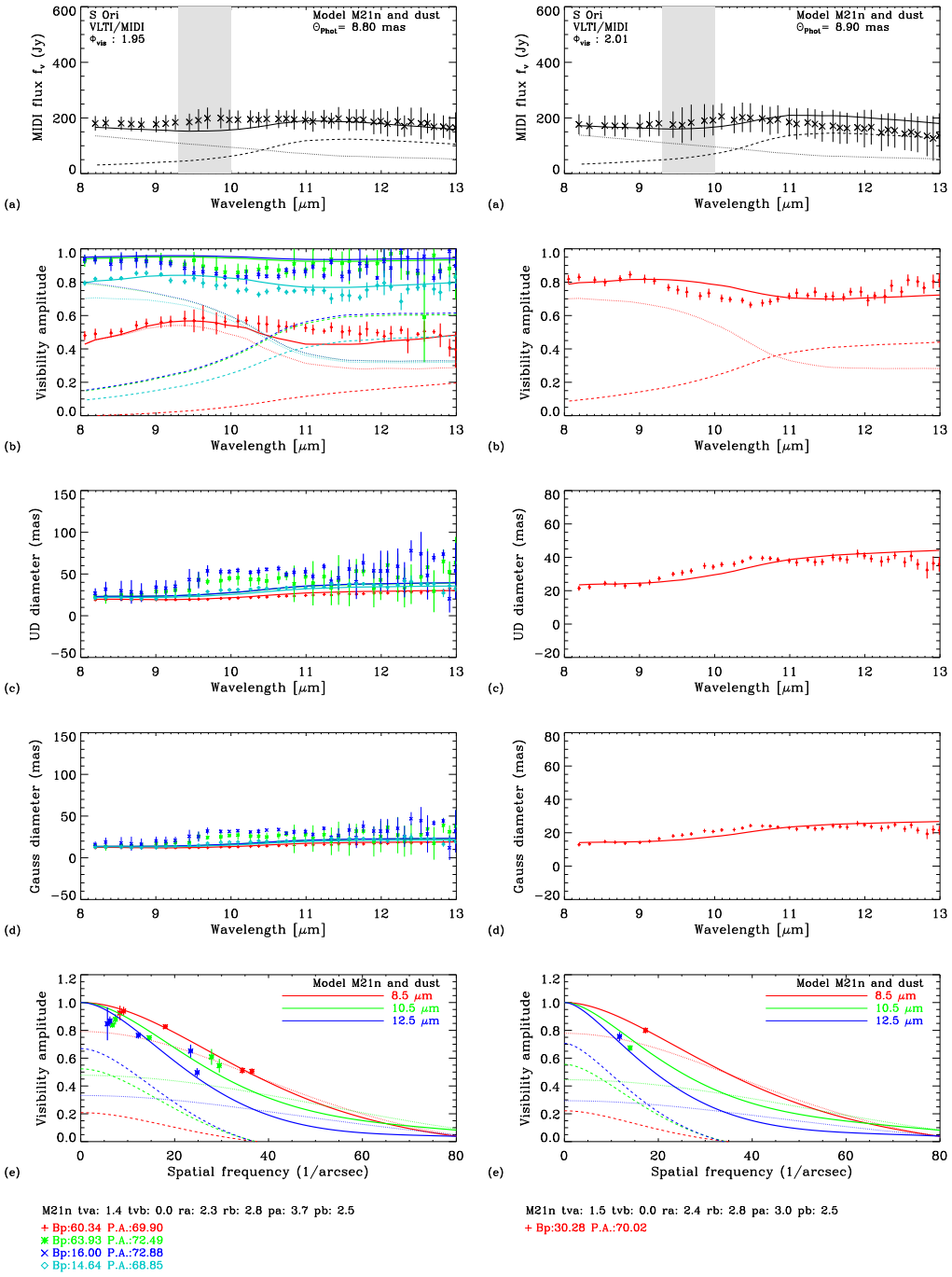

Figure D.2: S Ori epoch C (left) and epoch D (right)

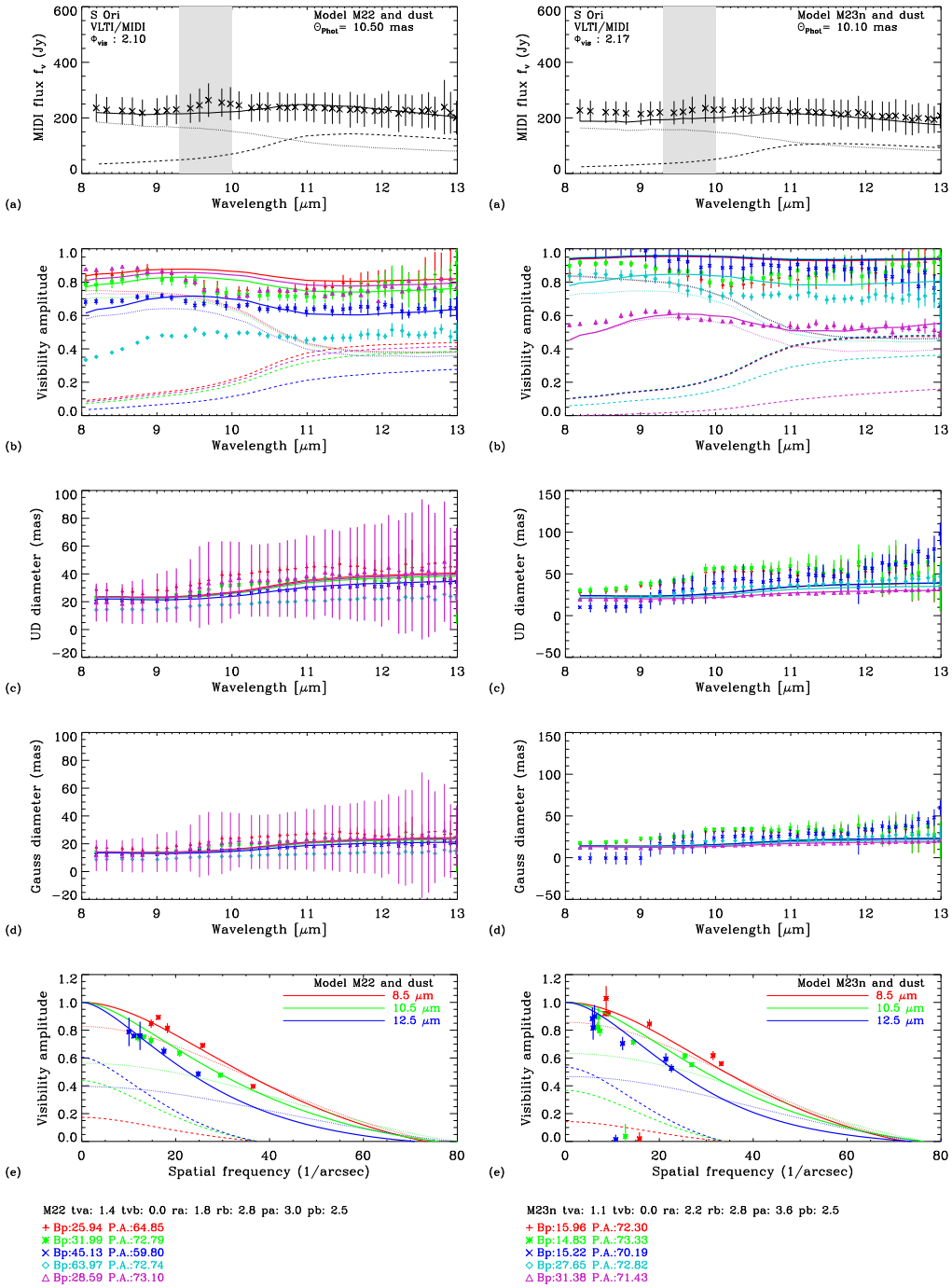

Figure D.3: S Ori epoch E (left) and epoch F (right)

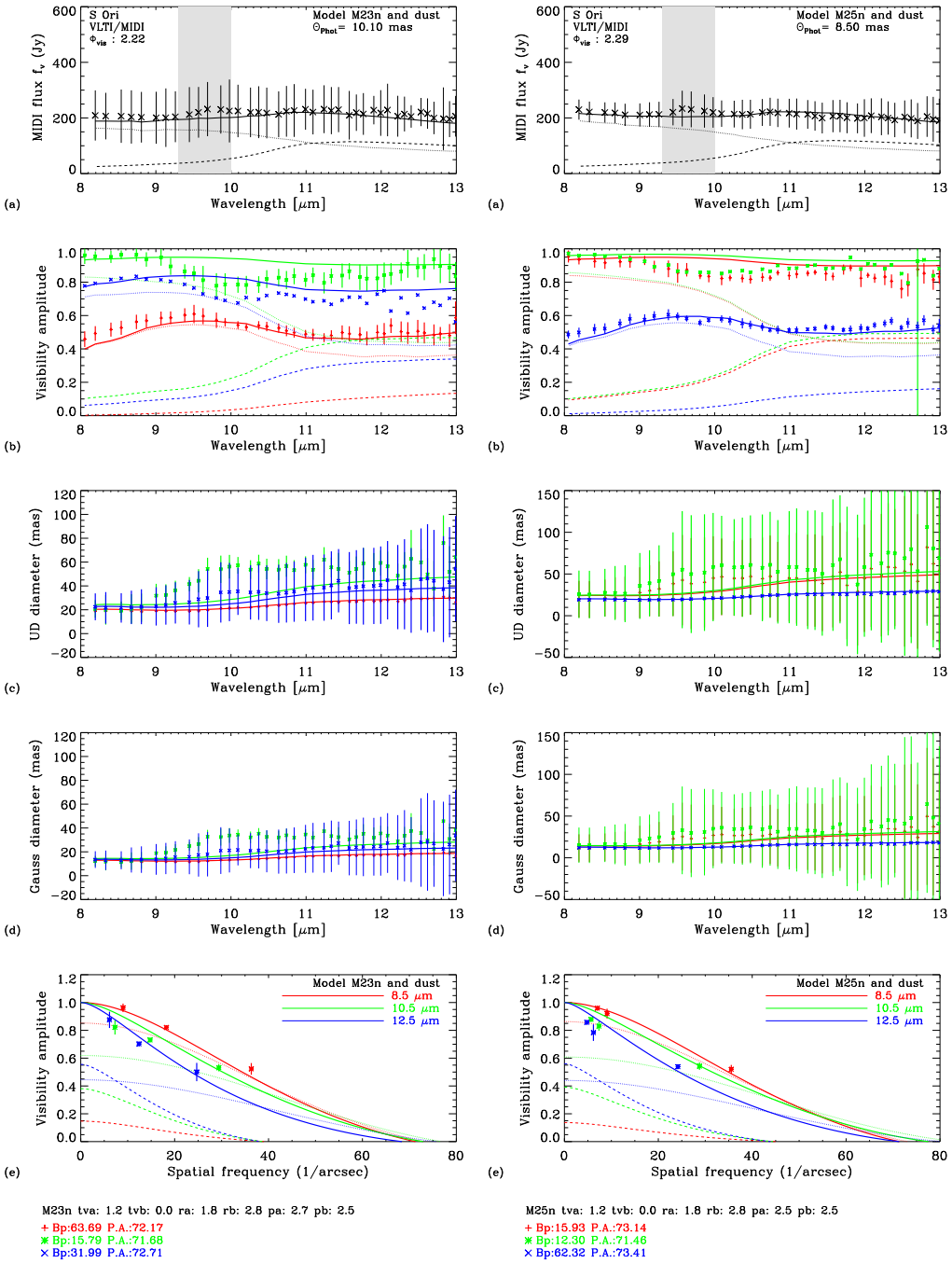

Figure D.4: S Ori epoch G (left) and epoch H (right)

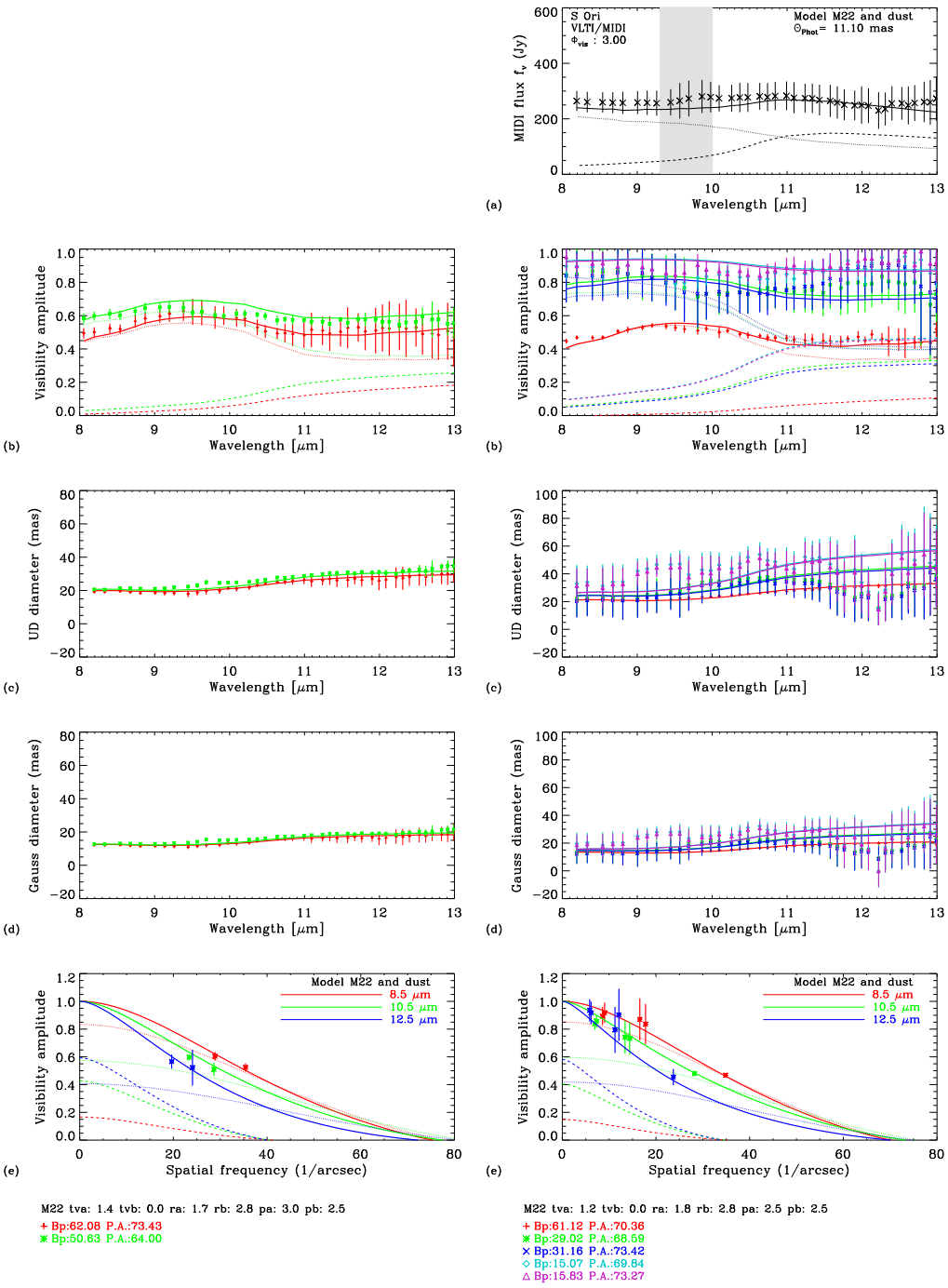

Figure D.5: S Ori epoch I (left), the photometry was due to the poor quality of the data omitted from the analysis. Epoch J (right)

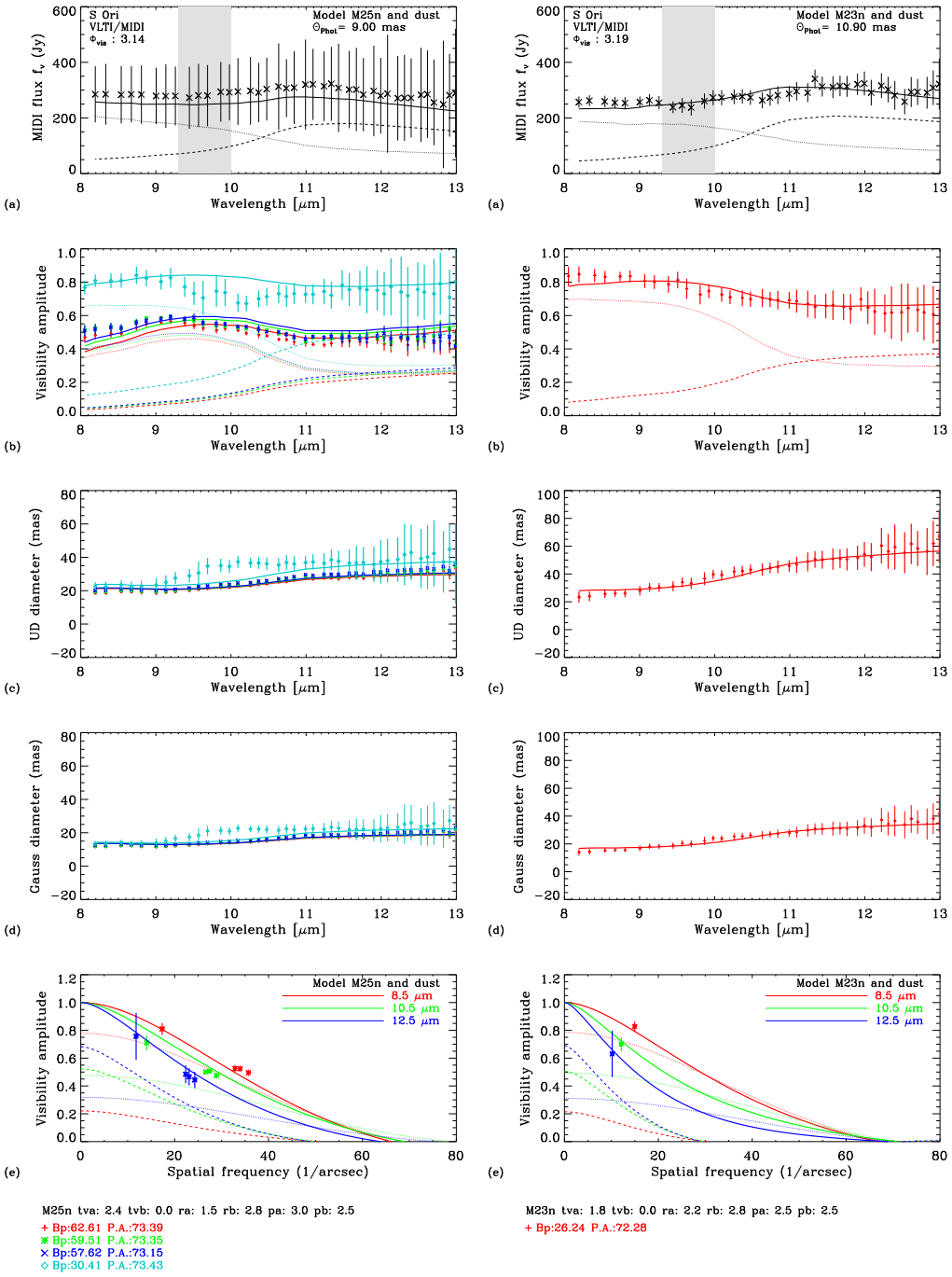

Figure D.6: S Ori epoch K (left) and epoch L (right)

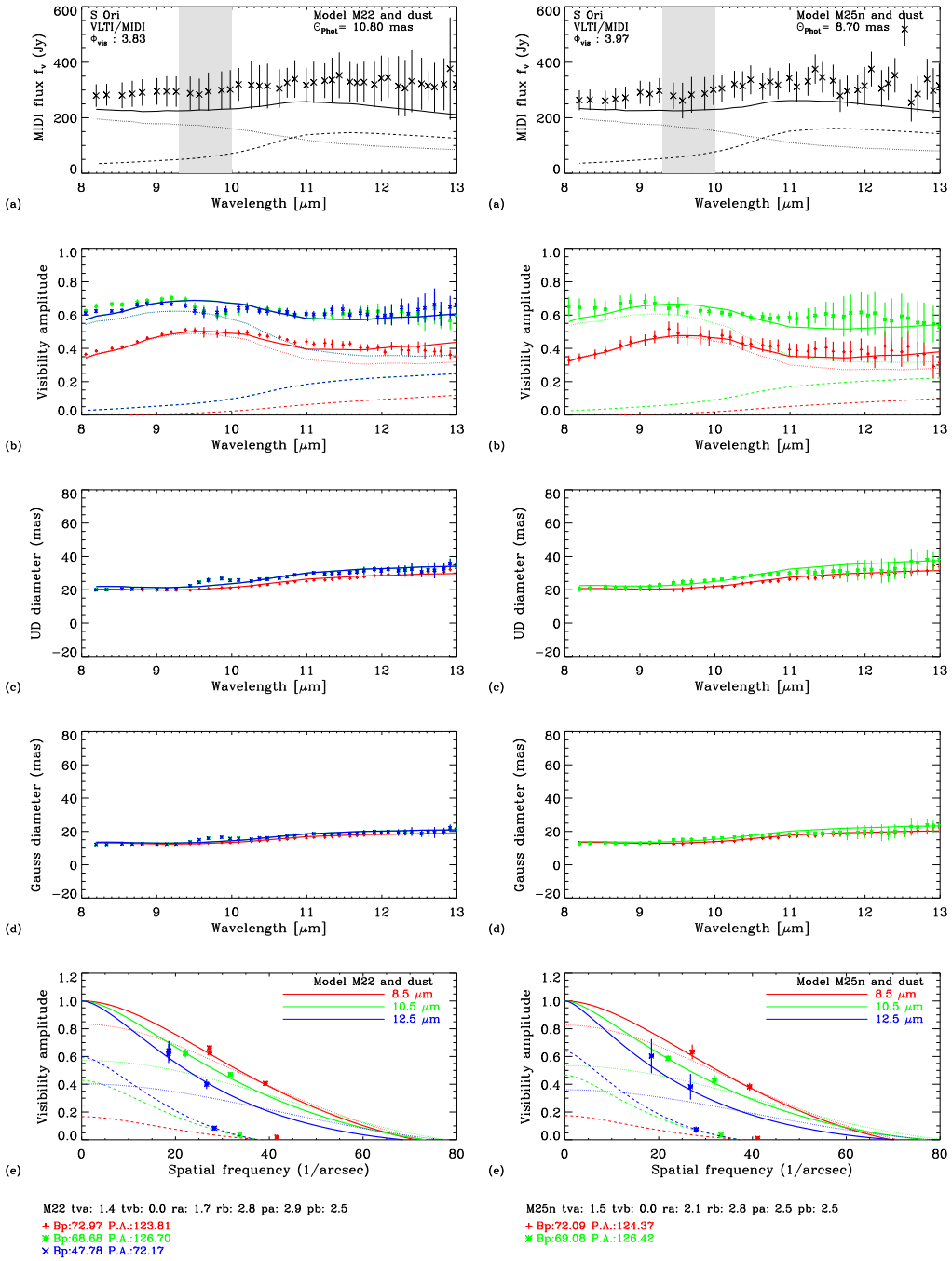

Figure D.7: S Ori epoch M (left) and epoch N (right)

Appendix E

GX Mon epochs 1 – 12

In the following all the observational epochs are presented. The plots show VLTI/MIDI interferometric observations of GX Mon at 8-13μm. The panels show (a) the flux, (b) the visibility amplitude, (c) the corresponding UD diameter, (d) the corresponding Gaussian FWHM diameter as a function of wavelength. Panel (e) shows the visibility amplitude as a function of spatial frequency for three averaged bandpasses of 8-9 μm, 10-11 μm, and 12-13 μm. The gray shade indicates the wavelength region around 9.5 μm that is affected by atmospheric absorption. The epoch of observations and the stellar phase is indicated in the panel (a). The crosses with error bars denote the measured values. The solid lines indicate our best-fitting model, as described in Sect. 8.3.4. It consists of a combination of a radiative transfer model describing the surrounding dust shell and a dust-free dynamic model atmosphere representing the central star. The contributions of the stellar and dust components alone are indicated by the dotted and the dashed line, respectively. The best fitting M model and dust shell parameters for each epoch together with projected baseline length (B_p) and position angle (P.A.) are listed below the panel (e). Symbols and colors correspond to the individual observations.

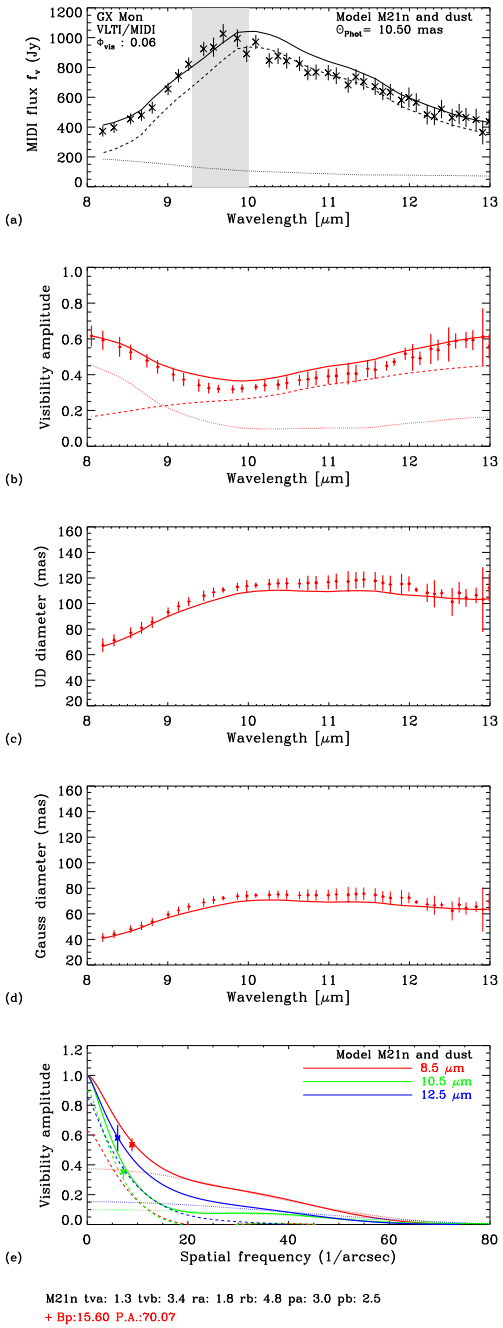

Figure E.1: GX Mon epoch B

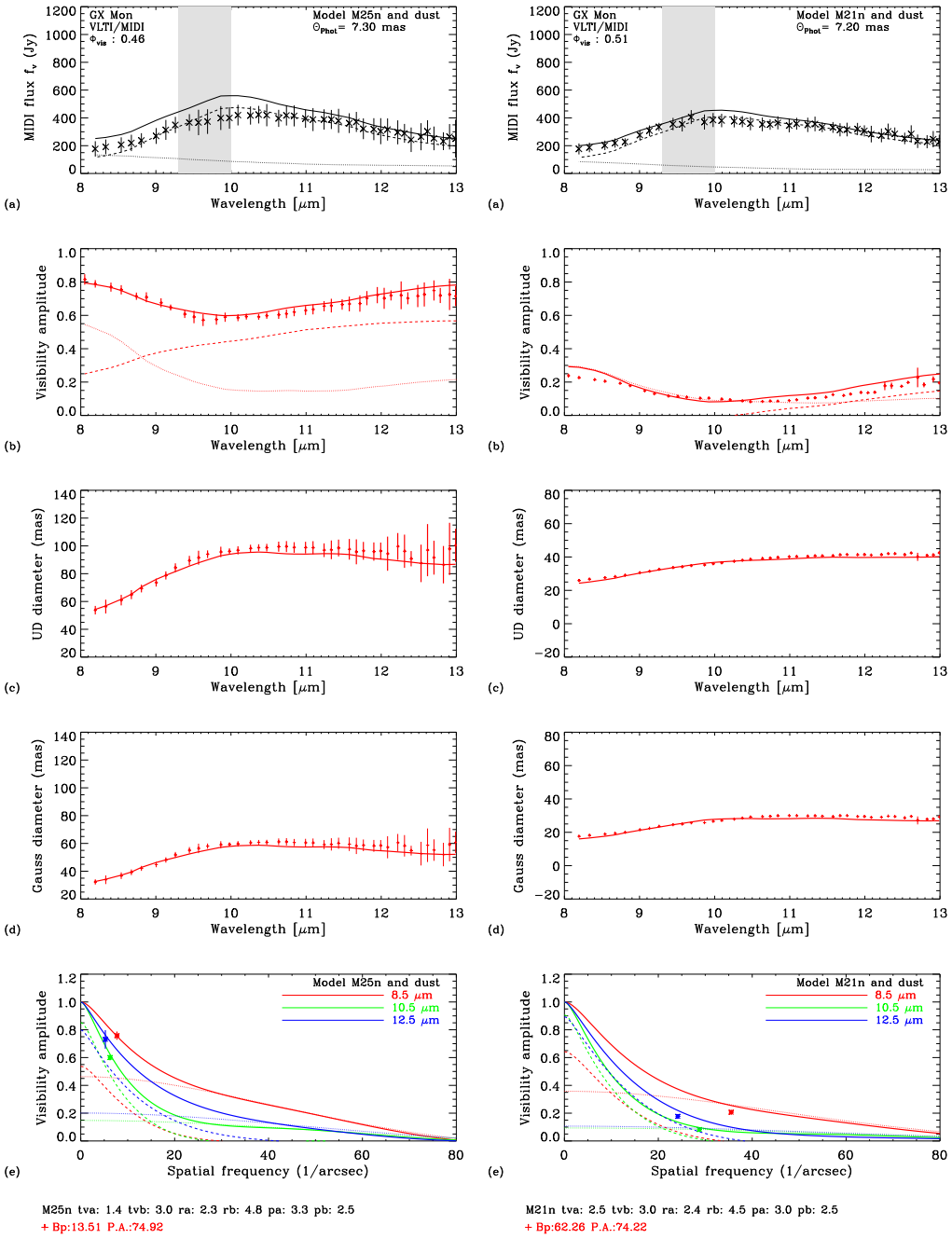

Figure E.2: GX Mon epoch C (left) and epoch D (right)

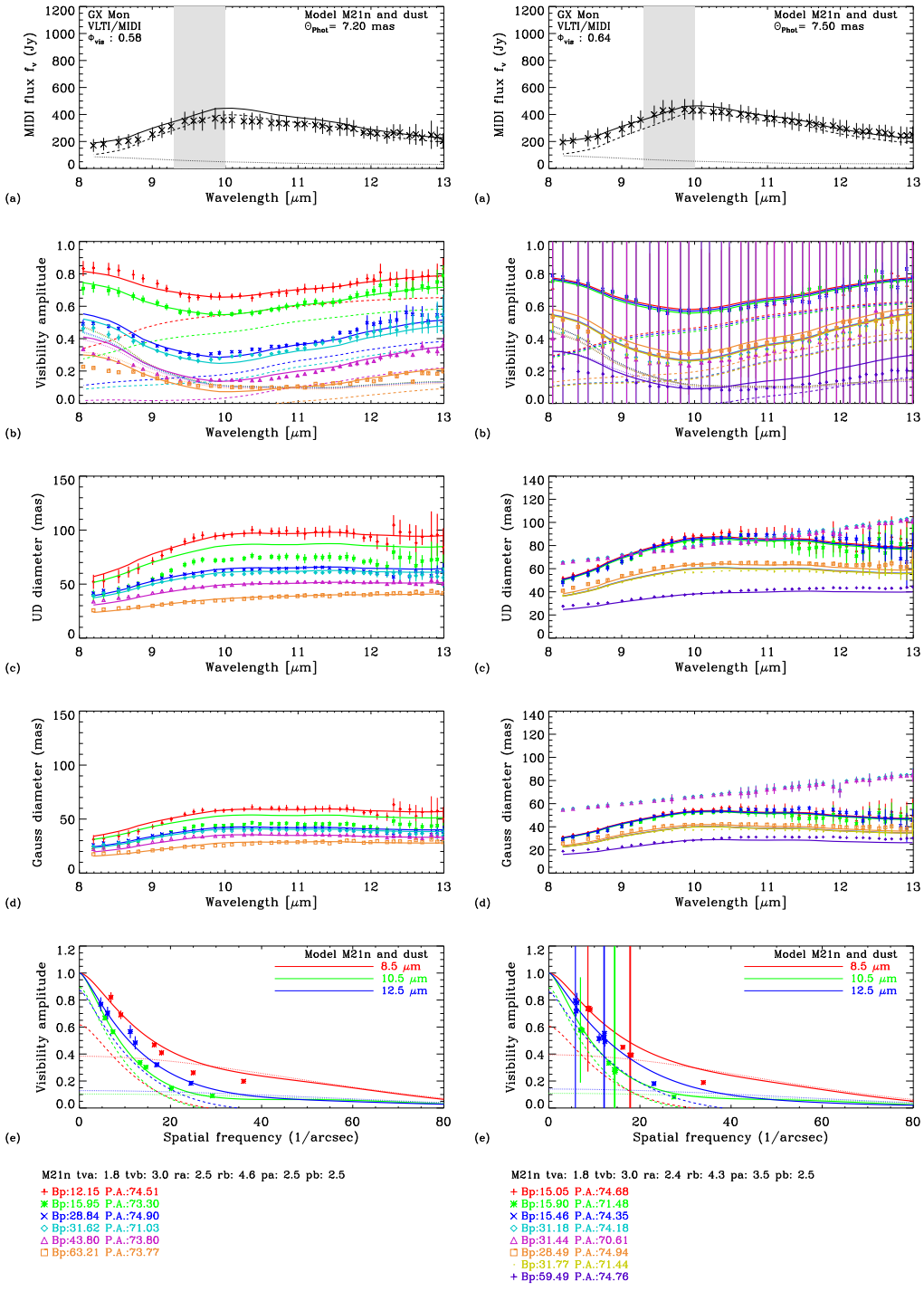

Figure E.3: GX Mon epoch E (left) and epoch F (right)

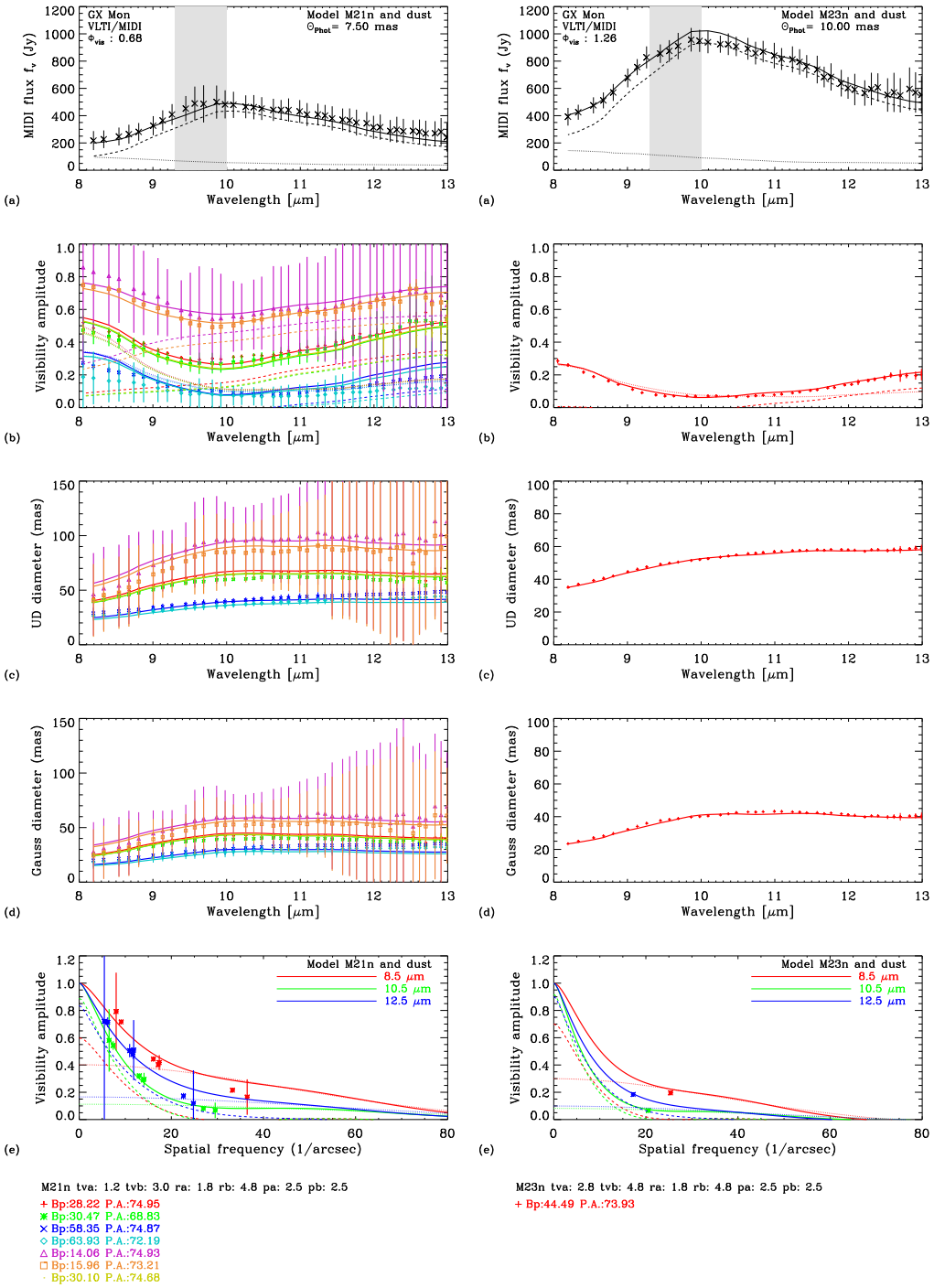

Figure E.4: GX Mon epoch G (left) and epoch H (right)

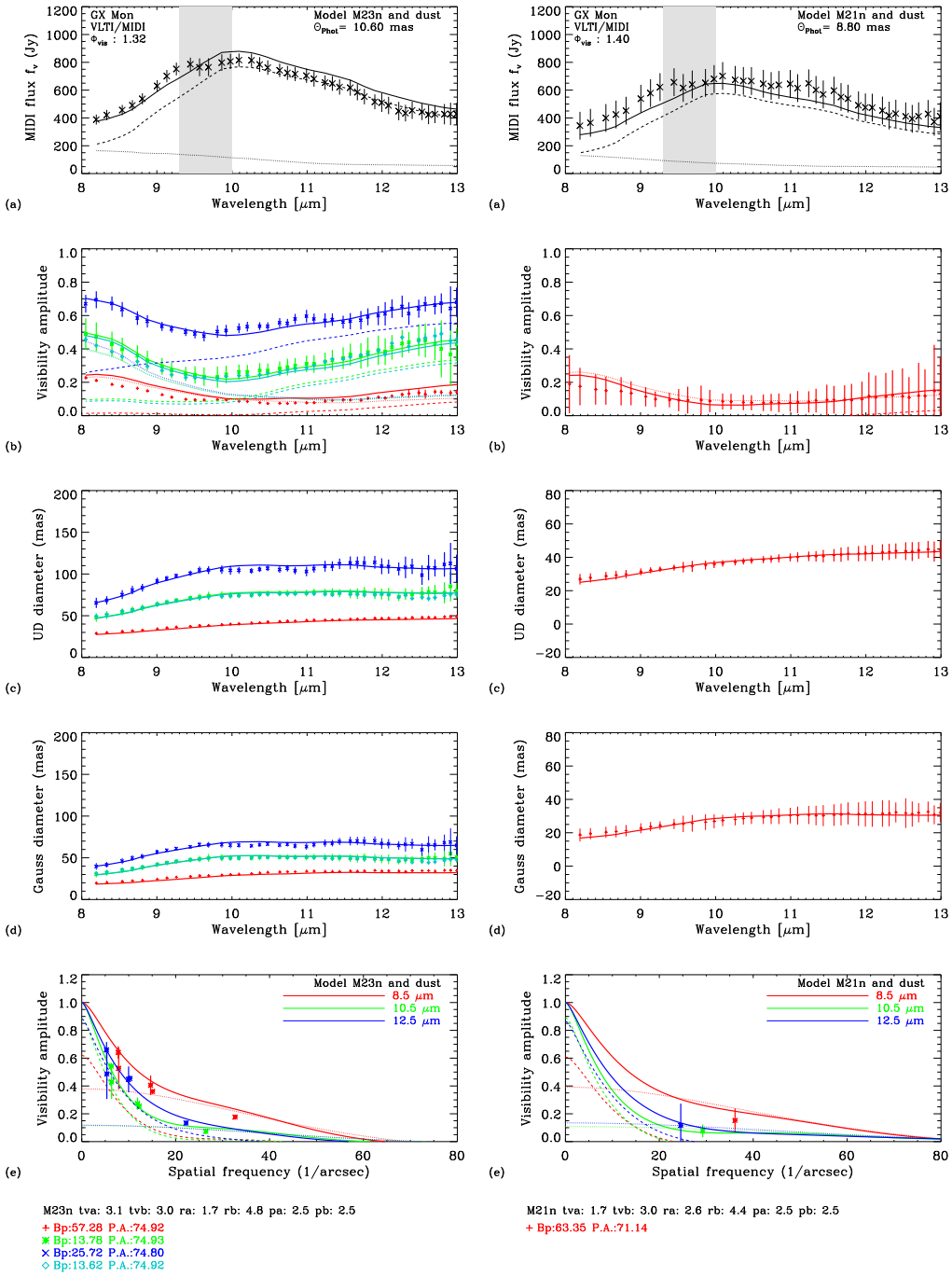

Figure E.5: GX Mon epoch I (left) and epoch J (right)

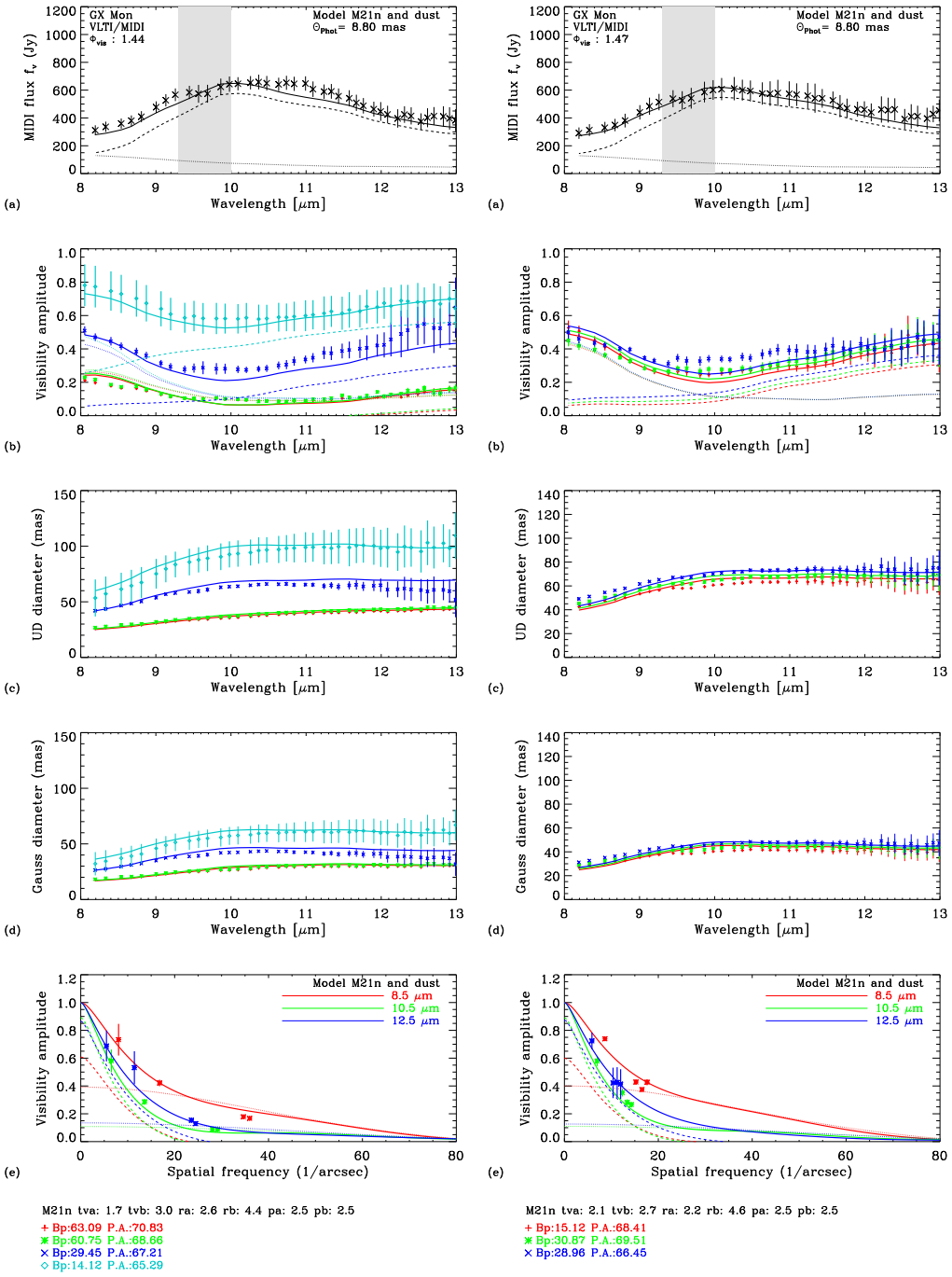

Figure E.6: GX Mon epoch K (left) and epoch L (right)

Appendix F

R Cnc epochs 1 – 2

In the following all the observational epochs are presented. The plots show VLTI/MIDI interferometric observations of R Cnc at 8-13μm. The panels show (a) the flux, (b) the visibility amplitude, (c) the corresponding UD diameter, (d) the corresponding Gaussian FWHM diameter as a function of wavelength. Panel (e) shows the visibility amplitude as a function of spatial frequency for three averaged bandpasses of 8-9 μm, 10-11 μm, and 12-13 μm. The gray shade indicates the wavelength region around 9.5 μm that is affected by atmospheric absorption. The epoch of observations and the stellar phase is indicated in the panel (a). The crosses with error bars denote the measured values. The solid lines indicate our best-fitting model, as described in Sect. 9.3.2. It consists of a combination of a radiative transfer model describing the surrounding dust shell and a dust-free dynamic model atmosphere representing the central star. The contributions of the stellar and dust components alone are indicated by the dotted and the dashed line, respectively. The best fitting M model and dust shell parameters for each epoch together with projected baseline length (B_p) and position angle (P.A.) are listed below the panel (e). Symbols and colors correspond to the individual observations.

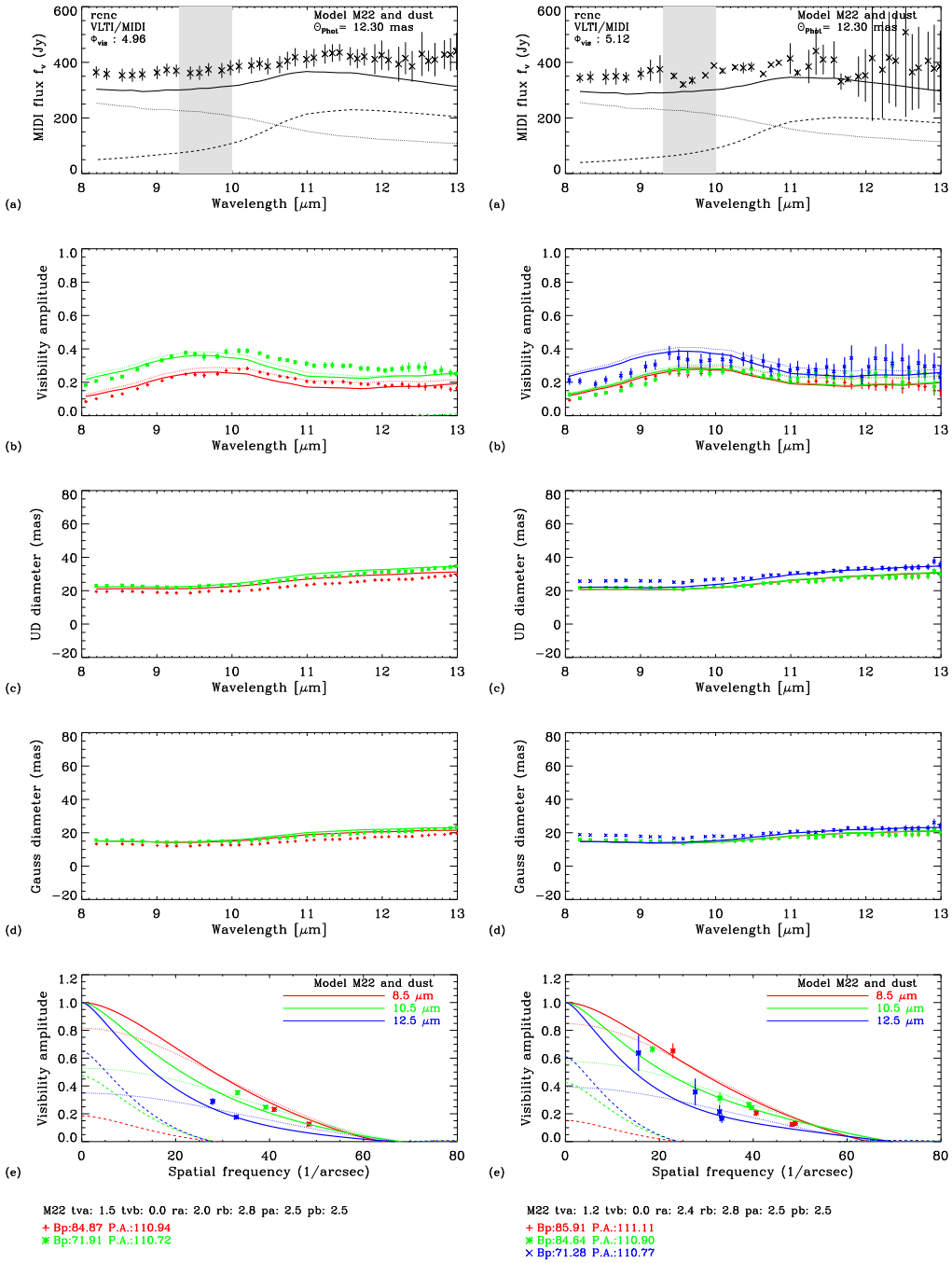

Figure F.1: R Cnc epoch A (left) and epoch B (right)

Motivation

La motivation générale de ce travail est d'apporter des réponses à des questions qui résistent depuis longtemps et concernent la dernière étape de l'évolution des étoiles de masse intermédiaire et faible qui se trouvent sur la branche asymptotique des géants « AGB » du diagramme HR. Ces étoiles subissent alors une importante perte de masse par expulsion de gaz et de poussière dans le milieu interstellaire, l'enrichissant ainsi du produit de la nucléosynthèse qui s'est déroulée auparavant dans leur cœur. Environ, 80% de toutes les étoiles traversent cette phase évolutive. Les étoiles AGB sont ainsi la principale source de poussière dans notre Galaxie (>50%), enrichissant le milieu interstellaire de matériau pour la formation d'étoiles et de planètes des générations suivantes.

Les étoiles AGB sont caractérisées par une importante perte de masse, qui se traduit par la formation d'une enveloppe circumstellaire autour du cœur de l'étoile. Les mécanismes responsables de cette perte de masse ne sont pas encore bien compris, et sont évidemment très étudiés. Les interactions entre pulsation, propagation d'onde de choc, formation de poussière et pression de radiation sont complexes, et il n'existe pas aujourd'hui de modèle de ces étoiles riches en oxygène capable de décrire l'ensemble du phénomène. Il est donc important de contraindre tous les processus en cause au moyen de toujours plus de données d'observation. La structure interne des étoiles AGB est constituée d'un cœur inerte de carbone et d'oxygène (C/O) entouré de deux couches bien séparées de matériel en fusion nucléaire. La composition moléculaire photosphérique est déterminée par l'abondance de C/O (Höfner, 2009). Les étoiles sont qualifiées ou bien de riches en carbone si C/0 ou de riches en oxygène dans le cas contraire. Le rapport C/O doit normalement augmenter au cours de l'évolution de l'étoile qui transporte vers la surface les éléments synthétisés dans le cœur. La partie la plus externe de l'atmosphère, soumise à des pulsations de grande amplitude qui produisent des ondes de choc, voit température et densité diminuer, ce qui fournit les conditions requises pour la formation de molécules et la condensation de grains. La partie externe de cette enveloppe est alors très opaque, ne laissant pas échapper le rayonnement de l'étoile, et on pense donc que c'est le vent produit par la pression de radiation sur les grains de poussière qui pousse l'enveloppe vers l'extérieur. Cette perte de masse peut atteindre un taux élevé jusqu'à $10^{-4}M_{\odot}$ par an (Matsuura et al., 2009) avec des vitesses d'expansion de 5 à 30 km/s (Höfner, 2005). Il reste cependant une incertitude sur l'efficacité de l'opacité de la poussière pour générer les vents importants des enveloppes riches en oxygène (Woitke, 2006; Höfner & Andersen, 2007). Environ 70% de la matière stellaire finit par se disperser dans l'espace au cours d'une phase dénommée « super-vent » qui ne dure que quelques dizaines de milliers d'années, et l'étoile AGB évolue alors vers l'état de nébuleuse planétaire (Sedlmayr, 1994). Le but du travail présenté dans cette thèse est d'analyser les enveloppes circumstellaires des AGB afin de mieux contraindre le

phénomène de perte de masse.

Une grande partie du flux lumineux des AGB est émis dans l'infrarouge. Les observations au sol sont limitées à quelques fenêtres spectrales dans le proche infrarouge (bandes J, H, K) et dans l'infrarouge moyen (bandes L, M, N, Q), le reste étant absorbé par des bandes moléculaires de l'atmosphère, et de plus gêné par l'émission thermique de la même atmosphère, qui produit un bruit de fond s'ajoutant à l'émission de l'étoile et de son enveloppe. Cependant les télescopes terrestres permettent bien plus facilement que les instruments spatiaux d'observer les variables AGB à grande amplitude à de nombreuses phases différentes de leur cycle d'activité. La résolution angulaire d'un télescope est limitée par son ouverture de diamètre d, et au sol par la turbulence atmosphérique. Pour l'observation de sources complexes telles que les étoiles AGB, la haute résolution angulaire (HRA) est essentielle, le diamètre angulaire typique étant d'environ 10 mas (milli-arc-seconde). La résolution d'un diamètre angulaire aussi petit nécessiterait un diamètre de télescope qui n'existe pas aujourd'hui. L'interférométrie est l'unique technique qui offre une alternative réalisable en combinant les faisceaux lumineux de deux ou plusieurs télescopes de dimensions individuelles relativement modestes, réalisant l'émulation d'un télescope virtuel dont la dimension (distances D entre les télescopes qu'on appelle les lignes de base) peut alors aller jusqu'à plusieurs centaines de mètres. L'augmentation de ces bases permet alors d'accéder à des très hautes résolutions angulaires, qui seraient celles d'un télescope virtuel de diamètre D. Une telle résolution de quelques mas permet de mesurer les diamètres stellaires et même des profils d'intensité le long du diamètre des étoiles proches. A partir de 3 télescopes interférométriques utilisés en mode « clôture de phase », il est possible d'obtenir des premiers éléments d'imagerie, tels que des informations sur une asymétrie de forme de l'étoile. La luminosité et l'atmosphère très étendue de ces étoiles en font des cibles privilégiées pour les observations en HRA.

Les instruments AMBER (proche infrarouge) et MIDI (infrarouge moyen) du VLTI de l'ESO au Cerro Paranal au Chili nous permettent d'étudier les enveloppes de molécules er de poussières le long des cycles d'oscillation. Les observations en proche infrarouge donnent accès à l'estimation du diamètre photosphérique, la température effective, les variations centre bord de l'intensité, alors que les observations MIDI en infrarouge moyen accèdent aux informations sur l'enveloppe et la zone de formation des poussières. En particulier, le but de ce projet est d'étudier la connexion entre le mécanisme de pulsation et la condensation des grains de poussière afin de pouvoir, en retour, mieux comprendre la perte de masse. En effet, malgré des progrès théoriques et observationnels remarquables, bien des aspects du fonctionnement des étoiles AGB demeurent mal décrits. Ce travail de thèse s'attaque aux questions suivantes : (i) Quel est le rôle joué par la pulsation de l'étoile et sa connexion avec le processus de formation de poussière et de perte de masse ? (ii) Quelle est la stratification de la composition chimique de l'atmosphère de ces étoiles ? (iii) Quelles sont les types de poussières dominantes dans une étoile donnée ? (iv) La nature de la poussière change-t-elle au cours d'un cycle de pulsation ? (v) La quantité de poussière varie-t-elle au cours d'un cycle de pulsation ? et (vi) Quel est le mécanisme de formation géométrique au cours de l'évolution de la phase AGB vers celle de nébuleuse planétaire ?

Pour tenter d'apporter des réponses à ces questions, nous avons étudié au moyen de multiples observations interférométriques 4 étoiles Mira riches en oxygène : RR Aql, S Ori, GX Mon et R Cnc. Les observations ont été effectuées avec diverses configurations du VLTI. Ceci permet de comparer des données obtenues à des phases différentes de leur pulsation mais dans des couver-

tures similaires du plan uv . Les observations testent ainsi les mêmes profondeurs d'atmosphère. Cet échantillonnage de données interférométriques, d'une richesse unique, permet de suivre la visibilité et la photométrie le long des cycles de pulsation. Les données peuvent ensuite être comparées au modèle d'atmosphère dynamique (sans poussière) représentant la source centrale, avec le modèle de transfert radiatif qui représente l'enveloppe de poussière. Les modèles d'atmosphère dynamique qui incluent la formation d'une enveloppe de poussière sont encore très rares, nos données sont donc comparées à la meilleure approche de modélisation aujourd'hui disponible. Il va en sortir les résultats suivants :

- Etude précise de la visibilité et de la photométrie en infrarouge moyen sur plusieurs cycles d'oscillation (2 séries de mesures pour R Cnc, 12 pour GX Mon, 13 pour RR Aql et 14 pour S Ori).
- Suivi détaillé de la variabilité sur plusieurs cycles
- Analyse d'observations en proche infrarouge pour RR Aql
- Estimation du diamètre stellaire (modèles uniforme et gaussien) pour chaque série de données dans chaque canal spectral.
- Estimation du diamètre photosphérique par ajustement des données au moyen d'un modèle d'atmosphère dynamique libre de poussière
- Estimation du diamètre angulaire (infrarouge moyen) par ajustement d'un modèle ad hoc de transfert radiatif pour l'enveloppe de poussière, la source centrale étant décrite par le modèle dynamique libre de poussière.
- Etude de la chimie des poussières pour chacune des 4 étoiles.
- Suivi des variations de l'épaisseur optique, du rayon interne de l'enveloppe de poussière et de la distribution de densité pour chaque type de poussière.
- Etude de l'écart éventuel à la symétrie sphérique
- Simulation des variations attendues de la visibilité et de la photométrie de cycle en cycle et à l'intérieur d'un cycle.

Les résultats obtenus permettent de raffiner l'état de l'art des codes d'atmosphère dynamique de transfert radiatif, qui en retour nous aide à mieux comprendre les processus physiques à l'œuvre.

Les deux premiers chapitres de la thèse sont dédiés à une introduction générale. Tout d'abord une introduction générale sur les étoiles AGB (1.1), comprenant l'évolution (1.1.1 et 1.1.2), la variabilité (1.1.4), la formation de molécules et de poussières (1.1.5) et la perte de masse (1.1.7). Le chapitre 2 traite de l'interférométrie infrarouge. Après une brève introduction sur les bases théoriques de l'interférométrie optique (2.1) le chapitre est dédié aux instruments AMBER et MIDI du VLTI. Description des instruments eux-mêmes (2.2.4 et 2.2.5), suivie de sections traitant de la préparation des observations (2.3), des observables (2.3.2 et 2.3.2) ainsi que des procédures spécifiques de traitement des données AMBER et MIDI (2.5 et 2.4). Le chapitre 3 commence la partie « pratique » par la description des données VLTI exploitées dans la suite. Tous les chapitres suivants représentent mon travail personnel effectué dans le cadre de cette thèse. J'ai pris en charge la réduction des données, leur application à l'approche de modélisation, la détermination de tous les paramètres stellaires, et les simulations destinées à interpréter les résultats en terme de physique stellaire. L'exception est le développement des codes (complexes) de transfert radiatif et de modèle dynamique d'atmosphère sans poussière (4.1 et 4.2) qui sont dus à Ireland et al. (2004a,b) et Ohnaka et al. (2006).

Le chapitre 3 traite de la théorie de la calibration des données et décrit un peu en détail les procédures d'exploitation de l'important volume de données obtenues pour ce travail. Ceci inclut le suivi des conditions ambiantes des observations (3.2) ainsi que les différentes approches de réduction et calibration, avec leur impact sur les résultats (3.4 et 3.5).

Le chapitre 4 explique l'analyse par modélisation effectuée ensuite. Les modèles de Hofmann et al. (1998); Bessell et al. (1996); Ireland et al. (2004a,b). Le modèle ad hoc de transfert radiatif **mpi_mcsim** (Ohnaka et al., 2006) est décrit en (4.2) et la section (4.3) décrit l'approche proposée par Wittkowski et al. (2007) de la modélisation, radiative de l'enveloppe de poussière ajoutée à la source centrale décrite par une atmosphère dynamique sans poussière. La section (4.4) détaille les étapes du processus de simulation, dans l'investigation des variations théoriquement prédites de cycle à cycle et à l'intérieur d'un cycle.

Les chapitres 5 à 9 décrivent les observations interférométriques des 4 étoiles citées. 13 époques d'observation MIDI de RR Aql dans le chapitre 5, les observations AMBER de la même étoile dans le chapitre 6. Les chapitres 7, 8, et 9 traitent des observations MIDI des 3 autres étoiles. La section 9.5 contient des résultats préliminaires de mesures de l'étoile R Cnc avec d'autres instruments, dans le cadre d'un programme de coopération.
Le chapitre 10 mentionne la prospective qu'annoncent les nouveaux instruments à venir dans le cadre du VLTI
Le chapitre 11 résume l'ensemble du travail et des résultats présentés.
La thèse se termine par six annexes, sur la sélection de « l'étoile du mois » pour la calibration des mesures AMBER (Annexex A), les tables de calibration MIDI (B), et la liste des époques d'observations effectuées avec MIDI pour chacune des 4 étoiles (C, D, E, F).

Conclusions

Cette thèse présente des résultats d'observations multi-époques d'étoiles évoluées de la branche asymptotique des géantes (AGB). Les étoiles ont été observées au VLTI au Chili au cours de plusieurs cycles de pulsation au moyen des interféromètres AMBER en proche infrarouge et MIDI en infrarouge moyen. Nous avons exploité de telles mesures avec MIDI sur plusieurs cycles des 4 étoiles Mira riches en oxygène RR Aql (13 époques), S Ori (14 époques), GX Mon (12 époques) et R Cnc (2 époques), ainsi que des mesures ponctuelles avec AMBER sur RR Aql et R Cnc. Nous avons pu ainsi étudier les caractéristiques de l'atmosphère et de l'enveloppe de poussière circumstellaire. Les données exploitées ont été modélisées au moyen de modèles de base de disque uniforme et de profil gaussien. Les données AMBER ont été modélisées au moyen de modèles d'atmosphère dynamique auto-excitée et sans poussière incluant la région de formation du continu photosphérique et la couche supérieure moléculaire (Ireland et al., 2004a,b). En supplément de ces modèles de base, les données MIDI ont été ajustées au moyen de la combinaison d'un modèle radiatif de l'enveloppe de poussière circumstellaire au dessus d'un modèle d'atmosphère sans poussière et pulsante par auto-excitation qui représente le profil de la source centrale. L'enveloppe de poussière utilise le code de transfert radiatif mcsim_mpi (Ohnaka et al., 2006). Les données interférométriques sont ainsi comparées à la meilleure approche de modélisation actuellement disponible. Les mesures interférométriques ont été effectuées au moyen de nombreuses configurations des bases interférométriques permettant de comparer utilement les différentes observations entre elles, en utilisant les mêmes longueurs et angles de base, pour pouvoir suivre les visibilités et la photométrie sur plusieurs cycles de pulsation des étoiles. Ces études aboutissent aux conclusions suivantes : (i) Les données interférométriques obtenues sur les 4 étoiles Mira oxygénées ne montrent aucune évidence significative de variabilité intra-cycle dans nos fourchettes d'incertitude (de 5 à 20%) et dans notre fourchette de phase couverte par les mesures (0.45 – 0.85 pour RR Aql, 0.9 – 1.20 pour S Ori, 0.25 – 0.65 pour GX Mon et 0.95 – 1.10 pour R Cnc). (ii) Les données n'ont pas non plus mis en évidence de variabilité significative d'un cycle à l'autre. (iii) Des variations photométriques plus ou moins significatives (de 1 à 5 σ) sont par contre visibles aussi bien en intra-cycle qu'entre cycles différents entre 8 et 13 μm. Ces données photométriques sont cependant entachées de trop d'incertitude pour que leurs variations puissent être considérées comme confirmées sur la base de nos mesures. Des mesures complémentaires au moyen d'un photomètre dédié, comme VISIR, seront nécessaires pour confirmer cette tendance. Cette étude est la première comparaison entre des mesures interférométriques et une combinaison de modèles d'intensité centrale et d'enveloppe radiative, le tout couvrant une large fourchette de valeurs de la phase de pulsation et pendant plusieurs cycles. Notre étude démontre que les spectres de visibilité et de photométrie peuvent être bien décrits par une telle combinaison de modèles. Pour chaque époque étudiée, nous pouvons choisir le meilleur modèle d'atmosphère dynamique, et les

paramètres de l'enveloppe de poussière tels que son épaisseur optique, son rayon intérieur, la loi de puissance de sa distribution de densité, ainsi que le diamètre angulaire photosphérique. Nous avons exploré deux types de poussière, des grains de silicate ou bien de Al_2O_3 avec une dimension fixe de grains choisie égale à $0.1\,\mu$m. Nous avons montré que l'enveloppe optiquement mince de RR Aql peut être modélisée au moyen des seuls grains de silicate avec un diamètre interne de l'ordre de 4 à 5 rayons photosphériques. L'addition d'une enveloppe de Al_2O_3 n'améliore en rien l'ajustement du modèle aux données. On ne peut cependant pas exclure l'existence d'une enveloppe poussiéreuse interne de Al_2O_3 avec une épaisseur optique moindre que celle des silicates. L'enveloppe de poussière de GX Mon est bien modélisée par une combinaison des deux types de grains, avec un rayon interne de Al_2O_3 de l'ordre de 2 à 2.5 rayons photosphériques, et un rayon interne de silicate environ deux fois plus grand, de 4 à 5 rayons photosphériques. Les enveloppes de poussière de S Ori et R Cnc peuvent être modélisées au moyen des seuls grains de Al_2O_3 sans aucune contribution de silicate, avec un rayon interne de 2 à 2.5 rayons photosphériques. Nos résultats sont compatibles avec ceux de Lorenz-Martins & Pompeia basés sur des données IRAS (2000). De nos résultats et des taux de perte de masse déjà publiés, on peut en déduire une possible séquence de condensation de poussière : R Cnc avec une chimie de grains de Al_2O_3, au taux de $0.2 \times 10^{-7}\,M_\odot$/an, S Ori avec également une chimie de grains de Al_2O_3, au taux de $2.2\ 10^{-7}\,M_\odot$/an, GX Mon avec une chimie des deux types de poussière ensemble au taux de $5.4\ 10^{-7}\,M_\odot$/an, et RR Aql avec une chimie de poussière de silicate au taux très rapide de $9.1\ 10^{-7}\,M_\odot$/an. Ces résultats vont dans le sens de la suggestion de Little-Marenin & Little (1990) et Blommaert et al. (2006) selon laquelle la poussière des étoiles de faible perte de masse est dominée par des grains de Al_2O_3 alors que celle des étoiles à taux de perte de masse plus important est plutôt dominée par les grains de silicate. Nous avons effectué des simulations des variations attendues de nos données photométriques et interférométriques en fonction de la phase du cycle en faisant varier les paramètres des modèles avec la phase. Ces simulations confirment que dans nos barres d'incertitude, on ne peut pas espérer détecter de variation significative, ni intra-cycle ni d'un cycle à l'autre. Les ordres de grandeur des variations attendues en flux photométrique et en visibilité sont inférieurs à 25 et 20% respectivement, trop faibles pour être clairement mis en évidence par nos mesures. Les résultats de ce travail permettront d'améliorer et de raffiner les codes de transfert radiatif et d'atmosphères dynamiques, et de progresser dans les modèles décrivant le processus de perte de masse et le mécanisme de vent stellaire. Les observations à venir dans le but de mieux contraindre ces modèles nécessiteront une meilleure précision photométrique, par exemple en utilisant l'instrument dédié VISIR au VLT, ainsi qu'une couverture plus complète des phases des cycles de pulsation. Plus de mesures interférométriques en proche infrarouge seront également nécessaires pour mieux contraindre les couches moléculaires atmosphériques proches de la photosphère.

Bibliography

Alvarez, R. & Plez, B. 1998, Astronomy and Astrophysics, 330, 1109

Arsenault, R., Alonso, J., Bonnet, H., et al. 2003, The Messenger, 112, 7

Balick, B. & Frank, A. 2002, ARA&A, 40, 439

Begemann, B., Dorschner, J., Henning, T., et al. 1997, Astrophysical Journal, 476, 199

Benson, P. J., Little-Marenin, I. R., Woods, T. C., et al. 1990, ApJS, 74, 911

Bessell, M. S., Brett, J. M., Wood, P. R., & Scholz, M. 1989, Astronomy and Astrophysics, 213, 209

Bessell, M. S. & Scholz, M. 1989, in IAU Colloq. 106: Evolution of Peculiar Red Giant Stars, ed. H. R. Johnson & B. Zuckerman, 67–80

Bessell, M. S., Scholz, M., & Wood, P. R. 1996, Astronomy and Astrophysics, 307, 481

Blommaert, J. A. D. L., Groenewegen, M. A. T., Okumura, K., et al. 2006, Astronomy and Astrophysics, 460, 555

Boboltz, D. A. & Wittkowski, M. 2005, Astrophysical Journal, 618, 953

Bonaccini, D., Hackenberg, W., Davies, R. I., Rabien, S., & Ott, T. 2000, The Messenger, 100, 27

Bordé, P., Coudé du Foresto, V., Chagnon, G., & Perrin, G. 2002, Astronomy and Astrophysics, 393, 183

Cohen, M., Walker, R. G., Carter, B., et al. 1999, Astronomical Journal, 117, 1864

Danchi, W. C., Bester, M., Degiacomi, C. G., Greenhill, L. J., & Townes, C. H. 1994, Astronomical Journal, 107, 1469

Deguchi, S. 1980, Astrophysical Journal, 236, 567

Driebe, T., Hofmann, K., Ohnaka, K., et al. 2008, in The Power of Optical/IR Interferometry: Recent Scientific Results and 2nd Generation, ed. A. Richichi, F. Delplancke, F. Paresce, & A. Chelli, 507–+

Feast, M. W., Glass, I. S., Whitelock, P. A., & Catchpole, R. M. 1989, Monthly Notices of the Royal Astronomical Society, 241, 375

Fedele, D., Wittkowski, M., Paresce, F., et al. 2005, Astronomy and Astrophysics, 431, 1019

Fox, M. W. & Wood, P. R. 1982, Astrophysical Journal, 259, 198

Freytag, B. & Höfner, S. 2008, Astronomy and Astrophysics, 483, 571

Gail, H.-P. & Sedlmayr, E. 1999, Astronomy and Astrophysics, 347, 594

Glindemann, A., Algomedo, J., Amestica, R., et al. 2003, in Society of Photo-Optical Instrumentation Engineers (SPIE) Conference Series, Vol. 4838, Society of Photo-Optical Instrumentation Engineers (SPIE) Conference Series, ed. W. A. Traub, 89–100

Goebel, J. H., Bregman, J. D., & Witteborn, F. C. 1994, Astrophysical Journal, 430, 317

Habing, H. J. & Olofsson, H., eds. 2003, Asymptotic giant branch stars

Haniff, C. A., Scholz, M., & Tuthill, P. G. 1995, Monthly Notices of the Royal Astronomical Society, 276, 640

Herbst, T., Ragazzoni, R., Andersen, D., et al. 2003, in Presented at the Society of Photo-Optical Instrumentation Engineers (SPIE) Conference, Vol. 4838, Society of Photo-Optical Instrumentation Engineers (SPIE) Conference Series, ed. W. A. Traub, 456–465

Herwig, F. 2005, ARA&A, 43, 435

Hofmann, K., Scholz, M., & Wood, P. R. 1998, Astronomy and Astrophysics, 339, 846

Hofmann, K.-H., Balega, Y., Scholz, M., & Weigelt, G. 2000, Astronomy and Astrophysics, 353, 1016

Hofmann, K.-H., Balega, Y., Scholz, M., & Weigelt, G. 2001, Astronomy and Astrophysics, 376, 518

Höfner, S. 2005, in ESA Special Publication, Vol. 560, 13th Cambridge Workshop on Cool Stars, Stellar Systems and the Sun, ed. F. Favata, G. A. J. Hussain, & B. Battrick, 335–+

Höfner, S. 2008, Astronomy and Astrophysics, 491, L1

Höfner, S. 2009, in Astronomical Society of the Pacific Conference Series, Vol. 414, Cosmic Dust - Near and Far, ed. T. Henning, E. Grün, & J. Steinacker, 3–+

Höfner, S. 2011, e-prints arXiv1102.5268H

Höfner, S. & Andersen, A. C. 2007, Astronomy and Astrophysics, 465, L39

Huggins, P. J. 2007, Astrophysical Journal, 663, 342

Hughes, S. M. G. & Wood, P. R. 1990, Astronomical Journal, 99, 784

Iben, Jr., I. & Renzini, A. 1983, ARA&A, 21, 271

Iglesias, C. A. & Rogers, F. J. 1993, Astrophysical Journal, 412, 752

Ireland, M. J. & Scholz, M. 2006, Monthly Notices of the Royal Astronomical Society, 367, 1585

Ireland, M. J., Scholz, M., Tuthill, P. G., & Wood, P. R. 2004a, Monthly Notices of the Royal Astronomical Society, 355, 444

Ireland, M. J., Scholz, M., & Wood, P. R. 2004b, Monthly Notices of the Royal Astronomical Society, 352, 318

Ireland, M. J., Scholz, M., & Wood, P. R. 2008, Monthly Notices of the Royal Astronomical Society, 391, 1994

Ivezic, Z. & Elitzur, M. 1997, Monthly Notices of the Royal Astronomical Society, 287, 799

Jacob, A. P. & Scholz, M. 2002, Monthly Notices of the Royal Astronomical Society, 336, 1377

Karovicova, I., Wittkowski, M., Boboltz, D. A., & Scholz, M. 2009, in American Institute of Physics Conference Series, Vol. 1094, 15th Cambridge Workshop on Cool Stars, Stellar Systems, and the Sun, ed. E. Stempels, 981–984

Karovska, M., Hack, W., Raymond, J., & Guinan, E. 1997, The Astrophysical Journal Letters, 482, L175

Karovska, M., Nisenson, P., Papaliolios, C., & Boyle, R. P. 1991, The Astrophysical Journal Letters, 374, L51

Kemper, F., Waters, L. B. F. M., de Koter, A., & Tielens, A. G. G. M. 2001, Astronomy and Astrophysics, 369, 132

Kervella, P., Gitton, P. B., Segransan, D., et al. 2003, in Society of Photo-Optical Instrumentation Engineers (SPIE) Conference Series, Vol. 4838, Society of Photo-Optical Instrumentation Engineers (SPIE) Conference Series, ed. W. A. Traub, 858–869

Koike, C., Kaito, C., Yamamoto, T., et al. 1995, Icarus, 114, 203

Kozasa, T. & Sogawa, H. 1997a, Astrophysics and Space Science, 255, 437

Kozasa, T. & Sogawa, H. 1997b, Astrophysics and Space Science, 251, 165

Kurucz, R. 1993, ATLAS9 Stellar Atmosphere Programs and 2 km/s grid. Kurucz CD-ROM No. 13. Cambridge, Mass.: Smithsonian Astrophysical Observatory, 1993., 13

Kwok, S. 2008, in IAU Symposium, Vol. 252, IAU Symposium, ed. L. Deng & K. L. Chan, 197–203

Lagarde, S., Lopez, B., Antonelli, P., et al. 2006, in Presented at the Society of Photo-Optical Instrumentation Engineers (SPIE) Conference, Vol. 6268, Society of Photo-Optical Instrumentation Engineers (SPIE) Conference Series

Lançon, A. & Wood, P. R. 2000, A&AS, 146, 217

Lattanzio, J. 2003, in IAU Symposium, Vol. 209, Planetary Nebulae: Their Evolution and Role in the Universe, ed. S. Kwok, M. Dopita, & R. Sutherland, 73

Lawson, P. R. 2000, in Principles of Long Baseline Stellar Interferometry, ed. P. R. Lawson, 325

Le Bouquin, J., Lacour, S., Renard, S., et al. 2009, Astronomy and Astrophysics, 496, L1

Leinert, C., Graser, U., Richichi, A., et al. 2003, The Messenger, 112, 13

Leinert, C., van Boekel, R., Waters, L. B. F. M., et al. 2004, Astronomy and Astrophysics, 423, 537

Little-Marenin, I. R. & Little, S. J. 1990, Astronomical Journal, 99, 1173

Lopez, B., Danchi, W. C., Bester, M., et al. 1997, Astrophysical Journal, 488, 807

Lopez, B., Wolf, S., Lagarde, S., et al. 2006, in Presented at the Society of Photo-Optical Instrumentation Engineers (SPIE) Conference, Vol. 6268, Society of Photo-Optical Instrumentation Engineers (SPIE) Conference Series

Lorenz-Martins, S. & Pompeia, L. 2000, Monthly Notices of the Royal Astronomical Society, 315, 856

Matsuura, M., Barlow, M. J., Zijlstra, A. A., et al. 2009, Monthly Notices of the Royal Astronomical Society, 396, 918

Mattsson, L., Wahlin, R., & Höfner, S. 2010, Astronomy and Astrophysics, 509, A14+

Mérand, A., Bordé, P., & Coudé du Foresto, V. 2005, Astronomy and Astrophysics, 433, 1155

Millan-Gabet, R., Pedretti, E., Monnier, J. D., et al. 2005, Astrophysical Journal, 620, 961

Miyata, T., Kataza, H., Okamoto, Y., Onaka, T., & Yamashita, T. 2000, Astrophysical Journal, 531, 917

Molster, F. J. & Waters, L. B. F. M. 2003, in Lecture Notes in Physics, Berlin Springer Verlag, Vol. 609, Astromineralogy, ed. T. K. Henning, 121–170

Monnier, J. D. 2003, Reports on Progress in Physics, 66, 789

Monnier, J. D., Bester, M., Danchi, W. C., et al. 1997, Astrophysical Journal, 481, 420

Monnier, J. D., Danchi, W. C., Hale, D. S., et al. 2000, Astrophysical Journal, 543, 861

Monnier, J. D., Geballe, T. R., & Danchi, W. C. 1998, Astrophysical Journal, 502, 833

Monnier, J. D., Millan-Gabet, R., Tuthill, P. G., et al. 2004, Astrophysical Journal, 605, 436

Morel, S., Rantakyrö, F., Rivinius, T., et al. 2008, in 2007 ESO Instrument Calibration Workshop, ed. A. Kaufer & F. Kerber, 451

Neri, R., Kahane, C., Lucas, R., Bujarrabal, V., & Loup, C. 1998, A&AS, 130, 1

Niccolini, G., Woitke, P., & Lopez, B. 2003, Astronomy and Astrophysics, 399, 703

Ohnaka, K. 2004, Astronomy and Astrophysics, 424, 1011

Ohnaka, K., Bergeat, J., Driebe, T., et al. 2005, Astronomy and Astrophysics, 429, 1057

Ohnaka, K., Driebe, T., Hofmann, K., et al. 2006, Astronomy and Astrophysics, 445, 1015

Ohnaka, K., Driebe, T., Weigelt, G., & Wittkowski, M. 2007, Astronomy and Astrophysics, 466, 1099

Ohnaka, K., Izumiura, H., Leinert, C., et al. 2008, Astronomy and Astrophysics, 490, 173

Onaka, T., de Jong, T., & Willems, F. J. 1989, Astronomy and Astrophysics, 218, 169

Ossenkopf, V., Henning, T., & Mathis, J. S. 1992, Astronomy and Astrophysics, 261, 567

Paladini, C., Aringer, B., Hron, J., et al. 2009, Astronomy and Astrophysics, 501, 1073

Perrin, G., Coudé du Foresto, V., Ridgway, S. T., et al. 1999, Astronomy and Astrophysics, 345, 221

Perrin, G., Verhoelst, T., Ridgway, S. T., et al. 2007, Astronomy and Astrophysics, 474, 599

Petrov, R. G., Malbet, F., Weigelt, G., et al. 2007, Astronomy and Astrophysics, 464, 1

Pojmanski, G., Pilecki, B., & Szczygiel, D. 2005, Acta Astron., 55, 275

Quirrenbach, A. 2001, ARA&A, 39, 353

Quirrenbach, A., Mozurkewich, D., Armstrong, J. T., et al. 1992, Astronomy and Astrophysics, 259, L19

Ragazzoni, R., Herbst, T. M., Gaessler, W., et al. 2003, in Presented at the Society of Photo-Optical Instrumentation Engineers (SPIE) Conference, Vol. 4839, Society of Photo-Optical Instrumentation Engineers (SPIE) Conference Series, ed. P. L. Wizinowich & D. Bonaccini, 536–543

Ragland, S., Le Coroller, H., Pluzhnik, E., et al. 2008, Astrophysical Journal, 679, 746

Ragland, S., Traub, W. A., Berger, J., et al. 2006, Astrophysical Journal, 652, 650

Ratzka, T. 2005, PhD thesis, Max-Planck-Institute for Astronomy, Königstuhl 17, 69117 Heidelberg, Germany

Sacuto, S., Aringer, B., Hron, J., et al. 2011, Astronomy and Astrophysics, 525, A42+

Samus, N. N., Durlevich, O. V., & et al. 2004, VizieR Online Data Catalog, 2250, 0

Samus, N. N., Durlevich, O. V., & et al. 2009, VizieR Online Data Catalog, 1, 2025

Scholz, M. & Takeda, Y. 1987, Astronomy and Astrophysics, 186, 200

Schwarzschild, M. 1975, Astrophysical Journal, 195, 137

Sedlmayr, E. 1994, in Lecture Notes in Physics, Berlin Springer Verlag, Vol. 428, IAU Colloq. 146: Molecules in the Stellar Environment, ed. U. G. Jorgensen, 163

Sloan, G. C. & Price, S. D. 1998, ApJS, 119, 141

Stencel, R. E., Nuth, III, J. A., Little-Marenin, I. R., & Little, S. J. 1990, The Astrophysical Journal Letters, 350, L45

Tatulli, E., Millour, F., Chelli, A., et al. 2007, Astronomy and Astrophysics, 464, 29

Tej, A., Lançon, A., Scholz, M., & Wood, P. R. 2003, Astronomy and Astrophysics, 412, 481

Tevousjan, S., Abdeli, K., Weiner, J., Hale, D. D. S., & Townes, C. H. 2004, Astrophysical Journal, 611, 466

Thompson, R. R., Creech-Eakman, M. J., & Akeson, R. L. 2002a, Astrophysical Journal, 570, 373

Thompson, R. R., Creech-Eakman, M. J., & van Belle, G. T. 2002b, Astrophysical Journal, 577, 447

Tielens, A. G. G. M. 1990, in Topical Seminar on Astrophysics and Particle Physics, p. 13 - 17, 13–17

Tristram, K. R. W. 2007, PhD thesis, Max-Planck-Institut für Astronomie, Königstuhl 17, 69117 Heidelberg, Germany

Tsuji, T. 2000, Astrophysical Journal, 538, 801

Tuthill, P. G., Danchi, W. C., Hale, D. S., Monnier, J. D., & Townes, C. H. 2000, Astrophysical Journal, 534, 907

van Belle, G. T., Dyck, H. M., Benson, J. A., & Lacasse, M. G. 1996, Astronomical Journal, 112, 2147

van Belle, G. T., Sahlmann, J., Abuter, R., et al. 2008, The Messenger, 134, 6

van Belle, G. T., Thompson, R. R., & Creech-Eakman, M. J. 2002, Astronomical Journal, 124, 1706

van der Veen, W. E. C. J., Huggins, P. J., & Matthews, H. E. 1998, Astrophysical Journal, 505, 749

Vardya, M. S., de Jong, T., & Willems, F. J. 1986, The Astrophysical Journal Letters, 304, L29

Vlemmings, W. H. T. & van Langevelde, H. J. 2007, Astronomy and Astrophysics, 472, 547

Wallace, L. & Hinkle, K. 1997, ApJS, 111, 445

Waters, L. B. F. M., Molster, F. J., de Jong, T., et al. 1996, Astronomy and Astrophysics, 315, L361

Weiner, J., Tatebe, K., Hale, D. D. S., et al. 2006, Astrophysical Journal, 636, 1067

Whitelock, P., Marang, F., & Feast, M. 2000, Monthly Notices of the Royal Astronomical Society, 319, 728

Wishnow, E. H., Townes, C. H., Walp, B., & Lockwood, S. 2010, The Astrophysical Journal Letters, 712, L135

Wittkowski, M., Boboltz, D. A., Driebe, T., et al. 2008, Astronomy and Astrophysics, 479, L21

Wittkowski, M., Boboltz, D. A., Ohnaka, K., Driebe, T., & Scholz, M. 2007, Astronomy and Astrophysics, 470, 191

Wittkowski, M., Glindemann, A., & Paresce, F. 2005, in Astronomical Society of the Pacific Conference Series, Vol. 340, Future Directions in High Resolution Astronomy, ed. J. Romney & M. Reid, 626–+

Wittkowski, M., Hummel, C. A., Aufdenberg, J. P., & Roccatagliata, V. 2006, Astronomy and Astrophysics, 460, 843

Woitke, P. 2006, Astronomy and Astrophysics, 460, L9

Wolf, S. 2003, Astrophysical Journal, 582, 859

Wolf, S., Henning, T., & Stecklum, B. 1999, Astronomy and Astrophysics, 349, 839

Wood, P. R. 1990, in Astronomical Society of the Pacific Conference Series, Vol. 11, Confrontation Between Stellar Pulsation and Evolution, ed. C. Cacciari & G. Clementini, 355–363

Wood, P. R. 1995, in Astronomical Society of the Pacific Conference Series, Vol. 83, IAU Colloq. 155: Astrophysical Applications of Stellar Pulsation, ed. R. S. Stobie & P. A. Whitelock, 127

Wood, P. R., Alcock, C., Allsman, R. A., et al. 1999, in IAU Symposium, Vol. 191, Asymptotic Giant Branch Stars, ed. T. Le Bertre, A. Lebre, & C. Waelkens, 151–+

Woodruff, H. C., Eberhardt, M., Driebe, T., et al. 2004, Astronomy and Astrophysics, 421, 703

Woodruff, H. C., Tuthill, P. G., Monnier, J. D., et al. 2008, Astrophysical Journal, 673, 418

Wyatt, S. P. & Cahn, J. H. 1983, Astrophysical Journal, 275, 225

Yaari, A. & Tuchman, Y. 1995, in Astronomical Society of the Pacific Conference Series, Vol. 83, IAU Colloq. 155: Astrophysical Applications of Stellar Pulsation, ed. R. S. Stobie & P. A. Whitelock, 139

Young, J. S., Baldwin, J. E., Boysen, R. C., et al. 2000a, Monthly Notices of the Royal Astronomical Society, 315, 635

Young, J. S., Baldwin, J. E., Boysen, R. C., et al. 2000b, Monthly Notices of the Royal Astronomical Society, 318, 381

Acknowledgment

I would like to begin by thanking my family, especially my mother for all the support, encouragement and for her uncritical never-ending belief in me, which only a mother can offer.

Most importantly, I would like to thank my supervisor, Markus Wittkowski, for his support throughout the project and for guidance when it was required. He also provided me, as the PI of the MIDI and AMBER program on late type stars, with the very rich set of data analyzed in this thesis.

I also would like to express thanks to my co-supervisor Eric Fossat, especially for his help with the administration, all the french translations, and moreover for the personal support when needed. I am thankful to both of my supervisors for giving me the opportunity to do my PhD thesis with them.

I take pleasure in acknowledging the European Southern Observatory (ESO) and its financial support with a studentship, and other amazing opportunities included in the 'package'. ESO is truly a great scientific environment to be part of. In this place, I would like to express special thanks to Bruno Leibundgut, the Director for Science, who supported me in the difficult moments with coordination of my PhD. I wish to all students to have such opportunity to be able to come and talk to somebody who has the incredible gift to listen, understand, and solve the problem in the best possible way. I extend my thanks to Michael Scholz, my formal collaborator, for his overmail guidance, scientific advice and suggestions which improved my work. I also thank Michael Irreland who took over developing his codes, and Gerard van Belle for many helpful scientific discussions.

I thank all who are involved in making publicly available the MIDI and AMBER data reduction software packages.

My thanks also go to all the scientists who helped me during my observing runs at the VLTI.

I benefited from discussions with Leonard Burtscher and Konrad Tristram concerning various aspects of the project.

I received very profitable scientific and professional advice from Dietrich Baade who really took his time for me.

I want to thank Isabelle Percheron for giving me advice how to improve my work and also for corrections and proof reading of the instrumental part of my thesis.

Now, I would like to thank to all my friends, students and fellows from ESO for a good company, laughs and for help to get through difficult times when needed. Thanks to Nadine, Karin, Michael, Steve, Giuseppina, Eli, Paula for reading the thesis (on top of my job applications etc.) so carefully, and for helpful comments, suggestions that contribute to make it better. I also want to thank Mathias for help with the programming, and for picking up the phone anytime I had not only a computer related problem.

I am very grateful to Greg, Matthias, Marghe, Behrang, Ati, and Giacomo for welcome distractions and moral support. Thank you for being my friends and such a good company on top of that.

I want to thank my office-mate Carolina for all the good times in our great office 405 where the time was always set to June 2008.

I thank all of you who helped me in some way or another and made the time so much nicer.

In the end, I would especially like to thank Filip who helped me to make everything happen.